

POLITECNICO DI TORINO

**Corso di Laurea Magistrale in Ingegneria dei Materiali**

Tesi di Laurea Magistrale

Functionalization and coatings on Ti surface for a better  
integration with soft tissues



**Relatrici**

Prof.ssa Silvia Maria Spriano

Ing. Sara Ferraris

**Candidata**

Angelica Luceri

29 Marzo 2019

Alla mia famiglia

"Devo liberarmi del tempo e vivere il presente giacché non esiste altro tempo che questo  
meraviglioso istante."  
Alda Merini

# Ringraziamenti

Un grazie sincero alla Professoressa Silvia Spriano e Sara Ferraris per la disponibilità e gentilezza. Vorrei ringraziare Alessio Varesano e Claudia Vineis del Centro Nazionale Ricerche (CNR-OSMAC) di Biella, per la collaborazione e i preziosi consigli e a Mirko Prato dell'Istituto Italiano di Tecnologia (IIT) di Genova, per la disponibilità. Ringrazio anche il Centro Nazionale Ricerche (CNR) di Torino, per avermi permesso di utilizzare i laboratori.

Un ringraziamento all'Institute of Polymers Composites and biomaterials (CNR-IPCB) di Napoli, per la collaborazione.

Grazie di cuore ad Anna, Cecilia, Laura e Francesca, per la loro presenza costante, ottime amiche e compagne di viaggio, che mi hanno ascoltato e supportato nei momenti di crisi.

Grazie a Luisa, Guido, Paolo, Tommaso, Leandro, Paolo, Michele, Pietro e Alberto, che, tra una pizza e un caffè, mi hanno fatto sentire a casa.

Grazie a tutti "i Gialli", per avermi fatto crescere e cambiare, per avermi fatto capire cosa significa essere un gruppo. Siete stati tutti un punto di riferimento importante.

Grazie zia Rosaria, una zia speciale, una seconda mamma. Grazie per esserci sempre anche se in maniera discreta e silenziosa.

Grazie a chi è lassù, per avermi lasciato il regalo più importante.

Grazie Fede per avermi sempre spronata e aiutata. Grazie per esserci quando ho bisogno, per avermi fatto da guida e poi avermi lasciata proseguire da sola. Sei un esempio. Anche se non lo dimostro, ti voglio bene.

Infine grazie alle due persone più importanti. Grazie papà per tutto: per tutti i sacrifici che hai fatto, per tutte le volte in cui ti sei svegliato all'alba per andare a lavorare, per tutte le volte in cui hai fatto anche ciò che non volevi pur di farci felici.

Grazie mamma, grazie per tutte le ore passate al telefono per consolarmi o tirarmi su, grazie per aver fatto ogni cosa pur di aiutare me e Fede a realizzare i nostri sogni, grazie per esserti rimboccata le maniche e avermi permesso di vivere quest'esperienza senza nessuna rinuncia. Spero un giorno di poter ripagare tutti i sacrifici che avete fatto.

Grazie anche per tutti i dolci e i pacchi che mi hai mandato, unica fonte di gioia nelle mie (e non solo) giornate di studio.

Grazie di cuore a tutti.

Vi voglio bene!



# Contents

<b>Introduction</b>	<b>iii</b>
<b>1 Keratin</b>	<b>3</b>
1.1 Biochemistry of $\alpha$ - and $\beta$ - keratin . . . . .	5
1.2 Properties . . . . .	7
1.2.1 Physicochemical properties . . . . .	7
1.2.2 Mechanical properties . . . . .	8
1.3 Extraction . . . . .	12
1.3.1 Oxidative methods . . . . .	12
1.3.2 Reductive methods . . . . .	13
1.3.3 Sulphitolysis method . . . . .	14
1.3.4 Use of ionic liquids . . . . .	15
1.3.5 Chemical-free hydrolysis . . . . .	16
1.4 Oral bacteria and keratin . . . . .	16
1.4.1 Oral bacteria . . . . .	16
1.4.2 Interaction between bacteria and keratin . . . . .	17
1.5 Fibroblasts and keratin . . . . .	18
1.5.1 Fibroblasts . . . . .	18
1.5.2 Wound healing . . . . .	18
1.5.3 Interaction between fibroblasts and keratin . . . . .	19
1.6 Keratin-based biomaterials . . . . .	20
<b>2 Coating</b>	<b>25</b>
2.1 Coating deposition process and techniques . . . . .	25
2.2 Theory of adhesion . . . . .	32
2.2.1 Mechanical interlocking theory . . . . .	32
2.2.2 Chemical/adsorbition theory . . . . .	32
2.2.3 Acid-base theory . . . . .	33
2.2.4 Diffusion or interdiffusion theory . . . . .	34
2.2.5 The electrostatic attraction theory . . . . .	34
2.3 Thermodynamic theory of adhesion . . . . .	36
2.4 Macroscopic adhesion testing . . . . .	37
2.4.1 Cause of failure . . . . .	38
2.4.2 Adhesion test . . . . .	39
2.5 Influence of different factors on coating adhesion . . . . .	45
2.6 Other considerations . . . . .	52

<b>3</b>	<b>Dental implants</b>	<b>55</b>
3.1	Oral cavity . . . . .	55
3.2	Structure of teeth . . . . .	55
3.2.1	Peridontum . . . . .	56
3.2.2	Peridontal disease . . . . .	57
3.3	Types of dental implants . . . . .	58
3.4	General features of dental implants . . . . .	62
3.4.1	Mechanical stability . . . . .	62
3.4.2	Biological stability . . . . .	64
3.4.3	Morphological stability . . . . .	65
<b>4</b>	<b>Materials and Methods</b>	<b>67</b>
4.1	Cutting, marking and polishing of samples . . . . .	67
4.2	Washing of samples . . . . .	68
4.2.1	Preparation of titanium cylinders . . . . .	68
4.3	Surface activation with plasma . . . . .	70
4.4	Surface activation with UV . . . . .	70
4.5	Coating deposition and functionalitation . . . . .	72
4.5.1	Solution of keratin at 7% wt . . . . .	73
4.5.2	Solution of keratin at 3% wt . . . . .	73
4.5.3	Solution of keratin at 1% wt . . . . .	74
4.5.4	Electrospinning . . . . .	76
4.6	Thermal treatment . . . . .	81
4.7	Surface characterization . . . . .	86
4.7.1	Tape test . . . . .	86
4.7.2	Scratch test . . . . .	88
4.7.3	SEM . . . . .	89
4.7.4	FESEM . . . . .	91
4.7.5	Roughness and homogeneity . . . . .	93
4.7.6	Wettability . . . . .	97
4.7.7	Stability in water . . . . .	97
4.7.8	Zeta potential . . . . .	99
4.7.9	FT-IR . . . . .	102
4.7.10	XRD . . . . .	104
4.7.11	XPS . . . . .	106
<b>5</b>	<b>Results and discussions</b>	<b>109</b>
5.1	Adhesion test . . . . .	111
5.1.1	Tape test . . . . .	111
5.1.2	Scratch test . . . . .	115
5.2	Thickness and homogeneity of the coating . . . . .	117
5.3	Wettability . . . . .	121
5.4	Stability in water . . . . .	124
5.5	Zeta potential . . . . .	126
5.6	FT-IR . . . . .	129
5.7	XRD . . . . .	134
5.8	XPS . . . . .	136
5.9	Roughness of titanium cylinder . . . . .	166
	<b>Conclusions</b>	<b>169</b>

*CONTENTS*

iii

**Bibliography**

**171**



# Introduction

In orthodontics, the fundamental aim is that to ensure goodness and success of a dental implant. Lot of studies have been conducted with regard to the portion of prosthesis in contact with the bone tissue, obtaining good results, but the main problem is related to the adhesion of the prosthesis to soft tissue, linked to the reduction of bacterial proliferation, due to the fact that the interface between trans-mucosal tissue and prosthesis, the part of collar and abutment, is widely different from interface between gingiva and teeth.

Because geometry, shape and topography influence interaction between dental implant and soft tissue, it is important to design the prosthesis, with the purpose of promoting adhesion and proliferation of gingival fibroblasts, reducing bacterial adhesion.

From a bibliography research, it has been found that commercially pure titanium is the best material for dental applications, due to its biocompatibility, in addition an important role is played by keratin, a protein which exhibits anti-bacterial properties and is capable to promote proliferation of fibroblasts. The main problem is adhesion of keratin to substrate: in fact weak bonds are created between coating and substrate, that easily causes the detachment from the titanium.

The aim of this dissertation is to analyze behavior of coated and functionalized titanium surfaces, treated in different ways, by keratin solution, in order to improve its adhesion to the substrate.

Keratin was deposited on disks of commercially pure titanium (grade 2), and its adhesion properties were studied.

The surface treatments on Ti carried out were:

- Polishing;
- Plasma treatment;
- Irradiation with UV.

Keratin adhesion was analyzed by using tape test and scratch test, and surface characterization was conducted: wettability, zeta potential, roughness, FT-IR, XRD, XPS analysis.

In addition, some titanium samples were functionalized by keratin and their characteristics were studied.

Adhesion properties of keratin nanofibers, deposited by Electrospinning technique at Centro Nazionale delle Ricerche (CNR-ISMAR) of Biella were analyzed. In order to evaluate keratin nanofibers behavior aligned on dental prosthesis, titanium cylinders were plasma-treated and electrospun nanofibers were deposited on the lateral surface, with SEM microscope, the morphology and the disposition of the fibers were analyzed: biological test will be conducted on these samples.



# Chapter 1

## Keratin

The term keratin, from the Greek *κερας*, meaning “horn”, indicates a group of filament-forming proteins of epithelia and is the most important biopolymer in animals (1). Keratins, represented in Figure 1.1, have a molecular weight between 40 and 70 kDa. Their structure is approximately 40% hydrophilic and 60% hydrophobic (2). They are characterized by a three-dimensional fibrillar hierarchical structure, and consists of small, nanometric amino acids that polymerise in a well-known sequence. Each keratin protein can vary in the number and sequence of amino acids, in charge, size and polarity. The amino acid sequence influences molecular structure and properties of secondary, tertiary and quaternary keratin proteins, the three-dimensional structure, and the type of the bonds (3).

Several functional groups are present in keratin, as disulphide (-S-S), carboxyl acid (-COOH) and amino ( $-NH_2$ ), which make keratin chemically reactive under certain conditions (4). In particular keratins are characterized by a large amount of sulfur-containing amino acid cysteine, with the thiol functional group, -SH. The thiol groups tend to pair up and, through oxidation, form a covalent sulfur-sulfur bond, a disulfide, known also as SS-bond or disulfide bridge, shown in Figure 1.2. The high content of cysteine makes keratin stable by forming network structure through joining adjacent polypeptides by disulfur cross-links, as shown in Figure 1.3. This disulfide bridges give important properties to keratin, in fact confer additional strength and rigidity by permanent, thermally cross-linked (5). Keratins also contain a high portion of glycine, the smallest of the 20 amino acids, characterized by a side-group formed by a hydrogen atom, and a high portion of alanine, whose functional side group is a methyl group. In Figure 1.4 is represented a general structure of amino acid molecule: for glycine -R is replaced by -H, for alanine, instead, by methyl group  $-CH_3$ . The amino group ( $-NH_2$ ) and the carboxyl group (-COOH) are the other functional groups of the molecule. In Table 1.1 the amino acid amount of extracted samples compared with the original wool is shown (6).

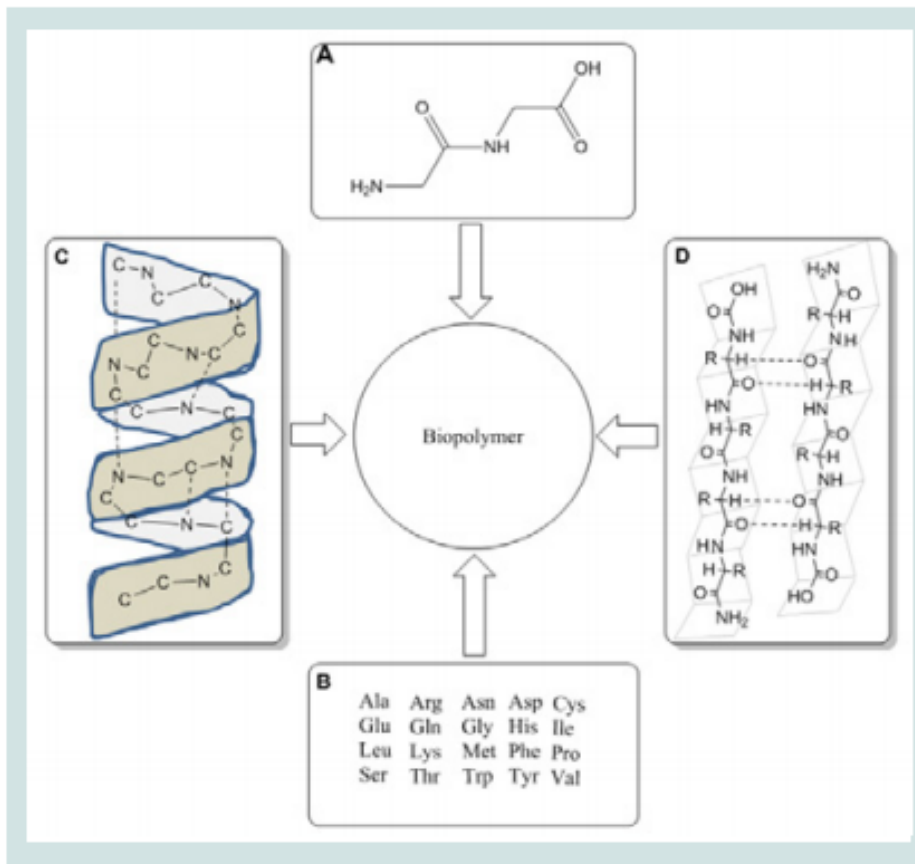


Figure 1.1: (A) unit of polypeptide, (B) sequence of amino acid, (C)  $\alpha$ -helix keratin structure, (D)  $\beta$ -sheets keratin structure (F1)

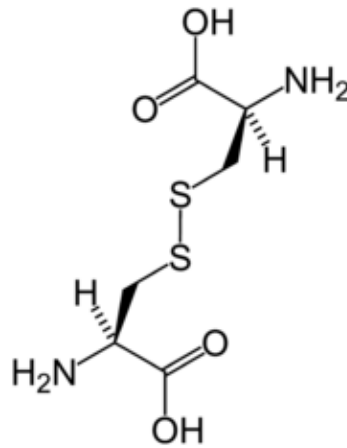


Figure 1.2: Disulfide bond (-S-S) (F2)

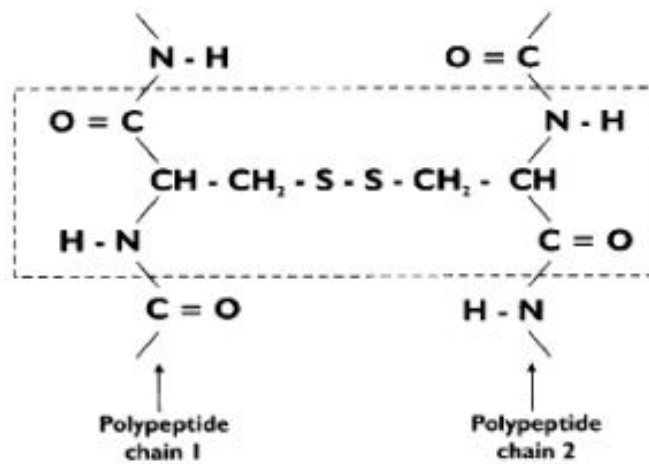


Figure 1.3: Representation of the diamino-acid cysteine residue linking two polypeptide chains by covalent bonding (F3)

## 1.1 Biochemistry of $\alpha$ - and $\beta$ - keratin

Generally keratins are divided into two groups:

- Alpha-keratins: they have an alpha-helical tertiary structure and are found in all vertebrates, in hair, horns, claws.
- Beta-keratins: they are formed by  $\beta$ -sheets and are found in reptile shells, claws of bird, nails (7).

$\alpha$ -keratin can constitute its filamentous state through the coiled coil assembly and, heteropolymeric pair formation of type I or acidic keratins and type II or basic keratins protein molecules. This two chains represent the monomeric unit of the keratin (Figure 1.5 (a)): each of one is constituted by a central alpha-helical rod (of a length of 46 nm), with a non helical C- and N- terminal regions, which create bonds with other intermediate filaments and matrix. In the central rod region, there are points without helical links, named in figure L1, L12, L2.

In order to form the  $\alpha$ -keratin structure, as shown in Figure 1.6 (a), hydrogen bonds, formed

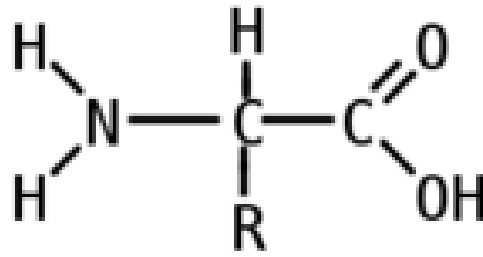


Figure 1.4: General structure of amino acid molecule F4

between two isolated right-handed chain, stabilize the structure and cause the chain to twist and form a left-handed coiled-coil, called dimer, of length of 45 nm, by disulphide cross link, utilising the many cystein amino acids found in  $\alpha$ -keratin. Then dimers create protofilament, with a diameter of 2 nm, by aggregating end-by-end and staggering side-by-side via disulphide bonds. Two protofilaments create a protofibril and four protofibrils create a helical shape with a diameter of 7 nm. Then this structure packs in a supercoiled conformation and links with the matrix proteins rich of cysteine or glycine (1).

Based on the amount of disulfide bonds,  $\alpha$ -keratin can be classified in: hard alpha-keratins, characterized by high cysteine content, which causes an increase in sulfur-sulfur bonds creation improving mechanical properties, and in soft alpha-keratins, characterized by a smaller content of disulfide bonds, making the structure more flexible (7).

The unit molecule of  $\beta$ -keratin consists of three regions, shown in Figure 1.5 (b): central domains, which is the central part of a polypeptide chain, folding several times and forming  $\beta$ -sheet and C- and N- regions with different lengths and compositions. In beta-keratin 32 amino acids form central rod domain, 23 and 47 amino acids form respectively head and tail domains. The plated sheets arrange into filaments, C- and N- terminal constitutes the matrix and wind around central region, in order to create  $\beta$ -keratin (1).

The  $\beta$ -sheet structure, shown in Figure 1.7 (a), is characterized by inter-chain hydrogen bonds which packed  $\beta$ -strands which can be parallel or antiparallel. The formation of  $\beta$ -keratin is a process which involves a central region of a one polypeptide chain to form four lateral strands linked by hydrogen bonds, creating a pleated sheet. Then two pleated sheets are related, superpose and run in opposite direction creating a filament of 4 nm of diameter (Figure 1.7 (b)). The terminal part of the peptide creates the matrix (1).

An X-ray diffraction shows that keratin can be distinguish in feather pattern and amorphous pattern: the feather pattern and  $\beta$ -keratins have the same characteristic reflection, while the amorphous pattern forms the amorphous matrix of  $\alpha$ -keratinous tissues (1). As shown in Figure 1.8,  $\alpha$ -keratin gives a pattern with an equatorial reflection of spacing 0.98 nm, which corresponds to the distance between  $\alpha$ -helical axes, and a meridional reflection of spacing 0.515 nm which relates to the  $\alpha$ -helix pitch projection. The  $\beta$ -keratin has a prominent axial repeat of 0.31 nm reflection, which is the distance between residues along the chain in a  $\beta$ -sheet, the 0.47 nm equatorial arc, which is the distance between chains in a  $\beta$ -sheet and the broad equatorial reflection at 0.97 nm, corresponding to intersheet distance.

As said before, each keratin protein is characterized by a chain of amino acids, as the primary structure: the amino acid sequence and the particular position of an amino acid in the chain can influence the three-dimensional structure of the molecule and its properties.

Post-translational modifications of keratin, such as the formation of disulphide bonds, phosphorylation, glycosylation, inter- or intrachain peptide bonds, influence the conformation of

Table 1.1: Comparison between amino acid extracted and contained in wool (T1)

Amino acid	Wool fiber (mole%)	Keratoses (mole%)	Kerateine (mole%)	Sulfo-kerateine (mole%)	Hydrolyzed keratin (mole%)
CYA	0.2	7.8	0.3	0.4	0.2
ASP	9.3	10.5	9.6	8.4	8.8
SER	11.7	11.6	11.0	11.9	10.7
GLU	15.6	17.7	15.6	14.6	19.5
GLY	7.3	6.7	8.1	8.1	9.0
HIS	0.5	0.5	0.5	0.5	0.5
ARG	5.9	6.0	6.4	6.1	5.9
THR	6.8	7.0	6.6	7.5	6.2
ALA	5.7	5.8	5.6	5.2	8.3
PRO	3.1	3.2	3.2	4.2	3.7
LANT	0.4	0.6	0.6	0.7	2.3
1/2CYS	9.5	0.0	8.1	10.6	0.5
TYR	2.5	2.2	3.0	2.7	2.4
VAL	5.5	5.3	5.3	5.1	5.8
MET	0.4	0.1	0.3	0.2	0.5
LYS	4.0	3.5	3.5	2.8	3.4
ILE	2.9	2.7	2.8	2.6	2.9
LEU	7.1	7.3	7.6	6.3	7.9
PHE	1.8	1.6	2.0	1.7	1.6

keratin molecule, and molecular weight and pI values. Phosphorylation and dephosphorylation are perhaps the most important post-translational modifications of keratins: prevent the interaction of keratins with other molecules, cause changes in solubility, modify the conformation of keratin filaments.

All intermediate filaments are proteins with a tripartite secondary structure made up by N-terminal head domain, a  $\alpha$ -helical rod domain and a C-terminal tail domain. Each domain is divided in subdomains. Domains and subdomains interact with those of other keratin molecules, forming heterodimers, tetramers and then keratin filament. This structure can change under physical forces, such as tension or compression, or under chemical processes.

The tertiary structure is a heterodimer formed by the rod domains of one acidic and one basic keratin in parallel orientation. This constitutes the first building block of keratin filaments. They are heteropolymer containing equimolar amount of type I and type II keratins. Keratins are characterized by the capacity for creating a complex quaternary structure, including the formation of a tetramer, an octamer and a "unit length filament" (3).

## 1.2 Properties

### 1.2.1 Physicochemical properties

The presence of intermolecular and intramolecular disulfide bridges and interchain peptide linkages make keratins insoluble. In order to obtain keratin derivatives, different methods have been proposed: for alpha-keratinous materials, reduction, oxidation and sulphitolysis methods have been used, while, for beta-keratinous materials, alkaline thioglycollate and a combination of a disulfide bond-breaking reagent and a protein denaturant have been used. This method are used

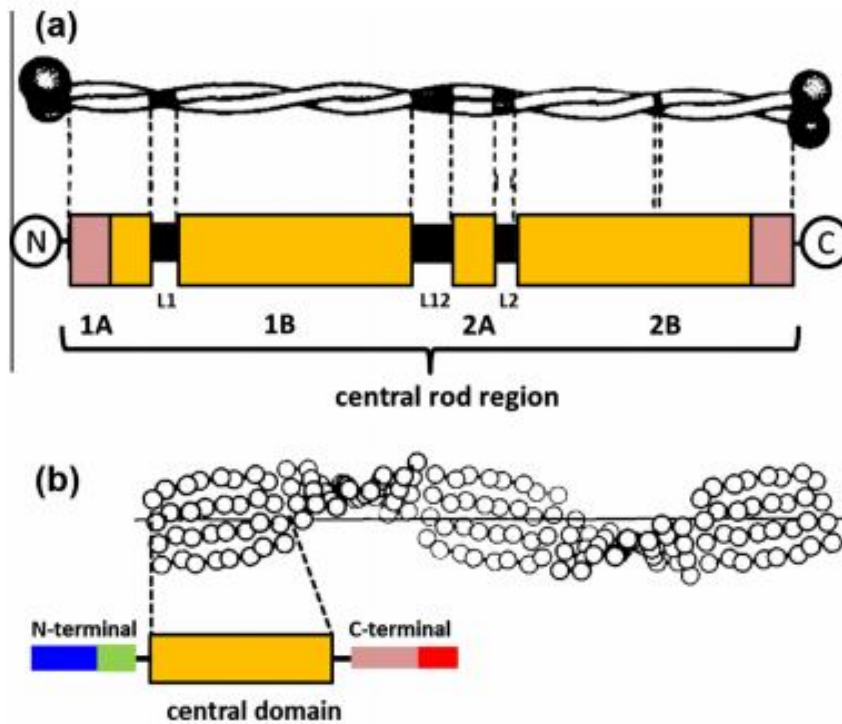


Figure 1.5: (a) Molecular unit of  $\alpha$ -keratin filament, (b) Molecular unit of  $\beta$ -keratin filament (F5)

in keratin extraction processes and will be explained later.

Generally to determine physicochemical properties of keratins, they have to be placed in solutions of urea and reductant agents.

Based on molecular weight and pI, this solubilized keratins are separated through electrophoresis phenomena.

As said before, based on two-dimensional gel-electrophoresis technique, it was found two groups of keratins, type I and type II: type I keratin proteins tend to be smaller, characterized by a molecular weight between 40 and 56,5 kDa and containing more acidic amino acids, such as aspartic acid; whereas type II keratin proteins are larger, with a molecular weight in the range of 50-70 kDa and containing more basic amino acids, such as lysine (3). Bowden et al. found different pI values for keratins of type I and type II: type I keratins have a pI in the range between 4.9–5.4, whereas type II keratins have a pI in the range between 6.5–8.5. Differences in molecular weight and pI values of keratin proteins in various species are based on: genes contained in keratin, post-transcriptional processing of the messenger RNA, post-translational processing of the protein or variations in the number of phosphorylated or glycosylated amino acid residues (3).

## 1.2.2 Mechanical properties

Mechanical properties of the keratinous materials change according to the host animals originated, to the different organization of cells at micro and macroscale and to hydration level. In general the  $\beta$ -sheet has a higher stiffness than  $\alpha$ -helix, and is possible to see a transition from  $\alpha$ -helix to  $\beta$ -sheet under tensile load. Figure 1.9 shows a scheme of this transition during which hydrogen bonds are reformed: a progressive unraveling of the  $\alpha$ -helical coiled coil domains, a refolding of the stretched  $\alpha$ -helices into  $\beta$ -sheets, and a spatial expansion of the  $\beta$ -structured zones occur (1).

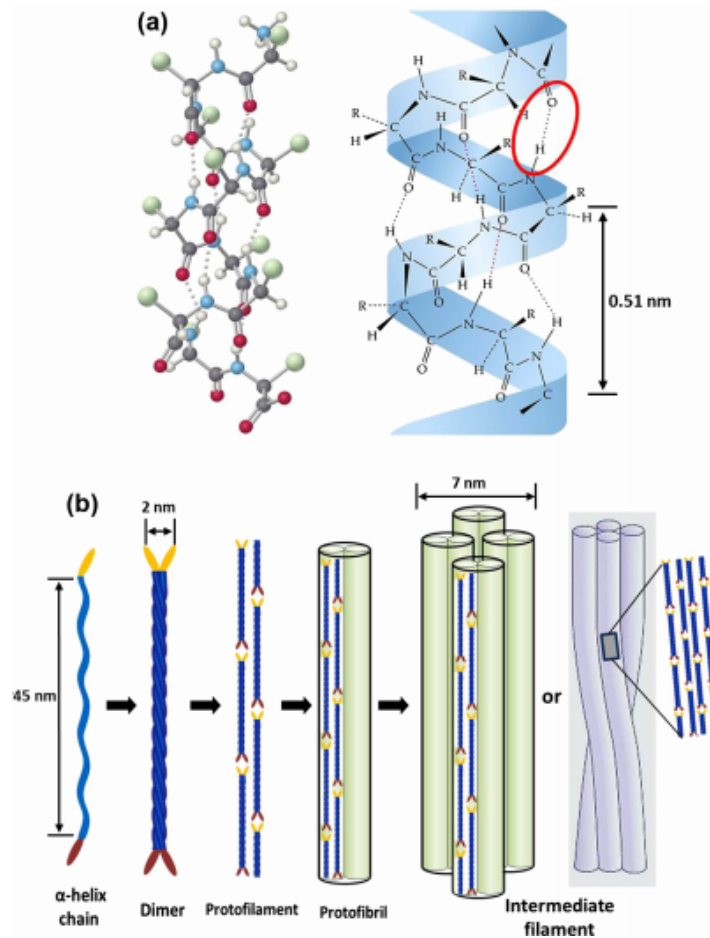


Figure 1.6: (a) Structure of  $\alpha$ -keratin filaments. Hydrogen bond is shown. (b) Formation of an intermediate filament starting from a  $\alpha$ -helix chain (F6)

The tensile stress-strain curve exhibits three regions:

- a near linear Hookean region in which chains are stretched, with bond arrangement altered but without changes in structure;
- a yield region in which the  $\alpha$ -helical coiled coils start unraveling and forming  $\beta$ -pleated sheets;
- a post-yield region with increasing slope where a majority of  $\beta$ -sheets are formed.

In general, Young's modulus changes in a range between 0,005 to 4,5 GPa, whereas strength changes between 12 and 221 MPa, under the same humidity conditions.

Figure 1.10 shows stress-strain curves of different keratinous material. The curves are characterized by:

- an elastic region, with a Young's modulus in the range between 1 and 5 GPa;
- a plastic region, with a lower slope;
- a change in slope, which represents strengthening of failure, if the slope increases or decreases.

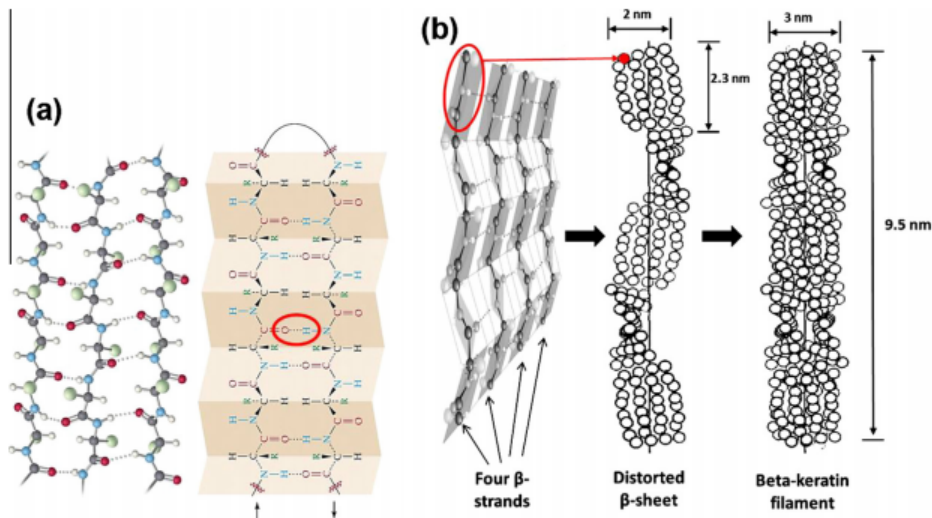


Figure 1.7: (a) structure of  $\beta$ -keratin filament. (b) formation of  $\beta$ -keratin filament (F7)

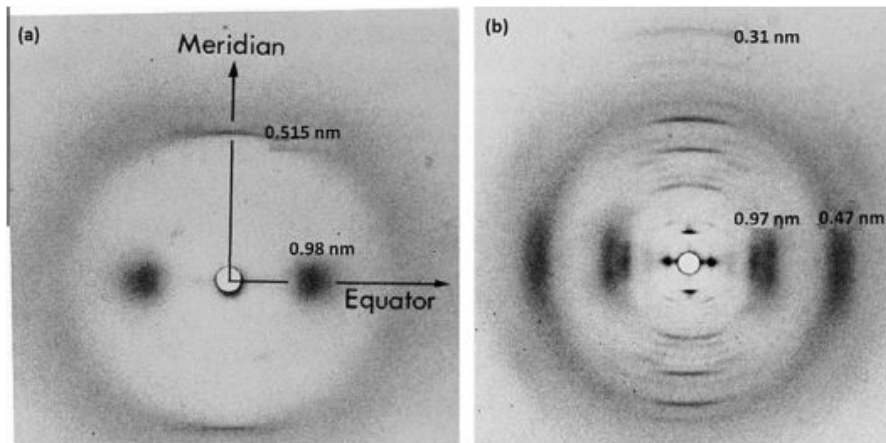


Figure 1.8: (a) X-ray diffraction pattern of  $\alpha$ -keratin and (b) X-ray diffraction pattern of  $\beta$ -keratin (F8)

Different responses are a consequence of the structural organizations of the filaments and matrix, the arrangements of keratinized cells and/or sample preparation (1).

Because keratin is a filament form protein, orientation, packing and volume fraction of filaments influence the mechanical behavior of  $\alpha$  and  $\beta$  keratins.

It's possible to increase hardening by mineralization with calcium or others salts. Szewciw et al. studied the contribute of calcification to whale baleen  $\alpha$ -keratin. Although little is known about whale baleen, it is the highly calcified keratinous material (with a content of calcium of 41 mg/g while wool contains 2,8 mg/g). Calcium salt crystallite are deposited between intermediate filaments, this increases stiffness and strength. Tensile tests on different baleen bristles and wool reveal that calcification increases stiffness of the baleen. In Figure 1.11 are reported whale baleen bristles from sei, humpback and minke whales compared with wool fibers, (b) natural and decalcified wool fibers, (c) natural and decalcified sei baleen bristles, (d) natural and decalcified humpback baleen bristles, and (e) natural and decalcified minke baleen bristles. The sei and humpback baleen have a higher content of calcium salt than minke, and it explains higher Young's modulus and yield strength. Figure 1.11 (b), (c), (d) and (e) shows how decalcification changes

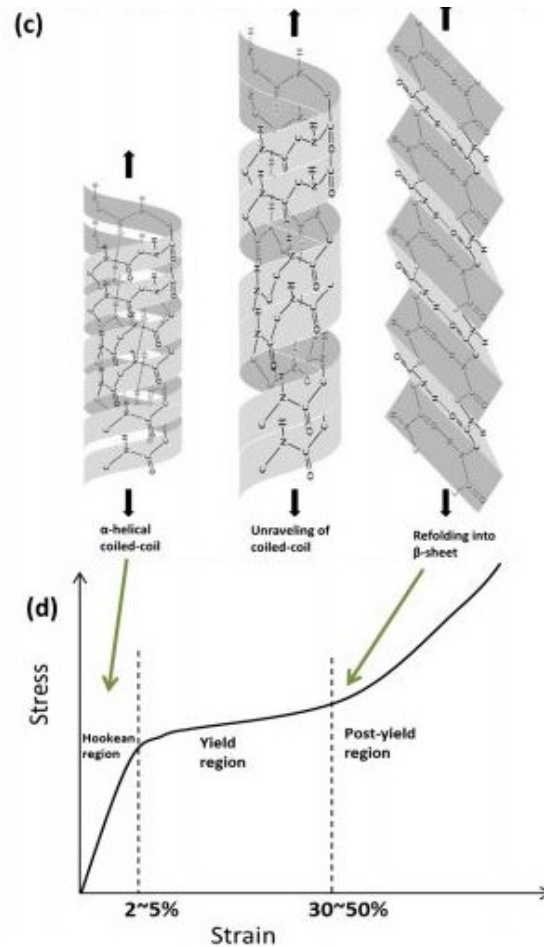


Figure 1.9: Transition from  $\alpha$ -helix to  $\beta$ -sheet keratin under tensile load (F9)

mechanical properties of wool and three baleen bristles: it is possible to note that decalcification results in a decrease of Young's modulus (9).

Mechanical properties of  $\alpha$  and  $\beta$ -keratin can change with different level of humidity. An humidity increase causes a decrease in stiffness and strength and an increase in breaking strength. It is possible to note that matrix protein are water sensitive, whereas intermediate filaments are crystalline and they are not affected by water content. Water can interact with protein molecules in different way:

- molecules of water are arranged between chains, acting as a cross link and swelling agent and causing a reduction of interaction due to the increase between interchain space;
- water can cause an increase in the mobility of the chain because it replaces secondary bond, such as hydrogen bond, between chains;
- a three dimensional water-keratin molecule network is formed. It reduce stiffness and increase the segmental mobility of the molecules (1).

Figure 1.12 show a schematic diagram of this mechanisms.

Keratin is viscoelastic. Viscoelasticity plays an important role in keratinous material, because it favours energy absorption and damps load fluctuation. A viscoelastic material undergoes creep, which represents deformation in relation to time with a constant load, and stress relaxation, which represents stress reduction in relation of time with strain constant. As a consequence

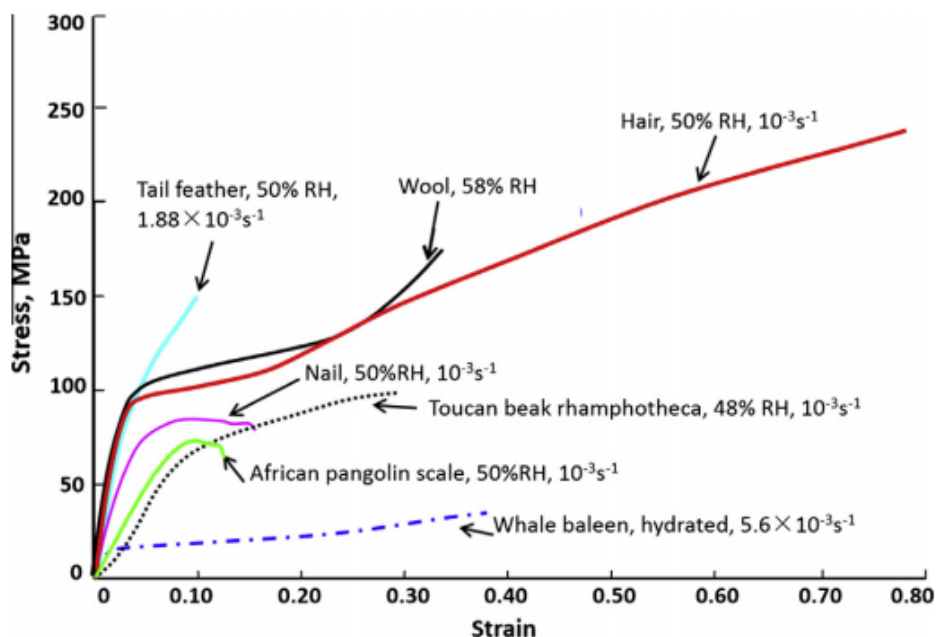


Figure 1.10: Tensile stress-strain curves of different keratinous materials (F10)

of this, the material has strain rate sensitivity, i.e. strain rate influences mechanical properties and a transition from ductile to brittle fracture behaviour is possible, if strain rate increases. Generally, in keratinous tissues, an increase of strain rate produces an increase in stiffness and strength with decrease of breaking strain (1).

### 1.3 Extraction

To extract keratin, disulphide bonds have to be broken. Keratin can be extracted by:

- unprotected solubilization: this way is characterized by the degradation of both the backbone peptide bonds and the interchain disulfide bridges;
- protected solubilization: in this case keratin macromolecules are intact, due to a preferential cleavage of the disulfide bridges, and a disruption of the intermolecular hydrogen bonds.

In both cases, there is the difficulty of maintaining the solubilized polypeptides in a colloidal state. Solubilized keratins tend to precipitate because of their hydrophobicity and disulfide bridges tend to reassemble from the newly resulted sulfhydryl groups (10). To extract keratin, disulphide bonds have to be break, for this reason different method have been proposed: oxidative, reductive, sulphitolysis, chemical-free method and using ionic liquids.

#### 1.3.1 Oxidative methods

An oxidative solubilization of keratin occurs with the use of oxidizing agents, such as hydrogen peroxide, organic peracids, inorganic persalts. In general, it is seen as a cooperative effect of oxidative agents and alkali. Today, the most system used is made up by peracetic acid and peroxide inorganics and alkali, due to its efficiency and the fact that is environmentally ecofriendly (11).

Yamanda et al. found a method to solubilized hair and wool in only one-stage, using hydrogen peroxide in concentration between 25-35% in weak alkaline medium, at a pH value in the range

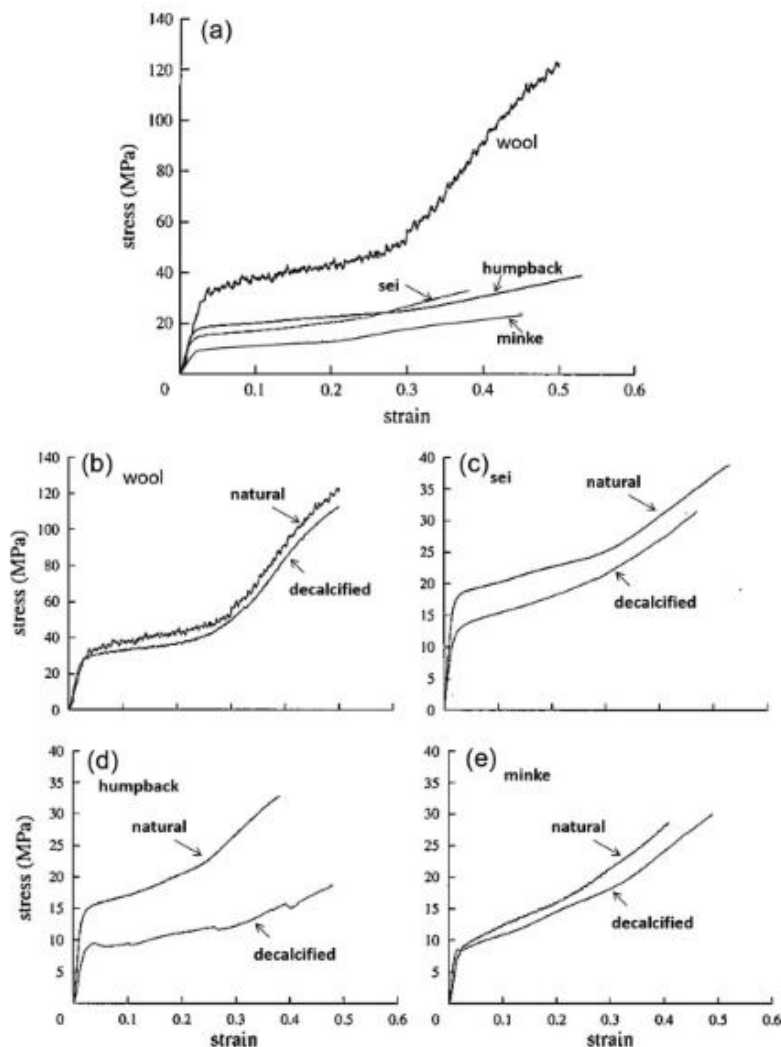


Figure 1.11: Baleen bristles from sei, humpback and minke whales compared with wool fibers, (b) natural and decalcified wool fibers, (c) natural and decalcified sei baleen bristles, (d) natural and decalcified humpback baleen bristles, and (e) natural and decalcified minke baleen bristles (F11)

of 8-9. This method has a solubilization yield of 99,7% and the keratin obtained has a molecular weight between 25 and 67 kDa (12).

### 1.3.2 Reductive methods

Niloofer et al. studied a method to extract keratin from wool and feather, based on enzymatic treatment with a reducing agent. They washed wool and feather in an aqueous solution containing a non-ionic detergent and sodium carbonate. Then the fatty matter was removed and the solvent was evaporated in ambient condition, then the samples were washed in distilled water. The fibers were cut and dried at  $100^{\circ}\text{C}$  for an hour. It was discovered that to obtain the maximum extraction is important to use 1 g/L sodium dodecyl sulfate as surfactant, and 2,6% (v/v) protease as savinase, in addition to 8.6 and 6.4 g/L sodium hydrogen sulfite as reducing agent for wool and feathers, respectively, at liquor to fiber ratio of 25 mL/g for 4 hr. Extracted keratin were composed of high-sulfur matrix protein and  $\beta$ -keratin. FT-IR analysis shows that there are not significant changes in the structure of fiber after enzymatic hydrolysis (13).

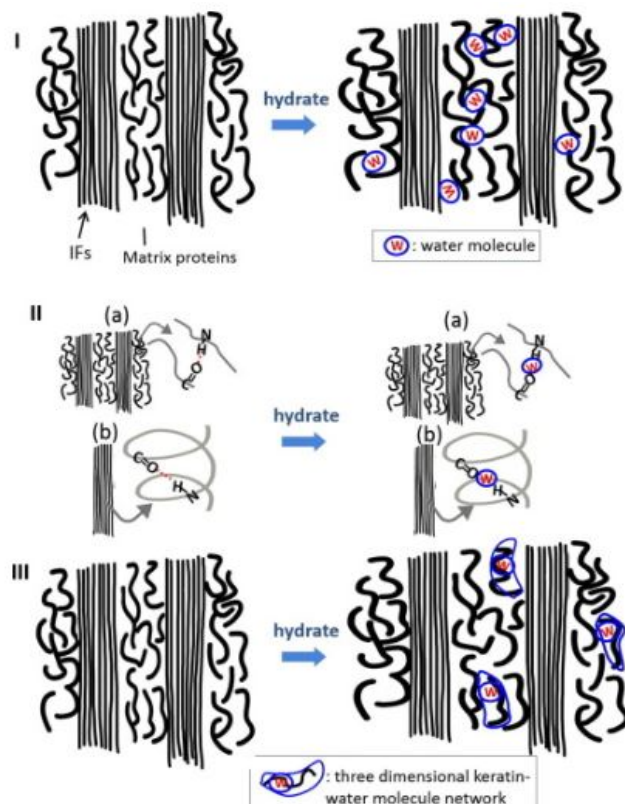


Figure 1.12: (I) water act as cross links and a swelling agent (II) water may replace the hydrogen bonds and (III) in the matrix, water may form a three dimensional keratin–water network (F12)

Wang et al. used sodium sulphide to dissolve human hair and to extract keratin. Waste human hair were washed, dried and cut into 5-10 mm pieces. 1 g of hair is put into a mixed solution containing 60 g/L sodium sulphide  $Na_2S \cdot H_2O$ , 2 g/L of urea and 10 g/L of sodium dodecyl sulfate. The solution was stirred every 30 minutes, to prevent the hair from sticking. After 120 minutes the solution was cooled and then filtered, and the dried residue was weighed. The filtrate was centrifuged and the supernatant liquid were dialysed for 48 h (every 12 h change distilled water), then dried, and the keratin powder was obtained. In this condition dissolution rate was more than 92,29%, and was found that increases with sodium sulfite concentration and with an increase of dissolution temperature. The extraction rate of keratin was 62,98% (14).

Also Jiang Shui-qing et al. used sodium sulfite as two disulfide bond reducing agent, sodium hydroxide as stratum corneum disrupting agent, twelve sodium dodecyl sulfate as keratin stabilizing agent. They found the effect of NaOH amount, of  $Na_2SO_3$  and of reaction time on the yield of keratin. The yield of keratin increases with the increasing of NaOH amount (Figure 1.13) (15).

### 1.3.3 Sulphitolysis method

Sulfitolysis describes the cleavage of a disulfide bond by sulfite, in order to give a thiol and a S-sulfonate anion. Varesano et al. extracted keratin from wool by sulphitolysis with sodium metabisulfite. First the fiber were washed in order to eliminate fatty matter. A solution of 300 mL consisting of urea and  $Na_2S_2O_5$  was prepared, the cleaned fibers were added to this solution and the pH value was adjusted to 6,5 with NaOH. The solution was shaken for 2 hours at  $65^\circ C$ , then was filtered (filters had pore size of 30  $\mu m$  and 5  $\mu m$ ) and dialyzed against distilled water,

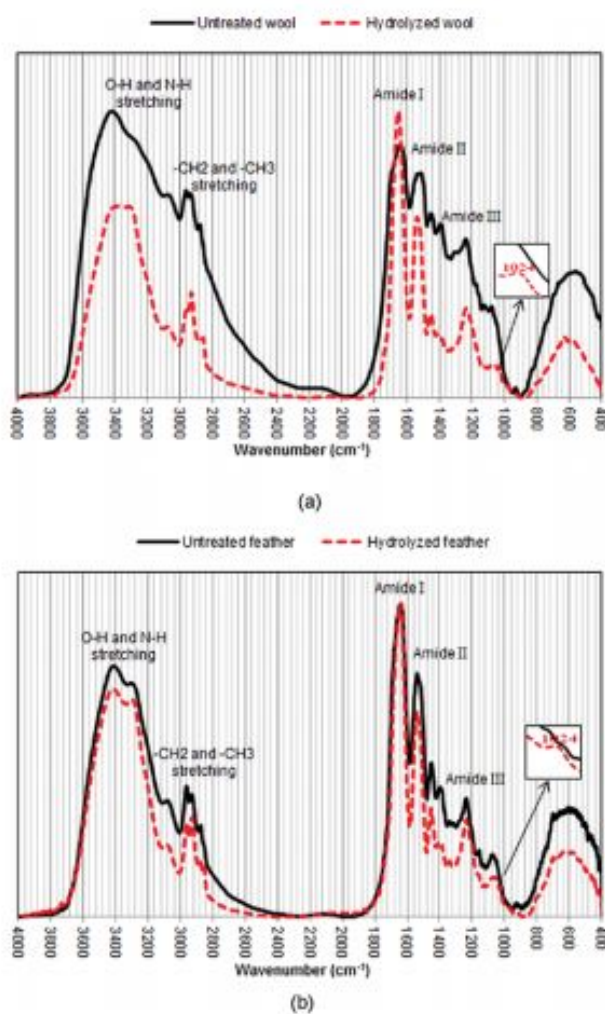


Figure 1.13: FT-IR spectra of (a) wool and (b) feather (F13)

at room temperature for 3 days. After this time the keratin solution was frozen and lyophilized in order to obtain keratin powder (16).

### 1.3.4 Use of ionic liquids

To accelerate dissolution of natural polymer, ionic liquids, a group of salts existing as liquids at low temperatures, are used. They have different advantages: are eco-friendly, non flammability, chemical and thermal stable, inexpensive and easily recyclable, in addition they have remarkable solubility due to their own ionic structure comparing with traditional solvents.

Yimei et al. selected common water-soluble imidazole ionic liquids to dissolve poultry feather and to extract keratin. Generally some additives are used, in order to improve extraction efficiency. In this case  $Na_2SO_3$  is used to unfold the disulphide bonds and to accelerate the dissolution of keratin. Duck feather were used, after they were washed, dried and cut into small pieces. The optimum extraction conditions for keratin are: 20 wt.% of water in IL-water, 10 wt.%  $Na_2SO_3$  in liquid phase, the weight ratio of liquid/feather = 20, extraction temperature at 90°C, and extraction time of 60 min. They found that amino acids of keratin and feather were the same: arginine, threonine, serine, glutamic acid, and cystine. They compared molecular weight value of extracted keratin with those of published data and found correspondance (17).

### 1.3.5 Chemical-free hydrolysis

This method is environmental ecofriendly and is an alternative to traditional method: the use of heat and pressure can break disulfide bridges and attacks the peptide backbone. It is possible to choose between steam hydrolysis/steam explosion and superheat water. Steam explosion involves hot steam, between  $180^{\circ}\text{C}$  and  $240^{\circ}\text{C}$ , and a pressure of 1-3,5 MPa. The biomass is treated in this conditions, and a compressive explosion follows, leading to a mixture of water-soluble peptides, free amino acids and a solid residue (18).

Yin et al. proposed a method to extract keratin using water at  $220^{\circ}\text{C}$  for 120 minutes. In this way total cystine bridges are cleaved. The resulting oligopeptides had the ability to self-assemble in needle-like crystals which tend to nucleate heterogeneously and develop highly repetitive structures (19).

## 1.4 Oral bacteria and keratin

### 1.4.1 Oral bacteria

The oral cavity is formed by different surfaces, each coated with a plethora of bacteria, called bacteria biofilm. Some of this bacteria are the cause of oral diseases, such as caries and periodontitis, which are the most common (20). This characteristic microorganisms find in oral cavity a good environment to grow, thanks to the presence of water and nutrients and a moderate temperature. Resident microbes of the water adhere to teeth and gum and are able to resist to flow that would take them from mouth to stomach, where some of them are destroyed by hydrochloric acid (21).

In oral cavity, an important role is played by saliva. It consist of approximately 99% water, containing various electrolytes, such as sodium, potassium, calcium, chloride, magnesium, bio-carbonate phosphate and proteins, enzymes, immunoglobulins, polypeptides and oligopeptides. It has important functions in protection and lubrication of oral cavity, is responsible for initial digestion, is critical for maintaining the chemical-physical integrity of tooth enamel, due to mineralization and demineralization, and for tissue repair. Saliva has also antibacterial properties, due to the presence of: immunoglobulin A, which neutralize viruses, bacterial, enzyme toxins, lysozyme, which hydrolyze cellular wall of some bacteria, lactoferrin, which causes bacteriocidal or bacteriostatic effects on several microorganisms, peroxidase, which offers antimicrobial activity (22).

In oral cavity of healthy individuals, it is possible to distinguish two types of bacteria: Gram-positive and Gramnegative (Table 1.2), according to the result in the Gram stain test, used to classify bacteria into two groups according to their cell wall. During the test a crystal violet stain is used: if bacteria take up the stain and appear to be purple-colored at microscope is a Gram-positive bacteria; whereas if bacteria cannot retain the violet stain is a Gram-negative bacteria.

In the first case, the peptidoglycan layer in the bacterial cell wall is thick and rigid and retains the stain after the decolorization stage of the test; in the second case, alcohol degrades the outer membrane of gram-negative cells and makes the cell wall porous.

In gram-negative bacteria, the peptidoglycan layer is between an inner cell membrane and bacterial outer membrane. Gram-positive bacteria are more receptive to antibiotics than gram-negative bacteria because of the absence of outer membrane (23).

Table 1.2: Gram-positive and Gram-negative bacteria (T2)

GRAM-POSITIVI	GRAM-NEGATIVI
<i>Actinomyces</i>	<i>Actinobacillus</i>
<i>Arachnia</i>	<i>Bacteroides</i>
<i>Bacterionema</i>	<i>Capnocytophaga</i>
<i>Bifidobacterium</i>	<i>Eikenella</i>
<i>Lactobacillus</i>	<i>Fusobacterium</i>
<i>Micrococcus</i>	<i>Haemophilus</i>
<i>Peptostreptococcus</i>	<i>Leptotrichia</i>
<i>Propionibacterium</i>	<i>Moraxella</i>
<i>Rothia</i>	<i>Neisseria</i>

### 1.4.2 Interaction between bacteria and keratin

A lot of studies show that keratin has the capacity to promote fibroblasts proliferation and is resistant to enzymes that break down other proteins, such as trypsin, but there is a group of enzymes capable of degrading keratin. Some of this are: protease, keratinase and beta-keratinase (24).

In general degradation is confined to gram-positive bacteria, such as *Bacillus*, *Lysobacter*, *Nester-nokia*, *Kocurica* and *Microbacterium*, but recently it is discovered that also gram-negative bacteria have the same effect on keratin. These keratinolytic micro-organisms live in different ecological and environment conditions and have different capacities to degrade keratin.

Keratinolytic activity was studied by Mikx et al. using fluorescein isothiocyanate (FITC)-labeled keratin, obtained mixing keratin and FITC in 200 ml of 0.2 M carbonate bicarbonate buffer and stirred for 4 h at room temperature. Labeled keratin was pelleted, washed in bio-carbonate buffer and sterilized with acetone. Cells of several bacteria were grown, washed and suspended in 2.5 ml of 0.2 M phosphate buffer with 1 mM dithiothreitol (DTT). To this suspension 0.5 ml of 0.4% (wt/vol) FITC-labeled keratin in the same buffer was added, and the suspension was then incubated for 24 h at 37°C. The degradation of keratin was estimated by measuring the fluorescence of the degradation products in the supernatant of the reaction mixtures in a luminescence spectrometer. It was been exploited the insoluble nature of substrate to separate it from FITC-labeled degradations products which are measurable in the surfactant of the reaction mixture. Different high-molecular-weight products were released by the bacteria tested, indicating endokeratinolytic activity. DTT stimulated the activity and might have made the keratin more accessible to enzymatic degradation by reduction of S-S bridges. Keratinolytic activity varied among the different bacteria and between strains of the same species (25).

Riffel et al. studied a method to select and characterize microorganisms with keratinolytic activity isolated from a poultry processing plant. Identification is based on morphological and biological tests and on the analysis of Gram-stained cells, and the results are compared with data of standard species. Three isolates were Gram-negative, one was Gram-positive. They analyzed the effect of temperature on growth and proteolytic activity. Bacterial strains were isolated from feather waste and were inoculated onto plates and incubated at 22°C, 30°C, 37°C, 46°C, 55°C for 24 hours. Bacteria presented different temperature range of growth and optimal proteolytic activities between 30°C and 37°C. The capacity to degrade different keratin wastes was also evaluated: keratinase was produced on all substrate, but maximum value was obtained on feather meal and feathers. Some of isolated showed maximum keratinolytic activity in shorter

time than those of others. In addition, during feather degradation, pH values increased with a trend similar to other keratinolytic microorganisms and this represents an indication of the keratinolytic potential of microorganisms (26).

Matikevičienė et al. selected keratin-degrading bacteria from poultry processing plant wastewater and studied their capacity to degrade chicken feathers. Keratinolytic activity was monitored for 24, 48 and 72 hours. All microorganisms were grown at  $37^{\circ}\text{C}$  and showed different levels of keratinolytic activities, depending on cultivation time. The highest activity was observed after 48 hours, except for one bacteria whose keratinolytic activity maximum was after 24 hours. After 72 hours, keratinolytic activity decreased by all bacteria (27).

Cochis et al. studied antibacterial activity of Ag-doped keratin nanofibers. They analyzed uncoated mirror polished titanium surface, polished titanium surface with keratin nanofiber coating and polished titanium surface with Ag-doped keratin nanofiber coating and studied bacterial adhesion after 24, 48 and 72 hours. Polished titanium surface was the most contaminated specimens. Polished Ti surface with keratin nanofiber has a behavior similar to the previous case. Good results have been obtained with the use of silver ions as antibacterial agent. It was found that silver damages bacterial cell membranes and can stop DNA transcription and cellular respiration.  $\text{Ag}^+$  interacts with thiol groups and inhibits respiratory enzymes. The effect of silver is very rapid, a good result has been obtained after 24 hours and after 48 and 72 hours the Ag antibacterial effect increases (28).

## 1.5 Fibroblasts and keratin

### 1.5.1 Fibroblasts

Fibroblasts, the principal active cells of connective tissue, first studied in the nineteenth century, are large, flat and spindle-shaped. Fibroblasts and fibrocytes are two states of the same cells, the first refers to an active state, the latter to a less active state. They derive from mesenchymal cells and have important functions in physiological processes: synthesis of extracellular matrix and collagen, epithelial differentiation, regulation of wound healing. They primarily contribute to the secretion of extracellular matrix components to maintain the structural integrity of connective tissues. They secrete the necessary precursors for the production of all extracellular matrix compounds, including the base material and its strands.

Historically, human fibroblast lines were used to discover the pathogenesis of several diseases. In recent years, various studies have been conducted to verify the capacity of fibroblasts to regenerate the skin structure (29).

### 1.5.2 Wound healing

The most important function of fibroblasts is wound healing: in wounds, fibroblasts are stimulated by different factors, like epidermal growth factor (EGF) or transforming growth factor- $\beta$  (TGF- $\beta$ ). Fibroblasts generate extracellular matrix, which represents a scaffold for other cells and have cytoskeletal elements which reduce the size of lesion and promote wound healing (30). Wound healing process consists of 4 stages (Figure 1.14):

- Hemostasis: in the first minutes of injury, platelets in blood adhere to the injured site, assume an amorphous shape, more suitable for clotting. In this way the activation of fibrin occurs, which brings platelets to each other: a clot is formed, which prevents further bleeding;
- Inflammation: in this phase phagocytosis process occurs, in which white blood cells break up damaged and dead cells, debris and bacteria;

- Proliferation: this phase is characterized by angiogenesis, collagen deposition, granulation tissue formation, epithelialization and wound contraction. In this stage fibroblasts growth and form extracellular matrix, using collagen and fibronectin. Concurrently, epithelial cells proliferate and form a cover on new tissue at the top of wound. The size of wound decreases;
- Maturation (remodeling): in the final stage collagen is realigned and cell no longer needed are removed (31).

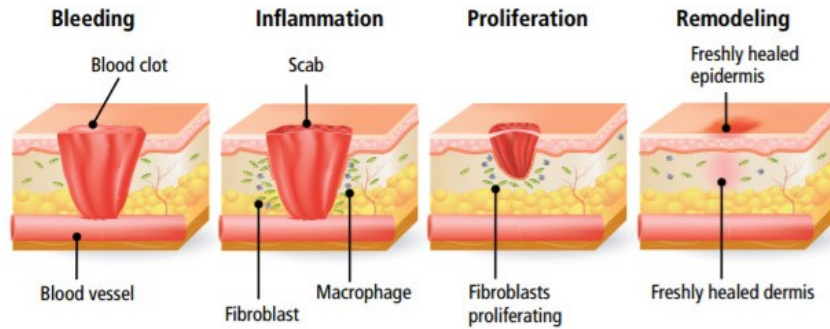


Figure 1.14: Different stages of wound healing: hemostasis, inflammation, proliferation and maturation (F14)

### 1.5.3 Interaction between fibroblasts and keratin

Wang et al. exploited the capacity of keratin to polymerize in aqueous solution to form hydrogels, whose properties were studied and compared with those of collagen hydrogels. Keratin, extracted by human hair, was mixed with  $5 \mu\text{l}$  LDS buffer and  $2 \mu\text{l}$  sample reducing agent and made up to  $20 \mu\text{l}$  with deionized water. The samples were heated at  $75^\circ\text{C}$  for 10 minutes prior to gel electrophoresis. After washing, membranes were blocked with 5% dry milk in phosphate-buffered saline (PBS) containing 0.05% Tween20 (PBST) for 30 minutes and then incubated. The keratin solution was adjusted to a concentration of  $10 \text{ mg/ml}$  and sterile-filtered with a  $0.2\text{-}\mu\text{m}$  cellulose filter. Keratin gelation was started by mixing the required volume of keratin solution with  $1\text{M}$   $\text{CaCl}_2$  solution at a ratio of 50:1 (v/v). The mixture was kept in an incubator at  $37^\circ\text{C}$  and 5%  $\text{CO}_2$  overnight for complete gelation. To prepare collagen hydrogel the required volume of collagen was neutralized with  $1 \text{ M NaOH}$  in PBS and allowed to gel at  $37^\circ\text{C}$  for 30 minutes. From a physical point of view, both structure are porous, but as it is possible to see in Scanning Electron Spectroscopy image, keratin hydrogel are characterized by smaller and interconnected porous, whereas collagen hydrogel present a networks of long fibrous bundles and a larger porous structure, as shown in Figure 1.15. To study cell proliferation, the total amount of double-stranded DNA (dsDNA) was monitored. After 1 day from cell seeding, almost equal amounts of dsDNA were recorded in all samples, after 2 days, cell proliferation in keratin hydrogel was lower than in collagen hydrogels and controls. Between day 2 and day 4, dsDNA levels in keratin sample increased by four time, in collagen and controls samples by seven and ten times. After 10 days, cells proliferation reached a plateau in both hydrogels types. In keratin dsDNA levels was 76% of that in collagen hydrogels. From a physical point of view, it is possible to see differences between cells proliferate on keratin, collagen and control groups (Figure 1.16):

- cells in control group: assumed spindle shape from day 2 of culture, and maintained this morphology over day 4 and 6 (Figure 1.16 (a, d, g));

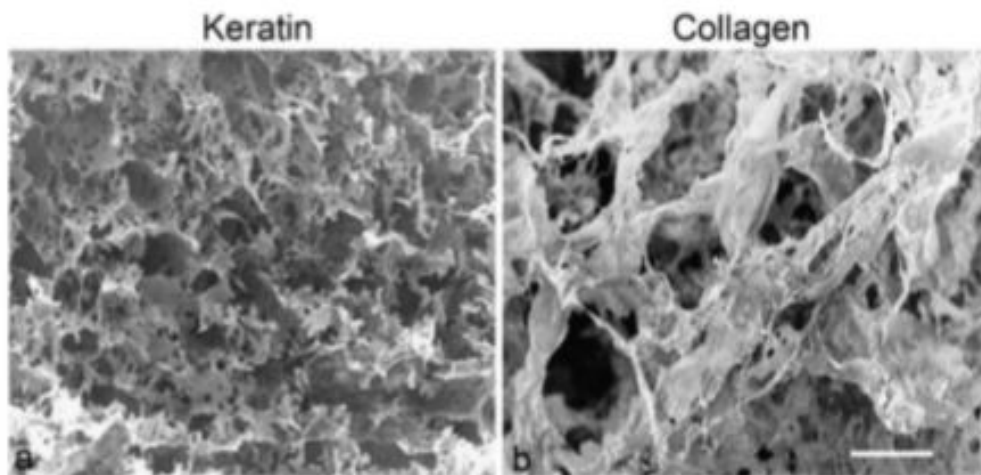


Figure 1.15: Different structure of Keratin and collagen hydrogels (F15)

- cells on keratin hydrogels: assumed spindle shape at day 6 of culture, before were round (Figure 1.16 (b, e, h));
- cells on collagen hydrogels: a small portion of cells exhibited spindle shape at day 4 of culture, most cells at day 6 (Figure 1.16 (c, f, i)).

It is also possible to see that, in control and collagen groups, cells were homogeneously distributed on the whole surface, whereas in keratin group they were distributed in localized zones.

Over the culture period of 6 days, the areas on the hydrogel surfaces on which cells were seeded contracted, whereas the rest of the surface area remained stable, resulting in the formation of a ring on the hydrogel surfaces. (32)

## 1.6 Keratin-based biomaterials

Keratin is employed as biomaterial in different applications, thanks to its physical, chemical and biological behavior. Many studies have been done to fabricate and characterized keratin-based products, such as films, fibers, coating materials, gels. The discovery of methods for modulating physical and mechanical properties led to the creation of biomaterials with the appropriate characteristics for their applications of interest (33).

### Keratin fibers

Generally keratin is used in composites and nonwoven fabrics. Recently, the electrospinning process, used to create fiber of biopolymer with a very small diameters (in the range between micro and nano scale), has been used with regenerated keratin extracted from hair and wool. Ferraris et al. tried to align keratin sub-micrometric fibers onto nanogrooved titanium surface in order to study host tissue response. In this way, aligned keratin fibers impart both topographical and chemical stimuli to fibroblasts. In this case, it is suggested in dental implants, to improve soft tissue healing around transmucosal implants and to create a seal against bacteria penetration (33).

Nanofibers are mostly involved in tissue engineering, a great research area which involves the use of living cells with the aim of promoting remodeling of tissues in some active manners, or repairing, replacing, maintain, enhancing their functions. Specific characteristics for materials to be

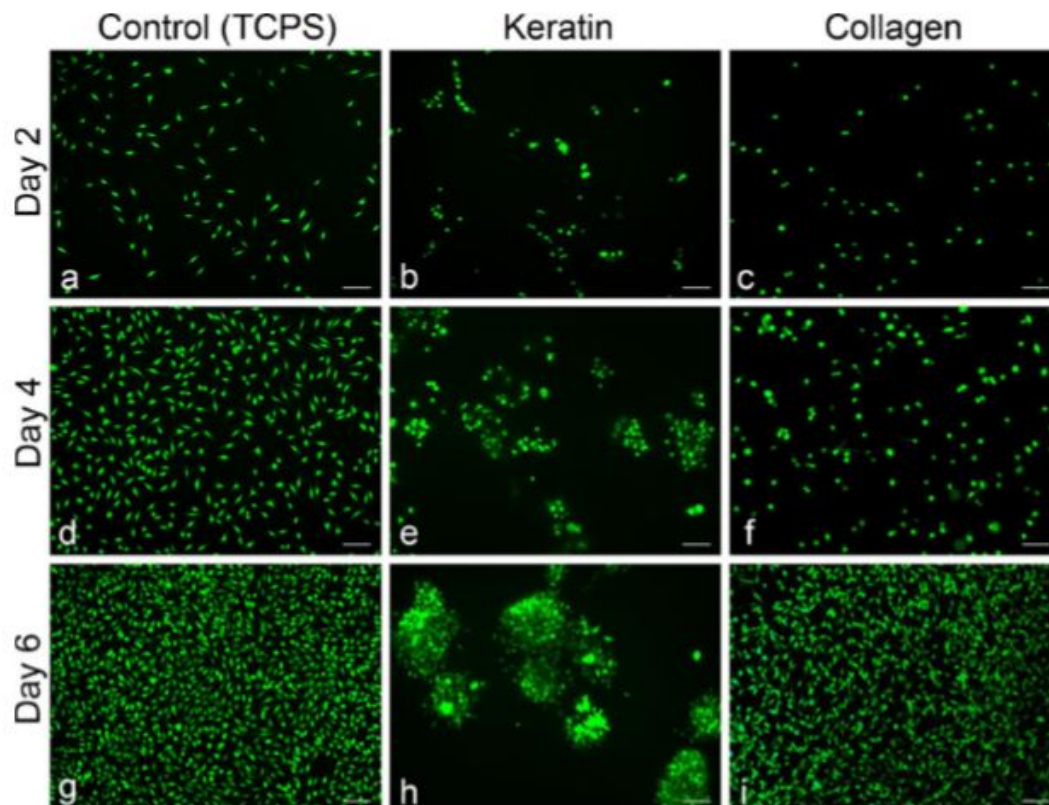


Figure 1.16: Fibroblast morphology and distribution: Cells growth on tissue culture plastic surface after 2,4,6 days (a,d,g); cells grown on keratin hydrogel after 2,4,6 days (b,e,h); cells grown on collagen hydrogel after 2,4,6 days (c,f,i) (F16)

used in medical applications are required: high porosity, with appropriate pore size distribution, high surface area, biodegradability, structural integrity, in order to avoid the collapse of pores during neo-tissue formation. Electrospinning process allows to obtain complex fibers, seamless and three-dimensional, that favor cells growth.

Esparza et al. used electrospun keratin nanofibers to produce scaffold for tissue engineering applications. To prepare the solution for electrospinning process, 5 g of PVA were dissolved into 50 mL of deionized water, and was stirred overnight at 80°C. After cooling 1,2 g of citric acid was added as PVA crosslinking agent, and with the addition of NaOH the pH value was adjusted at 6,0. A keratin solution ( 1.0 g of freeze dried keratin powder was added in 10 mL of deionized water at room temperature), was added. The solution was stirred and used in electrospinning process. The result is shown in Figure 1.17. A DSC analysis (Figure 1.18) showed that PVA maintained crystalline structure after electrospinning and crosslinking, but caused shift in glass transition and melting temperatures. Thermal treatment imparted water stability to nanofibers. Then cell proliferation tests were conducted: after 14 days of incubation, cell proliferation on mats containing feather keratin is higher than on PVA alone. It depends on the presence of keratin: proteins increase the adhesion and proliferation cells due to their integrin bond, keratin also increased hydrophilicity, which leads to an increase in cell proliferation (34).

Xinxin Zhao et al. tried to create a keratin-PCL scaffold with calcium phosphate coating for bone tissue regeneration. A solution of 10% wt of PCL and keratin extracted from human hair was prepared in HFIP, which allowed to obtain "beadless" fibers. Different scaffolds were produced: PCL, PCL-keratin, CaP-PCL, CaP-keratin-PCL, HA-PCL.

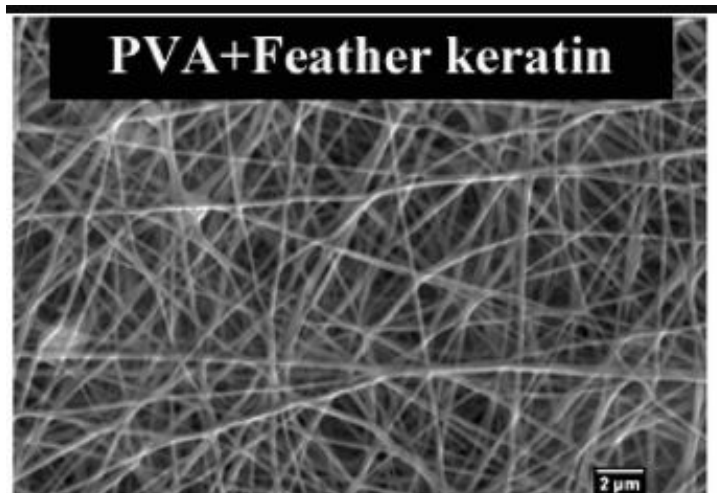


Figure 1.17: Electrospun PVA + feather keratin fibers (F17)

Mechanical tests, Figure 1.19, revealed that the presence of crosslinked keratin and CaP increased mechanical strength of scaffolds. Also biological test were performed: a culture of hMSCs was

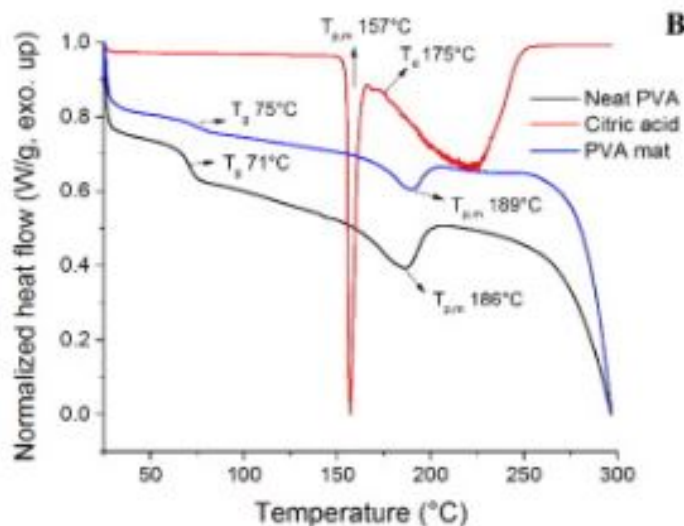


Figure 1.18: DSC analysis of neat PVA, citric acid, and crosslinked PVA electrospun fiber mats (F18)

made on this scaffolds and analyzed after 4 days. This tests showed the cell viability on keratin-PCL e CaP-keratin-PCL was higher than PCL and HA-PCL, due to the presence of LDV cell binding motifs on keratin in promoting cell adhesion (35).

### Keratin films

Another important application of keratin involves the production of films, but they have a main limit: poor strength and flexibility. A lots of method have been studied in order to increase physical strength and flexibility, maintaining biological activity.

For example, Yamauchi created glycerol containing keratin films, with the addition of chitosan: mechanical strength was improved and the system showed antibacterial properties.

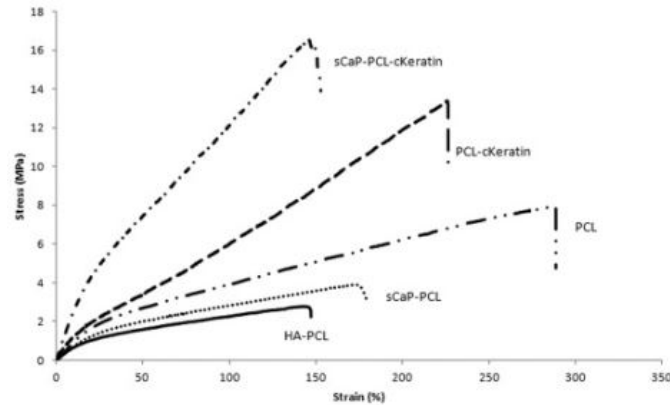


Figure 1.19: Stress-strain curves of sCaP-cKeratin-PCL, cKeratin-PCL, PCL, sCaP-PCL, HA-PCL (F19)

Tonin et al. studied properties of poly(ethylene oxide) (PEO) and keratin blended films: keratin inhibits PEO crystallization and PEO interferes with the keratin self-assembly at appropriate level by inducing  $\beta$ -sheet secondary protein structure with high thermal stability and good structural properties (18).

Atri et al. tried to improve mechanical properties of keratin films by diafiltration. Keratin, extracted by wool, was purified by conventional dialysis and a diafiltration against a 10 kDa membrane with double distilled water was done. Several analysis were performed in order to evaluate any changes in keratin structure: diafiltration did not change the components of keratin extract, the polypeptide chains were arranged to  $\beta$ -sheet plate in form of crystallites. Mechanical test showed that diafiltration has significantly improved the mechanical properties of keratin film with Young's modulus of about 13 MPa and 40% extensibility. Diafiltration might also remove some polar amino acids such as tyrosine, this might affect the swelling, water absorption and consequently mechanical properties of the keratin films (6).

An alternative method to solution-cast keratin films is compression molding of S-sulfo keratin powder, it allows to obtain translucent and flexible film with different shape (4). Keratin films can be applied in different field.

Hamouche et al. used a keratin film to produce a humidity sensor. To produce the film, a droplet of keratin solution was placed on a glass-substrate and heated at  $60^{\circ}\text{C}$ . After drying the film adhered to the surface and was transparent. The film obtained had not homogeneous thickness and was characterized by high surface roughness, was porous and contained residual cuticle and cortical cells. The most important characteristics given by keratin film was the hydrophilic property critical for high-speed humidity sensor (36).

Sanchez Ramirez et al. used keratin and citric acid to produce a transparent film, to be used in packaging for food industry. Keratin, extracted by wool, and citric acid were dissolved in distilled water and shaken. The solution was poured in a polyethylene bowl, then the film was separated from the support and cut. This film had a high elongation to break, but the most important property of the film obtained was excellent antibacterial property, given by the action of citric acid (37).

### Keratin as biosorbent

Recently keratin has been used in application for the purification of metal contaminated water. Conventional water treatment techniques require complicated operational set-up, are expensive and selective for few materials. A lots of studied shows a binding of keratin wool to heavy metal

ions. Keratin wool is used to remove metals such as mercury, copper, silver, chromium and aluminum. A type of keratin, called mohair, is used to remove copper from aqueous stream (4).

Zang studied biosorption capacities of keratin extracted from different source: in particular it was found that the bleached and dyed hair were most capable to remove heavy metal ions from aqueous solution.

Fadillah et al. used  $\alpha$ -keratin-coated alginate Biosorbent for adsorption of Fe ions. To obtain a biosorbent human hair were used: a mixture of hair and alginate with some composition was dissolved in 50 mL of water. The obtained  $\alpha$ -keratin-alginate solution, encapsulated with  $CaCl_2$  2 % (w/v) solution immersed in ice cubes. The result was filtered and dried at 60 °C for 8 hours. Then, the optimal composition was carried out by adsorption test on Fe ions in aqueous solution at the optimum condition of pH (7.0) and contact time (60 minutes). It was showed that the composition between keratin and alginate can affect the density of the resulting composite. The influence of pH and time is shown in Figure 1.20. As it is possible to see, the optimum pH value is 7,0. The pH effect can be explained considering the carboxylic ( $-COOH$ ) from alginate and amino ( $\sim NH_2$ ) groups present from  $\alpha$ -keratin on the biosorbent. At lower pH, the carboxylic groups retain their protons and amino groups get protonated, thereby, reducing the probability of binding to any positively charged ions. In addition, at lower pH, this is mostly due to the competition of  $H^+$  ion adsorption with metal ions so it caused the adsorption capacity at low pH is relatively small. While, at the pH more than 8 case the precipitation of iron hydroxide,  $Fe(OH)_3$  (38).

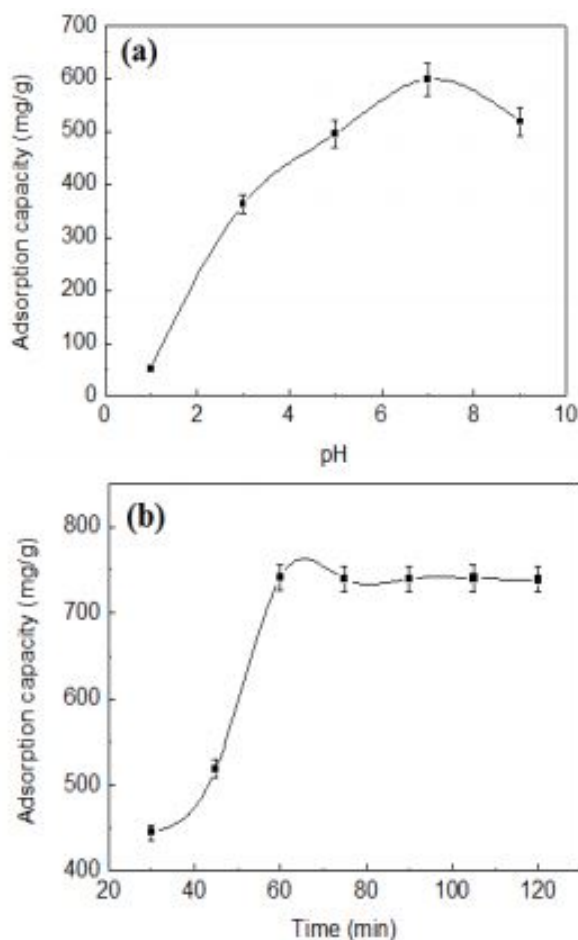


Figure 1.20: (a) Influence of pH solution and (b) contact time to adsorption of Fe ions (F20)

## Chapter 2

# Coating

The term “coating” is used to indicate a solid or liquid material which is deposited on a substrate as a continuous or discontinuous film. The aim of coatings can be functional or aesthetic, or both. Coatings are used to improve or change the surface properties of the substrate, such as wettability, corrosion or wear resistance, or to add completely new properties, such as magnetic or electrical behavior, whereas aesthetic coatings are used to improve appearance. It is possible to distinguish between coatings which cover the entire surface of the substrate, all-over coatings, and coatings which only cover parts of it, non-all-over coatings (39).

### 2.1 Coating deposition process and techniques

Coating deposition processes can be divided into different groups, depending on the modes in which the coating is deposited:

- Vapor deposition: with this process a layer is deposited atom-by-atom or molecule-by-molecule. The thickness changes between one atom to millimeters and is possible to obtain multiple layer by depositing different materials. There are two main techniques for vapor deposition: PVD and CVD. In Physical Vapor Deposition (PVD) process, shown in Figure 2.1 the material is vaporized from a solid or liquid source, atoms or molecules obtained are transported in the form of vapor on the substrate and here they condense. This process occurs in vacuum or low pressure. This technique allows to deposit thin films in the range of few nanometers to several nanometers. It is possible to deposit a single element, but also an alloy by reactive deposition process: the reaction between the depositing materials and the gas of the environment, or with a co-depositing material, occurs and compounds are formed.

Different materials can be used as coating or substrate: in Figure 2.2 is shown an example of PVD deposited coating: the substrate is a carbon fiber, which is covered with AlN coating. It is possible to see the differences in surface characteristics between the uncoated fibre (b) and the fiber with AlN coating (a).

There are different categories of PVD process, reassumed in Figure 2.3: vacuum deposition, sputter deposition, arc vapor deposition, ion plating.

In vacuum deposition, also known as vacuum evaporation, the material to be deposited is evaporated from a thermally heated source and reaches the substrate without, or with little collisions with gas molecules. The vacuum allows to reduce contamination in the deposition system. The rate of this process is very high compared with that of others method.

In sputter deposition process, particles are physically ejected from a solid surface, called

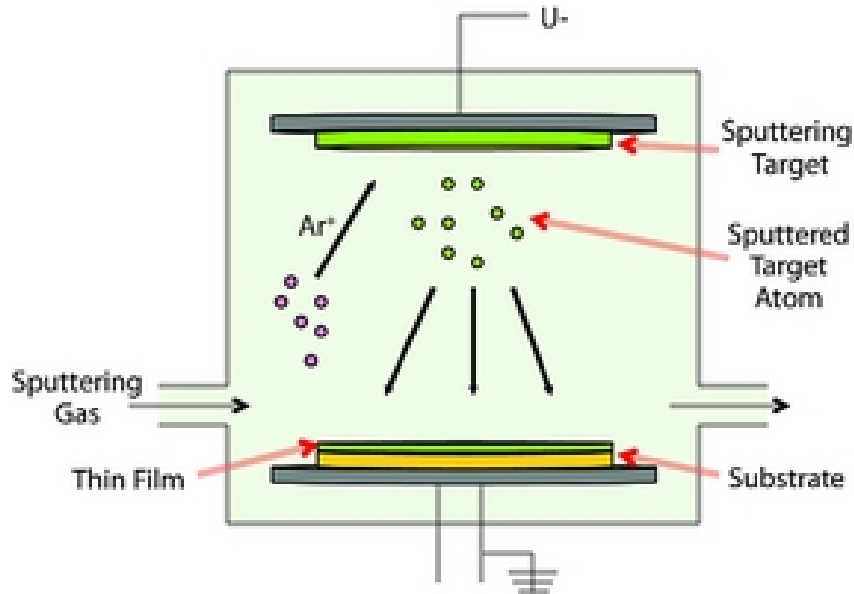


Figure 2.1: Scheme of Physical Vapor Deposition (PVD) process (F21)

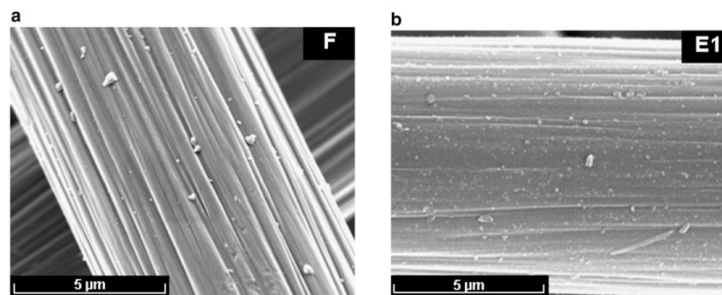


Figure 2.2: (a) AlN coating on carbon fibers, (b) uncoated fiber (F22)

target, by energetic bombarding particles, usually a gaseous ion accelerated by a plasma. The process occurs in vacuum in which there are few or no collisions of sputtered particles.

Arc vapor deposition involves the use of high current, low voltage arc, in order to vaporize an electrode (cathodic or anodic) and deposit the vaporized material on the substrate.

Another technique is the electron-beam physical vapor deposition (EBPVD), in which an electron beam is used to bombard a target anode. Atoms are ejected from the target and transformed into the gaseous phase which precipitate in solid form, creating a coating on the substrate.

Ion plating, also known as ion-assisted deposition (IAD) or ion vapor deposition (IVD), involves current or bombarding particles, to deposit material vaporized by evaporation, sputtering, erosion or decomposition of a chemical vapor precursor (40).

Chemical vapor deposition (CVD) is a method which utilizes chemical vapor precursors, transformed in atoms or molecules by reduction or decomposition, which react on the surface creating the coating. The atoms can also react with the gas in the system in order to obtain a compound which is deposited on the substrate (39).

Generally metals and ceramics are used as coating materials, deposited on various substrate.

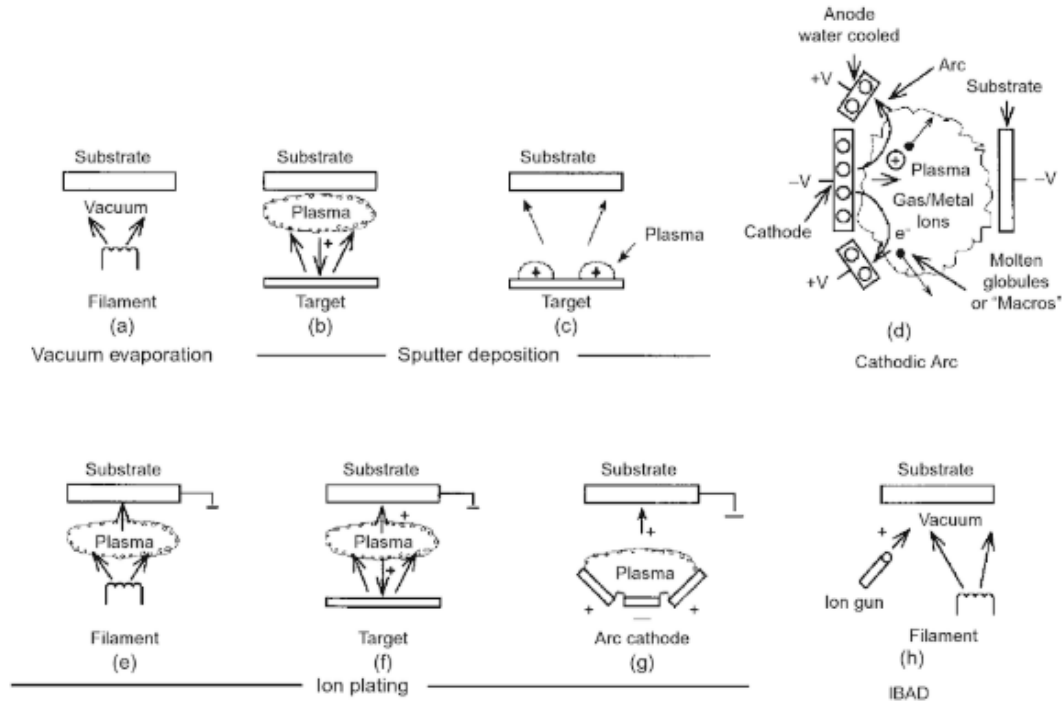


Figure 2.3: PVD processing technique: (a) Vacuum Evaporation, (b) e (c) Sputter Deposition in Plasma environment, (d) Sputter Deposition in a vacuum, (e), (f), (g) Ion Plating in Plasma environment with a Thermal Evaporation Source, with a Sputtering source, with an Arc Vaporization source, (h) Ion Beam-Assisted Deposition (IBAD) (F23)

In Figure 2.4 is shown a  $TiO_2$  coating on a glass substrate, deposited by CVD method.

It is possible to classify this process according to the value of pressure in: atmospheric pressure CVD, low pressure CVD and high pressure CVD, or in hot wall and cold wall CVD, if the chamber is heated by an external source and the substrate is heated by heat of the chamber, or if only the substrate is heated by induction or by a current, while the chamber is at room temperature (39)(40).

An important technique is the Plasma-enhanced chemical vapor deposition (PECVD) (Figure 2.5): it is a chemical vapor deposition process in which chemical reactions, involved in the process, occur after creation of a plasma of the reacting gases. The plasma is generally created by radio frequency (RF). PECVD process allows deposition at lower temperatures, which is often critical in manufacturing of semiconductors and of organic coatings, such as plasma polymers, that have been used for nanoparticle surface functionalization (41).

- **Spraying:** a coating can also be sprayed on a surface by a device which uses compressed gas, usually air, to atomized and direct the particles. Generally this technique is use to cover large surface with a uniform coating of liquid. Coating materials are in the form of powder, wire, or rod and are fed to a torch or gun with which they are heated to near or somewhat above their melting point.

There are different variants of this process. In general thermal spraying is a technique in which coating materials are melted by electrical or chemical means and sprayed in form of micrometers-size particles onto the surface (Figure 2.6). The coating obtained has a thickness between few microns to several millimetres.

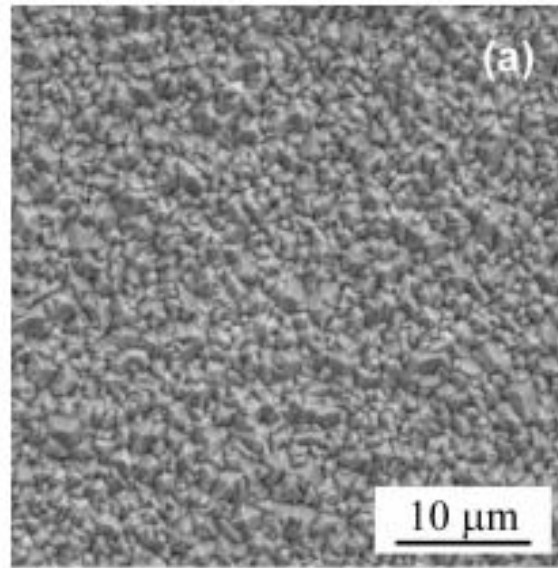


Figure 2.4:  $TiO_2$  coating on glass substrate deposited by CVD technique (F24)

Plasma spray process (Figure 2.7) uses a DC electric arc to generate a stream of high temperature ionized plasma gas, which acts as the spraying heat source. The powder of the material to deposit is injected outside of the gun nozzle into the plasma, where it is melted, and hurled by the gas onto the substrate surface. The drops reach the substrate, then they flatten, solidify and form the coating. Changing different parameters, such as plasma gas composition, flow rate, feedstock type, distance between substrate and nozzle, is possible to obtain coating with the desired characteristics.

A variant is Vacuum plasma spraying: the process is done in a chamber at low pressure, the plasma is energized by an electrical field. In general the volatile plasma by-products are evacuated by the vacuum pump. Advantages of this low-pressure plasma technique include improved bonding and density of the deposit, improved control over coating thickness and allows higher deposit efficiency.

The high velocity oxy-fuel spray (HVOF) (Figure 2.8) process is relatively recent. The system involves a combustion chamber in which a mixture of gaseous and liquid fuel and oxygen are ignited and combusted. The combustion of the gases produces a high temperature and high pressure in the chamber. The hot gas travels inside the nozzle and a powder of feed stock is injected in the gas stream and is accelerated towards the surface to be coated. Due to the high velocity of the particles, the resultant coatings are generally very dense, adherent and contain inclusions (42).

An example of the surface obtained by spraying technique is shown in Figure 2.9. In this case,  $Ni_{20}Cr$  is used as material coating, deposited by plasma spray method.

- Other techniques: it is possible to mention converting coatings in which the surface of the material is subjected to a chemical and electrochemical reaction by the coating material. Planting is also important, in which a metal is deposited on a conductive surface. There are different techniques for this method, one of these involves a metal sheet placed on a solid surface, and then it melts by applying heat and pressure. Examples include chromate conversion coatings, phosphate conversion coatings, bluing, black oxide coatings on steel

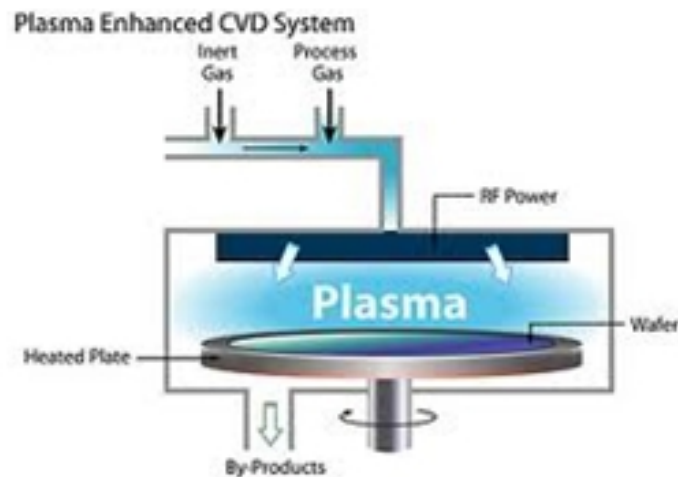


Figure 2.5: Scheme of Plasma-enhanced chemical vapor deposition (PECVD) (F25)

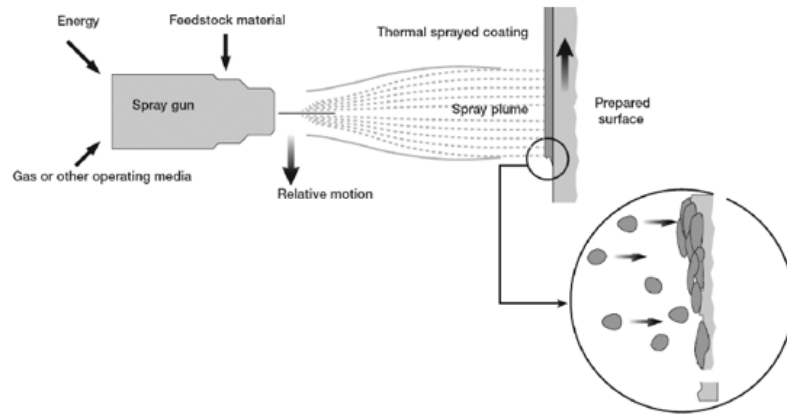


Figure 2.6: Scheme of Thermal spray process (F26)

(Figure 2.10). .

Another method is electroplating, in which metal in the ionic form creates a non-ionic coating with the support of electrons. The system consists of: a chemical solution with the ionic form of the metal, an anode and a cathode, where electrons are supplied to produce the non-ionic coating. It is also possible to obtain a non-galvanic plating, exploiting simultaneous reactions in an aqueous solution (39). This technique is used to obtain better aesthetic characteristics or to improve properties of different materials used as substrate. In Figure 2.11 is shown an aluminum substrate covered by electroplating, using bromide salts to improve corrosion resistance.

In industrial processes, dip coating can be used to obtain thin film from sol-gels precursor. The process is divided in different steps: the substrate is immersed in a solution of the coating material and has remained inside the solution for a while. The thin layer deposits itself on the substrate while it is pulled up. The excess liquid will drain from the surface: with evaporation of the solvent, the thin layer is formed.

An example is shown in Figure 2.12, which represents a rhodium dipping on yellow gold.

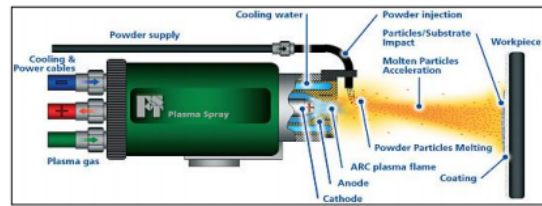


Figure 2.7: Scheme of Plasma spray process (F27)

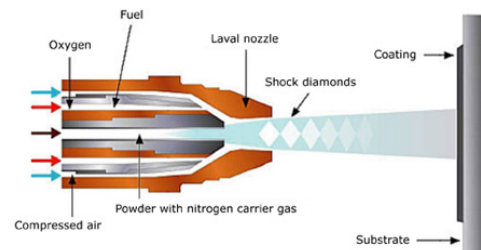


Figure 2.8: Scheme of High-Velocity Oxy-Fuel spray technique HVOF (F28)

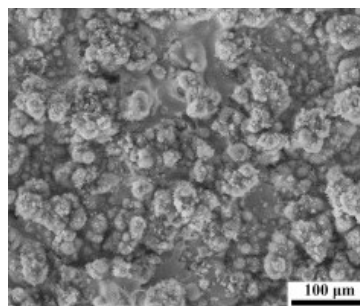
Figure 2.9: Morphology of plasma spray  $Ni_{20}Cr$  coating deposited by plasma spray method (F29)

Figure 2.10: Phosphate coating (F30)

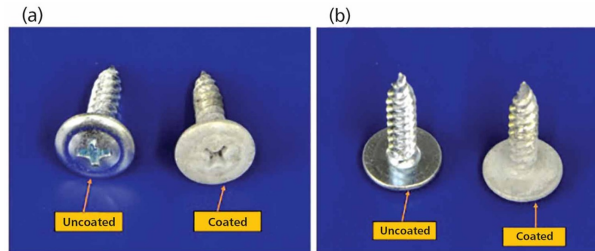


Figure 2.11: Aluminum electroplating using bromide salts (F31)



Figure 2.12: Rhodium dipping on yellow gold (F32)

## 2.2 Theory of adhesion

In a coating/substrate system, two different materials are in contact and to make adhesion possible, intrinsic adhesion forces must be generated at the interface. Surface chemistry, fracture mechanics, rheology, mechanics of materials and other subjects are involved in the description of adhesive phenomenon.

To describe the theory of adhesion is important to note the difference between “intrinsic adhesion” and “measured adhesion”: the first refers to direct molecular forces of attraction between coating and substrate, the second refers to the strength of bond which can be measured with methods that will be described later. There are several models that describe the adhesion mechanisms (43).

### 2.2.1 Mechanical interlocking theory

This model proposes adhesion as a result of the mechanical interlocking of the coating into the superficial asperities and the pores of the substrate. In this theory, an important role is played by roughness, porosity and wettability of the substrate. The tensile strength depends on the crevice angle on the adhered surface, whereas shear strength is improved by a roughness increase.

Leeden and Frens indicated three different type of superficial irregularities (Figure 2.13), but only defect "b" is important for interlocking adhesion, while the role of defects "a" and "c" depends on the direction of the applied force. In addition, coating material must have proper viscosity in order to penetrate into the pores (43).

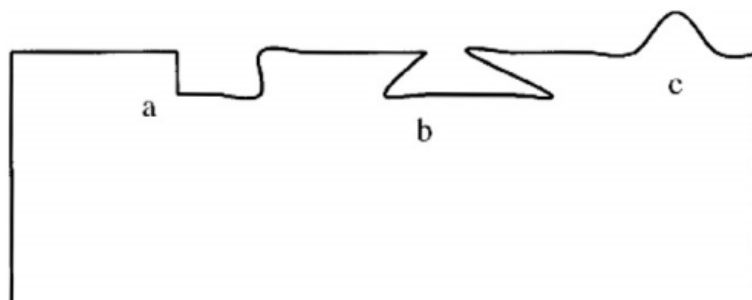


Figure 2.13: Three types of superficial defects (F33)

Mechanical interlock is the dominant mechanism that describes adhesion strength in a system made up by metal substrate and polymeric coating. It was studied by Won-Seock et al. for steel/carbon fiber reinforced polymer system (Figure 2.14). They found that the adhesion strength increases with an increase in roughness, and the mechanical interlock provokes energy dissipation processes during fracture (44).

### 2.2.2 Chemical/adsorption theory

This model, proposed by Sharpe and Schonhorn, is based on the interatomic and intermolecular forces established between atoms and molecules of the two surfaces. These forces include secondary bonds, such as Van der Waals bonds and hydrogen bonds, and primary bonds, like covalent, ionic and metallic bonds.

Paint systems containing reactive functional groups, such as hydroxyl or carbonyl, tend to adhere more tenaciously to substrate characterized by the same groups. For this reason, bi-functional molecules are used as adhesion promoters: one end has functionality which can react with paint,



Figure 2.14: Cross section of a steel/composite bonded interface (F34)

and the other end has functionality which can react with substrate, creating strong and durable bondings. They are based on silane and are employed as additive in paint formulation and as primers on glass and metal substrates. An example of the covalent bond created at the interface with steel surface through chemisorption is represented in Figure 2.15 (45).

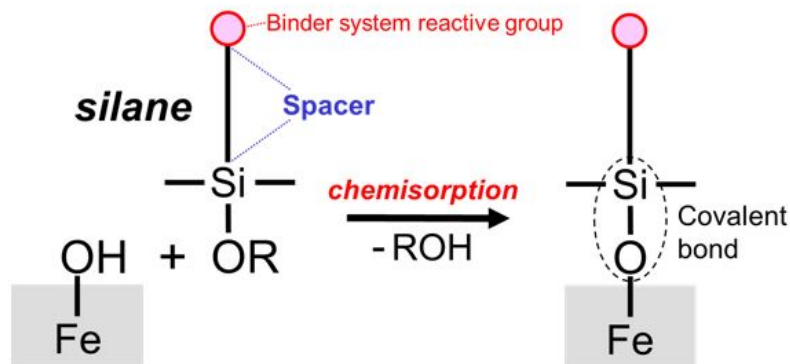


Figure 2.15: Chemical reaction of silane adhesion promoter with steel surface (F35)

Adsorption theory is also known as thermodynamic theory and involves wetting, rheological and chemical knowledge.

In order to obtain a good wetting, the substrate must have a surface energy higher than that of the liquid coating, as it will be explained later. Metal, glass and certain polymers have higher surface energy than that of paint binders, so these materials can be used as substrate. In some cases, certain plastic substrates with very low surface energy, such as polypropylene, silicon rubber, fluoroplastics, can be used as substrate if they undergo surface preparation processes, (chemical treatment, flame, corona treatment), which increase surface energy. (45)

### 2.2.3 Acid-base theory

Fowkes et al. proposed acid-base interactions as a major type of intrinsic adhesion force. The two surfaces can behave as an acid by accepting electron (a Lewis acid) or proton donation (Bronsted acid), as a Lewis base by donating electrons or accepting protons, or possessing both acid and basic behavior (43)(46).

This mechanism was studied by Neubauer et al. analysing the acid-base interaction of aromatic sulfur heterocycles adsorbing on  $\text{Ag-Al}_2\text{O}_3$ . As it is possible to see in Figure 2.16, three types of bond are created:  $\pi$ -Ag, S-H and S-Ag. The first type,  $\pi$ -Ag, has a high adsorption energy and is formed by two mechanisms: the silver cations form the usual  $\sigma$ -bonds with their s orbitals, and

the d orbitals of the silver cations can back-donate electron density to the antibonding  $\pi$ -orbital of the sulfur heterocycles. S-Ag interaction is based on the hard and soft acid base (HSAB) theory: the silver cation of  $\text{Ag-Al}_2\text{O}_3$  is a soft acid, while the sulfur heterocycles are Lewis base, where the S-atom has two lone pairs of electrons: a  $\sigma$  lone-pair and one  $\pi$  lone-pair electron. Also S-Ag interaction is described by HSAB theory: the silver cation acts as soft acid and interacts with the sulfur heterocycle as a soft base (47).

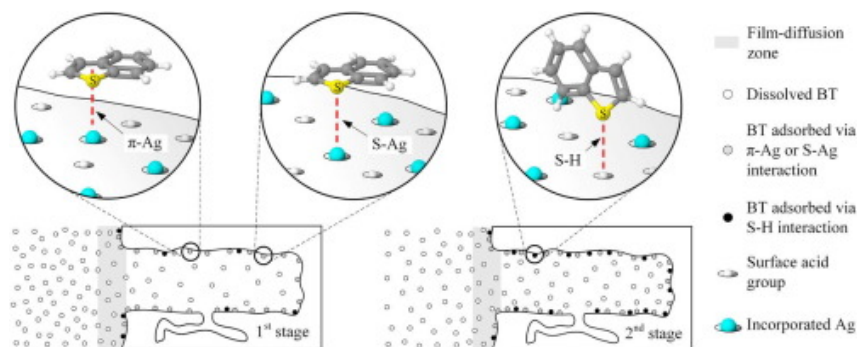


Figure 2.16: Creation of  $\pi$ -Ag, S-H and S-Ag bonds (F36)

## 2.2.4 Diffusion or interdiffusion theory

In this theory, adhesion is the result of interdiffusion of the macromolecules of the two materials (Figure 2.17). Some characteristics are required: molecules at the interface must be mobile enough to mix with one other, the two materials must have similar solubility parameters and must be miscible and compatible (43). In general, this type of adhesion occurs between two polymers: a transient zone is formed by the interaction of the macromolecules of the superficial layers. Macromolecules play an important role in determining the strength of the bond, which is influenced by chain length of the macromolecule, polymer structure, contact time, concentration and temperature (43).

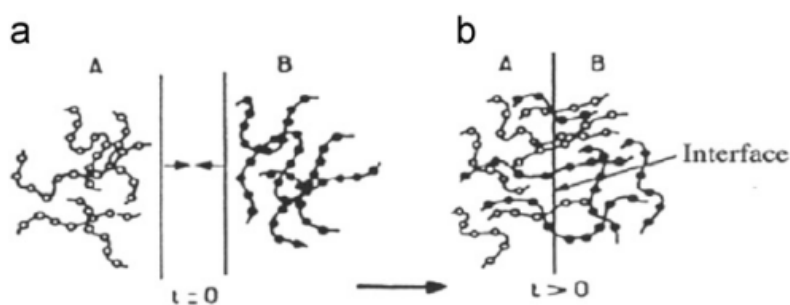


Figure 2.17: Diffusion theory of adhesion (F37)

## 2.2.5 The electrostatic attraction theory

The electrostatic attraction theory is based on the mutual sharing of electrons at the interface between the two materials. In this case an electrostatically charged double layer of ions is formed at the interface and the system is seen as a capacitor. This model is applicable between two incompatible materials, such as metal and polymer, as shown in Figure 2.18. The attraction

forces occur when one surface carries a net positive charge and the other a net negative charge. The forces at the interface depends on the charge density (43). For example, this type of adhesion bond is created between low density polyethylene (LDPE) and Aluminum substrate. The presence of the electric double layer affects the mechanical behavior at the interface. This model

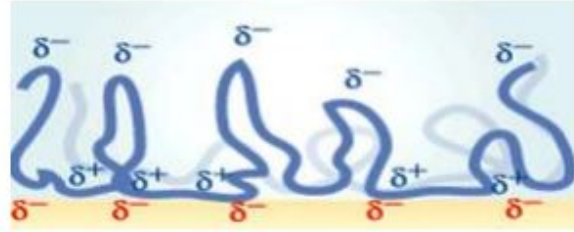


Figure 2.18: Electrical double layer formed at the interface between a polymer and a metal (F38)

is applicable in the case of incompatible materials, such as polymer and metal.

## 2.3 Thermodynamic theory of adhesion

From a thermodynamic point of view, the adhesion of a coating to a substrate depend on different parameters, such as free energy of the surface, wettability, forces of attraction.

When a liquid drop is deposited on a surface, the liquid can spontaneously spreads on the surface forming a thin film or can form a sessile droplet on the surface. In the first case, an intimate molecular contact is established and results in the elimination of air pockets and in the penetration of the liquid in the asperities of the surface. In the second case, the adhesion of the film to the substrate is worse. The behavior depends on the surface tension of the two components and it is possible to define a contact angle by the Young's equation:

$$\gamma_s = \gamma_{sl} + \gamma_l \cos \theta$$

where  $\gamma_s$  is the surface tension of the solid substrate in equilibrium with the saturated vapor of the liquid,  $\gamma_{sl}$  is the interfacial surface tension of the solid and the liquid drop,  $\gamma_l$  is the surface tension of the liquid in equilibrium with its own saturated vapor and  $\theta$  is the contact angle formed between the solid-liquid interface (Figure 2.19). Depending on the value of the superficial tension, and consequently of the contact angle, it is possible to define if a surface is wettable by a liquid and this is important for the formation of adhesive bond: coating with surface energy less than that of the substrate will wet the surface and if an intimate contact between coating and substrate is achieved, a physical interaction develops, forming strong bonds. It is necessary to specify that spreading is not the only requisite for a good adhesion, but it is highly desirable for maximizing contact area and minimizing interfacial flaws and defects.

When molten powders are deposited on the surface, coalescence must occur (Figure 2.20): it depends on surface tension, radius of curvature, and viscosity of the molten powder. In order to minimize coalescence time, low viscosity, small particles and low surface tension are required.

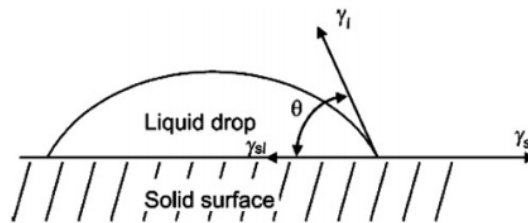


Figure 2.19: Liquid drop on solid surface in equilibrium (F39)

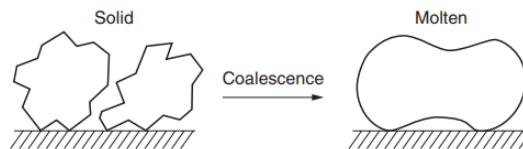


Figure 2.20: Coalescence of molten powders (F40)

Another important aspect, that must be taken into account, is represented by the forces of attraction or Van der Waals forces: when atoms or molecules are brought sufficiently close, exhibit attraction for each other. In some cases, repulsion can occur: if there are fixed electrical charge distribution or fixed magnetic polarization, or when the matter is compressed enough

that outer electron orbits begin to interpenetrate each other. Van der Waals forces are the sum of three contributes. “London forces” or “dispersion forces” are caused by the fluctuation in the electron density that produces temporary electrical dipoles, which generate attraction (Figure 2.21). This forces are common to all the matter in fact, despite being weak interactions, cumulative effect is great. The second contribute is given by the so-called “Keesom forces”, which

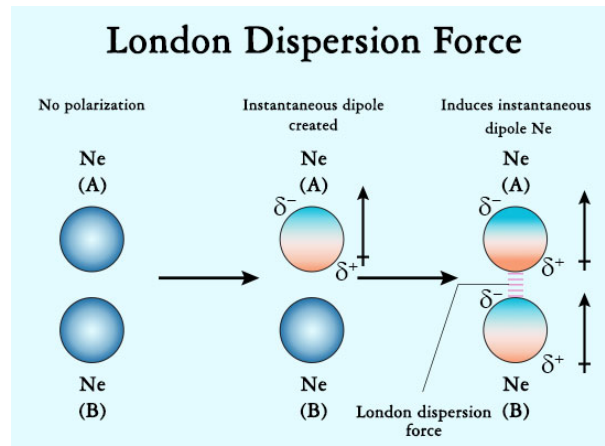


Figure 2.21: London forces (F41)

represent the attraction between permanent dipoles and depend on the dipole moments of the two molecules (Figure 2.22).

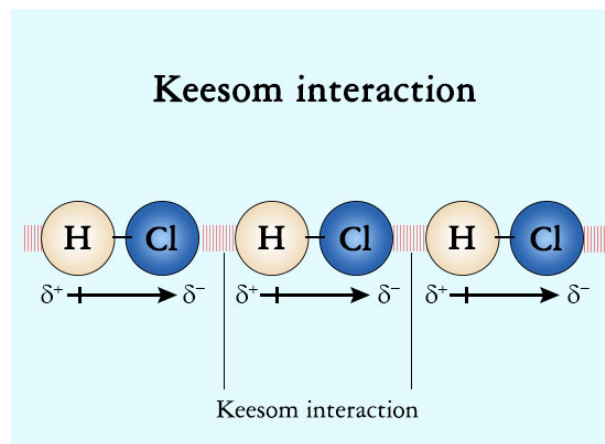


Figure 2.22: Keesom forces (F42)

The third contribute is given by “Debye forces” which represent dipole-induced dipoles forces, caused by a permanent dipole which induces a dipole in a neighboring molecule, and in this case the potential energy of interaction is proportional to molecular polarizability (Figure 2.23).

Also acid-base interactions lead to strong bonding, for example are hydrogen bonding, Lewis acid–base interactions, and Brønsted-type acid–base interactions (43)(46)(48).

## 2.4 Macroscopic adhesion testing

As it has been said before, coatings are used to improve or to add properties or certain characteristics of the substrate. To achieve this goal, it is important that the coating is adherent to

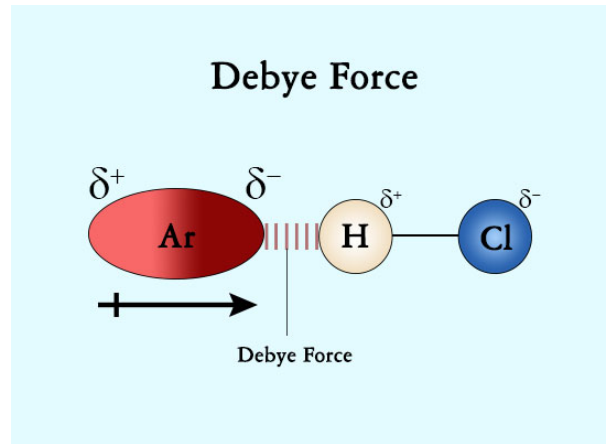


Figure 2.23: Debye forces (F43)

substrate without degrading the behavior of the system. To evaluate it, adhesion tests are made on the coating and the substrate, in this way adhesion level is analyzed. When the adhesion of coating is evaluated, it is possible to study the pre-treatment of the piece and how different parameters can affect the coating behavior.

The American Society for Testing and Material (ASTM), defines adhesion as "the state in which two surfaces are held together by interfacial forces which may consist of valence forces or interlocking forces or both" (49). The experimental adhesion can be defined as the maximum force per unit area exerted when two materials are separated; or as the work done in separating two materials from one another. In practice, plastic phenomena always occur and this does not allow to evaluate the true work of adhesion (50).

The weak boundary layer theory explain the fact that bond failure at the interface is caused by either a cohesive break or a weak boundary layer. Failure can occur in the adhesive or adherend, if impurities are concentrated near the bonding surface and form weak attachment to the substrate.

Bikerman indicated seven different classes of weak boundary layers (Figure 1.10), such as air pores, impurities at the interface, and reactions between two components (43)(51).

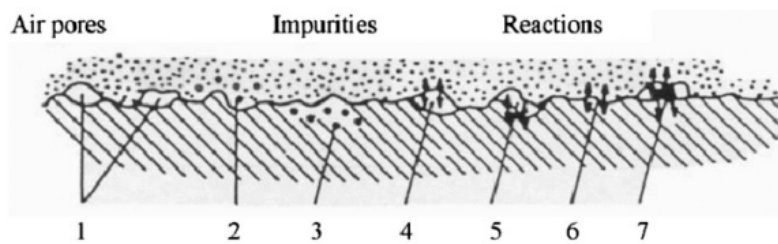


Figure 2.24: Theory of weak boundary layers. (1) air pores, (2) and (3) impurities at the interface, (4), (5), (6), and (7) reactions between the two materials (F44)

### 2.4.1 Cause of failure

Different factors, acting alone or in combination, can put under stress the bonding between coating and substrate, causing the destruction of the system (Figure 2.25). One of the first

cause of failure is represented by mechanical stress, which can involve the bulk of the system and the interface zone. In this case, the two common types of stress are tensile stress, acting perpendicular to the surface and shear stress, acting on the plane of contact. Also changes in temperature can cause the failure of the system: if the two materials have different coefficients of expansion, at the interface stress conditions occur, this event is disadvantageous because the effect of the temperature is less evident than mechanical or chemical effects. It is also possible a chemical cause, if some molecules such as water, gases or ions, penetrate in the coating and achieve the interface zone, causing the loss of adhesion (48). Depending on substrate and coating

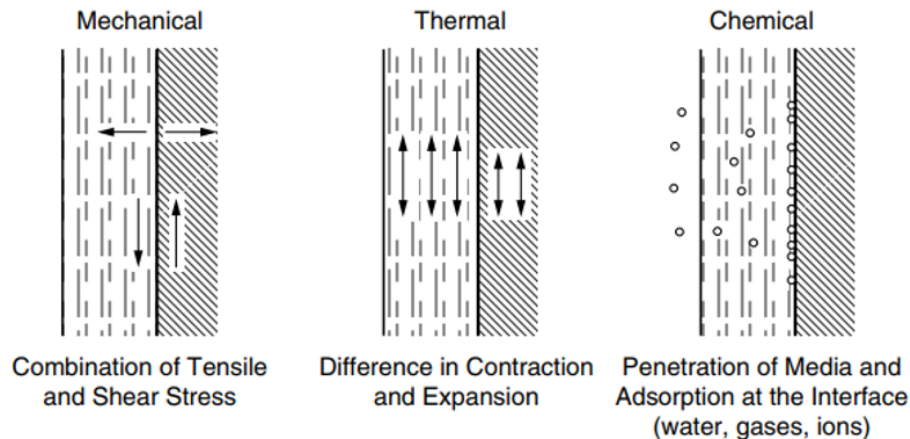


Figure 2.25: Cause of failure of coating/substrate system (F45)

properties, different types of possible failure can occur in any adhesion test, and, from the surface, the failure can propagate into the substrate (Figure 2.26)(50).

### 2.4.2 Adhesion test

Adhesion test methods are divided into three groups: nucleation methods, mechanical methods and miscellaneous methods. In nucleation methods, it is evaluated the breaking of individual coating-substrate atomic bond and the sum of the individual atomic forces constitutes the macroscopic adhesion. This methods are based on measurement of nucleation rate, critical condensation and residence time of the depositing atoms. Mechanical methods use different technique to remove the coating from the substrate. It is possible to divide this methods into two groups, if there is a detachment normal of lateral of the film from the substrate. Miscellaneous methods are techniques that cannot be labelled as practical test, but can have a academic interest (50)(52).

The most common technique are:

- Pull-off test: it is the simplest and most used test to evaluate coating-substrate adhesion. The ASTM D4541 standard describes test apparatus and protocols: a dolly is glued onto the coated surface and then is pulled exerting a perpendicular forces on the surface in order to remove the coating (Figure 2.27) (52). Generally, to glue the dolly to the coating a two-component epoxy-adhesive are used. Using this test, it is possible to evaluate:
  1. The maximum perpendicular force that can be applied on surface area before a piece of material is detached;
  2. If, at a defined load, the coating remains intact or not.

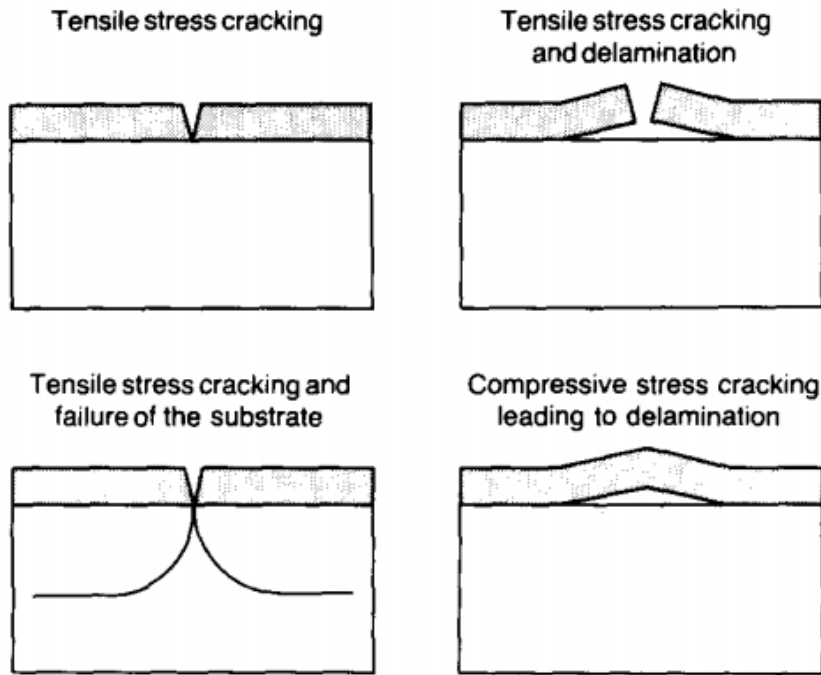


Figure 2.26: Types of failure of coating/substrate system (F46)

This method presents different disadvantages: the forces involved are a sum of tensile and shear forces, so is difficult to distinguish and interpret them, it is necessary a perfect alignment on the interface, in order to obtain a uniform loading, it is possible that the adhesive or the solvent using during the test may penetrate the coating, changing its characteristics and behavior.

A pull-off test was conducted by Yanli Cai et al. on magnesium-containing hydroxyapatite ( $Mg_xFHA$ ) coating on Ti-6Al-4V substrate. The test was performed using a Al-rod glued onto the coating surface with an epoxy resin and was cured at room temperature for 24 h. SEM analysis was used to evaluate the failure mode at the fracture interface. Figure 2.28 shows the results of pull-test on  $Mg_0FHA$  (a) and on  $Mg_2FHA$  (b) on Ti-6Al-4V. As it is possible to note, cohesive fracture occurs in both cases (53).

A variant of this method is the tangential shear or lap shear technique, in which a parallel force is applied on the surface and the shear stress measured represent the tangential force per unit area required to break the bond between coating and substrate.

- Ultracentrifugal method: this method is used in order to avoid the use of adhesive or solder. The sample is spun at extremely high speed. At a critical high speed rotation, coating separates from the substrate, because can no longer withstand the centrifugal stress.
- Cross-cut test: in this case, to evaluate the adhesion of the coating, a lattice pattern is cut into it, using different cutting tools. The test is based on the amount of coating flakes separated from the substrate (48). An example is shown in Figure 2.29.
- Scratch test: the standard ASTM C1624-05 for scratch adhesion testing defines modes to evaluate strength and failure of coatings on metallic or ceramic substrates. In this test, a diamond stylus is used to create a scratch on the coating surface, applying a stepwise or

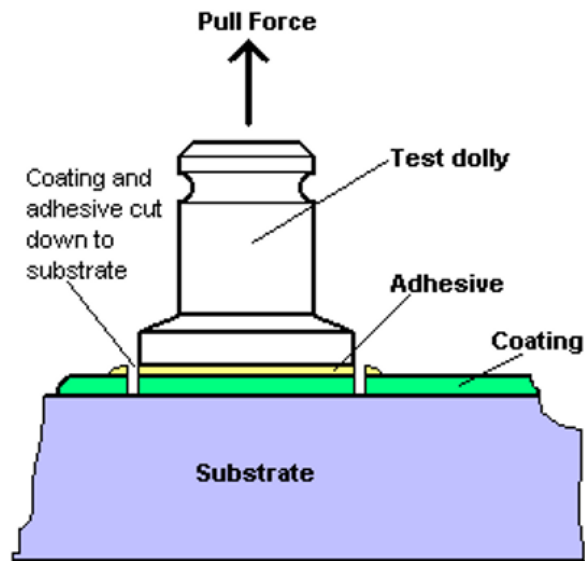
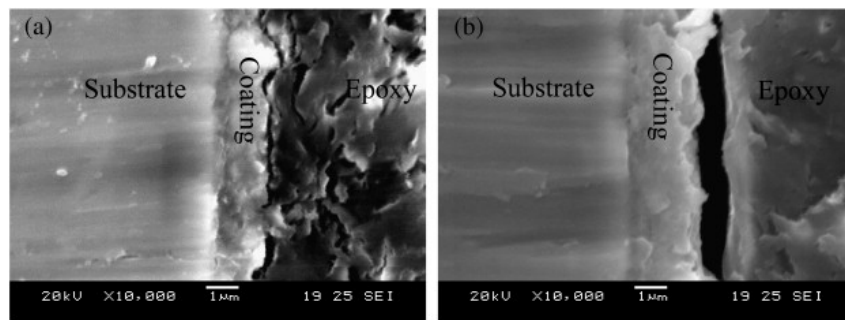


Figure 2.27: Pull-off test (F47)

Figure 2.28: Cross-sectional view of (a)  $Mg_0FHA$  and (b)  $Mg_2FHA$  coatings on Ti6Al4V substrate (F48)

gradually increasing normal force with a constant speed. Generally, a Rockwell C geometry stylus is used, with different radii in order to change the contact pressure (Figure 2.30). When the scratch is done, the surface is observed under a microscope, analyzing damages such as delamination, buckling, and deformation (54). It is defined a critical load which is the load that causes the separation between coating and substrate in a regular way, is related to adhesion strength and damage resistance of the system and depend on the stylus characteristics and on the coating's properties (50).

As it has already said, there are three different modes to do the starch test:

1. In constant load: the scratch is done by applying a constant load. More scratches are made by increasing load each time, in order to determine the load corresponding to a specific damage;
2. In progressive load: the scratch is done applying a normal force with a load which increases in a linear way. The critical load is defined as the load that causes first a damage;
3. Incremental load: the scratch is done applying a load which incrementally increase

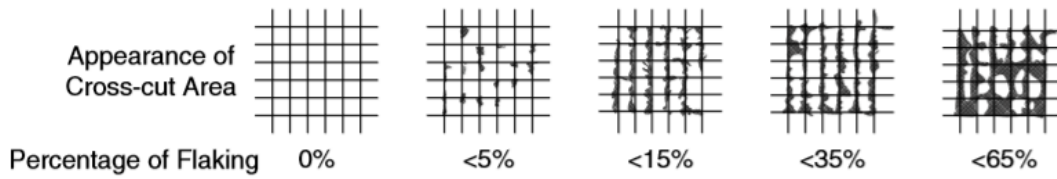


Figure 2.29: Cross-cut test (F49)

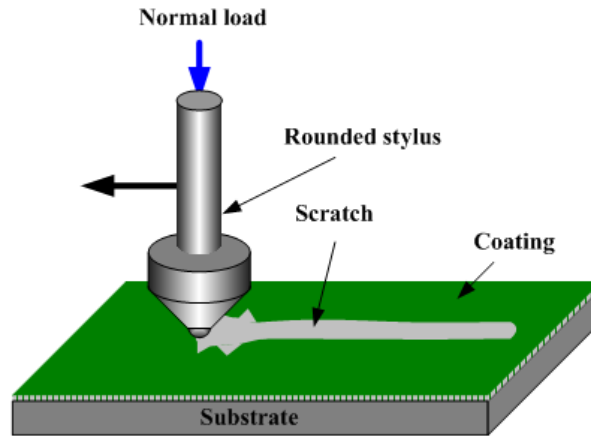


Figure 2.30: Scratch test (F50)

(54).

The Figure 2.31 shows the scratches obtained applying the different techniques. It is possi-

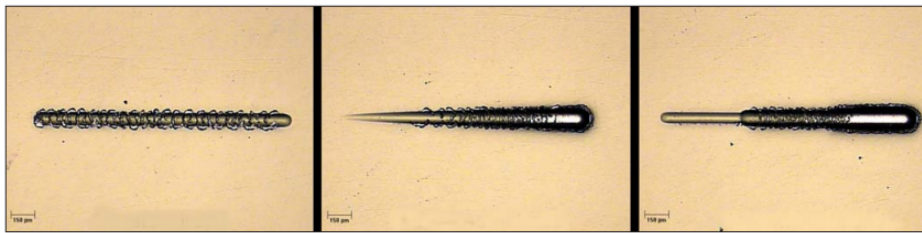


Fig. 3 — The three main scratch modes are constant load, progressive load, and incremental load (from left to right).

Figure 2.31: Three different scratches obtained by applying constant load, progressive load and incremental load (F51)

ble to use an acoustic emission sensor to detect any high-frequency elastic waves generated in coating/substrate system, which indicates delamination, cracking, chipping.

Choudhary and Mishra studied adhesion of Aluminum Nitride coatings, deposited at different temperatures on a stainless steel substrate, using acoustic emission during scratch test. In Figure 2.32 (a), it is possible to see the acoustic emission curves recorded during scratch test, at three different substrate temperatures: the acoustic emission kept low and was less than 1.5%. This indicates that the coating is relatively ductile and has lower defect density, such as voids and cracks and also possesses low intrinsic stresses. The ductile nature of AlN coating increases with temperature, infact the depth of penetration of the

indenter increases in coating formed at higher temperatures, as shown in Figure 2.32 (b). Figure 2.33 shows optical images of scratch test in progressive mode on coating obtained at  $400^{\circ}\text{C}$ . It can be easily observed that till the end load (20 N), there is no adhesive delamination in the coating. Moreover, at the end load (20 N), only fine pores could be seen along the scratch track (55).

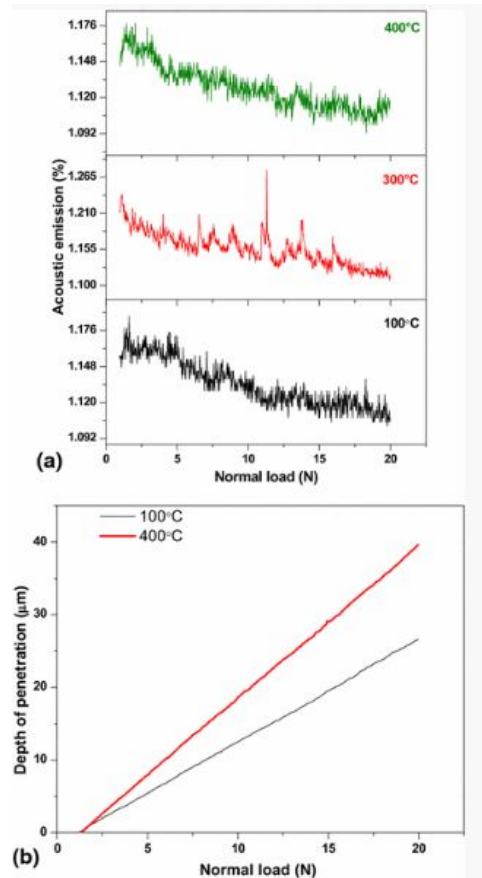


Figure 2.32: (a) acoustic emission and (b) penetration depth curves obtained by scratch test on AlN coatings formed at different temperature (F52)

- Indentation and shockwave-loading methods: a crack at the interface coating-substrate is mechanically created using conventional indentation procedures. In this case, most of the deformation occurs within the film, but there is a certain debonding effect at the interface. The adhesion is related to the crack propagation resistance. The bond between coating and substrate is uniquely related to the fracture resistance, which involves the residual stress and the strength controlling defect. According to this test, if at the interface of the plastic zone created by indentation, cracks are formed, this area has a lower thickness than the coating and substrate. If the coating or the substrate breaks before the separation at the interface occurs, the interface toughness is at least as large as that of the weaker component. In the Figure 2.34 it is shown a scheme of the indentation coating adhesion film and how the crack size changes with load increasing. In some techniques, the aim is to produce delamination by shockwave loading methods. It is possible to use erosive particles or a laser beam and the results depending on the energy absorption by the coating. The laser method involves a laser which probes the coating surface and the absorbed energy induces a stress way which can be monitored. If the incident probe is pulsed, the

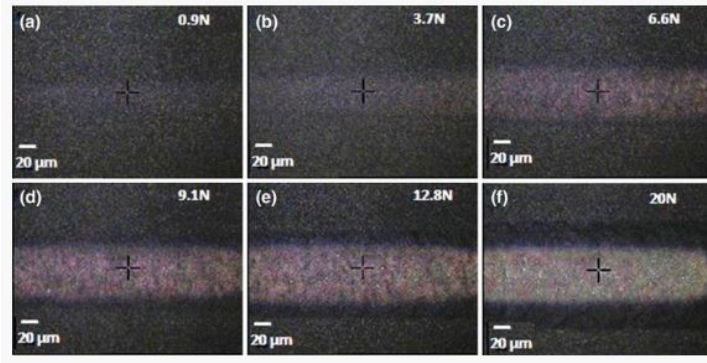


Figure 2.33: Optical scratch images obtained on AlN coating at different loads (F53)

propagation of thermal way is used to detect zone with cracks or debonded regions (50). This test was conducted by Campos-Silva et al. in order to analyze adhesion between FeB/ $Fe_2B$  on the surface of borided AISI 316 steel. Boriding is a thermochemical process with the aim of improving hardness through a diffusion of boron in a clean metal steel surface at high temperature. Vickers interfacial indentation tests were performed with indentation selected from a range of 0.49 to 2.9 N based on the FeB layer thickness. The results are shown in Figure 2.35 and show that the fracture resistance at the interface is a function of the FeB layer thickness: if the FeB layer deep increase, the capacity to resist the initiation and propagation of a crack at the interface increases. The same behavior was observed across the set of boriding conditions for the adherence of the FeB/ $Fe_2B$  system. In addition, it was evaluated that the compressive behavior and intensity of residual stresses decreased as the FeB coating thickness increased (56).

- Impact test: it is important for determining the stone-chip resistance of coatings. A steel ball hits the surface and the transfer of forces through the coating leads to a debonding. In the debonding area, there are two types of stress: compressive stress in the center of the circular detachment zone and shear stress in the annular region. Considering the dimensions of the debonding area, it is possible to evaluate adhesion forces of the coating (Figure 2.36). The effect of different factors must be taken into account: coating thickness, mass, diameter and speed of the steel ball and its time of impact (48).

Bouzakis et al. studied adhesion of TiAlN coating obtained by PVD, with nano-impact test: the indenter reaches the surface and is re-accelerated from a small distance against the film. An appropriate automation enables repetitive impacts at the same position on the sample surface at a set frequency. The evolution of the indentation depth during the repetitive impacts is continuously monitored. The results were compared with those obtained by FEM calculation. These results show that, by the developed FEM simulation model, the film loading, fracture initiation and evolution can be accurately described (57).

- Thermographic detection of defect: with this method, a mapping of the distribution of temperature on the surface is obtained. It is possible to detect defects and debonding areas: the heat flux proceeds toward the surface, and it is constant, if it does not encounter a defect or debonding area, that produces variations in the surface temperature, as it is possible to see in Figure 2.37 (48).
- Blister method: in this method, a fluid is injected at the interface between coating and substrate. An increase of the hydrostatic pressure causes the separation of the coating from

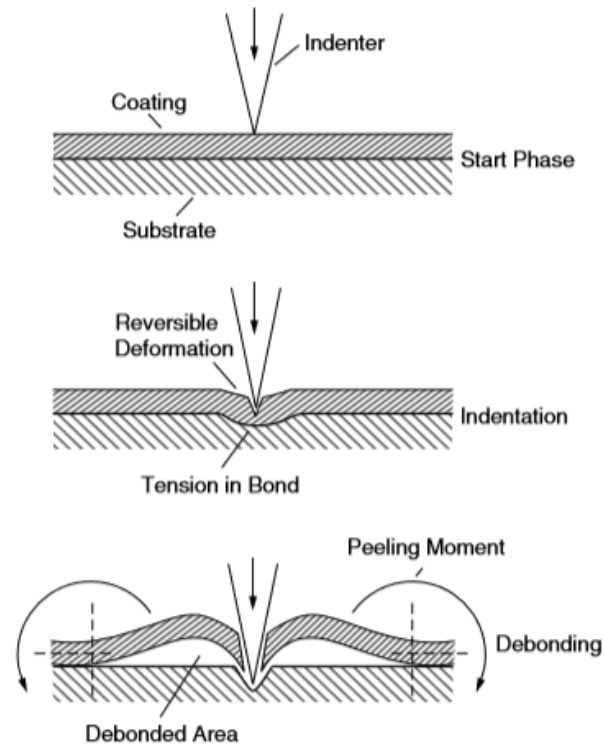


Figure 2.34: Indentation coating test (F54)

the surface (58).

- X-ray method: it is a nondestructive method in which a X-ray spectroscopy is used to study qualitatively the adhesion of epitaxial coating deposited on single-crystal substrate and the strength of the bond. It is possible to use this technique only under conditions, in addition no numerical values are obtained (58).
- Pulsed-laser or electron beam method: the substrate is only partially covered by the coating and a laser or an electron beam is used to generate a compressive stress waves in the surface non covered. The wave propagates through the sample and it is reflected by the coated surface and inverted into a tensile wave (58).

## 2.5 Influence of different factors on coating adhesion

In all applications, the performance of the final product depends on the bond created between coating and substrate. For this reason, several studies have been done with the aim of determining the factors which controls adhesion and improve the characteristics of the system. For example, surface treatments allow to obtain a good coating/substrate interfacial adhesion.

A properly prepared surface provides a better adhesion of the coating and the formation of strong bond at the interface. First of all, the surface has to be clean: it is necessary to eliminate absorbed molecules which can evaporate at the contact with the coating, creating splashing and pores, causing a decrease in mechanical behavior of the coating and substrate and low adherence (59).

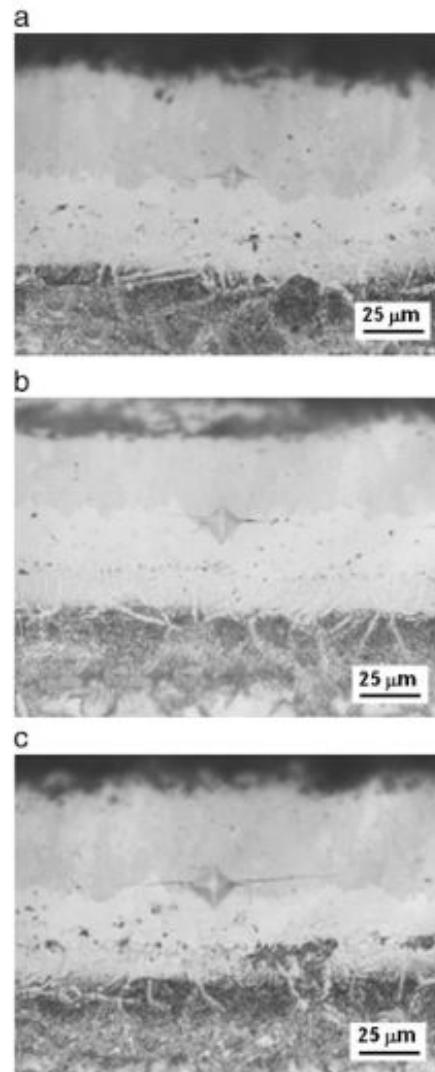


Figure 2.35: Vickers interfacial fracture toughness on FeB/ $Fe_2B$  system: (a) 0.98 N, (b) 1.96 N, and (c) 2.94 N (F55)

Moura e Silva et al.(60) studied the adhesion problems of two systems: two coatings of W-Ti-N and W-DLC:H (W-Diamon Like Carbon) deposited by a reactive unbalanced magnetron sputtering semi-industrial equipment, on pieces of (111) mono-oriented Si and Aisi M2 high speed steel used as substrates. Substrates were cleaned in acetone and ethanol ultrasonic baths and then where placed in the deposition chamber. Before deposition they were cleaned by ion bombardment. They compared the results with analysis developed previously on the same type of coatings at laboratory level.

Results from scratch-test reveal that critical load, function of the partial pressure of the reactive gas, of the coating W-Ti-N is lower in industrially deposition if compared with those laboratory deposited ones. The same result has been found for W-DLC:H coatings. To explain the problem of adhesion, an RBS/ERDA (Rutherford Backscattering Spectrometry/Elastic Recoil Detection Analysis) elemental spectra of a W-DLC:H is done and reveals the presence of W accumulation at the substrate/interlayer interface. Regarding W-Ti-N coating, in order to understand if at the interface there is contamination due to the presence of oxygen in the residual atmosphere

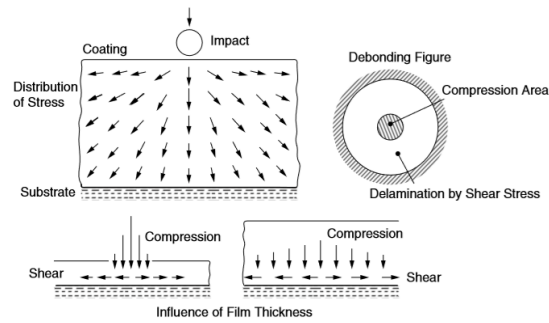


Figure 2.36: Impact test and stress involved (F56)

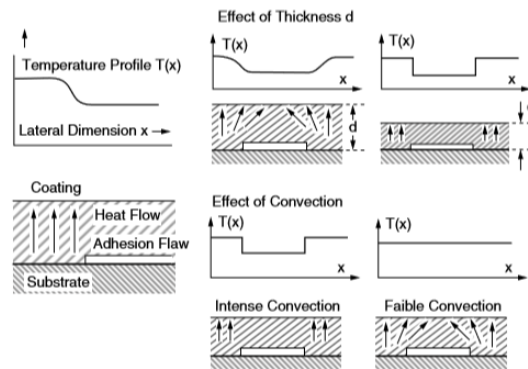


Figure 2.37: Schematic representation of thermographic detection of debonding area (F57)

in deposition chamber, an Auger spectroscopy was done. A coating of W-Ti-N with a very low thickness was deposited to allow the in-depth step analysis Auger spectroscopy after etching of the sample surface by ion bombardment. (Figure 2.38). The result reveals that there is no significant increase of oxygen at the interface, but an unexpected increase of W and Ti has formed a sub-layer between coating and substrate. This is confirmed by the presence of a contamination layer, amorphous and with homogeneous thickness, considered the source for lack of adhesion, as is possible to see in Figure 2.39, obtained by TEM analysis.

Another important parameter, which controls adhesion of a coating to a substrate, is the roughness of surface: it increases surface area for particle-to-substrate contact and allows a better anchorage of the coating. In order to achieve the adequate surface profile, to reduce grease and to make chemical and morphological modifications on the surface degreasing and sandblasting methods are used. The surface obtained is characterized by peaks and valleys due to the impact of high-velocity abrasive particles. In order to remove residual dust, the substrate must be cleaned after sand-blasting, using a solvent and then is dried using clean compressive air. The coating must be deposited after preparation to prevent oxidation and contamination (61).

Varacalle et al.(62) studied the adhesion of Al and Al-Zn coatings on A36/1020 steel deposited by twin-wire electric arc (TWEA). Substrates were prepared by grit-blasting using conventional grit (copper slag, coal slag and chilled iron) and metallic grit. Bond strength of coating were measured. They found that metallic grit produced higher surface roughness than conventional grit. Regarding Al coatings and its deposition method, they discover the relation between bond strength and other parameters: higher current greatly influences bond strength, while spray

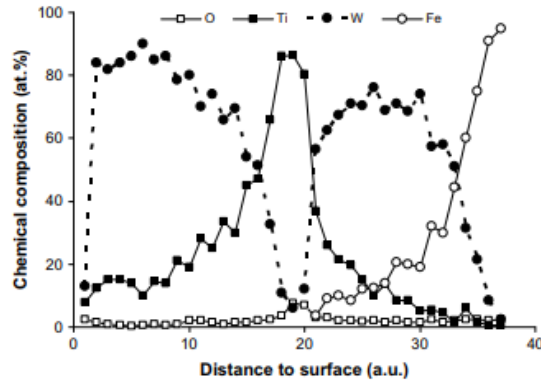


Figure 2.38: Auger in-depth profile chemical composition results of a W-Ti coating (F58)

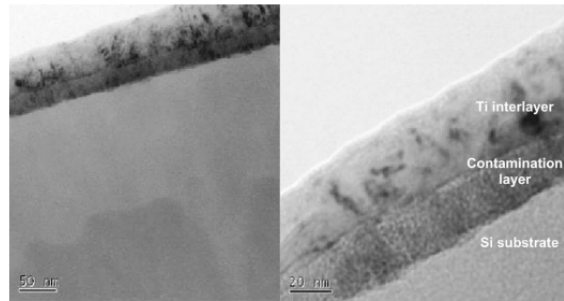


Figure 2.39: HR-TEM micrographs of the interface substrate/interlayer zone of a W-DLC:H coating (F59)

distance and low pressure contribute less to the increase of the adhesion force. Considering substrates covered with Al-Zn, it is possible to note that bond strength is higher in surface treated using metallic grit, in the same way of previous case.

But grit-blasting process presents some disadvantages: it causes a microcracks on the substrate and the decrease of mechanical properties, in addition disposal of chemical waste must be considered (63). As it has already said, inclusion of sand on the surface can have the opposite effect and can decrease the coating adhesion. In order to avoid this problems, physical and chemical modifications, required to have better adhesion, are obtained with new pretreatments solutions.

Danlos et al.(63) tried an alternative method to clean and prepare the surface of the substrate by using a laser. This new method is characterized by the combination of cleaning and heating laser process and is conducted before the deposition of a coating by thermal spay method, two lasers are used: a first millisecond laser heats the surface and a nanosecond ablation laser cleans it (Figure 2.40). In order to optimize the process and to benefit from the maximum surface temperature, a delay between the two lasers is chosen. The laser preheating action is fundamental to avoid the distortion of the substrate or soot deposition which occurs with traditional methods. They studied two substrates: Aluminum alloy 2107 and titanium alloy Ti-6Al-4V, both were mechanically polished to a mirror surface, before being subjected to laser treatment. The morphologies of the two surfaces were analyzed by a SEM and are shown in Figure 2.41: it is possible to see the difference between Aluminum 2107 (1) and Ti-6Al-4V (2) substrates, before the treatment (a), sandblasted (b), after a preheated by laser (c) and after

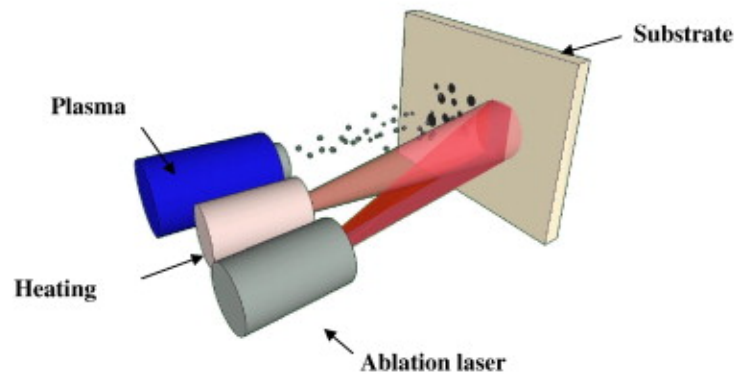


Figure 2.40: Representation of the device for laser treatment and thermal spray (F60)

ablation by laser (d). As it is possible to see in the figure, the surfaces after sandblasting

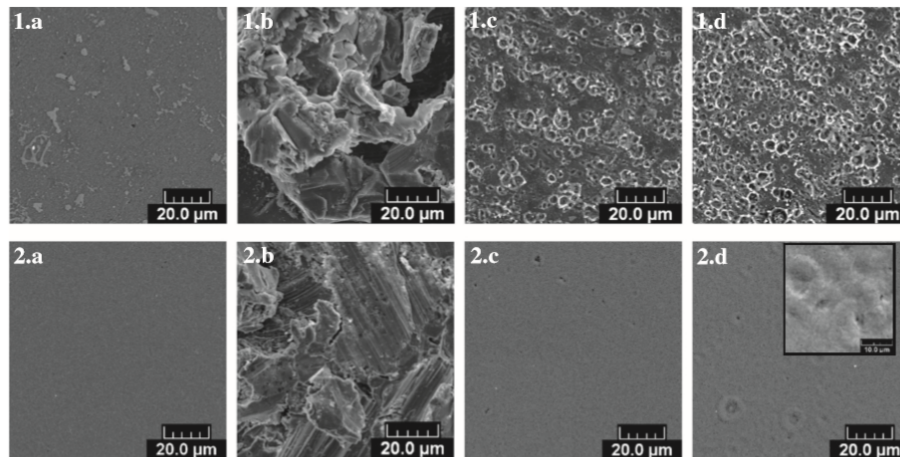


Figure 2.41: SEM observations of Aluminum 2017(1) and Ti-6Al-4V(2) surfaces, (a) reference; (b) sandblasted; (c) preheated by laser and (d) ablated by laser (F61)

presents high roughness than surface before the treatment, due to the impact of the particles with high velocity on the substrates. Important differences are evident between Aluminum 2017 and Ti-6Al-4V after laser treatment: the first is characterized by a non homogeneous surface with a great number of craters, the second presents a plane surface after preheating and ablation treatments. This is linked with the different thermal properties of this materials: Aluminum 2107 has a higher mass heat capacity and thermal conductivity than the titanium alloy, so evacuates thermal energy with more efficiency. Even if Ti-6Al-4V presents a high absorptivity, the energy required to melt it is higher than the one to melt Aluminum 2017, so the latter is more sensitive than the titanium alloy to temperature increase. In addition thermal diffusivity is different: in Aluminum 2017 is high enough to induce a dissipation of thermal energy in the volume, so energy is concentrated not only on surface defects, but also on less sensitive and deeper imperfections. This leads to the formation of more craters: in Ti-6Al-4V are few, so the energy is concentrated to the surface, causing the surface melting. In order to evaluate adhesion a Ni-Al coating is deposited on sandblasted (a) and laser treated (b) of Aluminum 2017 surfaces, as shown in Figure 2.42, and on Ti-6Al-4V sample. It is evident that sandblasted surface has high roughness, molten particles penetrate into the asperities and this slows the propagation

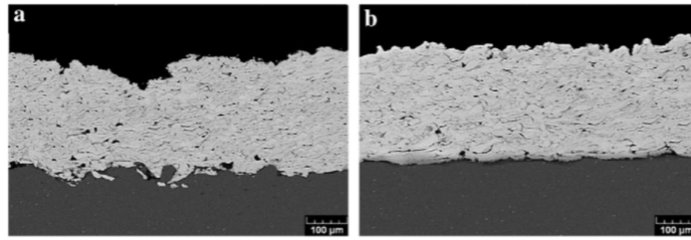


Figure 2.42: Cross section of Ni–Al coatings on Aluminum 2107 surfaces sandblasted (a) and preheated (b) (F62)

of the cracks, but it is possible to see that coating is not totally adhered to the surface, but at interface there are voids and grain inclusions. Conversely the irradiated surface is smoother and there is a good contact between coating and substrate. The adhesion of the coating to the substrate is evaluated by interfacial indentation. The results show that the adhesion seems to be directly connected with roughness: interfacial adhesion is higher on sandblasted surface. From a morphological point of view, by the same laser treatment, surface of Ti-6Al-4V is smoother than surface of Aluminum 2107, considering the adhesion value, the results reveal that in addition to physical anchorage, an important rule is played by chemical affinity. In aluminum surface an oxide layer has been observed, which increases bagnability of the surface and consequently the adhesion of the coating, whereas no oxygen has been detected in Aluminum 2107 surface. So a mixture of mechanical anchorage and chemical affinity seems to be most favourable to increase the adhesion at the interface.

Another laser treatment used to increase strength of bond at the interface is the texturing laser, which consists in creating holes on the surface, with precise diameters following a preset pattern (Figure 2.43). Its efficiency depends on laser and scanner parameters such as hole's geometry, the frequency and power of the laser. The chemical and mechanical modifications induced, increase the contact area between coating and substrate.

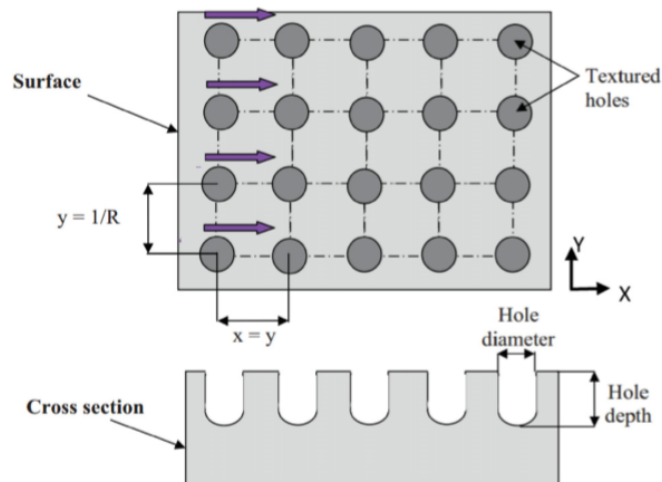


Figure 2.43: Schematic representation of laser textured surface (F63)

Kromer et al. studied the adhesion of a Ni-Al coating, depositing by atmospheric plasma spray, on 2017 aluminum surfaces treated in two different ways: the first one by grit-blasting

and the second by laser surface texturing technique. The two surface were studied before and after coating deposition.

Regarding the method which uses the laser, the adhesion of the coating depends on the pattern geometry and roughness: in particular the dimension of holes must be adapted to the sprayed powder average size and viscosity, and the depth and shaper must be optimized to reduce stress-concentration effects. The adherence was analyzed with two controlling test: pull-off and LASER adhesion test (LASAT). Surface compression is caused by the plasma and relaxation propagates in the sample leading to a volume movement up to the rear surface. It is possible to detect a damage measuring the rear free surface velocity, which is related with the shock wave propagation and with the adhesion force. By a pull-off test is possible to see that the surface treated by the laser allows to obtain stronger bonds and that the adhesion is better compared with the surface treated with conventional way, such as grit blasting. In addition, it is possible to note that the drilled-hole angle does not influence the adherence value but.

Figure 2.44 shows surfaces treated by grit-blasting and by laser (with different distance between the holes) before and after the test is performed. Is evident the anchoring role of the holes, in addition the surface shape obtained with the laser allows to increase the crack energy release rate. In Figure 2.45 are shown the result of the LASAT test. It is evident that pull-off test

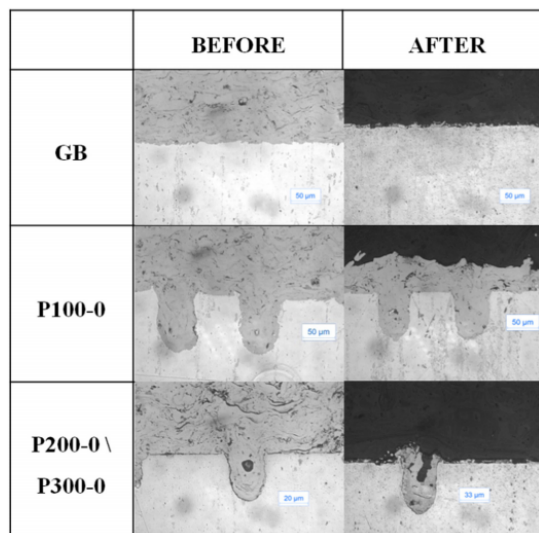


Figure 2.44: Different interface characteristics before and after tensile test for grit-blasted surface, 100  $\mu\text{m}$  distant holes and 200–300  $\mu\text{m}$  distant laserholes (F64)

and LASAT give the same results: the bond strength value in laser treated surface is higher than in grit-blasting treated surface. The necessary energy to separate the coating and the bonding increases with tightened patterning. Laser surface texturing allows to obtain a better coating adhesion to the substrate. Is possible to explain this considering that the crack propagating follows the surface. Holes represent obstacles, which increase the necessary energy for a crack to propagate. With tightened surfaces, the energy required to propagate at the interface is too high due to the irregularities, and crack propagates through coating (64).

Another important process parameter is the temperature at which the substrate is treated. Rahmati et al. studied its effect analyzing substrates of Ti-6Al-4V coated with Ta-O. The samples were heat treated at 300°C, 400°C and 500°C. The bond strength was studies by scratch test. In Figure 2.46 and Figure 2.47 are shown FESEM surface coated of Ti-6Al-4V sample (a) untreated, (b) treated at 300°C, (c) treated at 400°C, (d) treated at 500°C. It is possible to see that different

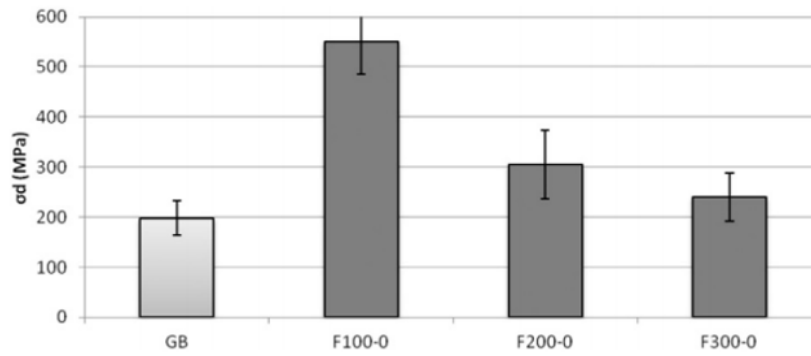


Figure 2.45: Debonding strengths determined from LASAT of different surfaces (F65)

treatment temperatures lead to different morphology: with an increase in temperature, coating becomes denser and smoother. An energy dispersive X-Ray analysis shows that the surface treated at higher temperature has the higher percentage of oxygen, while the lowest percentage is present in the surface before thermal treatment occurs: this means that oxidation increases gradually during thermal treatment. A scratch test indicates that high value of adhesion coating is that of the system treated at  $500^{\circ}\text{C}$ , and in general adhesion increases with an increase in temperature. This is due to the morphology of the system: the coating became denser with high temperature and this improves its adhesion to the substrate. In addition, an important role is played by the rise of oxygen element in the system: the free oxygen in the furnace reacts with Ta and  $\text{Ta}_2\text{O}_5$  is formed (65).

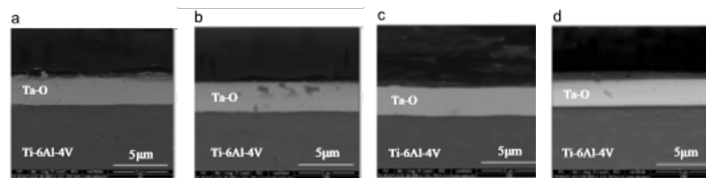


Figure 2.46: FESEM cross-sectional micrographs of coated samples: (a) untreated surface, (b) treated surface at  $300^{\circ}\text{C}$ , (c) treated surface at  $400^{\circ}\text{C}$ , and (d) treated surface at  $500^{\circ}\text{C}$  (F66)

## 2.6 Other considerations

During the coating deposition process some problems can occur. To obtain a good bond at the interface it is important to know the possible problems that may occur and find a solution.

One is represented by sagging and slumping. This phenomena occur in coatings applied to inclined surfaces, in particular, to vertical surfaces. Because of the effect of gravity, a downward flow occurs and leads to sagging or slumping, depending on the nature of the coating fluid. To resolve this situation, it is important to control the viscosity of the coating: in particular purely Newtonian or shear thinning system occur.

During coating deposition, the material deposited is not homogeneous, but imperfections such as waves or furrows usually appear. In this phenomena, an important role is played by surface tension and by the viscosity of the coating. The solution is the leveling, which leads to a reduction of the surface tension of the film. Concerning a corner, when a film is deposited around it, surface tension may increase or decrease the thickness of the coating (Figure 2.48) (50).

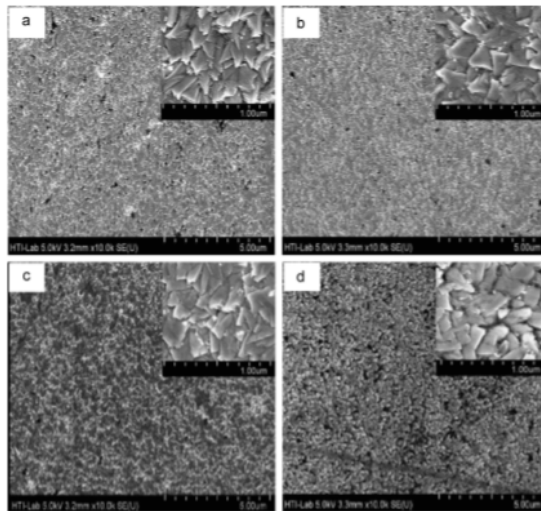


Figure 2.47: FESEM surface topography of Ti-6Al-4V: (a) untreated surface, (b) treated surface at  $300^{\circ}\text{C}$ , (c) treated surface at  $400^{\circ}\text{C}$ , and (d) treated surface at  $500^{\circ}\text{C}$  (F67)

If the surface presents a surface tension gradient, local distortion can occur. The flow of a liquid from a region of lower to higher surface tension caused by the surface tension gradient results in the formation of depressions of the liquid surface. The increase in the polymer concentration and the cooling due to solvent evaporation cause the surface tension and surface density to exceed those of the bulk. This creates an unstable configuration, which tends to move into a more stable one in which the material at the surface has a lower surface tension and density. Related to this, the formation of craters, which are circular depressions on a liquid surface, can be caused by the presence of a low surface tension component at the film surface. The spreading of this low surface tension component causes the bulk transfer of film materials, resulting in the formation of craters.

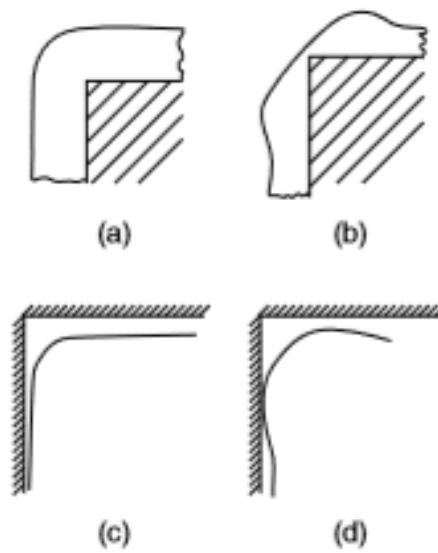


Figure 2.48: (a) Newly applied thick film at a corner; (b) decrease in the film thickness at the corner due to surface tension at a corner; (c) newly applied thin film at a corner; (d) increase in the film thickness at the corner due to surface tension (F68)

## Chapter 3

# Dental implants

### 3.1 Oral cavity

The oral cavity, or mouth, shown in Figure 3.1, is a part of the oral region, constitutes an inlet for the digestive system but has also a respiratory function. It is constituted by the hard and soft palates, the cheeks and the retro molar regions (66). The inside of the oral cavity is composed by dental arches of upper jaw and lower jaw, i.e. rows of teeth supported by alveolar bone. It is necessary to distinguish between “oral cavity” and “vestibulum oris”: the oral cavity is the front and the lateral part of the space delimited by teeth and occupied by the tongue, the vestibulum oris is the part between the teeth and the lips or cheeks. The entire oral cavity is coated by the oral mucosa which contains sensory receptors for temperature and touch, on the tongue there are also receptors for the sense of taste (1).

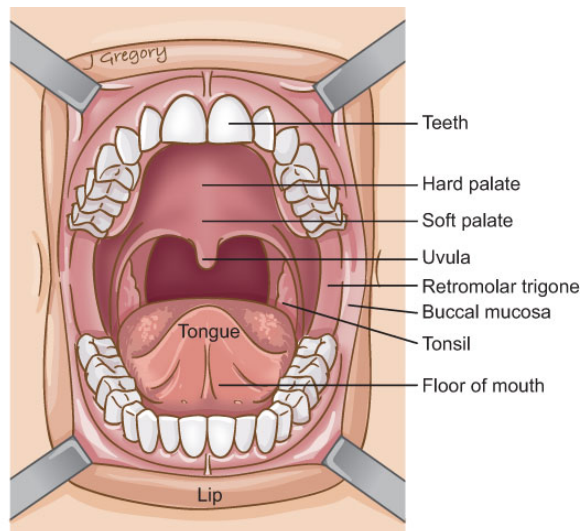


Figure 3.1: Oral cavity (F69)

### 3.2 Structure of teeth

The structure of the teeth is represented in Figure 3.2. It is possible to distinguish the structure of the teeth in three different part: crown, root and tooth collar. The crown is the visible part of

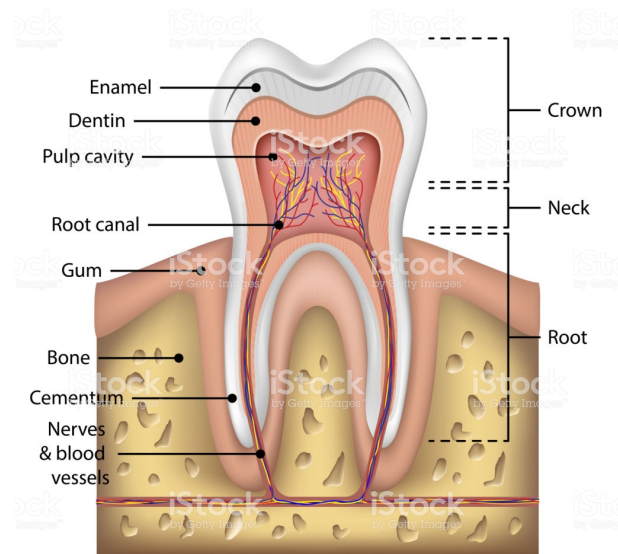


Figure 3.2: Tooth anatomy (F70)

teeth, it can take different shapes depending on the type of the teeth: in canine tooth is pointed, in incisor tooth is flattened, in molar and premolar tooth it is characterized by grooves.

The root is the non-visible part of the teeth, it is contained within the bone and has the function of supporting the tooth itself. Different types of teeth have different number of roots: canine tooth, incisors and lower premolars have one root, upper premolars can have one or two roots, and lower molars have two roots while upper molars have three roots. In the tooth region called "apical" there is a small opening (apical foramen) through which blood vessels, lymph vessels and nerves pass, entering the tooth to provide nourishment and innervation.

The tooth collar is the intermediate part between crown and root, gums develops around it.

The teeth consists of different tissues, three are hard substances: enamel, cement and dentine, and a soft substance: dental pulp.

The enamel consists of calcium, magnesium, phosphorus, carbonate, and potassium compounds, in addition of water and organic substances and represents the 96% of the material. It is translucent and is the most external part of the tooth.

The cement, as will be explained later, is a thin and resistant layer, which covers root's surface and has a protective function. It is made up of 65% by inorganic compounds, like calcium and phosphate. Cement is produced by cementoblasts.

Dentine is the substance which constitutes the tooth, is composed of about 70% by inorganic substances, and the remaining 30% by organic material and water. It is surrounded by enamel at the coronal level and, in the root area, is covered with cement. Dentine is produced by odontoblasts.

The pulp is a soft tissues which includes the nerve, blood vessels and other cells including odontoblast. It is inside the crown (crown pulp), it continues along the roots (root pulp) up to the apex of the tooth (67).

### 3.2.1 Peridontum

The periodontum, which literally means "around the tooth", is the tissue which surrounds and supports the teeth. It has an important role: it damps the forces acting on the teeth, in fact

there is a constant state of balance between the periodontal structures and the external forces. It is formed by gums, periodontal ligament, cementum, alveolar bone proper; each of these component has different properties, and are distinguished from the location and the architecture.

Gums (or gingiva) is a soft tissue which surrounds and protects the teeth, providing a seal around them and creating a barrier against infection. It is formed by an outer epithelium, which is keratinized and an inner network of connective tissue, within which there are gingival fibroblasts, cells important for the tissue repair and inflammatory response (68).

Periodontal ligament, also known as PDL, is a soft connective tissue, with the function of connecting the cementum of teeth to the gums and alveolar bone. It is formed by collagen bands and fibroblasts are the main cells in it, important for maintaining, repairing and forming alveolar bone and cementum (69).

Cementum, also known as root cementum, is a mineralized layer which cover the entire root surface, is similar to bone tissue, but, unlike the bone, is avascular and doesn't undergo dynamic remodelling. The most important cells in cementum are the cementocytes that lies in its lacuna (70).

Alveolar bone is an intramembranous bone forming with the formation of mandible and maxilla. It is important to distinguish between "alveolar process" and "alveolar bone". Alveolar process is that part which contains the teeth and the alveoli, it is characterized by a spongy bone, which is protected by cortical plate of compact bone. Alveolar bone, composed by cortical bone with blood vessels, lines the alveolus, contained in the alveolar process (71).

### 3.2.2 Periodontal disease

Periodontal disease is an infection of the part that surrounds the teeth: gums, cementum that covers the root, periodontal ligament and alveolar bone (Figure 3.3).

The first stage is gingivitis, that affects only gums, but it can progress to affect the bone around the teeth. In this case there are more severe forms of disease: periodontitis and advanced periodontitis. In gingivitis stage, the bacteria in dental plaque, which is a substance that forms



Figure 3.3: Difference between normal tooth and periodontitis (F71)

on teeth, causes the inflammation and damage of the gums. In this step neither the teeth nor the bone are damaged. If gingivitis is left untreated, it can become periodontitis. In this case pockets are formed around the teeth, after the inner layer of bone and gum pulls away from teeth. In these pockets debris accumulates, causing infection: the body's immune system fights

the bacteria while the plaque grows below the line gum. Toxins produced by the bacteria in plaque make the pockets deeper and more gum tissue and bone are destroyed. In this case teeth are no anchored and tooth loss occurs.

From what has been said, it is clear the plaque is the first reason of periodontal disease, but there are also other factors:

- bad habits, such as smoking;
- poor oral hygiene habits, such as not brushing teeth daily;
- Hhormonal changes;
- illnesses, which include cancer, HIV or diabetes;
- history of family disease (72).

### 3.3 Types of dental implants

Dental implantology is a branch of dentistry which has the aim of replacing the missing teeth with synthetic root anchored to the bone, in order to restore normal function and aesthetics of the system. Dental implants (Figure 3.4) are surgically positioned in the jaw bone underneath the gums, and during healing period osseointegration occurs.

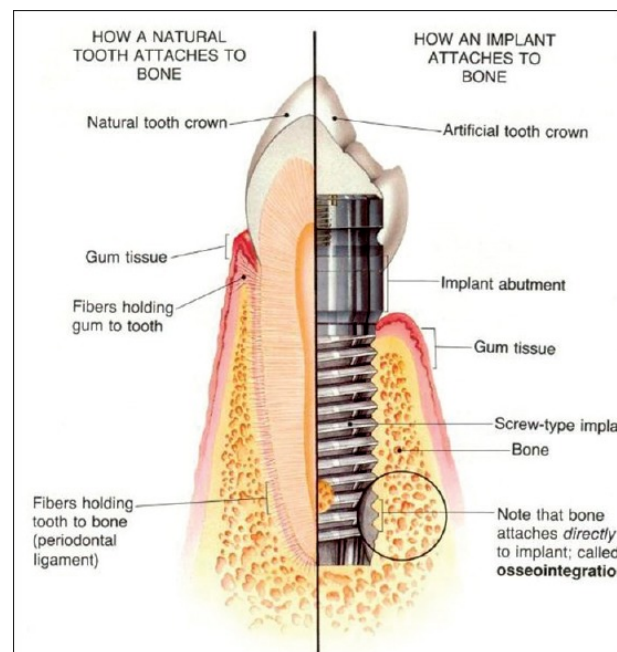


Figure 3.4: Dental implant (F72)

The concept of tissue-integrated prosthesis was studied at university of Lund and at laboratory for experimental biology at the University of Goteberg. A good osseointegration leads to permanent, interactive and functional interaction between implant and bone, when a topographically and precise recipient site is prepared in the bone. The anchorage stability, the healing period, different sizes and designs of implant, human microcirculation and intravascular behaviour of blood cells, were studied to obtain the better result.

The healing process consists of formation of blood clots because of the blood present between

fixture and bone. These clots are transformed by phagocytic cells, such as leukocytes, lymphoid cells, and macrophages. At this time, implant is placed and bone remodelling occurs. Haversian bone calcifies becoming dense and homogenous, and the surrounding bone is stimulated. If the devices is well designed for a good stress distribution and osseointegration happened correctly, cortical bone forms along the fixture surface with a thickness of few millimetres. A network of collagen bundles surround the osteocytes and a 100 Angstrom glycoprotein layer is formed. The Haversian bone becomes well organized and forms osteon (73).

The first researchers who implanted titanium devices in animals were Bothe at al. who remarked the tendency of this metal to fuse with bone.

In 1951 Leventhal studied how titanium screws placed in rat femurs after 16 weeks were difficult to remove and how the trabeculation was very similar to normal trabecular bone (74).

In 1951 Branemark et al. implanted titanium screw in dog's jaw bone and after 16 weeks they obtained the same result: it is possible to establish a bone-to-titanium contact.

In 1953 he called this mechanism "osseointegration", defined as "a direct connection between living bone and a load-carrying endosseous implant at the light microscopic level" (75) (76).

Then the research focused on how to improve bone-to-titanium interaction, to increase the life time of the implant and reduce bacterial adhesion.

There are different types of prosthesis:

- Subperiosteal implants: they are metallic structures surgically placed between surface bone and the periosteum, the implant pillars pierce the mucosa that covers them (Figure 3.5). They have low percentages of success because they are very different from the natural roots shape, and it makes the osteointegration process difficult and for this reason they are seldom used;

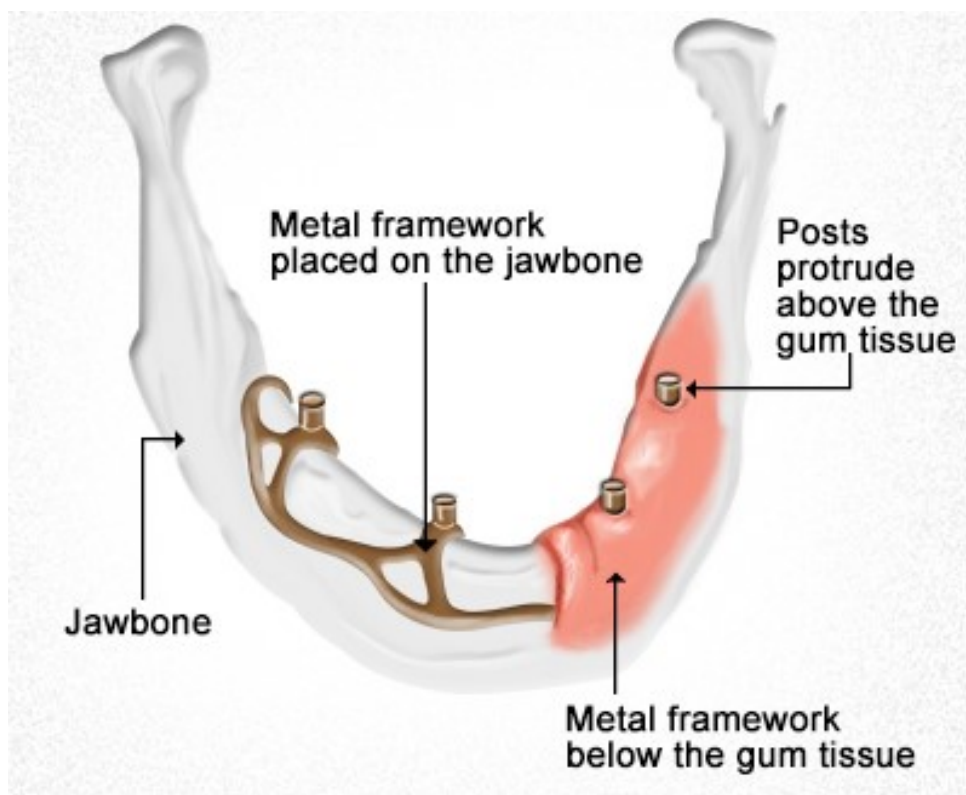


Figure 3.5: Subperiosteal implant (F73)

- Endosseous implants: the implant is directly inserted in the bone; they can be closed, placed under the periosteum and cannot communicate with the oral cavity; or open, which are equipped with a pillar having this function (Figure 3.6). There is another type of endosseous implant which is covered by an epithelial layer for a long period (several months) and then is exposed. This types of implant are very common for the simplicity of surgical technique and the possibility to replace it in case of failure;

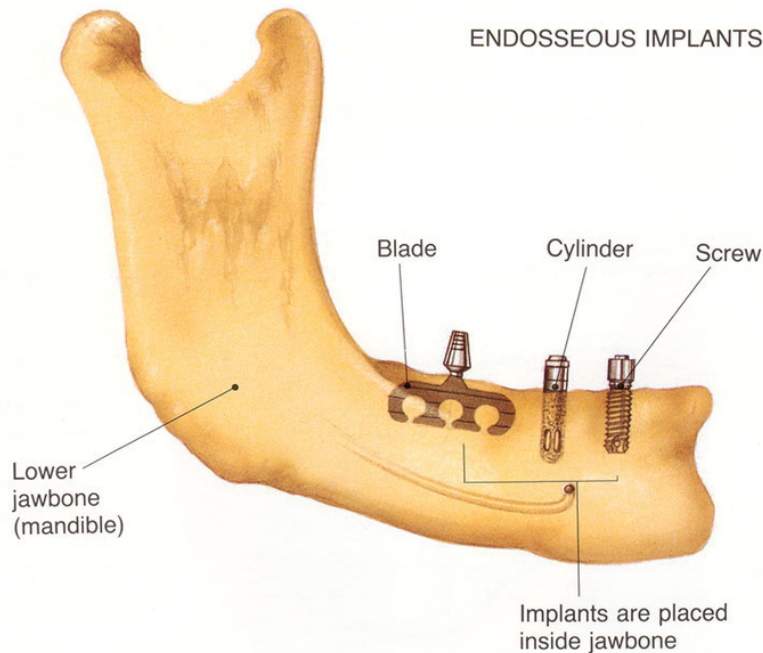


Figure 3.6: Endosseous implant (F74)

- Subperiosteal endosseous implants: they are a combination of the two previous type, in which one part is inside the bone, one is above it;
- Transosseous implants: are specific to the jaw and through vertically it (Figure 3.7);
- Transdental implants: they have the function of stabilizing the teeth in which are placed, so they are called endodontics. They have a kind of "biological collar" for the anchorage between the separation seal with the oral cavity and the periodontium of a natural tooth;
- Intramucosal implants: they are inserted into the mucosa by fixing to a base prosthetic and because they do not perforate the lining epithelium and do not remain permanently in the implant site (Figure 3.8), they are more suitable for classical prosthesis rather than implant prostheses (77).

A dental implant is constituted by three parts, represented in Figure 3.9:

- Implant: similar to a screw, in general made in titanium, which is anchored directly into the jawbone;
- Abutment: metallic structure which connect prosthesis to implant, is fixed on the top of exposed implant post (78);

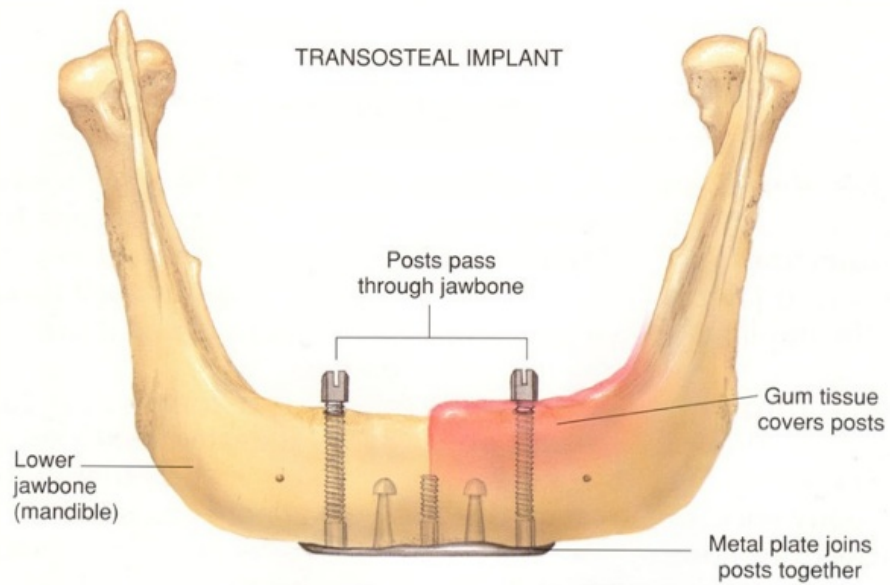


Figure 3.7: Transosseous implant (F75)

- Crown: artificial crown which replaces natural tooth (it can be a bridge or a dentature for people missing many or all teeth). Dental impressions, x-rays and other techniques are used in order to obtain a functional and look natural implant (79).



Figure 3.8: Intramucosal implant (F76)

### 3.4 General features of dental implants

The success or failure of implant is determined by the interface zone between the prosthesis and the receiving tissue: when the implant is positioned, blood clots form at the wound site and protein adsorption occurs, then fibroblasts proliferate in the blood clots creating an extracellular matrix. After one week, it is possible to see new bone around the implant surface through osseointegration. The implants and the materials used must have extraordinary requirements.

Dental implant must have the ability to provide its intended function from an engineering viewpoint, so certain mechanical and physical properties are required. They must be biocompatible, because of the interaction between the foreign material and the host living tissue. In most of medical applications, an implant device is expected to function for the life of the patient. So, one of the many universal implant requirements is the ability to form a suitably stable mechanical unit with the neighbouring hard or soft tissues (80).

#### 3.4.1 Mechanical stability

An important aspect that must be taken into account is the mechanical compatibility of dental implants, also called primary stability, which deals with biting force acting on the implant, transferring of these forces to the interfacial tissue, and with the biological reaction of the interface

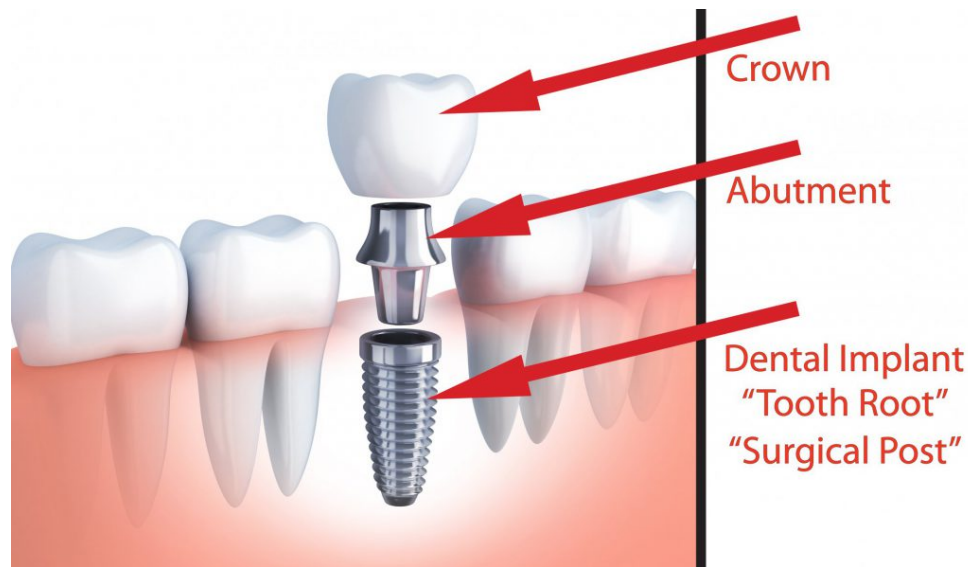


Figure 3.9: Different parts of a dental implant (F77)

to stress transfer conditions.

To make progress in this technology, it is necessary to study the manner in which mechanical stress are transferred, in order to avoid relative motion between implant and bone, which can cause abrasive phenomena and the destroy of the implant. It is studied that bite forces acting in patients with implants and in patients with natural teeth are the same, so it is important that neither bone nor implant be stressed beyond the long term fatigue capacity. In this case, fracture mechanisms time is considered the prime factor since damages accumulate over time (80). The behaviour and life of the implant is determined by stress concentrations and fixation of the implant. Osseointegration plays an important role in the success of the implant: it is based on the placement and the quality and quantity of trabecular bones. The reduction in size and in density of the bone can cause problem to the pleacemnet of the implant. To control this, different factors must be taken into account, such as applied loads, length and diameter of the implant, its geometry and surface and inteface between implant and bone. In general, if the elastic modulus is similar to that of the bone, a load applied causes stress and much more deformation on the implant, this provides a smooth transmission of the stress from the implant to the bone and decreases energy magnitude.

Fatma et al. studied how mechanical properties cause stress distribution on implant made with different materials: AISI 316L, CoCr alloys, ZTA (Zirconia-toughened alumina), YSZ (Yttria-stabilized zirconia), Ti-cp with nanotubular  $TiO_2$ . The equivalent Von Mises stress values and their concentration was evaluated: the results revealed that the critical zone is related to thread region, which can be fractured or can have a failure (Figure 3.10). Stress value is in the range between 226.95 MPa and 239,05 MPa. In order to guarantee an efficient stress transfer from implant to bone and to avoid the stress-shielding effect, Young's modulus must be as close as possible to that of the bone. All the materials studied have a low value of Young's modulus, in particular nanotubular titania has the lowest elastic modulus value and the closest one to the value bone.

Another important factor that must be taken into account is the amount of penetration of implant onto the bone: the highest value is that of cp-Ti with nanotubular  $TiO_2$  surface (0,013626 mm), the lowest was assigned by CoCr alloy (0,0037389 mm).

Also tests releted to fatigue life were conducted: the life prediction is based on the term of the

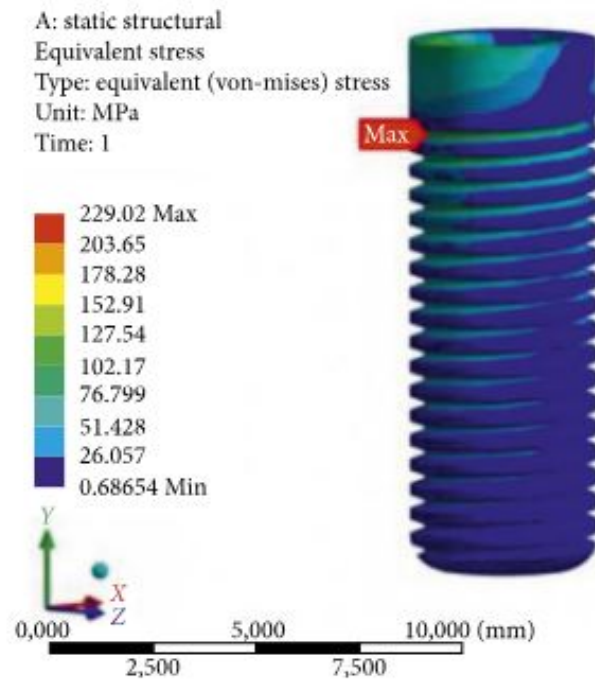


Figure 3.10: Equivalent von Mises stress on dental implant (F78)

cycle number corresponding to the cyclic stress value. This value is between  $4 \times 10^5$  and  $1 \times 10^9$  cycles. The life value for cp-Ti with nanotubular  $TiO_2$  surface was of  $1 \times 10^7$  cycles, for CoCr alloy was of  $1 \times 10^9$  cycles. Based on this analysis, cp-Ti with nanotubular  $TiO_2$  surface was considered the best performing material. To increase friction and obtain more fixation, multiple threaded are required to obtain mechanical locking between the implant surface and the bone (81).

### 3.4.2 Biological stability

As already mentioned, the material used for dental implant must be biocompatible and able to obtain biological stability or the so called secondary stability. Biocompatibility of metallic materials also equates with corrosion resistance because of the hostile service conditions in the mouth: all the implant part are in contact with saliva, an aqueous solution of 0,1 N chlorides with Na, K, Ca,  $PO_4$  and  $CO_2$  in different percentages. The pH values is generally between 5,5 and 7,5, but under plaque it can be lower than 2, and the temperature is about  $36,5^\circ C$ . In some cases food debris can decomposed forming sulphides causing devices discoloration (80).

Today, titanium is considered the most compatible material to vital tissue: it is passive in aqueous solutions, it is well documented that the excellent corrosion resistance of titanium materials is due to the formation of a dense, protective, and strongly-adhered film of thickness between 2 and 7 nm, the so called passive film, which is stable (80).

An important aspect of this material is the purity, it, infact, affects bacterial adhesion.

Violant et al. conducted an in vitro study to compare the bacterial cell attachment of a four-species of oral biofilm on titanium samples of grade 2 and 4, with machined or thermochemically modified surface. The treatment combines an increase in surface roughness by chemical etching and an increase in thickness and crystallinity of the titanium oxide layer by thermal treatment. Strains were growth on blood agar plates in an anaerobic chamber at  $37^\circ C$  for 48 hours. The

four strains were used to product biofilms in layers over sterilized titanium discs.

The titanium samples were divided in four groups: Ti of grade 2/machined surface, Ti of grade 2/treated surface, Ti of grade 4/machined surface, Ti grade 4/treated surface. Nine implants of each surface was exposed to the multispecies biofilm. After six days of incubation, cells proliferation was evaluated using 1, 2 ,3, 5% triphenyltetrazolium and spectrophotometry.

Figure 3.11 shows mean cells viability of the biofilm formed on the different implant afetr 7 days tested with TTC 1% solution. Figure 3.12 shows the bactrial attachment on the different implants surfaces.

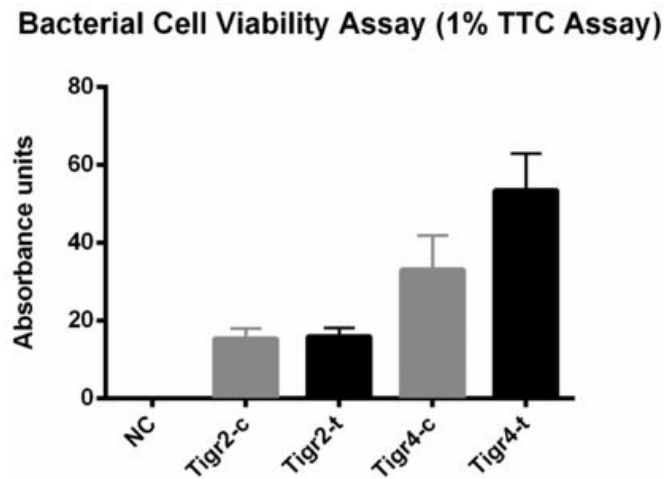


Figure 3.11: Bacterial cell viability assay (1% TTC assay) (F79)

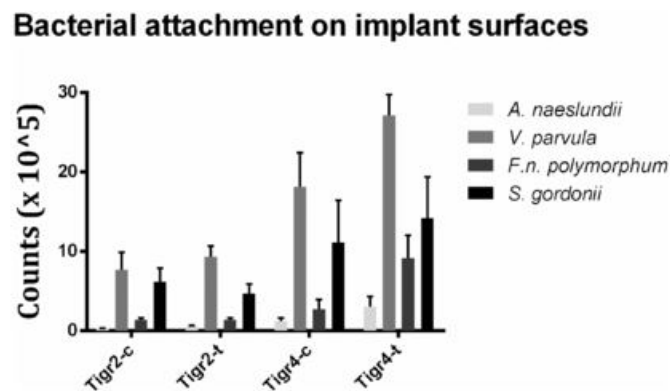


Figure 3.12: Bacterial attachment on implant surfaces (F80)

The tests revealed that titanium surface of grade 2 had a less bacterial load adhesion rather than titanium of grade 4, whereas both smooth surfaces showed lower biofilm adhesion. This leads to an important conclusion: the implant surface morphology and chemical properties influence bacterial adhesion and biofilm thickness, but not biofilm composition (82).

### 3.4.3 Morphological stability

Also morphological compatibility is necessary for the effectiveness of a dental product: it is important to consider the implant's surface, because it is the part which is in contact with the

bioenvironment, is very different morphologically and compositionally from the bulk, and the surface properties determine stability between implant and bone and the biological response. For example, surface roughness determines cell attachment and cell proliferation and play an important role in antibacterial response (80).

Considering two surface roughness parameters Ra and Sa, which are defined as the arithmetic mean deviation of a linear profile or a surface, some studies demonstrate that surfaces with Sa = 1-2  $\mu\text{m}$  showed stronger bone response than surfaces with Sa > 2  $\mu\text{m}$ . Moreover qualitative and quantitative measurements of biofilms did not change if Ra < 0,2  $\mu\text{m}$ , which represents the so-called "Threshold Ra" (83).

Teughels et al studied that an increase of surface roughness above Ra=0,2  $\mu\text{m}$  favours plaque adhesion and accumulation (84).

## Chapter 4

# Materials and Methods

### 4.1 Cutting, marking and polishing of samples

In this thesis work, commercially pure titanium of grade 2 has been used (ASTM B348, Gr2, Titanium Consulting and Trading). The samples are in the form of disks with the dimensions of 10 mm of diameter and 2 mm of thickness, obtained by cutting cylindrical bars.

As shown in Figure 2.1, the samples were characterized by evident signs of machining, for this reason polishing operations have been performed following this protocol: both faces of each samples were polished with SiC abrasive paper 320 grit. Then, one of the two faces was marked using an electric pen, in order to easily recognize the samples treated in different ways. The unmarked faces were polished with SiC abrasive paper 600, 800, 1000, 3200 and 4000 grit.

After polishing, two of the samples were made rough, using paper 1000 for 10" in a single direction as previously reported (85).



Figure 4.1: Samples before and after polishing

## 4.2 Washing of samples

In order to remove contaminations due to the previous treatments, disks were washed. In a first step, samples were immersed in a beaker containing acetone, with the marked face in contact with the bottom of the beaker. This operation has been carried out under laminar flow cabinet and with HEPA filter. After covering the beaker with aluminum foil, it was transferred in a sonicator (Figure 4.2) by setting 5-minute working time.

In a second step, the samples were transferred in abundant ultrapure water, while the acetone was recovered. The beaker was inserted in the sonicator for 10 minutes. At the end of ten minutes, the operation was repeated a second time, using new ultrapure water.

The use of sonicator is important to separate residuals and contaminations of various sorts, due to the transmission of mechanical vibrations amplified by a high frequency electric current (about 20 kHz) in a tank containing water, in which the beakers containing samples were placed. Electric energy is transformed into an acoustic impact energy between the water and the surfaces to be cleaned.

At the end of these operations, the samples were dried under a laminar flow cabinet and then they were packed in appropriate envelopes.



Figure 4.2: Ultrasonic machine

### 4.2.1 Preparation of titanium cylinders

In order to analyze how keratin nanofibers can be arranged on a dental implant, small titanium cylinders were used. In this case, titanium bars, produced by a dental implant company, were polished and made rough by O.C.M. A. S. Cervai Sas.

For the polishing process, papers of different grain were attached to a lathe, which was rotated in contact with the samples. The protocol followed was:

- 40" at 1500 rpm with paper of 40  $\mu\text{m}$ ;
- 40" at 1500 rpm with paper of 30  $\mu\text{m}$ ;
- 40" at 1500 rpm with paper of 20  $\mu\text{m}$ ;
- 40" at 1500 rpm with paper of 16  $\mu\text{m}$ ;

- 40" at 1500 rpm with paper of 9  $\mu\text{m}$ ;
- 40" at 1500 rpm with paper of 5  $\mu\text{m}$ ;
- 40" at 1500 rpm with paper of 3  $\mu\text{m}$ ;
- 40" at 1500 rpm with paper of 1  $\mu\text{m}$ ;

Then the bars have been made rough in the same way, using a paper of grain 1000, at the same velocity but for 10".

Then the bars were cut into small cylinders of length of 4 mm, using the cut-off machine Brillant 220, shown in Figure 4.3, and an alumina blade. The small cylinder obtained was shown in



Figure 4.3: Cut-off machine

Figure 4.4.

In order to eliminate impurities due to previous work, the samples were washed, following the same protocol described before and used for titanium disks:

- an acetone washing in sonicator for 5 minutes;
- two ultrapure water washings in sonicator for 10 minutes.

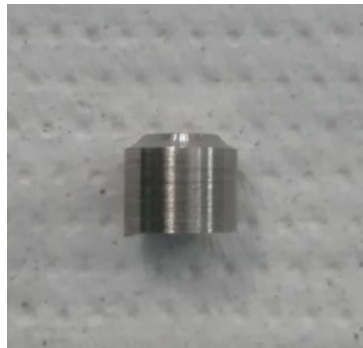


Figure 4.4: Titanium cylinder obtained by cutting bars

### 4.3 Surface activation with plasma

Plasma activation is a method of surface modification employing plasma processing. This treatment is done on various materials, such as metals, ceramics, glass, polymers and natural materials and has the aim to improve surface adhesion properties. A combination of reduction of metals oxides, ultra-fine surface cleaning from organic contaminants, modification of the surface topography and deposition of functional chemical groups occur on the samples surface during the treatment. Plasma activation can be performed at atmospheric pressure using air or typical industrial gases such as hydrogen, oxygen or nitrogen (86).

In particular, in biomedical applications it is used to remove the organic layer from titanium implants, in order to make osseointegration faster, to remove organic residuals at atomic level after the classical industrial washes and to sterilize heat-sensitive materials. (87)

In this work, a plasma surface activation in air was carried out, in order to make the surface of samples more reactive for the subsequent deposition of keratin coating. The plasma system used is shown in Figure 4.5. After cleaning the chamber and setting the process conditions, the samples were placed on an appropriate tray, covered with aluminum foil, and were inserted manually into the chamber.

The process takes place in air, for 10 minutes at a power of 100 Watt. Inside the chamber, the plasma generated creates reactive ion species that act on the surfaces to be treated. When the process was finished, the samples were sealed in aluminum foil and stored at room temperature before the deposition of the coating.

The samples which were plasma-treated were:

- Polished Ti;
- Titanium cylinders.



Figure 4.5: Plasma system

### 4.4 Surface activation with UV

To improve coating adhesion to a substrate, UV treatment can also be used. It is based on reactivity of titanium: if it is exposed to an atmosphere or to an environment containing free oxygen, on its surface a thin and tenacious oxide film is formed, due to the oxidation reactions that occur on the surface. This passive oxide layer, which has a thickness of few nanometers,

gives to the material important properties, such as corrosion resistance (88). The nano-structured titanium dioxide is characterized by photocatalytic properties: it can absorb the light-emitting, generating photo-catalytic effects, it can use the electromagnetic radiation energy absorbed to cause chemical reactions in other molecules that are close to surface of metal particles. In order to obtain this process, is necessary to use ultraviolet radiation, with a wavelength  $\lambda$  in the range of 400 nm and 10 nm. When UV radiation is absorbed by  $TiO_2$ , generates an electron-gap pairs, infact an electron is promoted to the conduction band, and a pair of negatively-charged free electron and a positively-charged electron hole is created. The molecules of water are decomposed by titanium dioxide gap in hydrogen and hydroxyl ions/radicals, whereas the electron reacts with the oxygen molecules to form superoxide ions. For this reason, UV treatment of titanium, especially  $TiO_2$ , before functionalization can make improvements due to an increase in superficial OH groups. This mechanism, known as photocatalysis, is represented in Figure 4.6.

Different studies have been conducted with the aim of understanding advantages of using UV-pretreated titanium (89).

Iwasa et al. studied osteoblasts attachment to UV-treated and to untreated titanium surfaces. They found that UV treatment enaches cells attachment and tried to explain this effect.

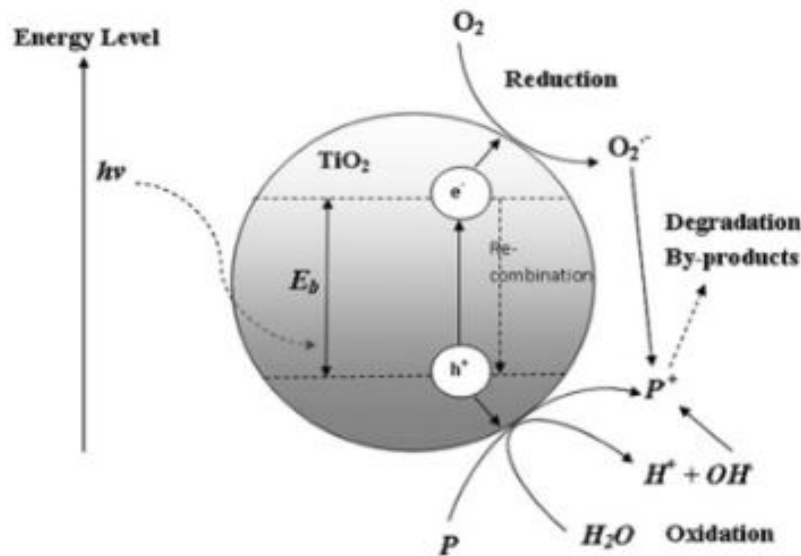


Figure 4.6: Mechanism of photocatalysis (F81)

As shown in Figure 4.7 (A), titanium surface has a net negative charge, whereas a UV-treated titanium surface has a positive charge, due to excited electrons from valence bands to conduction bands. In the first case the negative charge must be bridged by divalent cations such as  $Ca^{2+}$  to attract anionic proteins, whereas monovalent cations such as  $Na^+$  and  $K^+$  may block the anion sites of titanium surface for  $Ca^{2+}$ , this explain why titanium is considered a bioinert material. In the case of UV-treated titanium, UV irradiation causes an excitement of an electron from valence band to conductive band, leaving the surface electropositive. In this way, cells and proteins can directly attach on this surface (Figure 4.7 (B)). This treatment gives to titanium surface high bioactivity.

Titanium samples were UV irradiated for 1 hour before keratin coating deposition (90). The instrument used is shown in Figure 4.8

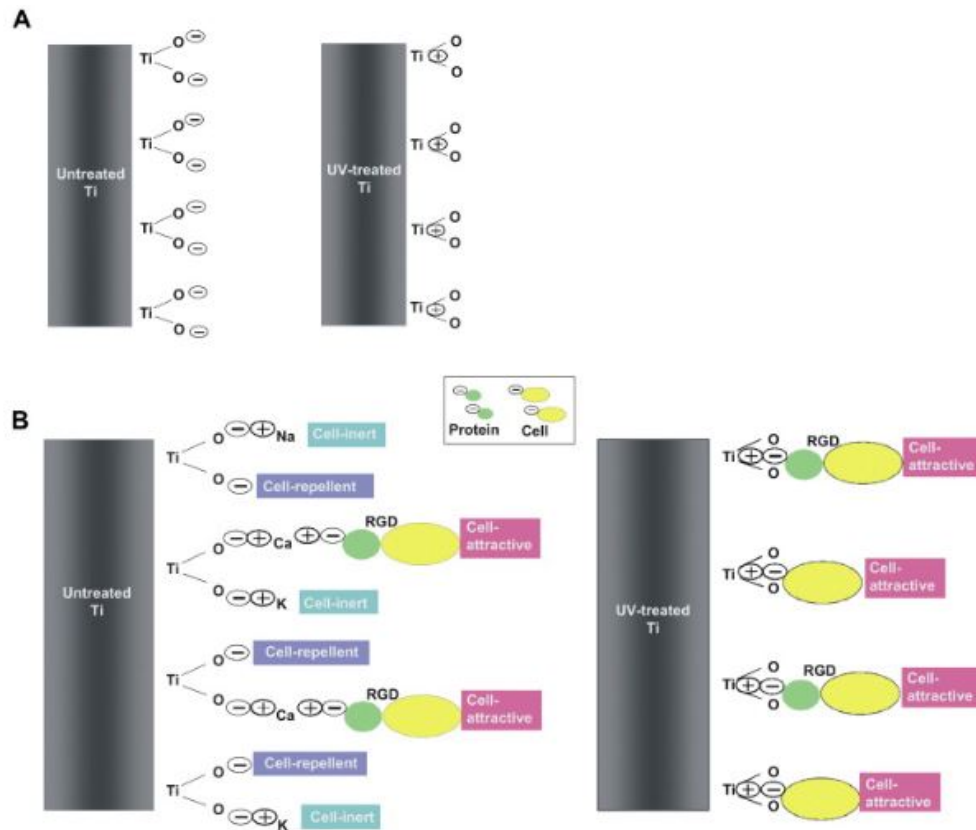


Figure 4.7: (A) Hypothetical electric status of untreated and UV-treated Ti surface, (B) Intercation of untreated and UV-treated Ti surface with ions, cells, proteins (F82)

## 4.5 Coating deposition and functionalitation

In this thesis work, different keratin solutions were prepared, modifying the keratin concentration: solutions of keratin at 7% wt, at 3% wt and 1% wt. Keratin flakes, extracted by wool, were used. To prepare the keratin solution at 7% wt, was used:

- 5 ml of water;
- 0,35 g of keratin flakes.

To prepare the keratin solution at 3% wt, was used:

- 3 ml of water;
- 0,09 g of keratin flakes.

To prepare the keratin solution at 1% wt, was used:

- 15 ml of water;
- 0,15 g of keratin flakes (Figure 1.8).

The keratin flakes were immersed into different beakers containing the three different volumes of water. In order to maintain the solutions in agitation, magnetic stirrers were used, as shown in Figure 4.10. The three solutions remained in agitation for a whole night. When the solutions were well mixed, they were used for samples coating and functionalization.

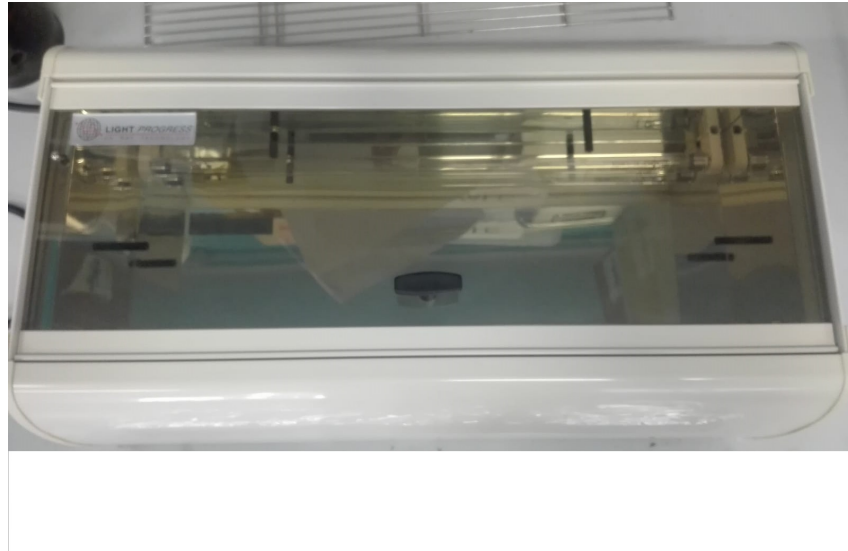


Figure 4.8: UV system

#### 4.5.1 Solution of keratin at 7% wt

The solution of keratin at 7% wt was used to obtain a coating on the surface of samples. In this case were also used particular samples, produced at the Technical University of Graz. Some of them are characterized by a particular structure, an hexagonal pattern, others are characterized by grooves, obtained by means of Electric Beam Welding (EBW) technique. The solution was manually deposited on the surfaces of different samples:

- Polished Ti;
- Ti + plasma;
- Ti + UV;
- Ti with hexagonal patterns;
- Ti with grooves.

In the case of polished and plasma- and UV- treated samples, the keratin solution was deposited and was spread in order to cover all the surface.

In the case of Ti with hexagonal patterns and grooves, a keratin layer was deposited on the surface of the two samples, then the excess solution was removed from the surface, in order to leave only the solution inside the wells of the hexagonal patterns and inside the grooves. Due to the high density of the keratin solution, the deposition of this coating did not occur homogeneously, infact it was impossible to deposit the same quantity of solution on the different surfaces, and was difficult to cover the whole surface of the single sample with a coating of homogeneous thickness.

For this reason a keratin solution, with a less concentration of keratin (3% wt) was prepared.

#### 4.5.2 Solution of keratin at 3% wt

The solution of keratin at 3% wt was used to obtain a coating to be deposited in a simpler and more homogeneous way than the previous solution. In this case, the coating was deposited on:

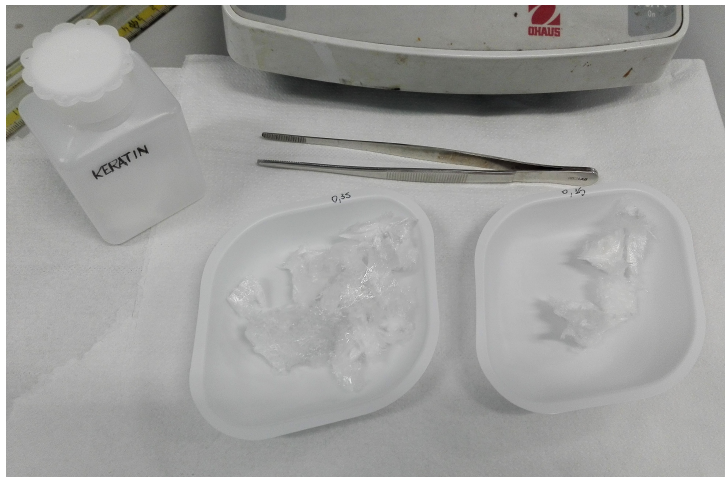


Figure 4.9: Keratin flakes



Figure 4.10: Keratin solutions in agitation on vibrating plates

- Polished Ti;
- Ti + plasma.

Differently from the previous case, this solution was less dense and it was possible to deposit the same quantity of coating on the various samples. In particular, on each disk was deposited a drop of  $30 \mu\text{l}$  and a thin and more homogeneous coating than the previous case was obtained.

#### 4.5.3 Solution of keratin at 1% wt

The solution with 1% wt of keratin was used to functionalize the samples. Three different samples have undergone this treatment:

- Ti;
- Ti + plasma;

- Ti + UV.

In order to functionalize the samples, the keratin solution at 1% wt obtained was divided into three beakers, each of which contained 5 ml of solution. The samples were immersed in the solution with the marked face in contact with the bottom of the beaker, then the beakers were closed and remained at room temperature for an hour. Past this time, the samples were washed in water milli-Q for a few seconds. The aim of this operation is to leave on the surface only the molecules chemically bound on the substrate and to eliminate the not bounded ones.

#### 4.5.4 Electrospinning

The term electrospinning derives from “Electrostatic spinning” and is used to indicate a simple and cost-effective technique which allows to produce fiber with an interconnected pore structure, with small diameter, in the range of micro and nanometer, and with high surface area. Fibers obtained show high flexibility in surface functionalities and mechanical properties superior than larger fiber (91).

The process is conducted at room temperature and under atmospheric conditions. The three basic components required to set up an electrospinning process are: a syringe with a small metal spinneret, a high voltage power supply and a grounded collecting plate, shown in Figure 4.11. Fibers are produced starting from a polymeric melts or from an appropriate solution in which

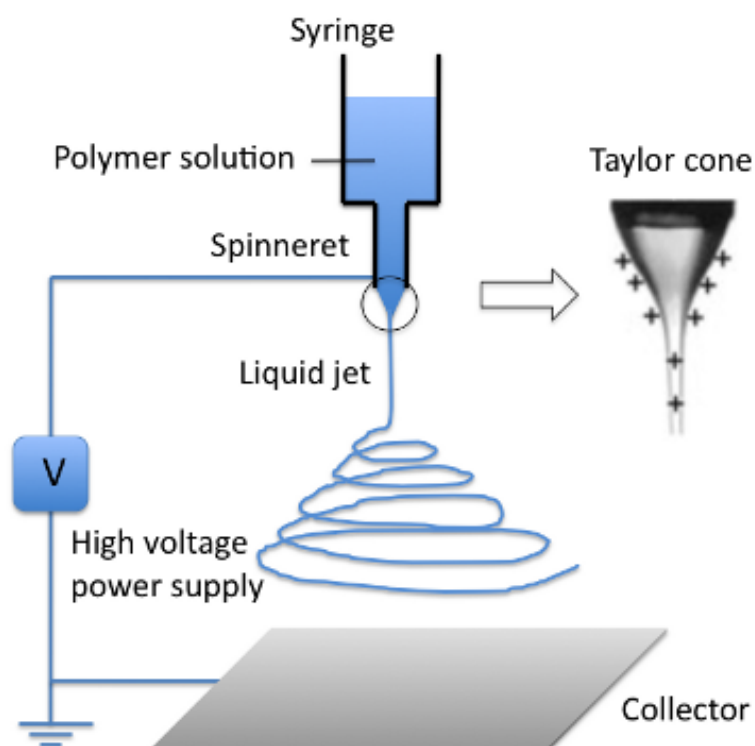


Figure 4.11: Electrospinning process (F83)

the selected polymer is dissolved, then is introduced into the capillary tube for electrospinning. In particular case, this operations should be conducted in ventilated rooms. A high voltage, in the range of 15-25 kV, is applied to create an electrically charged jet of polymer solution or melt and at the tip of the needle a drop is formed. An increase in the applied voltage, causes changes in the shape of the droplet, from hemispherical to conical, creating the so-called Taylor cone. The droplet is slowly stretched and when the intensity of electric field is equal to a critical value, the electrostatic forces are higher than surface tension of the polymer solution, so a jet is formed from the tip of Taylor cone and accelerate towards the grounded target collecting plane. At the tip of spinneret the jet is instable and a whipping elongation process occurs between the capillary tip and the collector: the repulsive Coulomb forces elongate the jet which become very long and thin in the direction of its axis (Figure 4.12). The path of the jet towards the counter is at the direct beginning, after turns laterally creating a series of loops in the plane, as shown in figure 4.13. The solvent evaporates as the jet travels in air and solid fibers are randomly

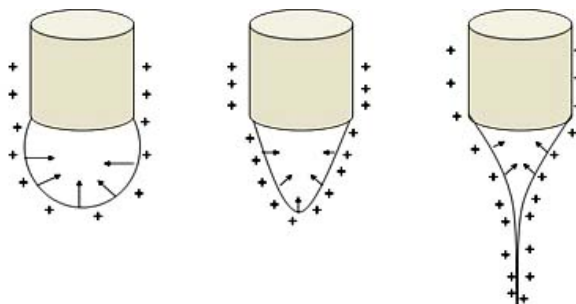


Figure 4.12: Modification in drop shape with an increasing of applied voltage (F84)

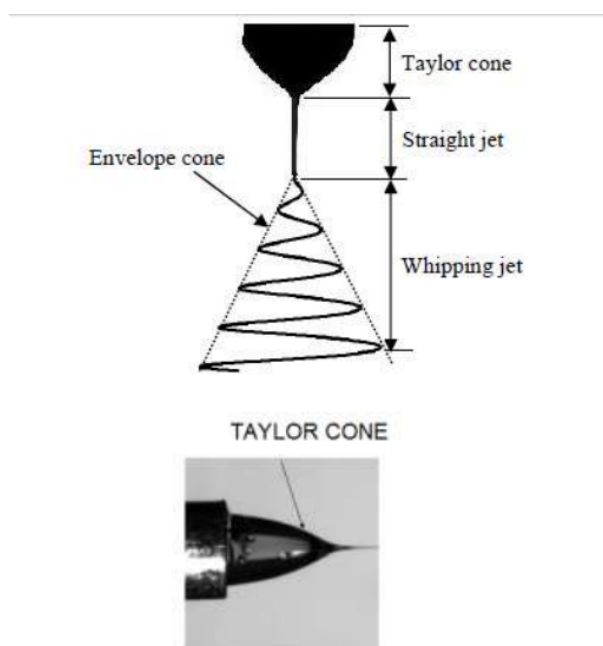


Figure 4.13: Behaviour of the electrospun jet (F85)

deposited on collector (92).

### Parameters

During the electrospinning process different parameters are involved, which must be controlled in order to obtain fibers with desired diameter or morphology. This factor can be classified as electrospinning parameters, solution and environmental parameters.

Electrospinning parameters are:

- Applied voltage: as already said, when applied voltage reaches a critical value, small-diameter nanofiber formation occurs, due to the stretching of the polymer solution in correlation with the charge repulsion within the polymer jet. If the applied voltage is beyond the critical value, beads or beaded nanofibers results. In addition an increase in applied voltage causes an increase in the diameter of the fiber;
- Solution flow rate: morphology of electrospun fibers depends on solution flow rate. For each polymeric system a critical flow rate is determined, increasing flow rate above this value causes the formation of beads in the fibers obtained;

- Distance between needle and collector: it influences deposition time, evaporation rate, whipping or instability interval. A critical distance needs to be maintained to prepare smooth and uniform nanofibers. Several studies have been demonstrated that when the distance is kept small, nanofibers are characterized by a large-diameter, whereas if this distance increases, nanofibers obtained have a small diameter.

Solution parameters are:

- Polymer concentration and polymer viscosity: if the concentration of the polymeric solution is low, polymer chains break into fragments before reaching the collector because of the applied electric field and surface tension, creating beads. An increase in polymer concentration causes an increase in viscosity. It is possible to say that a critical value of concentration/viscosity must be determined for polymeric system.
- Solution conductivity: it can influence formation of Taylor cone and diameter fibers. If the solution has low conductivity, the surface of the droplet has no charge, so there will not be the formation of the Taylor's cone, whereas increasing its conductivity, the charge on the droplet increases and the electrospun nanofibers have a small diameter, but overcoming a critical value Taylor's cone formation will be hampered.
- Polymer molecular weight and structure: it is seen that the more easily filamented polymers generally have high molecular weights, otherwise beads can be formed. As the molecular weight increases, the fiber diameter also increases. In addition a linear structure polymer is easier to thread, because of major inter-chain interactions.
- Solvent: the choice of an appropriate solvent is important to obtain smooth and beadless fibers. They should have a moderate boiling point: if they are highly volatile, the drying of the jet at the needle tip occurs, hindering the electrospinning process, at the same time less volatile solvents are avoided because the high boiling point prevents their drying.

Environmental parameters are:

- Humidity: it causes changes in morphology of nanofiber because it influences the solidification process. In addition humidity plays an important role in porous nanofiber formation, obtained using a binary solvent system.
- Temperature: an increase in temperature leads to an increase in the rate of evaporation of the solvent and a decrease in the viscosity of solution (93).

In this work titanium samples underwent electrospinning technique at the laboratories of CNR-ISMAR (Institute for Macromolecular Studies) of Biella, Piedmont. The instrument used for electrospinning was Spellman High Voltage Electronics Corporation, SL 50, Power supply, KDS 200, KD Scientific Inc., shown in Figure 4.14.

Keratin used in the electrospinning process was extracted from wool by sulfitolysis with sodium metabisulfite. Washed wool fibers were mixed with urea and  $Na_2S_2O_5$  for 2h at  $65^\circ C$ . The mixture was filtered and the aqueous solution was dialyzed at room temperature for 3 days. Then the keratin solution was frozen and lyophilized. The solution used was at 15% by weight of keratin in formic acid (HCOOH) (16). It was prepared the day before the deposition, and was mixed with a magnetic stirrer. 4 mL of solution was inserted into a plastic syringe and connected with a stainless-steel capillary (with internal diameter of 0,2 mm and external diameter of 0,4mm), and was inserted in the electrospinning system. The collector was covered with aluminum foil, in order to avoid that keratin jet get it dirty. The samples were placed on the collector using a conductive adhesive, (Figure 4.15)

The process parameters were:



Figure 4.14: Electrospinning instrument

- Voltage: 25 kV;
- Rate of 0,003 ml/min;
- Distance between collector and capillary: 15 cm;
- Deposition time: 5 minutes;
- Temperature:  $22,0 \pm 0,3^{\circ}\text{C}$ ;
- UR  $31,8 \pm 1,0\%$ .

The first electrospinning phase was carried out without samples on the collector, in order to test the deposition process. The white platina obtained on the aluminum foil indicated that the spinning process could begin.

The samples covered with keratin nanofibers were:

- Smooth Ti + plasma;
- Rough Ti;
- Rough Ti + plasma.



Figure 4.15: Samples placed on metal collector covered with aluminum foil

For the deposition on the rough samples two process parameters were changed: the rate was set at 0,01 ml/min and capillary-collector distance was set at 20 cm, in order to avoid that some droplets of solvent reached the samples, as happened during the deposition on smooth titanium samples. Because the aim of this work is to evaluate adhesion of keratin nanofibers to substrate with different characteristics the change of parameters do not bring differences in adhesion value.

In order to evaluate how nanofibers arranges on lateral surface of titanium cylinder, a electrospun nanofibers deposition was carried out at Centro Nazionale Ricerche- Institute of Polymers Composites and biomaterials (CNR-IPCB) at Napoli.

## 4.6 Thermal treatment

After the deposition of the coating and of the keratin nanofibers, and the functionalitation, the samples were placed in Petri dishes and have been subjected to a thermal treatment in an oven at  $180^{\circ}\text{C}$  for two hours.

The goal of the this operation is to stabilize the keratin coating. The samples after thermal treatment are shown in Figure 4.16, Figure 4.17, Figure 4.18, Figure 4.19, Figure 4.20, Figure 4.21, Figure 4.22, Figure 4.23.

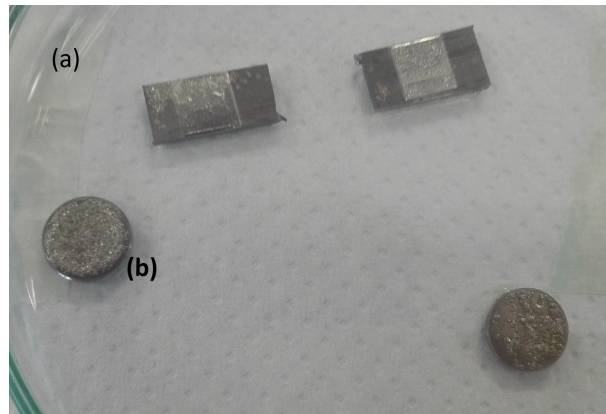


Figure 4.16: (a):Ti with grooves with keratin coatin 7% wt: (b)plasma-treatedTi with keratin coating 7%

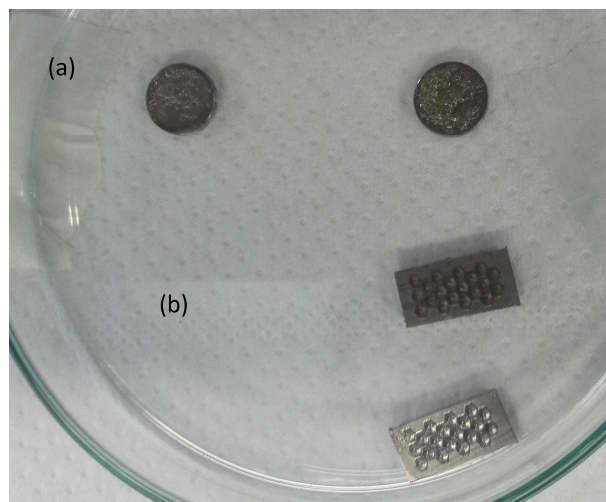


Figure 4.17: (a): UV treated-Ti with keratin coating 7%5wt; (b) Ti with exagonal structure with keratin coating 7% wt

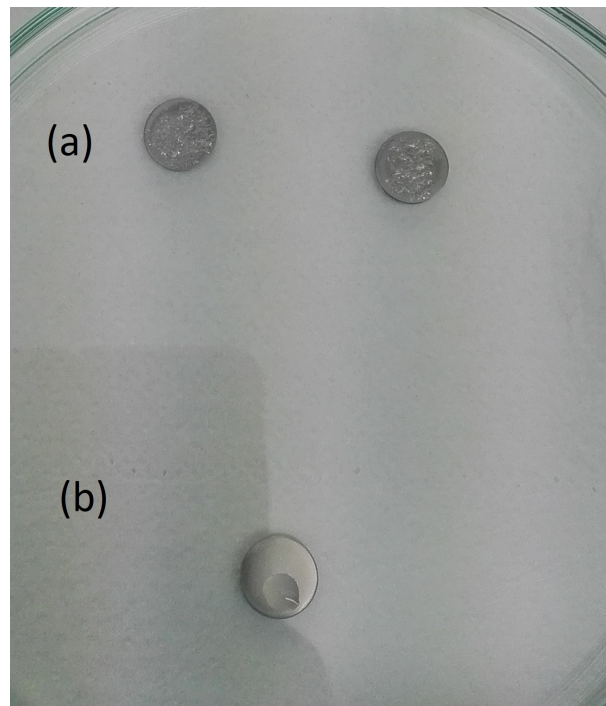


Figure 4.18: (a): Polished Ti with keratin coating 7% wt; (b) Polished Ti functionalized with keratin 1% wt

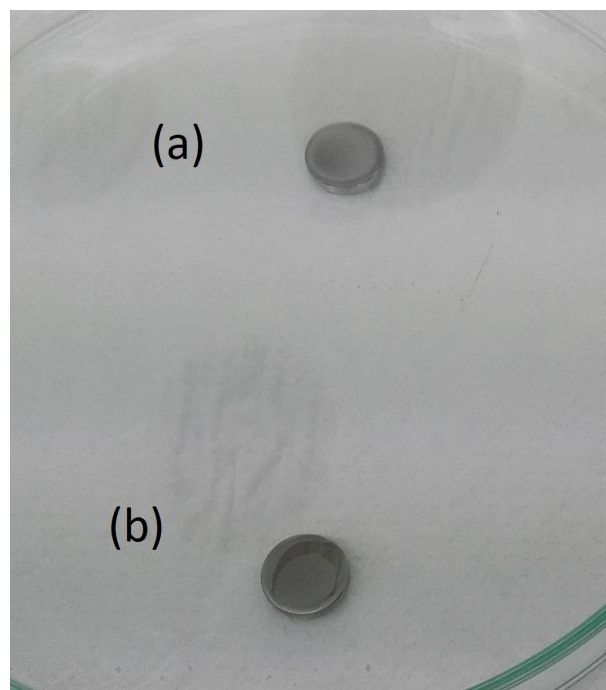


Figure 4.19: (a): UV-treated Ti functionalized with keratin 1% wt; (b) plasma-treated Ti functionalized with keratin 1% wt

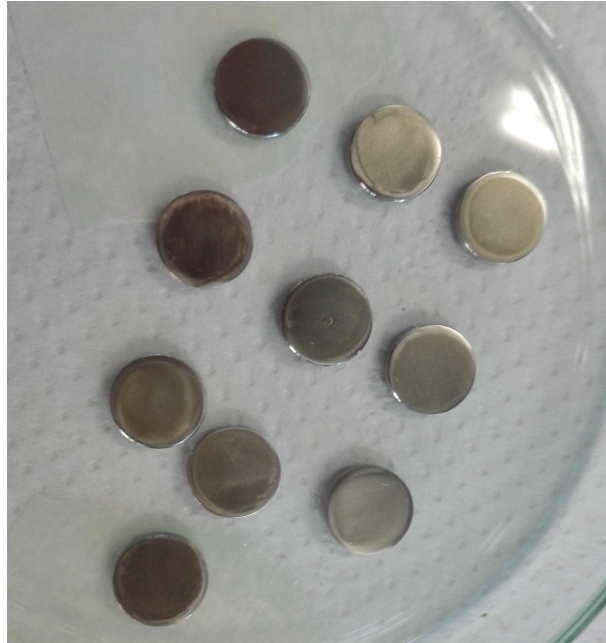


Figure 4.20: Titanium samples with keratin coating at 3% wt after thermal treatment



Figure 4.21: Rough Ti with keratin nanofiber



Figure 4.22: Rough plasma-treated Ti with keratin nanofiber

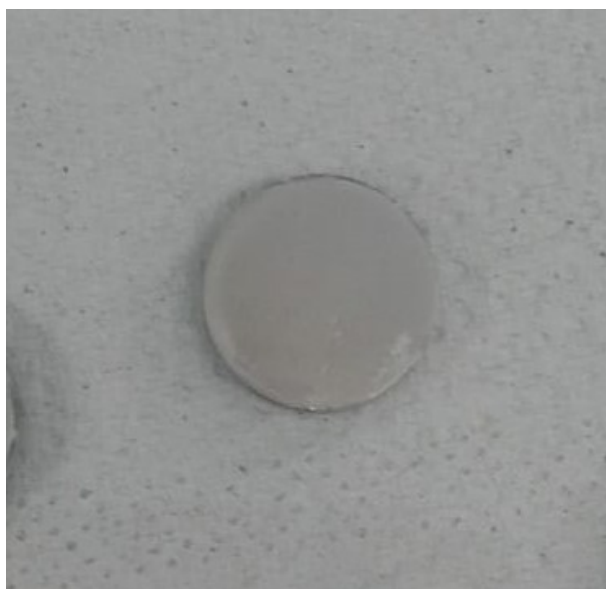


Figure 4.23: Smooth plasma-treated Ti with keratin nanofiber

In order to evaluate the thickness of the keratin coating, a particular sample was prepared in the following way: an adhesive paper was used to cover an half surface of a plasma-treated sample, whereas on the other half a keratin solution at 3% wt was deposited, using a micropipette. After thermal stabilization at room temperature, the adhesive paper was removed and the sample was thermal treated in an oven at  $180^{\circ}\text{C}$  for 2 hours, as the previous cases. The aim of this operation is that to obtain a sample characterized by a coating deposited on half surface: in this way it is possible to measure the difference in height between surface with and without coating, in order to evaluate the thickness of the coating. The result is shown in Figure 4.24 and a scheme of the cross section is represented in Figure 4.25

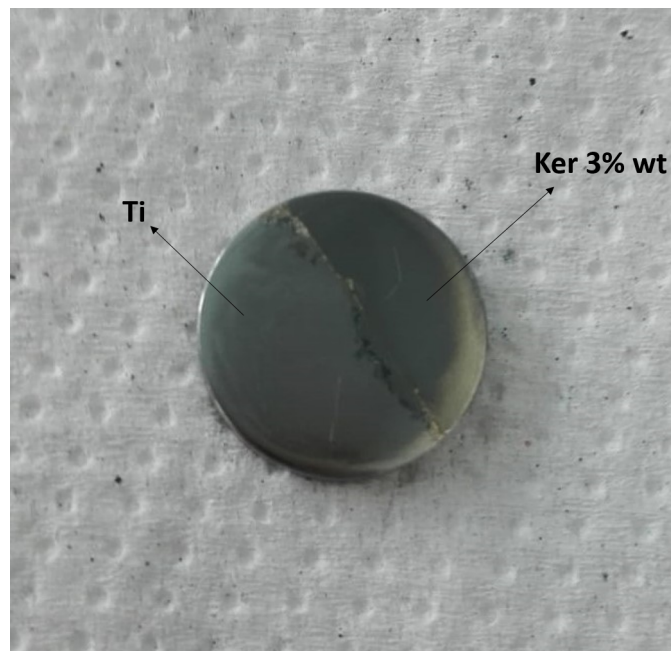


Figure 4.24: Plasma-treated sample with coating on half surface

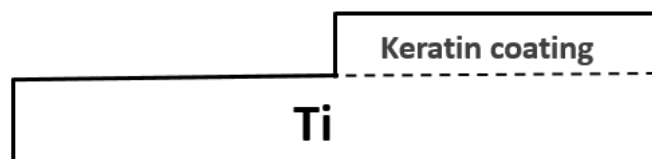


Figure 4.25: Scheme of the cross section of the sample

## 4.7 Surface characterization

### 4.7.1 Tape test

As already said in the chapter about coating, several tests are carried out in order to analyze the adhesion of a coating to a substrate. In this work a tape test was performed and was conducted by reference to the Standard Test Methods for Measuring Adhesion by Tape Test, ASTM D 3359-97. The experimental procedure includes the following operations:

- A cut is created with a sharpe tool in order to produce edges from which the coating can be lifted. It is possible to create different cut patterns. In this case grid pattern is used;
- An adhesive tape, conforming to EN ISO 2409, is applied to the zone to be analyzed and a certain pressure is performed in order to guarantee a good adhesion;
- The adhesive tape is removed from the sample, with a moviment parallel to the surface;
- The tested area is examined with a magnifying glass and the evaluation of the adhesion strength is based on the amount of the coating removed.

The Figure 4.26 shows the table used for the evaluation of the results, according to the norm ASTM D 3359-97.

In this work a Elcometer 107 Cross Hatch Cutter (Figure 4.27) was used, it is made up of 6 blades with a cutting distance of 1 mm, suitable for up to 60  $\mu\text{m}$  on hard surfaces, in accordance with ASTM regulation. The samples tested with this test were:

- Ti + Keratin 7% wt;
- Ti + plasma + keratin 7% wt;
- Ti + UV + keratin 7% wt;
- Ti + keratin 3% wt
- Ti + plasma + keratin 3% wt.
- Ti + plasma + keratin nanofibers.

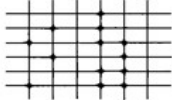
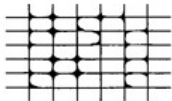
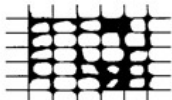
Classification	Surface of cross-cut areas from which listing has occurred. (Example for six parallel cuts.)	Rate of adhesion
5B	None	The edges of the cuts are completely smooth; none of the squares or the lattice are detached.
4B		Small flakes of coating are detached at intersections; less than 5% of the area is affected.
3B		Small flakes of coating are detached along edges and at intersections of cuts. The area affected is 5 to 15% of the lattice.
2B		The coating has flaked along the edges and at parts of the squares. The affected area is 15 to 35% of the lattice.
1B		The coating has flaked along the edges of cuts in large ribbons and entire squares have detached. The area affected is 35 to 65% of the lattice.
0B	Flaking and detachment in excess of 65%.	

Figure 4.26: Classification of test adhesion results (F86)



Figure 4.27: Elcometer 107 Cross Hatch Cutter (F87)

### 4.7.2 Scratch test

As already said, scratch test is a method used to evaluate coating adhesion to a substrate, using a spherico-conical stylus. A Rockwell diamond indenter, with a tip radius of  $200\ \mu\text{m}$  is used to scratch the sample, placed into the chamber.

The test consists of three steps:

- in the first step a prescan is done to measure of the surface is performed under the lower possible pressure, in order to not damage surface sample;
- a scratch is performed according to load, speed, depth conditions of the test;
- in the last step a postscan is performed in order to measure residual topography in damaged area.

Scratch test can be performed in different ways: with constant, progressive and incremental load. The output is misured in term of acoustic emission, penetration depth and frictional force. Analyzing the morphology of the scratch track and transvers cracks, it is possible to have information about failure mechanisms such as cohesive, interfacial, conformal and brittle chipping (Figure 4.28).

An important parameter is the so-called "load critical value", i.e. the load at which the first crack appears. This value is a measure of the coeshion of the coating. The value of load at which total peeling-off of the coating from the substrate surface occurs is called "upper critical load". This is a measure of the adhesion strength between coating and substrate (94).

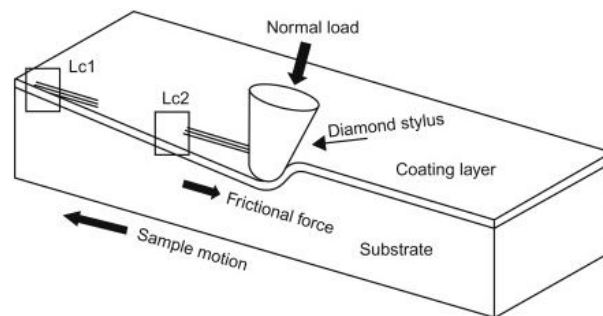


Figure 4.28: Scratch test (F88)

This test was conducted at CNR - Area di Ricerca di Torino del Consiglio Nazionale di Ricerche. A CSM Micro Scratch instrument scratch tester was used and the following conditions were setup:

- scratch length: 5 mm;
- applied load: progressive load increased from 1 N to 10 N;
- rate: 50 N/m.

The analysis was performed at room temperature on:

- Polished Ti;
- Ti + plasma + keratin at 3% wt.

### 4.7.3 SEM

Scanning Electron Microscopy (SEM) is used to study external morphology, chemical composition and crystalline structure of the surface of the a sample.

A focus beam of high-energy electrons is used and it is possible to obtain a 2-D images, with a magnification in a range between 20x to 30000x, and a spatial resolution of 50 to 100 nm.

The instrumentation (Figure 4.29) is made up by:

- Electron Source Gun: electron beam is emitted from an electron gun fitted with a tungsten filament cathode, exploiting its highest melting point and lowest vapor pressure compared with that of all metals, but in other case is possible to use lanthanum hexaboride ( $\text{LaB}_6$ ). The electron beam has an energy between 0,2-40 KeV;
- Electron lenses: the beam is accelerated down and passed through a combination of lenses and apertures: in this way is focused on a spot of about 0,4 to 5 nm. The beam passes through pairs of scanning coils or pairs of deflector plates in the electron column, and is deflected in the x and y axes so that it scans in a raster fashion over a rectangular area of the sample surface.
- Sample chamber: the sample is mounted on a stage in the chamber area and both the column and the chamber are evacuated by a combination of pumps. The level of the vacuum will depend on the design of the microscope.
- Electron detector: when the primary electron beam reaches the sample, electrons lose energy, due to randomly and repeated interactions with surface sample. The size of the interaction volume depends on the electron's landing energy, the atomic number of the specimen and the specimen's density. This energy exchange between the electron beam and the sample causes the reflection of high-energy electrons by elastic scattering, emission of secondary electrons by inelastic scattering and the emission of electromagnetic radiation: specialized detectors analyse them. Electronic amplifiers can be used to amplify the signals.
- Computer and display: the signals detected by the detector generate images on the computer monitors.

Figure 4.30 shows the interaction between electron beam and the sample: in particular, the formation of secondary electrons and backscattered electrons (95) (96).

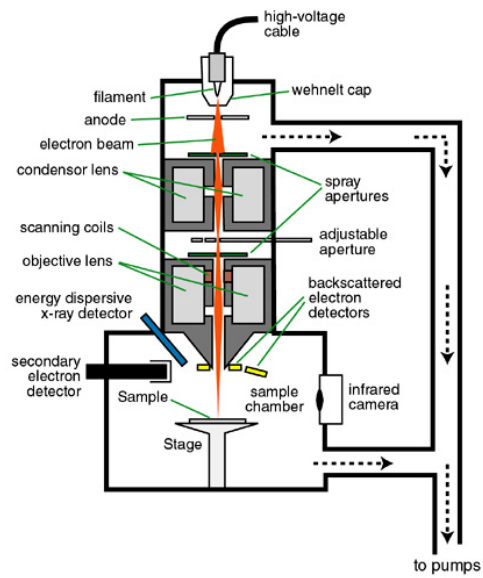


Figure 4.29: SEM instrumentation (F89)

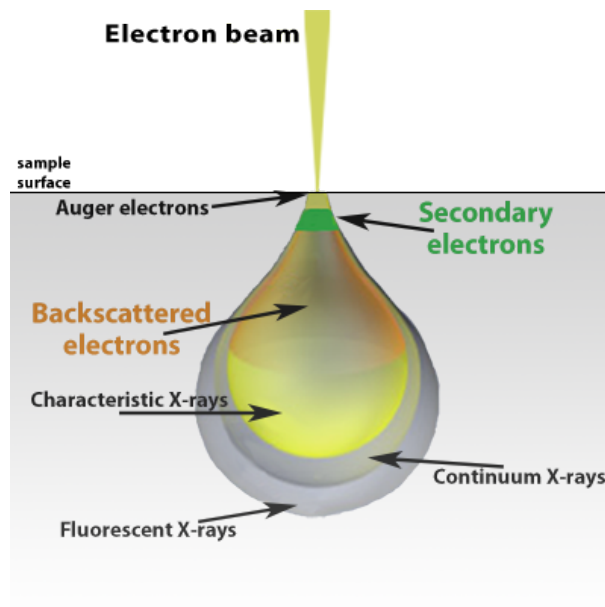


Figure 4.30: Interaction between electron beam and surface sample (F90)

#### 4.7.4 FESEM

Field Emission Scanning Electron Microscope (FESEM) is generally used to study topographic details of a surface. A focus beam of electrons is used to analyze the samples. In Figure 4.31 is shown a scheme of the instrument.

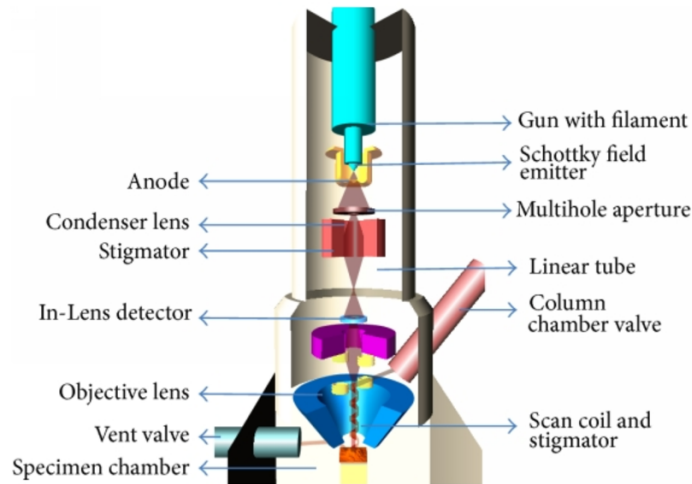


Figure 4.31: FESEM instrumentation (F91)

The set up is made up by:

- Source of electrons: a thin and sharp tungsten needle, with a tip diameter of  $10^{-7}$ -  $10^{-8}$  m, is used as a cathode in front of a primary and secondary anode. Generally the voltage between anode and cathode is between 0,5 and 30 KV. It is necessary an extreme vacuum,  $10^{-8}$  Torr, in the column of the microscope, for this reason a pump is used, in addition to a device that regularly decontaminates the electron source by a current flash;
- Column with lenses and aperture: electromagnetic lenses are used to focus the electron beam. Based on the current in the condenser, the diameter of the beam can be higher or smaller. Scan coils deflect the beam on the sample, following a zig-zag pattern and at the same time the image is formed on the monitor. The scan velocity determines the amount of noise in the image: rapid scan causes much noise.  
The objective lens is the lowest lens in the column. If the distance between lens and sample is small, the objective lens needs to apply a greater force to deflect the electron beam: this causes the smallest beam diameter, the best resolution, but also the poorest depth of field. Stigmator coils are used to correct irregularities in the x and y deflection of the beam and thus to obtain a perfectly round-shaped beam.
- Sample chamber: the sample, covered by a conductive layer is mounted on a holder and placed into a chamber in high vacuum. The sample can be moved in horizontal and vertical direction, can be tilted, rotated. The “secondary electron emission” detector is located at the rear of the object holder in the chamber.

When the primary probe bombards the sample, secondary electrons are emitted from the object surface with a certain velocity that is determined by the levels and angles at the surface of the object. Properties of secondary electrons depend on location and intensity of illumination of the

mirror. The signal produced by the scintillator is amplified (97). It is possible to view the images in two modalities:

- Secondary Electron (SE): it is used to map the surface of a sample; a detector located in the optical path is necessary to detect secondary electrons. A second detector is placed on the wall of the chamber that contains the sample and allows to detect secondary electrons having a small backscattered component
- Backscattered electron (BSE): it is used to show the compositional differences within the sample. The presence of elements with different atomic numbers and their distribution causes contrast in BSE images.

With FESEM analysis, it is possible to obtain topographical and elemental information at magnification of 10 x to 300000x, with virtually unlimited depth of field. The samples must be first of all resistant to low pressures and not very volatile and moreover they must be conductors; if these are not, a very thin metallization (50-100 Å) is used with a conductive material. It is necessary that the material can discharge to the ground the voltage that accumulates during the scanning with the electron beam, to avoid that artifacts are created in the image and that the sample degrades (98). FESEM analysis was conducted on:

- Smooth Ti + keratin nanofibers;
- Rough Ti + keratin nanofibers.

### 4.7.5 Roughness and homogeneity

#### Profilometer

Surface roughness is quantified by the deviation in the direction of the normal vector of a real surface from its ideal form. It can be calculated on a profile or on a surface.

There are different parameters, included in BS EN ISO 4287:2000 British standard, identical with the ISO 4287:1997 standard:

- $R_a$  (arithmetical mean roughness value): the arithmetical mean of the absolute values of the profile deviations ( $Z_i$ ) from the mean line of the roughness profile;
- $R_{mr}(c)$  (material component of the profile): the fraction of a line, which, insectioning a profile, cuts through material at a stipulated height  $c$  above the mean line (in  $\mu\text{m}$ ). Stated as a percentage;
- $R_{Sm}$  (mean peak width): mean value of the width of the profile elements  $X_{si}$  (previously  $S_m$ ); horizontal and vertical counting thresholds are stipulated for this evaluation;
- $R_t$  (total height of the roughness profile): difference between height  $Z_p$  of the highest peak and depth  $Z_v$  of the deepest valley within the evaluation length;
- $Rz_i$  (greatest height of the roughness profile): sum of the height of the highest profile peak and the depth of the deepest profile valley, relative to the mean line, within a sampling length  $l_{r_i}$ ;
- $Rz_{i1max}$  (maximum roughness depth): largest of the five  $Rz_i$  values from the five sampling lengths  $l_{r_i}$  within the evaluation length  $l_n$ ;
- $Rz$  (mean roughness depth): mean value of the five  $Rz_i$  values from the five sampling lengths  $l_{r_i}$  within the evaluation length  $l_n$ .

The most common used is  $R_a$ , represented in Figure 4.32 (99).



Figure 4.32: Arithmetical mean roughness value  $R_a$  (F92)

In order to evaluate the roughness of titanium bars, a contact profilometer was used at CNR - Area di Ricerca di Torino del Consiglio Nazionale di Ricerche. A diamond stylus, with a small radius, is moved in contact with the sample, for a certain distance and at determined contact force. A detector tip, equipped with the stylus, electrically detects the motion of the stylus and the signals go to an amplification and a digital conversion process occurs (Figure 4.33). In this way, small surface variations are measured as vertical stylus displacement in function of the position. In this work it was used for:

- Ti bars before polishing and being rough;
- Ti bars after polishing and being rough;
- Ti + plasma + keratin 3% wt.

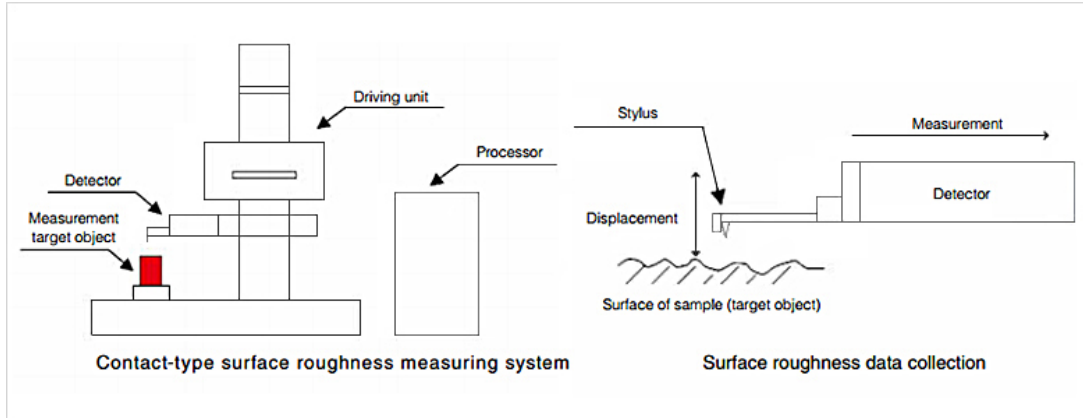


Figure 4.33: Contact-type surface profilometer (F93)

## LSM

In order to characterize 2D and 3D microstructure and surface, a confocal laser scanning microscope was used. This technique was born to overcome some limitations of traditional wide-field fluorescence microscopes: in a conventional system, the entire sample is flooded in light and all the parts in the optical path are excited, causing a fluorescence detected by a microscope's photodetector; whereas a confocal microscope uses the pinhole, i.e. the aperture of a confocal microscope, to block the out-of-focus informations and to detect only in focus informations.

One of the most advantages of this technique is represented by the better image's optical resolution, especially in depth direction. In this way, because much of the light from sample fluorescence is blocked by pinhole, the intensity of the signal is lower, for this reason sensitive detectors, usually a photomultiplier tube (PMT) or avalanche photodiode, are used, transforming the light signal into electrical one. The scanning of the sample is performed in a rectangular pattern, in the horizontal plane, using one or more oscillating mirrors. During the analysis the distance between sample and objective lens is changed, so the sample is optical sectioned and an image stack is generated. By analyzing the intensity distribution of a single pixel through the image stack, it is possible to calculate the corresponding height: a height map is formed combining the information of the whole stack over the whole field of view.

The scheme of the system, the image stack and the intensity of a one pixel are shown in Figure 4.34.

There are four types of confocal microscopes:

- Confocal laser scanning microscopes use 2 or 3 mirrors to scan the laser across the sample linearly along the x- and the y- axes, and "descan" the image across a fixed pinhole and detector;
- Spinning-disk confocal microscopes uses a series of moving pinholes on a disk to scan spots of light. Each pinhole is allowed to hover over a specific area for a longer amount of time, reducing the excitation energy needed to illuminate a sample when compared to laser scanning microscopes: phototoxicity and photobleaching of a sample are reduced, so this system is used for imaging live cells or organisms;
- Microlens enhanced or dual spinning-disk confocal microscopes are similar to the previous case, but a second spinning-disk containing micro-lenses is placed before the spinning-disk containing the pinholes. The microlens, associated to a single pinhole, capture a broad

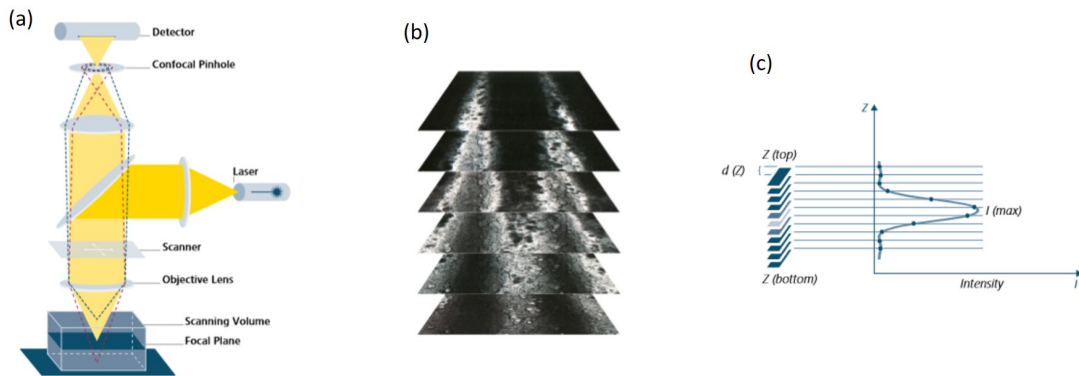


Figure 4.34: (a) Scheme of the confocal laser scanning microscope; (b) Image stack; (c) Intensity of one pixel (F94)

band of light, causing an increase in the amount of light directed into each pinhole and reducing the amount of light blocked by the spinning-disk;

- Programmable array microscopes (PAM) uses an electronically controlled spatial light modulator (SLM) that produces a set of moving pinholes.

With this instrument, it is possible to analyse also biological samples, that have to be treated with fluorescent dyes, in order to make selected parts visible. In other cases, it is possible to track single fluorescent molecules (100).

It is also possible to detect structure with weak contrast, due to the transparency of low reflection of the sample, using Circular Differential Interference Contrast (C-DIC), which is a polarization technique, that uses circularly polarized light, to include comprehensive geometric, functional and roughness studies, and create detailed surface analysis reports, surface texture analysis, contour analysis, grains and particle analysis, 3D Fourier analysis, analysis of surface evolution, and statistics.

It is generally used to analyse coatings, multi-layer structures, surface texture, or to conduct tribology or failure analysis (101).

In this work a laser scanning microscope ZEISS LSM 800 was used (Figure 4.35).

The sample tested were:

- Ti + plasma + keratin 3% wt on half surface;
- Titanium bars after polishing and being rough.

The protocol used to calculate surface roughness of titanium bars is shown in Figure 4.36: least square method is used to level the surface, using a polynomial expression of degree 3, form is removed, then using Gaussian filter of 2,5 and 244  $\mu\text{m}$ , the roughness is measured.



Figure 4.35: Confocal laser scanning microscope ZEISS LSM 800 (F95)

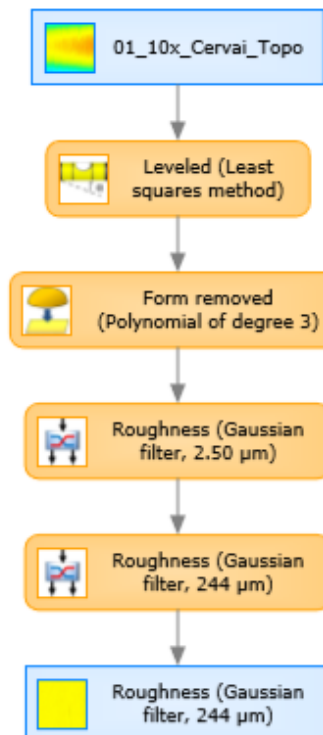


Figure 4.36: Method of measurement of roughness

#### 4.7.6 Wettability

Wettability is defined as the ability of a liquid to remain in contact with a solid surface, thanks to the interactions at molecular level between liquid and solid interface. In order to evaluate the degree of wettability of a material, the contact angle  $\theta$  is measured. It depends on the values of free energies per unit surface area of the solid-vapor, liquid-vapor, and solid-liquid interfaces, as already seen. Based on the contact angle value, it is possible to define if the surface is wettable or not, and consequently how strong are the bonds at the interface: small contact angle,  $\theta < 90^\circ$ , correspond to high wettability, while large contact angle,  $\theta > 90^\circ$ , correspond to low wettability (Figure 4.37), if  $\theta = 180^\circ$  the surface is not wettable, whereas  $\theta = 0^\circ$ , the surface is completely wettable (102).

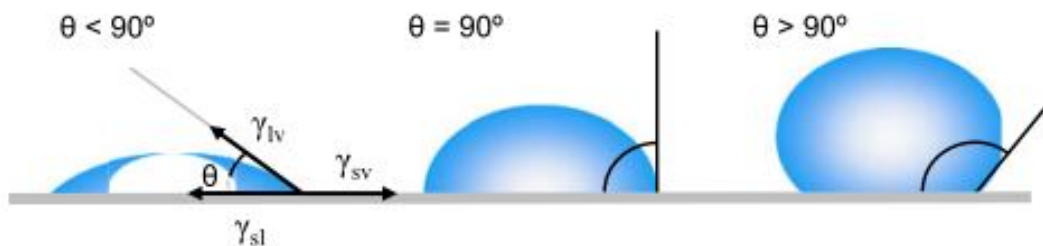


Figure 4.37: Illustration of contact angle (F96)

The aim is to evaluate if keratin coating changes hydrophilic or hydrophobic characteristics of the surface sample.

The instrument used was a KRUSS DSA 100 (Figure 4.38). The sample to be analyzed, was placed on a horizontal plate and with a front microscope it possible to capture sample images during the test. The measurements were made depositing at a distance from each other,  $5 \mu\text{l}$  of the solution with the aid of a micropipette. Once captured, the images were processed with the computer software and the static contact angle measurement was made.

This test was conducted using water on:

- Polished Ti;
- Ti + plasma + keratin 3% wt.

Then using a keratin solution at 3% wt, the contact angle test was performed on:

- Polished Ti;
- Ti + plasma.

#### 4.7.7 Stability in water

In order to analyze how keratin coating reacts to a long period in contact with water, a test of the stability in water was conducted on:

- Ti + plasma + keratin at 3% wt.

For this test, two beakers were filled with 10 ml of ultrapure water. In each beaker a sample was placed, with the uncovered face in contact with the bottom of the beaker. Then they were placed in incubator at  $37^\circ\text{C}$ . After 24 hours, the beakers were taken from the incubator. After



Figure 4.38: KRÜSS DSA 100

taking out the samples, the two beakers were washed with ultrapure water, while each sample was dried in order to evaluate any macroscopical change in the appearance in the coating. At this point the beaker were filled with other 10 ml of water and the samples were immersed into in the same way of previous case. Then the beaker were placed in the incubator. This operations were repeated after 7, 14, 21, 28 days with the same conditions.

### 4.7.8 Zeta potential

Generally the  $\zeta$  potential is used to describe the behavior of colloidal system, such as particle dispersions or emulsions and to evaluate their stability. But, based on the same theoretical background, zeta potential can be applied to the analysis of macroscopic solid surface, having a different meaning. In this case the charging behavior at solid-liquid interface is described, using the model of electrical double layer (EDL): on a solid surface, in contact with an aqueous solution, a charge is assumed, the charged solid surface causes a different charge distribution in the liquid phase. A double layer are formed, in fact is possible to distinguish the stationary immobile layer and the diffuse mobile layer of counterions. The plane which separate the two layers is the "shear plane" and the electrical potential at this point is the zeta potential (Figure 4.39). When zeta potential is measured, electrokinetic effects are involved, observed at the interface

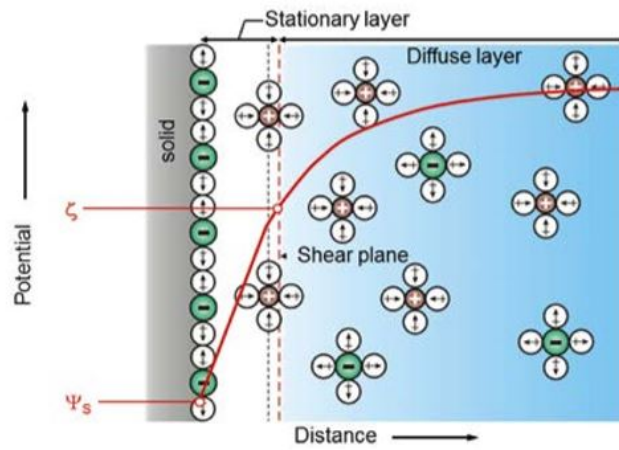


Figure 4.39: Model of the electrical double layer at solid-liquid interface (F97)

between a solid, liquid or gas phase with a liquid phase. In particular, if an aqueous solution flows into a capillary system, an electrical response is generated: a DC current or a continuous voltage is generated, depending on the measurement conditions. When the aqueous solution flows into the capillary, which can have a regular or irregular shape, on the solid surface a charge is generated, compensated by counterions in the aqueous solution: in this case shear force are generated on counterions, which flows in the direction of the flow. An electric force, opposed to the liquid flow is generated, due to the charge separation between capillary inlet and outlet. This generate an electrical potential difference detected by electrodes.

Different parameters can influence the measurement:

- The shear rate at solid-liquid interface, depending by the size of the capillary and the flow rate of the solution, affects the charge separation;
- The formation of a charge separation depends on the number of ions present in the aqueous solution and on their strength;
- The geometry of the capillary, such as capillary dimensions, influences the current or the voltage generated.

Generally the set-up for streaming potential is made up by a measuring cell, electrodes, voltmeter, a container which measuring liquid, a grounded metal cage to protect the system from external electromagnetic fields, a pump, pressure transducers and probes for pH measurement and conductivity of the solution.

The charge formation at solid-liquid interface occurs due to the acid-base reactions and due to physical adsorption of water ions. Both mechanisms depend on the pH value of the aqueous solution, so this is the most important parameter which influences the zeta potential. Figure 4.40 shows how zeta potential for solid surfaces with acidic, basic and amphoteric functionalities, changes at different pH value. It is possible to see that at a certain pH, zeta potential is 0 mV and reverses its sign. This point is known as isoelectric point (IEP), which is defined as the pH value of the aqueous solution at which there is an equilibrium between positively and negatively charged surface groups. The IEP is a good indicator of the chemistry of the functional groups

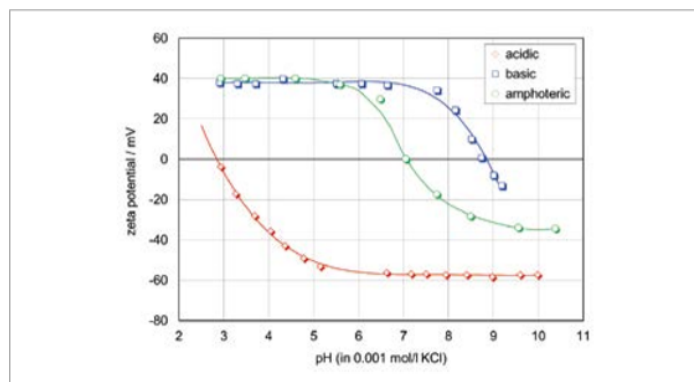


Figure 4.40: pH dependence of the zeta potential for surfaces which acidic, basic and amphoteric behavior (F98)

present on the surface of a solid. If the zeta potential is described as a function of pH by well-defined curves, surfaces exhibit only one type of functional group. The curve presents a plateau in different position depending on whether the surface has an acid, basic or amphoteric behavior.

However, in most cases, the samples analyzed show a heterogeneous composition of functional groups and hence the curve that will be obtained will be more complex. Furthermore, there is no evidence that the zeta potential is dependent on the size of the sample and the roughness of the surface (105).

In this work the  $\zeta$  potential analysis was conducted on the following couples of samples:

- Polished Ti;
- Ti + plasma;
- Ti + plasma + keratin 3% wt.

The aim was to analyze how different surface treatments and the presence of a keratin coating influence the formation of a charge of the samples surface.

The test was conducted with the Surpass electrokinetic analyzer, Anton Paar, shown in Figure 4.41.

Prior to start the analysis, the instrument was washed with ultrapure water by interposing a connecting tube between the two electrodes, then performing the closed loop filling procedure without titration, using as electrolyte solution 45 mg of KCl in 600 ml of ultrapure water. The couple of samples to analyze were fixed using an appropriate adhesive to a samples holder, which have been inserted in the appropriate space in the measuring cell, leaving a small gap between the two samples. This space was brought by rotating one of the graduated wheels included in the cell at 100  $\mu\text{m}$  in the initial step of adjusting the measurement parameters. With the use of a software, flow is controlled: it is possible to see the flow, expressed in [ml/min], as a function



Figure 4.41: Electrokinetic analyzer for zeta potential measurement

of the pressure, expressed in [mbar], by tracing two curves: the first is relative to the flow from left to right and the second to the flow in the opposite direction, thus allowing the detection of the pressure value to be set for a flow of 100 ml/min. The first measurement was done without titration to find the zeta potential of the sample at the pH of the electrolyte.

The analysis was divided into two steps: the first is represented by the acid titration analysis, the second by the basic titration analysis. For acid titration, an increase in ml of 0.05 M HCl was set to add during the measurement and for each step the software returned four measurements with corresponding average value. After the first analysis the samples were removed from the cell, the machine was washed with the same protocol described before; on the sample holder two others samples are fixed and placed in the cell, in this way for each analysis two different couples of samples were used. The basic titration analysis was conducted with NaOH 0.05 M, in the same way of the previous case.

The parameters that were measured are: pH, conductivity, temperature, flow current, pressure and flow.

### 4.7.9 FT-IR

Fourier Transform Infrared Spectroscopy, also known as FT-IR is a non-destructive technique used for the identification of organic, polymeric, and in some case, inorganic materials. The analysis is based on the absorption of infrared radiation, converted into rotational and vibrational energy by the sample molecules. The resulting signal at the detector presents as a spectrum, typically from 4000  $\text{cm}^{-1}$  to 400 $\text{cm}^{-1}$  (106).

The normal instrumentation (Figure 4.42) used is made up by:

- The source: infrared energy is emitted by the source, this beam passes through an aperture which controls the amount of energy presented on the sample;
- The Interferometer: The beam enters the interferometer where the “spectral encoding” occurs. The resulting interferogram signal then exits the interferometer.
- The sample: the beam hits the surface of the sample. Specific frequencies of energy are absorbed.
- The detector: the beam passes to the detector, which measures the spectral interferogram signal.
- The computer: the signal is sent to a computer and the Fourier transformation occurs. An infrared spectrum is obtained (105).

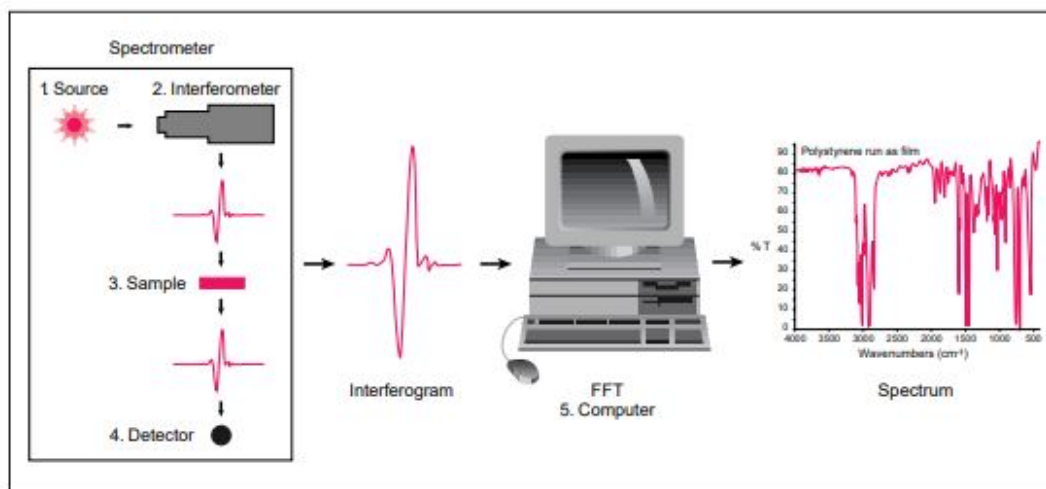


Figure 4.42: FT-IR instrumentation (F99)

Each molecule or chemical structure will produce a unique signal, based on this, chemical identification occurs. Spectrum peak amplitude has a direct proportionality with the amount of the substance present on the sample.

Generally a background spectrum of a reference material must be measured.

In this way, FT-IR analysis was performed to investigate keratin atomic bonds on the surface of Ti commercially pure, covered by keratin coating.

The samples tested were:

- Polished Ti;

- Polished Ti + keratin 7% wt;
- Ti + plasma + keratin 7% wt;
- Ti + UV + keratin 7% wt;
- Ti grooves + keratin 7% wt;
- Ti hexagonal + keratin 7% wt;
- Ti + plasma + keratin 3% wt;
- Polished Ti + keratin 1% wt;
- Ti + plasma + keratin 1% wt;
- Ti + UV + keratin 1% wt.

### 4.7.10 XRD

X-ray diffraction is a nondestructive technique, used to analyze crystalline phases in the material. It gives informations about structures, phases, preferred crystal orientations, average grain size, crystallinity, strain, and crystal defects.

The setup is made up by X-ray tube, a sample holder and X-ray detector (Figure 4.43).

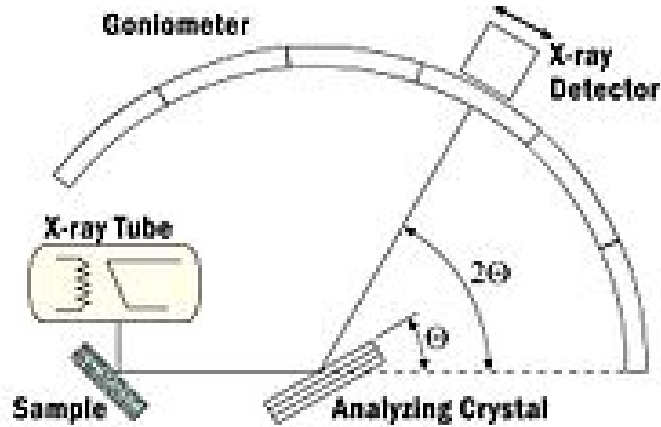


Figure 4.43: Scheme of XRD analysis (F100)

X-rays monochromatic beam is generated in the cathode ray tube, it has a defined  $\lambda$ . The beam irradiates the sample, the radiations diffracted by the sample are collected by a detector that transforms them into electrical impulses, which are then amplified and sent to a computer that allows them to be processed.

This analysis is based on the Bragg equation:  $n\lambda = 2d \sin \theta$ . In this equation  $n$  is an integer,  $\lambda$  is the characteristic wavelength of the X-rays,  $d$  is the interplanar spacing between rows of atoms, and  $\theta$  is the angle of the X-ray beam with respect to these planes (Figure 4.44). When

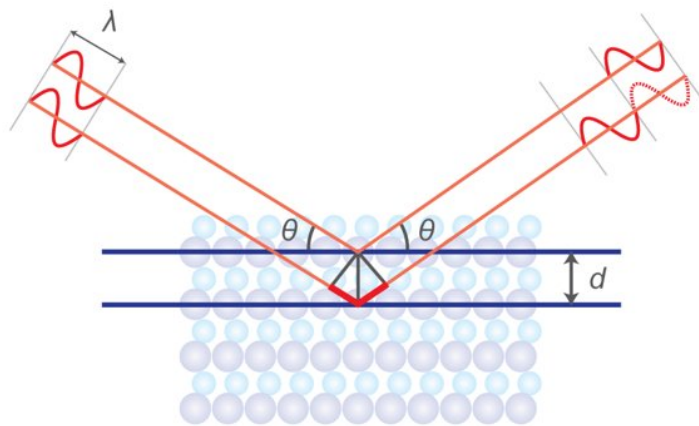


Figure 4.44: Scheme of X-rays irradiating the sample and reflected by itself (F101)

this equation is satisfied, X-rays scattered by the atoms in the plane of a periodic structure are in phase and diffraction occurs in the direction defined by the angle  $\theta$ . Comparing the spectrum

obtained to a database of known patterns is possible to make chemical identification. A XRD spectrum gives the following informations:

- from the angular position of the peak, it is possible to define the interplanar distance and the parameters of the materials;
- from the intensity of the peaks, it is possible to know the position of the atoms in the elementary cell;
- from the width of the peaks or the mid-height amplitude (FMHW), it is possible to obtain informations on the size of the crystals and on the possible deformation suffered by them (107).

This test was conducted on:

- keratin film at 7% wt in water;
- keratin film at 3% wt in water,

and the results were compared with the spectra of keratin film in formic acid.

### 4.7.11 XPS

X-Ray Photoelectron Spectroscopy (XPS) is a quantitative analysis technique used to measure the chemical composition of a surface. It gives informations about the elements present on the surface and how they are bonded to the other elements.

The analysis is based on the photoemission effect (Figure 4.45): when an atom or molecule absorbs an X-ray photon, an electron can be ejected, the kinetic energy (KE) of the electron depends upon the photon energy ( $h\nu$ ) and the binding energy (BE) of the electron. By measuring the kinetic energy of the emitted electrons, it is possible to determine which elements are present in material's surface, their chemical states and the binding energy of the electron. The binding energy depends upon a number of factors, including the element from which the electron is emitted, the orbital from which the electron is ejected and the chemical environment of the atom from which the electron was emitted.

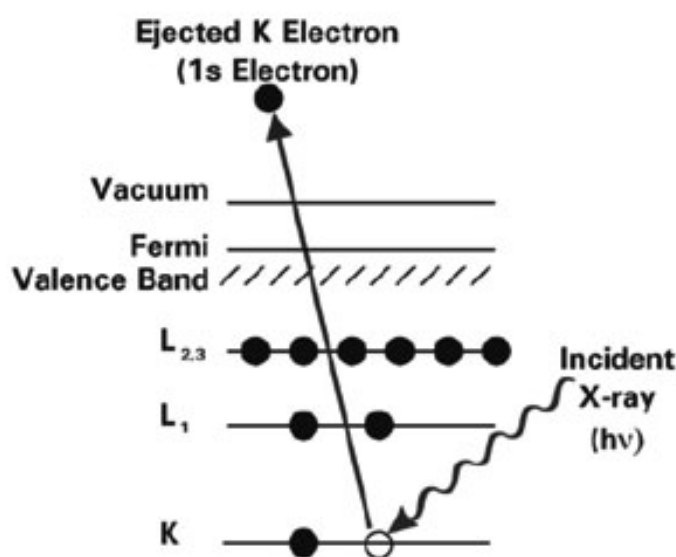


Figure 4.45: Photoemission effect involves in XPS analysis (F104)

A monochromatic beam of X-ray irradiates the sample, electrons are emitted by the sample with a certain kinetic energy. Measuring the number and the kinetic energy of the electrons emitted, it is possible to define their binding energy and allows the chemical composition of the sample. An hemispherical electron energy analyzer allows to select a certain value of kinetic energy, controlling the inner and outer potential, and a detector counts the number of electrons having that kinetic energy.

In Figure 4.46 is shown a scheme of the XPS analysis. This technique is defined superficial, because the depth of analysis is about 1-10 nm, and requires a high or ultra-high vacuum conditions.

A typical XPS spectrum, known as Survey spectrum, shows the number of electrons detected as a function of the binding energy. Each chemical element produces a characteristic set of peaks at specific energy values. The number of electrons with certain kinetic energy is related with the amount of that element on the surface of the sample. The best way to compare XPS intensities is by atomic percentage concentrations, since not all electrons emitted by the sample are detected by the instrument. In this way, intensities are represented as a percentage, correlating the intensity of interest to the total intensity of the electrons involved in the measure.

It is also possible to perform a high-resolution analysis: it is possible to distinguish different elements that show overlapping in Survey spectrum, but it is also useful to know the oxidation state

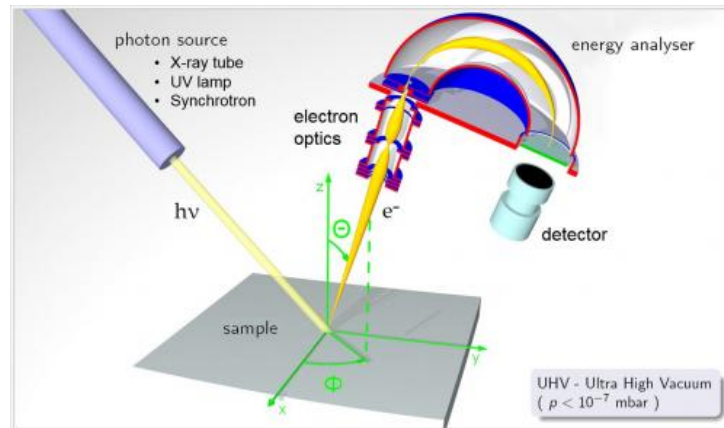


Figure 4.46: Scheme of XPS analysis (F105)

and the chemical around of an element.

It was possible to accurately determine the chemical composition of the first superficial layers and to add more information about the chemical elements of interest. The high-resolution spectrum revealed the types of chemical bond in which the keratin is involved (107) (108).

The analysis was conducted at Istituto Italiano di Tecnologia (IIT), Genova. The samples analyzed were:

- Polished Ti,
- Ti + plasma;
- Ti + UV;
- Ti + plasma + keratin 3% wt;
- Polished Ti + keratin 1% wt;
- Ti + plasma + keratin 1% wt;
- Ti + UV + keratin 1% wt.



# Chapter 5

## Results and discussions

The aim of this work is to analyse functionalized titanium samples and study adhesive properties of a keratin coating on titanium surfaces, treated in different ways, in order to find the surface treatment which can better improve the strength of bonds between coating and substrate. This system can be used in dental applications, due to the biocompatibility of titanium and due to the important role played by keratin in wound healing and proliferation of fibroblasts. After adhesion test, the surface was characterized with different techniques, in order to investigate the features of the coating.

The samples used during the tests are shown in Figure 5.1 Two types of coating were studied:

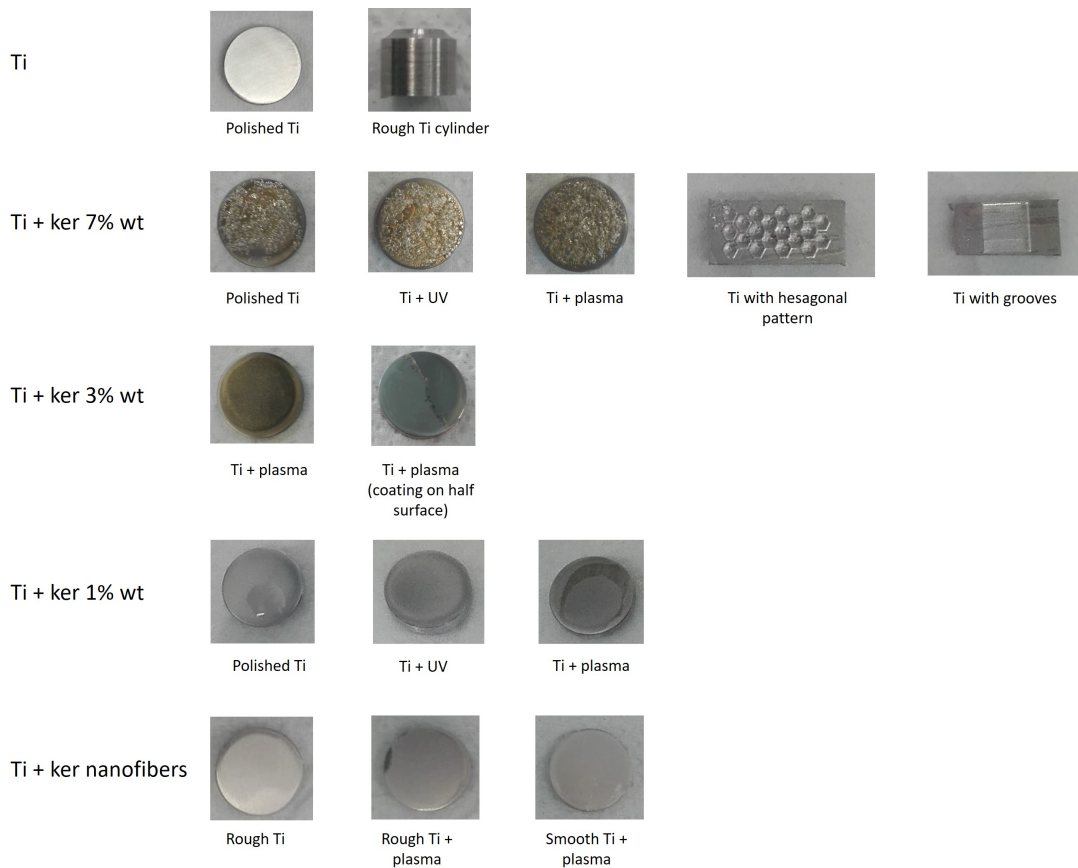


Figure 5.1: Summary of the samples used

keratin coating at 7% wt and keratin coating at 3% wt. As it is possible to see in the table, the appearance of the two coatings is completely different: in the case of keratin solution at 7% wt, it is non homogenous and characterized by bubbles, whereas the coating obtained with keratin solution at 3% wt is more homogenous and smooth.

Samples functionalized with keratin solution at 1% wt, have similar appearance, they do not show changes in appearance before and after functionalization, so it is impossible to distinguish different treatments performed.

Electrospun keratin nanofibers have a particular appearance: after deposition and thermal treatment, they are similar to a white film on the sample.

Samples with grooves or hexagonal pattern were also analyzed, using a coating of keratin at 7% wt, while titanium cylinder, after plasma treatment, was coated with aligned nanofibers.

## 5.1 Adhesion test

### 5.1.1 Tape test

In this work, the adhesion of a thin coating of keratin on substrates of commercially pure titanium was evaluated, in order to identify the surface treatments that can better improve adhesion properties.

A Tape Test was conducted on the following samples:

- Polished Ti + keratin 7% wt;
- Ti + plasma + keratin 7% wt;
- Ti + UV + keratin 7% wt;
- Ti + keratin 3% wt;
- Ti + plasma + keratin 3% wt.

As it is possible to note from Figure 5.7, there are a lot of differences between the samples which do not undergo any surface treatment and the samples which were treated with plasma or irradiated with UV. For each sample is possible to see: an image of the sample before tape test, an image after tape test, and an image of tape after peeling, which can have a different amount of removed coating on it.

In the case of polished Ti, it is evident that most of the coating was removed by the adhesive used during the test, it means that very weak bonds were created between coating and substrate. In the case of samples treated with UV and with plasma, an improvement in adhesion properties is clear. In both this cases, a small part of the keratin coating has detached during the engraving of the grid, but most remained adhered to the substrate after tape test: plasma surface treatment and UV irradiation have been improved bonds strength.

As already said, the keratin solution at 7% wt was dense and it was difficult to obtain an homogeneous coating. For this reason a keratin solution at 3% wt was prepared and deposited on polished Ti and on plasma-treated samples and, in both cases, tape test was conducted.

Although excellent results have been obtained with both treatment, UV and plasma, it was decided to continue this analysis only on the plasma-treated samples for various reasons: observing samples after tape test, it is possible to see that on the Ti surface treated with plasma a more homogeneous coating is present, in addition the plasma performs a double function, as it activates and decontaminates the sample; moreover it has been thought that generally the companies that produce dental prothesis have available and use the plasma.

Regarding untreated surface coated with keratin at 3%, it is possible to see that part of the coating has been detached from the substrate, but in smaller quantities than the case of keratin at 7% wt: it is possible to note that, an homogeneous coating has improved adhesion properties. In the case of plasma-treated Ti with keratin coating at 3%, tape test confirms that plasma treatment improves adhesion between substrate and coating, infact the only coating portion removed from the sample is that detached during engraving the grid, in a similar way of previous case.



Figure 5.2: Tape test on Polished + ker 7% wt



Figure 5.3: Tape test on Ti + plasma + ker 7% wt



Figure 5.4: Tape test on Ti + UV + ker 7% wt



Figure 5.5: Tape test on polished Ti + ker 3% wt



Figure 5.6: Tape test on Ti + plasma + ker 3% wt

Figure 5.7: Tape test on keratin coating

In order to compare the behavior of keratin in form of film and in form of fibers, another tape test was conducted on a titanium samples, treated with plasma in the same conditions of the previous cases, but coated with keratin nanofibers, obtained by electrospinning technique. The results was shown in Figure 5.8.



Figure 5.8: Tape test on Ti + plasma + keratin nanofibers

In this case, as it is possible to see, all the nanofibers were detached by the adhesive during the test, so the plasma treatment did not improve the nanofiber adhesion, but weak bonds were created between substrate and nanofibers.

To explain this behavior, a FESEM analysis was carried out on:

- Smooth Ti + keratin nanofibers;
- Rough Ti + keratin nanofibers.

Figure 5.9 and Figure 5.10 show the FESEM images at different magnifications. The lack of adhesion can be explained considering the numerous beads present: it is possible to see the presence of this defects on both samples, probably due to the conditions in which the test occurred. This defects have greatly reduced the adhesion capacity of keratin on titanium substrate, despite the plasma treatment.

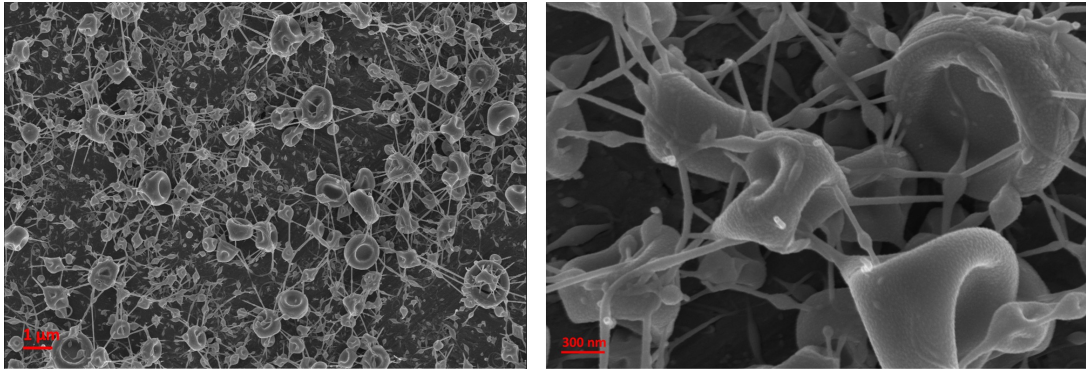


Figure 5.9: FESEM images of keratin nanofibers on smooth Ti at different at different magnifications

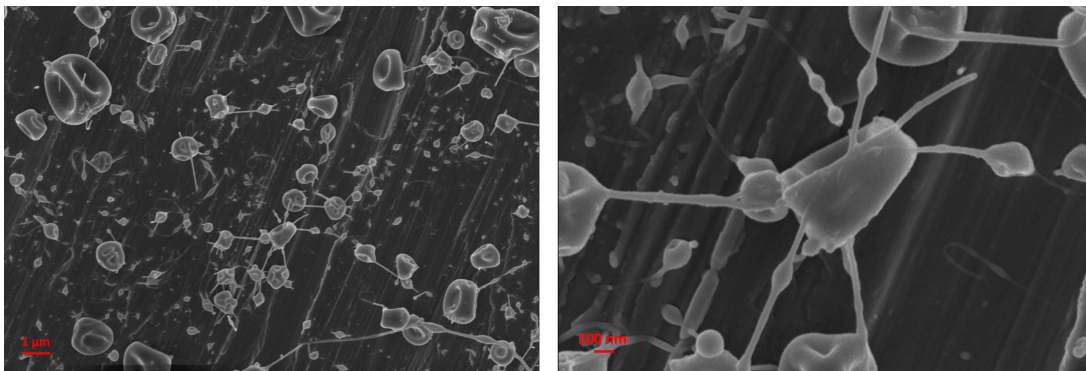


Figure 5.10: FESEM images of keratin nanofibers on rough Ti at different at different magnifications

### 5.1.2 Scratch test

In order to better understand adhesion properties of keratin coating, a scratch test was conducted. It was decided to analyse with this technique only plasma-treated titanium surface with keratin coating at 3% wt, because it was the sample with the better behavior during tape test. The result was compared with a titanium surface.

In Figure 5.11 a comparison between the scratch on keratin coating and on titanium surface is shown.

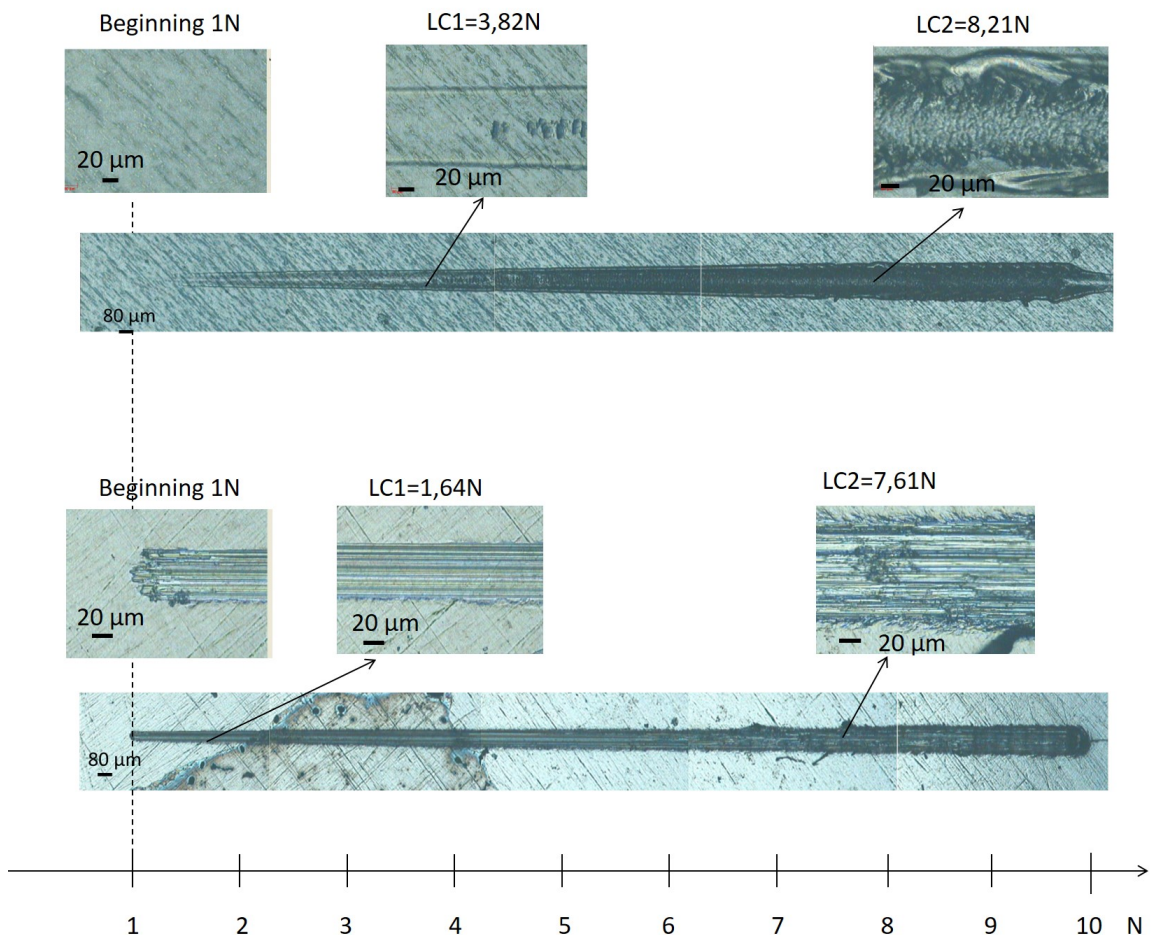


Figure 5.11: Scratch test on keratin coating and titanium surface

As it is possible to see, there are differences between the two tests. The analysis started with a load of 1N: at this load no trace can be seen on keratin coating, while on titanium surface is possible to see a crack at the beginning of the test.

Another important difference is the morphology of the scratch at 3,82 N for keratin and at 1,64 N for titanium. In the first case, the crack is homogeneous, with particular morphology in the center, while on titanium surface stripings characterized all the crack and became more packed with the increase of the load.

It is important to note the appearance of the scratch in keratin coating at 8,21 N. This point corresponds with the peak of acoustic emission: from the zoom, it seems that keratin coating has spread along the edge of the crack, but the titanium substrate is not exposed.

For both the samples, the friction coefficient was evaluated and the result are shown in Fig-

ure 5.12. As it is possible to see, the two curves have different trend: in the case of titanium, the starting value is higher (COF=0,4), compared with that of keratin, and increasing the distance, for titanium it assumes values very high (COF=0,6), while keratin curve presents a plateau at a value around 0,3. This means the keratin has a lower friction coefficient and, probably, this explain the appearance of coating at LC2. It can be said that keratin coating has an important function in protection of titanium substrate, in fact the only part damaged was that of keratin coating.

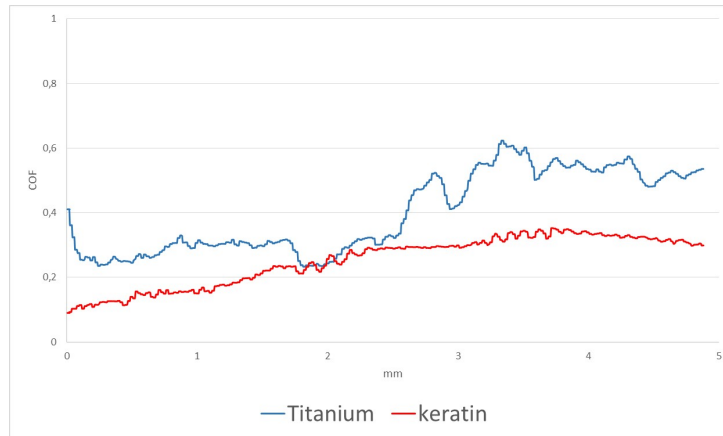


Figure 5.12: COF of titanium and keratin

## 5.2 Thickness and homogeneity of the coating

From the results obtained by tape test, it is evident that keratin coating at 3% wt has better adhesion properties on titanium substrate. For this reason it was decided to evaluate the thickness of this coating: the sample with an half surface coated was used.

Two different types of test were conducted, generally used to estimate the roughness of a sample: a profilometer and a confocal laser scanning microscope. Then the results were compared.

Regarding the profilometer, the test was conducted taking the uncoated titanium surface as reference and measuring the height of the step. Four measures were performed and the results are shown in Table 5.1. Average and standard deviation were also measured.

Table 5.1: Values of thickness of keratin coating at 3% wt

	Value [ $\mu\text{m}$ ]
Measure 1	11,76
Measure 2	8,49
Measure 3	12,7
Measure 4	11,15
Avarage	11,03
Standard Deviation	1,81

As it is possible to see, the thickness of the coating is around 11  $\mu\text{m}$ . Figure 5.13 shows the profile of the sample and the measure of the thickness of the coating.

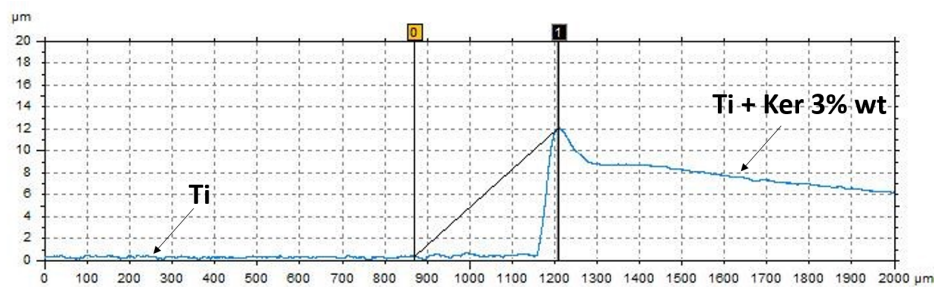


Figure 5.13: Measure of the thickness of the keratin coating

Using the same profilometer, it was evaluate the roughness of the keratin coating. Three tests were conducted and the results are shown in Table 5.2. Average and standard deviation are calculated. As it possible to see, the value of the roughness of the coating is around 0,5  $\mu\text{m}$ .

Then a confocal laser scanning microscope was used: it gives informations about keratin coating, in particular it evaluates the homogeneity of the coating on the substrate and its thickness. Figure 5.14 and Figure 5.15 show the keratin coating images obtained by LSM: in the first image is possible to see that the thickness of coating is homogeneous, except for some areas that have a slightly lower thickness. In this case, it is important to underline that cut off were used in order to eliminate weak signals. The second image shows that keratin coating is homogeneous in 3-D.

Table 5.2: Values of roughness of keratin coating at 3% wt

	Value [ $\mu\text{m}$ ]
Measure 1	0,04
Measure 2	0,06
Measure 3	0,05
Avarage	0,05
Standard Deviation	0,01

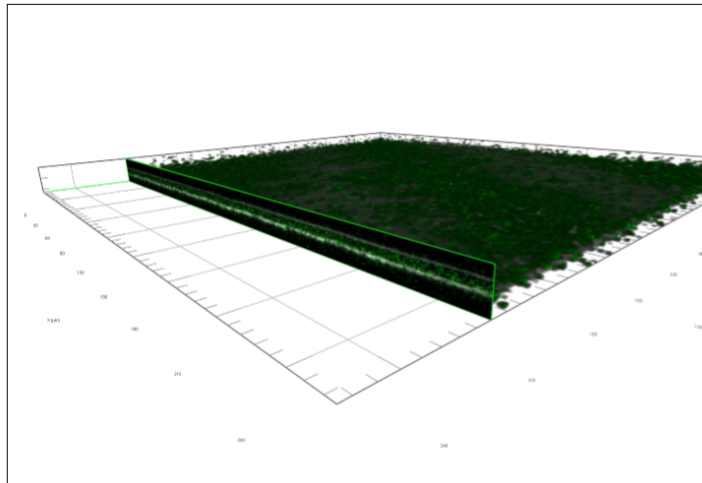


Figure 5.14: Scan of the coating in fluorescence detector

In Figure 5.16 shows the LSM image in widefield of coated substrate: in figure (a), because the coating is transparent, the substrate is visible, in figure (b) is possible to see the coating in fluorescence, which results to be homogeneous in two-directions.

Regarding the thickness of the coating, the image obtained by LSM is shown in Figure 5.17. As it is possible to see, there are two peaks: they refers to the reflection of light at the interface between coating and substrate and at external surface of the coating. The distance between the two peaks is correlated to the thickness of the coating.

Five analysis were conducted and the results are shown in Table 5.3. Avarage and Standard deviation were calculated. To do the analysis a reflective index of 1,55 was used, as found in literature. It was found that the thickness of the coating was around 6  $\mu\text{m}$ .

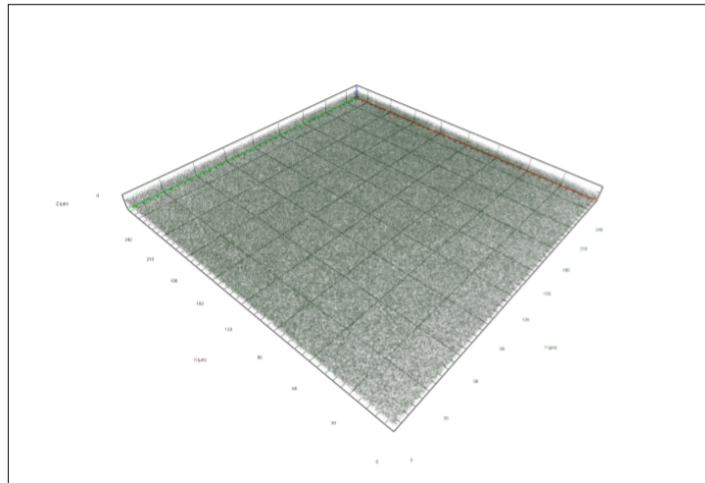


Figure 5.15: Scan of the coating in fluorescence detector

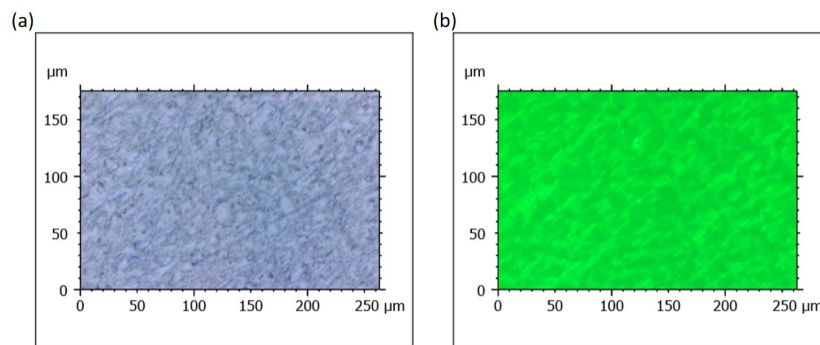


Figure 5.16: Scan of the coating in widefield

Table 5.3: Values of thickness of the coating evaluated with LSM

	<b>Value [<math>\mu\text{m}</math>]</b>
Measure 1	5,859
Measure 2	5,507
Measure 3	5,935
Measure 4	6,163
Measure 5	5,372
Avarage	5,767
Standard Deviation	0,323

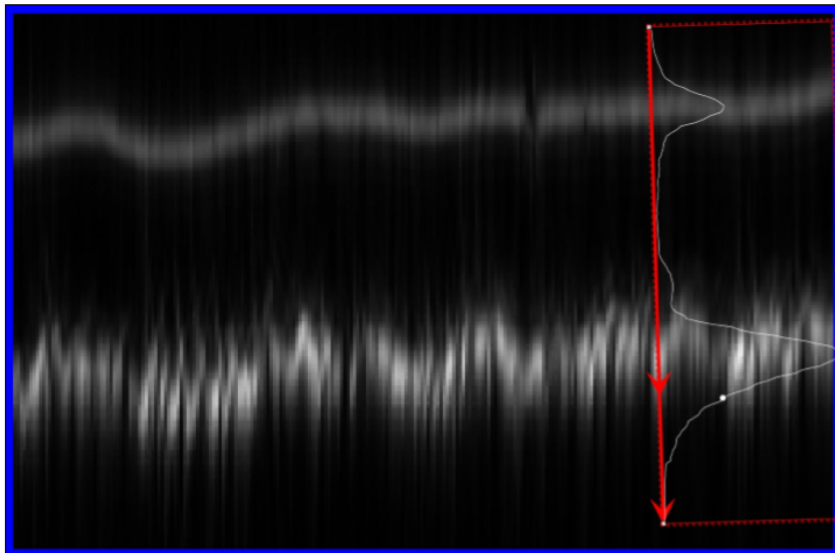


Figure 5.17: Measure of the thickness of the keratin coating using LSM

### 5.3 Wettability

In order to understand how surface treatments change the hydrophilic/hydrophobic characteristics of the materials, two wettability tests were performed, under ambient conditions.

In the first analysis, was studied the wettability properties, using ultrapure water on:

- Polished Ti;
- Ti + plasma + keratin 3% wt.

Table 5.4 shows the values of contact angles for the two samples. In both cases, the mean and standard deviation of the values obtained were calculated and the data were reported on a bar graph, in order to have a comparison of the different behaviour of two surfaces, in contact with the same liquid (Figure 5.18).

Table 5.4: Values of contact angles of water on polished Ti and Ti + plasma + ker 3% wt

	Polished Ti	Ti + plasma + ker 3% wt
	59.4	63.5
	75.6	47.7
<b>Values</b>	65.5	63.5
	71.6	57.2
	70.3	61.9
	74.1	66.6
<b>Average</b>	69,42	60.06
<b>Standard Deviation</b>	6.023	6.794

It was found that the contact angle on polished titanium surface is around  $70^\circ$ , in accordance with literature data (109), while the contact angle of water on keratin coating is around  $60^\circ$ : keratin shows hydrophilic properties, conformed by literature values (36).

As it can be seen, the contact angle of samples with keratin coating is lower than that without coating. This means that the presence of keratin in the form of thin homogeneous coating makes titanium substrate more hydrophilic, due to the functional groups exposed by keratin layer. This represents an important results, because the decrease in contact angle causes an increase in adhesion properties.

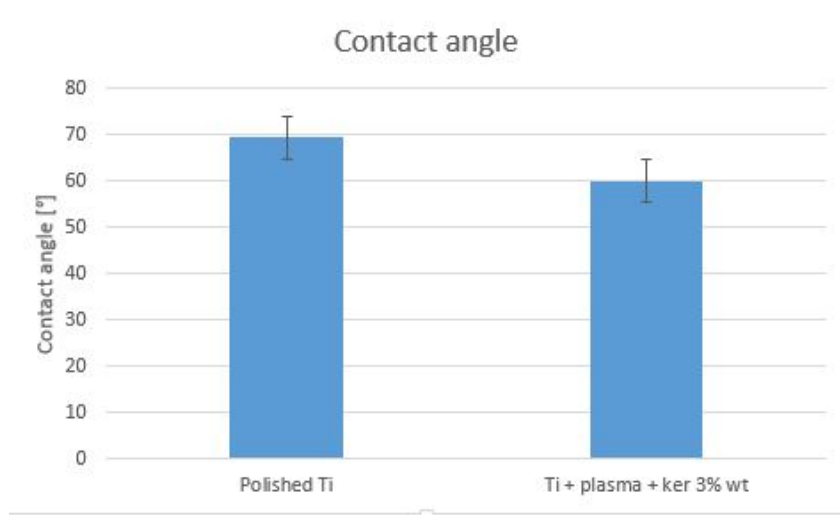


Figure 5.18: Average of the values of contact angles for polished Ti and Ti + plasma + ker 3% wt

Table 5.5: Values of contact angles of keratin solution 3% wt on polished Ti and Ti + plasma

	Polished Ti	Ti + plasma
Values	54,8	18.5

Then a second test was performed. In this case, it was evaluated how surfaces with different treatments are wet by keratin solution at 3% wt. The contact angle was measured on:

- Polished Ti;
- Ti + plasma.

In this case, only one measure was carried out for each sample, and the results are shown in Table 5.5. The angle contact value for the non-treated surface is higher than that of plasma-treated surface: the surface treatment has improved wettability. This is an important result, because wettability, and consequently  $\theta$ , gives information about surface energies, which are related with the formation of adhesive bonds. The value of  $\theta$  affects coating adhesion: if it is low, it causes an increase in the strength of bonds. In Figure 5.9 and Figure 5.10 are shown the images of the drop on keratin solution on the two surfaces: it is clearly possible to see the different wettability of the surfaces and, consequently, the different shape of the drop and in angle contact values.

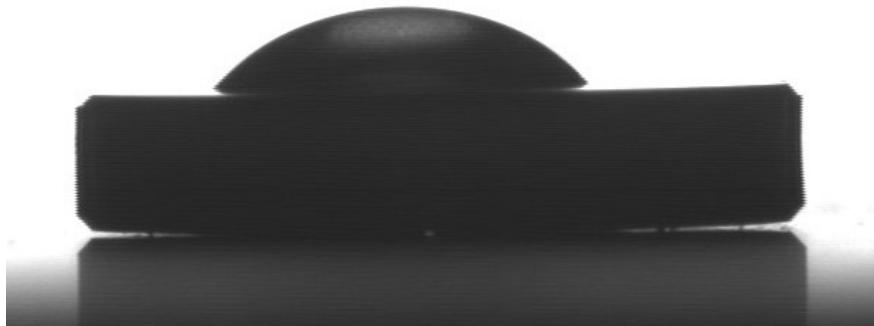


Figure 5.19: Keratin 3% wt drop on polished Ti



Figure 5.20: Keratin 3% wt drop on plasma-treated Ti

## 5.4 Stability in water

In order to evaluate the behavior of keratin in contact with water, a test of stability in water was performed on two plasma-treated samples, coated with keratin coating (3% wt). The samples were immersed in ultrapure water and the macroscopical changes in their appearance were analyzed after 1, 7, 14, 21 and 28 days.

In Figure 5.22, Figure 5.22, Figure 5.23, Figure 5.24, Figure 5.25 and Figure 5.26 are reported the images of the two samples (called 1 and 2) before the immersion and during the test. As it is possible to see, after one day of immersion the keratin appearance changes: it seem to have swollen, but there are not significative changes between its apperance after 1 day or 28 days, except for sample 2 at 28 days.

After thermal stabilization at room temperature, the apperance changes (Figure 5.27): the keratin coatings have assumed the appearance of a dry thin film, that in some parts has lost adhesion with the substrate.



Figure 5.21: Samples 1 and 2 before immersion



Figure 5.22: Samples 1 and 2 after 1 day of immersion



Figure 5.23: Samples 1 and 2 after 7 days of immersion



Figure 5.24: Samples 1 and 2 after 14 days of immersion



Figure 5.25: Samples 1 and 2 after 21 days of immersion



Figure 5.26: Samples 1 and 2 after 28 days of immersion



Figure 5.27: Samples 1 and 2 after dried at room temperature

## 5.5 Zeta potential

In order to investigate the surface charge,  $\zeta$ -potential tests were performed on the following samples:

- Polished Ti;
- Ti + plasma;
- Ti + plasma + keratin 3% wt.

Figure 5.28 shows a comparison of the curves of the different samples tested. As it is possible to see, all of them have a value of IEP identified for acidic pH, between 3,5 and 5,5, and consequently all the surfaces are negatively charged at physiological pH.

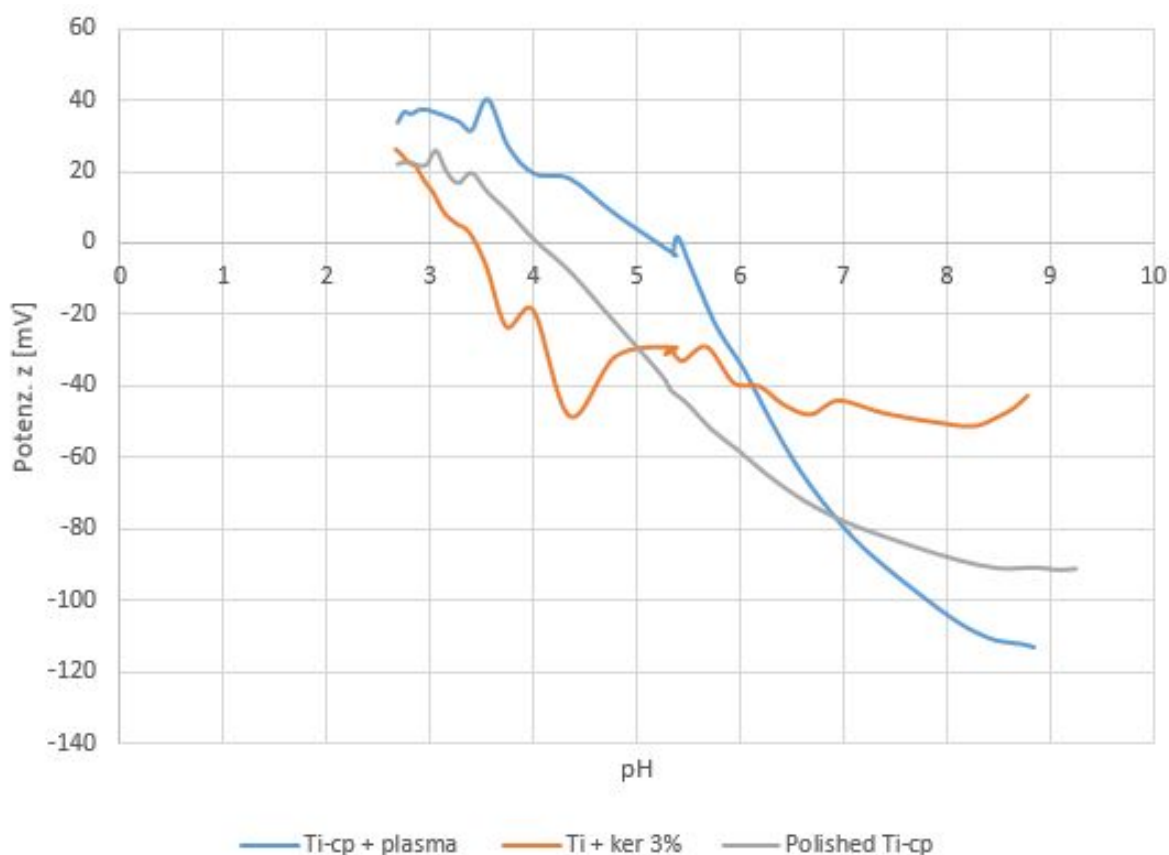


Figure 5.28:  $\zeta$ -potential of polished Ti-cp, Ti-cp + plasma and Ti-cp + plasma + ker 3% wt

Figure 5.29 shows the curve obtained during the analysis of samples of polished Ti. As it is possible to see, the IEP is in relation with a pH value of 4, according to previous works (110). In the figure are reported the deviation standard values of zeta-potential.

Figure 5.30 shows the curve obtained for a plasma-treated Ti sample. As it is possible to note, an anomaly is present for pH values around 5,5: it can be ascribed to an experimental error in the measurement. In any case, it is clear that a shift toward the basic range is due to the surface treatment that exposes an enhanced number of surface functional group with basic behavior. Also in this case, deviation standard values of zeta-potential are shown.

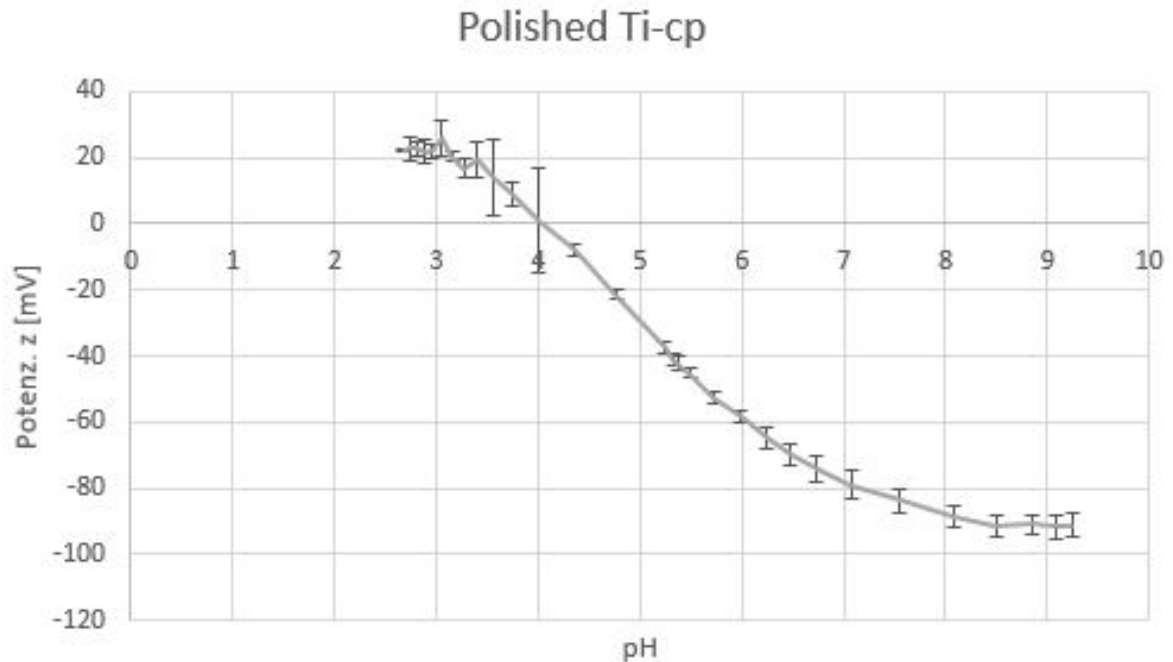
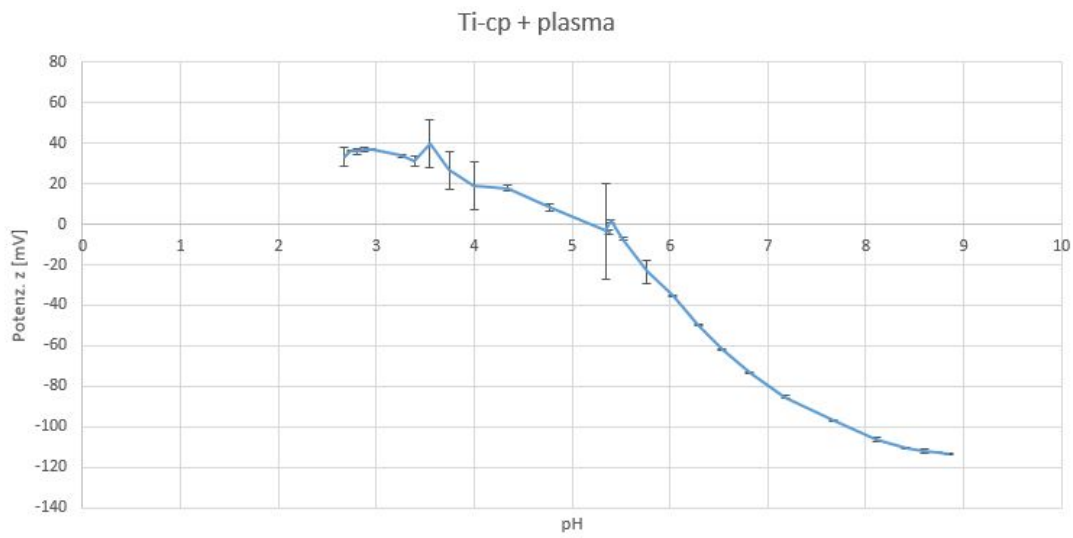
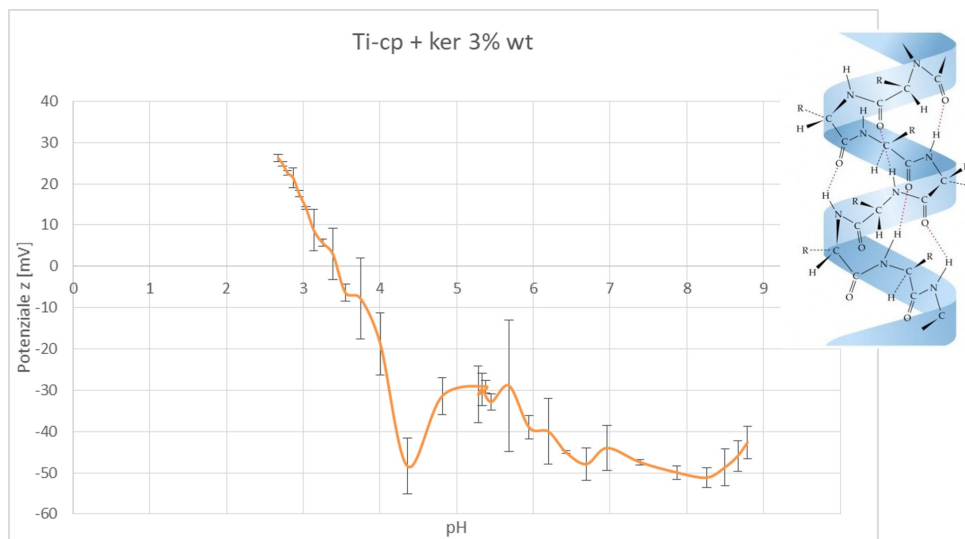


Figure 5.29:  $\zeta$ -potential of polished Ti-cp

Figure 5.31 shows the curve obtained for a plasma-treated Ti sample, on which a coating of keratin at 3% wt was deposited. In this case, the IEP value is identified for a pH value of 3,5. The deviation standard values are shown. It is also represented the molecular structure of keratin, for a better understanding of the functional groups present. It is important to underline that the pH value at room temperature for a keratin solution at 3% wt is around 5. A significant plateau can be observed in the basic region. It can be associated with the presence of homogeneous functional groups with acidic behavior (probably COOH groups looking at keratin structure and XPS results), while  $NH_2$  groups, present in the structure, behave as weak base and do not generate a plateau in acidic range.

The different values of IEP for plasma-treated Ti and for keratin coating can have important consequences in adhesion properties: infact the first sample presents groups with basic behavior, while the latter presents group with acidic behavior, favouring the formation of acid-base reactions, resulting in good adhesion between coating and substrate. It was demonstrated by Fowkes, that strenght of adhesive bonds depends on the thermodynamic work of adhesion and consequently on acid-base interactions. (111)

Figure 5.30:  $\zeta$ -potential of plasma-treated Ti-cpFigure 5.31:  $\zeta$ -potential of plasma-treated Ti-cp with keratin coating (3% wt) and molecular structure of keratin

## 5.6 FT-IR

The FT-IR analysis was carried out to observe the presence and the type of bonds on the sample surface. The following samples were tested:

- Polished Ti;
- Ti + keratin 7% wt;
- Ti + plasma + keratin 7% wt;
- Ti + UV + keratin 7% wt;
- Ti + plasma + keratin 3% wt;
- Ti + keratin 1% wt;
- Ti + plasma + keratin 1% wt;
- Ti + UV + keratin 1% wt;
- Ti with grooves + keratin 7% wt;
- Ti with hesagonal pattern + keratin 7% wt.

The results are reported in different graphs.

Figure 5.32 shows the FT-IR spectrum obtained for a polished Ti surface. As it is possible to see, no significant peak can be identified: the surface is clean.

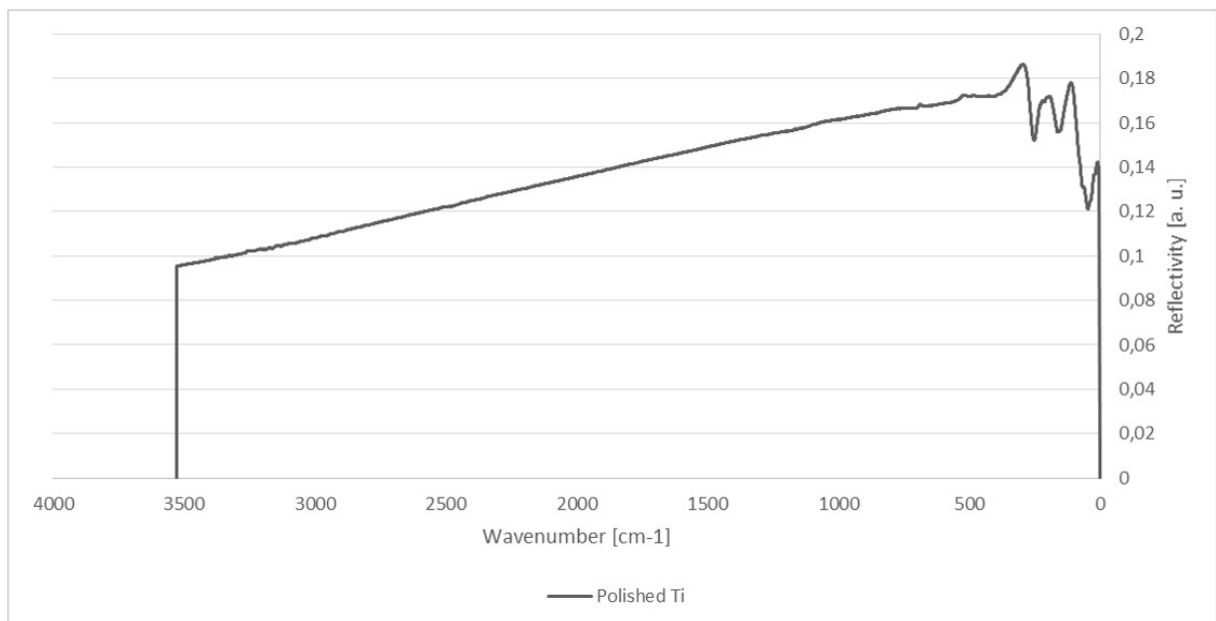


Figure 5.32: FT-IR characterization of polished Ti sample

Figure 5.33 represents the curves obtained for samples characterized by keratin coating. The molecular structure of keratin is also shown, in order to make simpler the identification of the peak.

It is possible to note the presence of peaks at certain value of wavenumber and each peak correspond to the presence of a functional group (112):

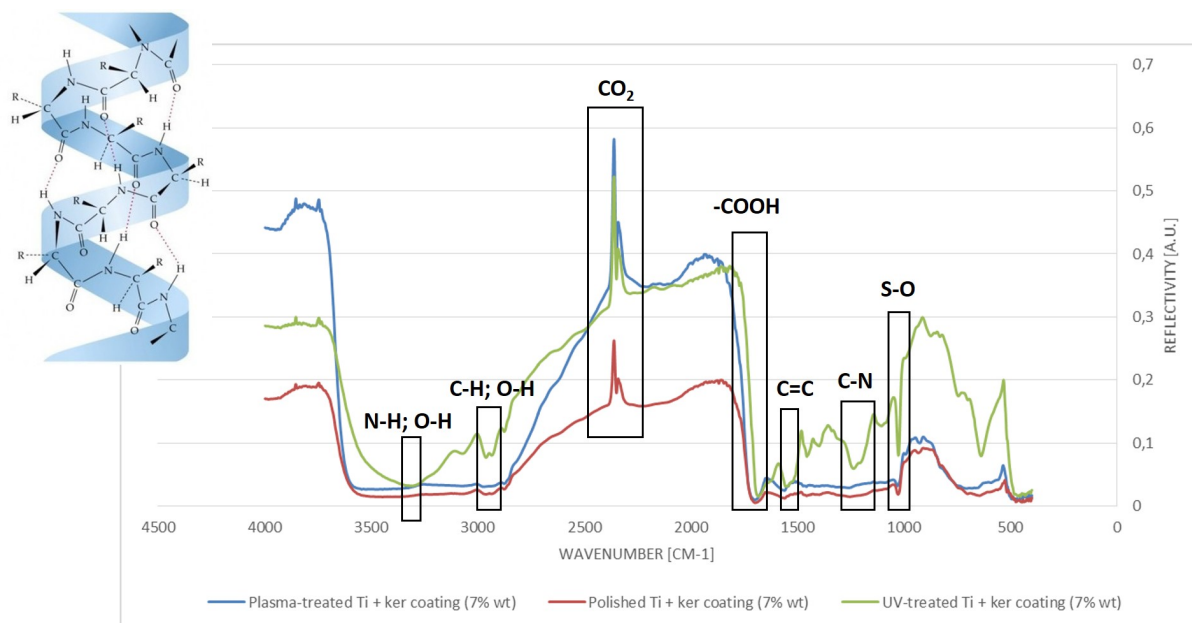


Figure 5.33: FT-IR characterization of samples with keratin coating (7% wt) and molecular structure of keratin (F106)

- S-O at  $1000\text{ cm}^{-1}$ ;
- C-N at  $1221\text{ cm}^{-1}$ ;
- C=C at  $1523\text{-}1542\text{ cm}^{-1}$ ;
- -COOH at  $1650\text{ cm}^{-1}$ ;
- $CO_2$  at  $2355\text{ cm}^{-1}$ ;
- C-H, O-H at  $2921\text{ cm}^{-1}$ ;
- N-H, O-H at  $3278\text{ cm}^{-1}$ .

From literature (113) it is possible to see that keratin shows characteristics adsorption bands related to the bond present:

- the amide A band is connected with the stretching vibration of N-H bonds, at a wavenumber of  $3282\text{ cm}^{-1}$ ;
- the amide I is connected to the stretching vibration of the carbonyl group, at a wavenumber between  $1700\text{-}1600\text{ cm}^{-1}$ ;
- the amide II derives mainly from in-plane NH bending with some contribution of CN stretching vibrations, at a wavenumber between  $1580\text{-}1510\text{ cm}^{-1}$ ;
- the amide III is a very complex band dependent on the nature of side chains and hydrogen bonding, at a wavenumber of  $1300\text{-}1220\text{ cm}^{-1}$ .

From Figure 5.33, it is possible to see that most of the peaks present in the spectra of the samples coated with keratin are identifying the same types of bonds, although the intensity is sometimes different. This may be due not only to a homogeneous distribution of the keratin coating but

also to its thickness, which could prevent the detection of different chemical bonds despite the different treatments carried out on the surfaces of the samples. The only differences in the three curves are identified for wavenumber in the range between  $1000$  and  $1500\text{ cm}^{-1}$ , and between  $3000$  and  $3500\text{ cm}^{-1}$ : the curve which represents the samples irradiated by UV shows a different trend, compared with the other two curves, in fact presents a significant peak, while in the same regions, polished Ti and plasma-treated Ti show a plateau. It can be ascribed to an experimental error.

Moreover, the curves show the typical peaks of keratin present in literature. In addition, the peak at  $2355\text{ cm}^{-1}$  represents  $\text{CO}_2$ .

In Figure 5.34 is shown the spectrum obtained for a plasma-treated Ti with keratin coating at 3% wt. In this case, due to the thickness of the coating, the analysis was conducted with a grazing angle, in order to detect all the informations. As it is possible to see, the typical peak for S-O, C-N, C=C, -COOH, C-O and O-H bonds are well identified, added to that of  $\text{CO}_2$ . In the region characterized by a wavenumber of  $3000 - 4000\text{ cm}^{-1}$ , it is difficult to distinguish different peaks.

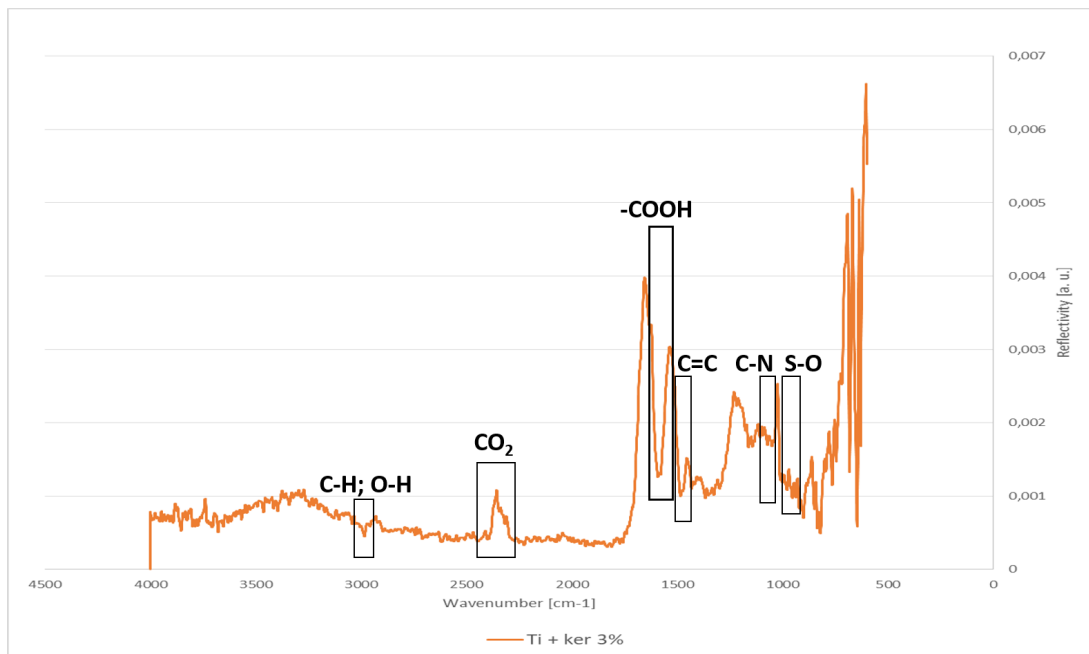


Figure 5.34: FT-IR characterization of plasma-treated Ti with keratin coating (3% wt)

In Figure 5.35 are reported the curves of functionalized samples. All the curves present the same trend and are characterized by the absence of peaks, except for those at  $500\text{ cm}^{-1}$  and  $2400\text{ cm}^{-1}$ . It is probably caused by the too thin keratin layer, which cannot be analyzed by FT-IR technique.

In Figure 5.36 is reported the FT-IR characterization of the titanium samples characterized by the hexagonal pattern. In this case, the peaks typical of keratin are well distinguished, added to that typical for  $\text{CO}_2$ . This indicates that for this system, keratin coated wells of the structure.

In Figure 5.37 it is reported the FT-IR curve obtained for titanium sample characterized by the presence of grooves. In this case, it is more difficult to see the keratin peaks: it is possible to see a peak for a wavenumber between  $1700-1500\text{ cm}^{-1}$  and one at  $3200\text{ cm}^{-1}$ . This can be explained considering the fact that, after the deposition of the keratin solution on the surface,

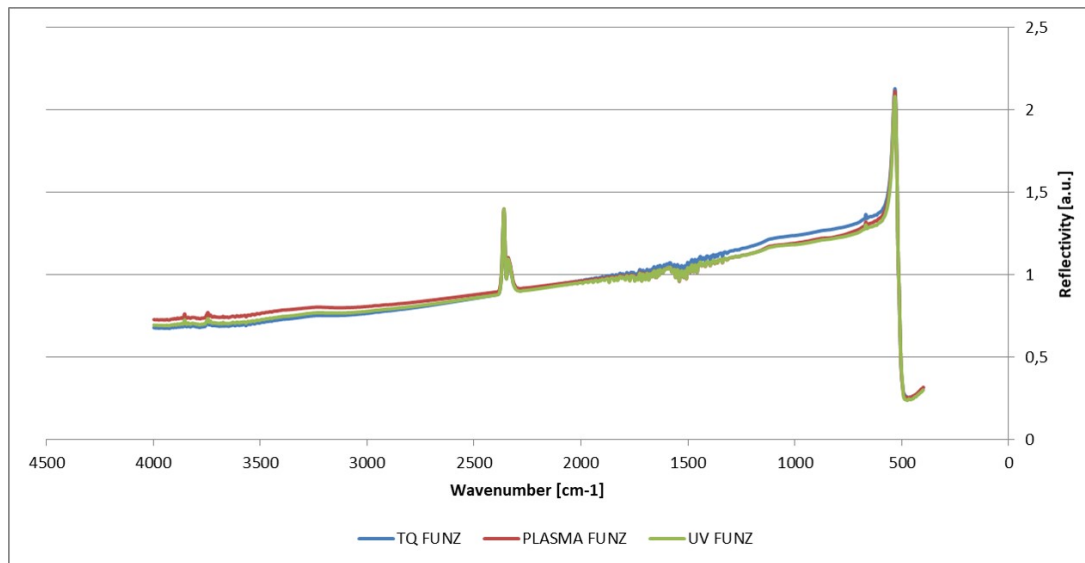


Figure 5.35: FT-IR characterization of samples functionalized with keratin solution (1% wt)

the excess was manually removed. Because grooves are less depth than hexagonal wells, all the keratin deposited was probably removed, for this reason there are not keratin typical peaks, differently from the previous case.

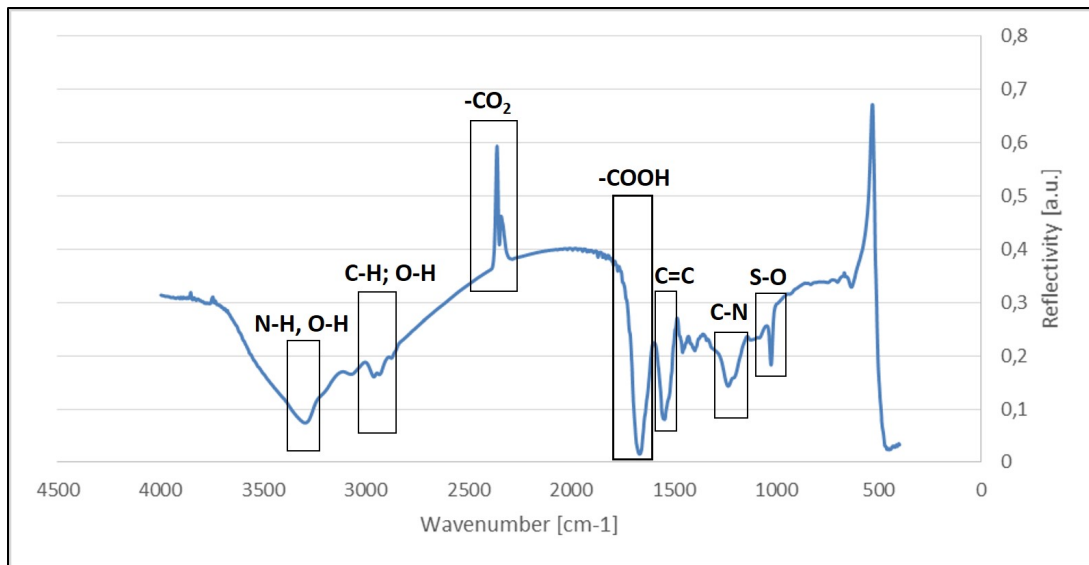


Figure 5.36: FT-IR characterization of Ti samples with hexagonal pattern and keratin solution (7% wt)

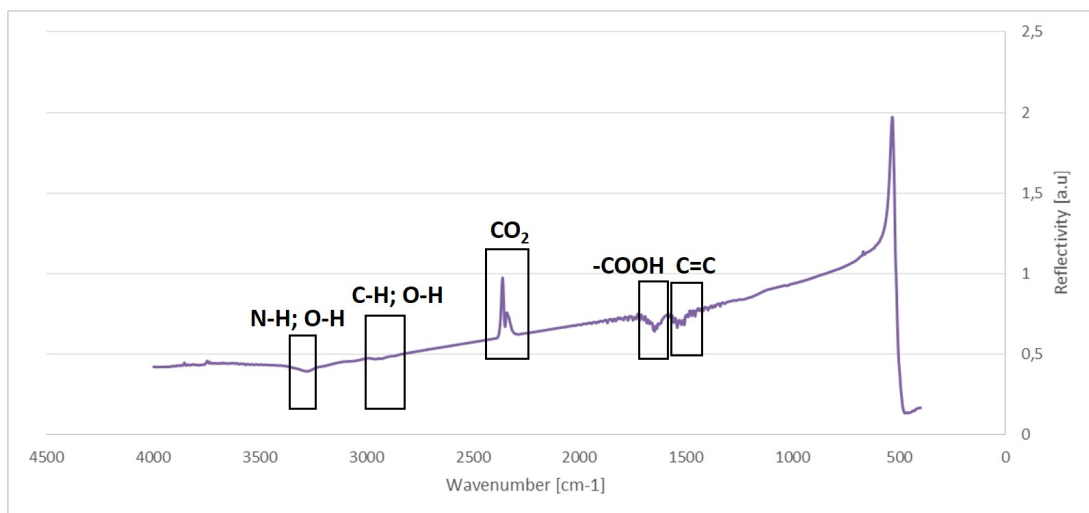


Figure 5.37: FT-IR characterization of Ti samples with grooves and keratin solution (7% wt)

## 5.7 XRD

An X-ray diffractometry measurement was carried out in order to identify crystalline phases present on the coated samples. Two crystal structures are generally observed for keratin:  $\alpha$ -keratin structure is identified by the peak at  $2\theta = 9^\circ$  and  $17,8^\circ$ , whereas the  $\beta$ -sheet structure is identified by the peaks at  $2\theta = 9^\circ$  and  $19^\circ$  (114).

It was analyzed:

- Ti + plasma + keratin film at 3% wt in water;
- Ti + plasma + keratin film at 7% wt in water.

The results were compared with a keratin film in formic acid, obtained by a previous work, and are shown in Figure 5.38 (115). As it is possible to see, the curves present important differences:

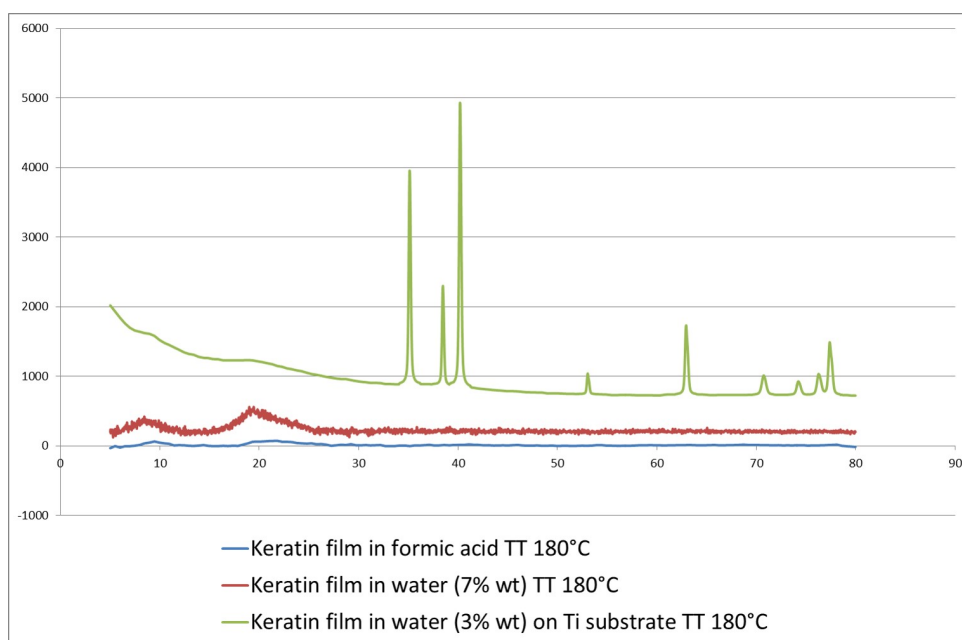


Figure 5.38: XRD spectra of keratin film in formic acid, in water (7% wt), and in water on Ti (3% wt)

for keratin film in water at 7% wt and in formic acid, it is identified the typical peak of the beta sheet of keratin, at  $2\theta = 9^\circ$  and at  $2\theta = 19^\circ$ . This peaks are more easily visible in Figure 5.39, in which a zoom of the area of  $\theta$  between 5 and 30 is shown. In particular, for keratin coating at 7% wt the peak at  $2\theta = 19^\circ$  is narrower, and this can be correlated with a nanocrystalline structure.

In the case of keratin film at 3% wt on Ti substrate, the curve shows the principal peak of titanium, at  $2\theta = 40,1^\circ$ , Due to the thickness of the coating. There are also the peak at  $2\theta = 9^\circ$  and at  $2\theta = 19^\circ$ , but the signal is too weak and the peaks of the substrate make identification difficult. Moreover, this peaks confirm the presence of the keratin coating.

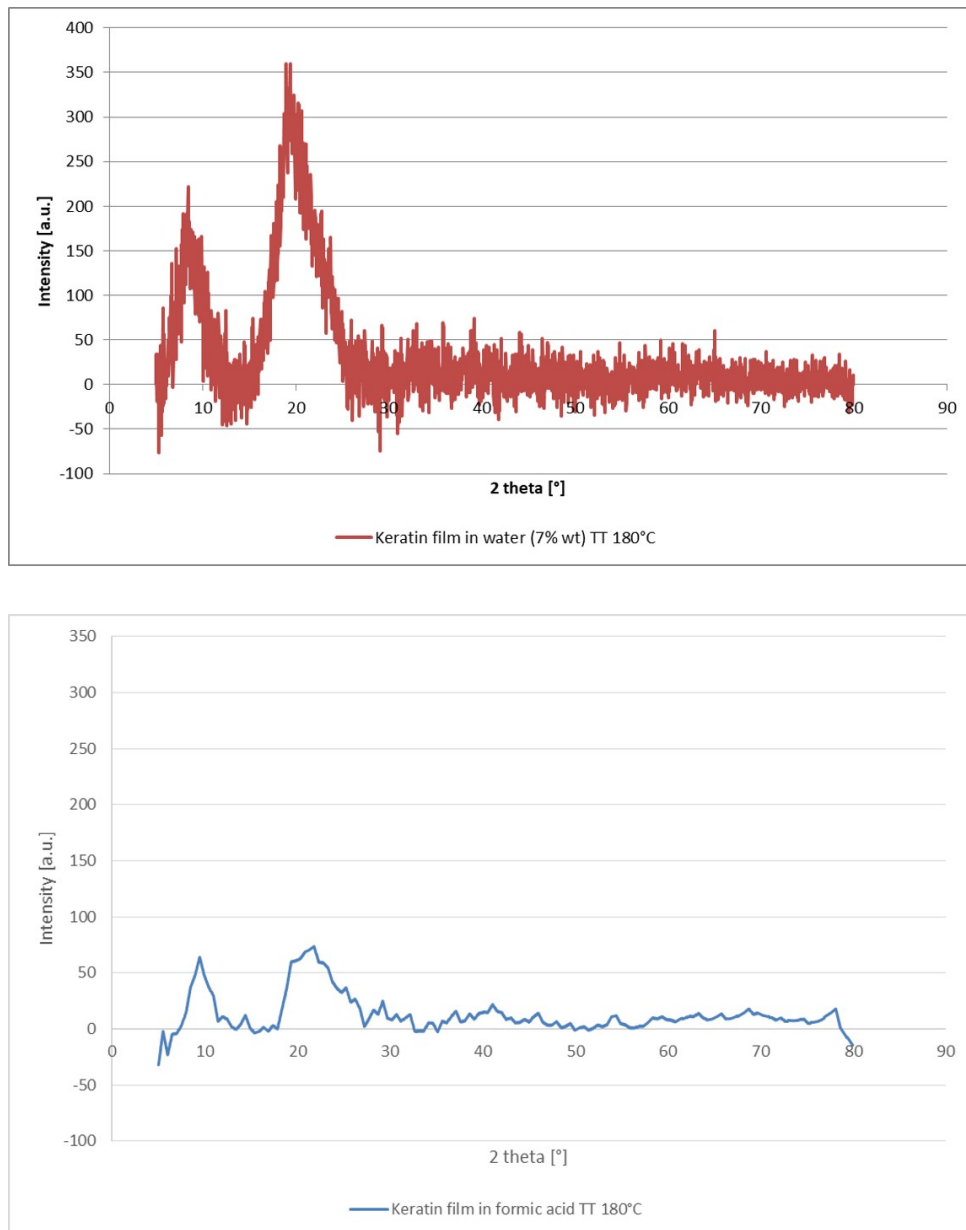


Figure 5.39: Zoom of XRD spectra for  $\theta$  between 5 and 30 for keratin film in water and in formic acid

## 5.8 XPS

In order to evaluate the different chemical groups present on the surface, different samples were subjected to a XPS analysis: from this test, it is possible to know which elements are present on the surface, their atomic percentage and their chemical surroundings.

The analysis was conducted on:

- Polished Ti;
- Ti + plasma;
- Ti + UV;
- Ti + plasma + keratin coating 3% wt;
- Polished Ti functionalized with keratin at 1% wt;
- Ti + plasma functionalized with keratin at 1% wt;
- Ti + UV functionalized with keratin at 1% wt.

In Table 5.6 are shown the atomic percentages obtained from the Survey spectra of the various samples.

Table 5.6: Atomic percentages from Survey spectra

	Polished Ti	Ti + plasma	Ti + UV	Ti + ker coat (3% wt)	Ti + ker (1% wt)	Ti + plasma + ker (1% wt)	Ti + UV + ker (1% wt)
<b>O</b>	45,14	50,75	53,18	19,14	32,69	17,24	26,41
<b>C</b>	32,67	18,20	21,36	63,63	48,44	67,17	54,88
<b>N</b>	1,21	0,98	0,84	11,44	7,09	12,96	11,38
<b>Ti</b>	18,78	19,48	21,23	0,00	8,37	0,04	5,35
<b>Zn</b>	0,49	0,38	0,75	0,03	0,06	0,01	0,13
<b>Si</b>	1,41	0,73	1,90	0,07	1,21	0,07	0,35
<b>Ca</b>	0,29	0,47	0,35	0,00	0,30	0,04	0,18
<b>S</b>			0,39	3,15	0,56	1,96	1,32
<b>Na</b>		5,41		2,54	1,29	0,50	
<b>F</b>		1,85					
<b>Al</b>		1,74					

It is possible to see that carbon is always present on the surfaces of the seven samples, but in different percentages: on titanium samples without keratin the percentages are lower than those of samples with keratin coating or functionalization, infact in the first case, the range is between 18-33%, whereas in the second case, the atomic percentage is between 48-68%. It can be explained considering the fact that titanium is superficial reactive, in addition the large carbon content in the last four samples is due to the presence of the keratin. It is also possible to note a significant amount of nitrogen in the samples with keratin coating or functionalized, while very

little amount is present in the samples without keratin.

Comparing titanium samples activated with plasma and UV, it is possible to note how plasma treatments have a cleaning function, infact plasma-treated Ti is the sample characterized by the lower percentage of carbon and other contaminant elements. In the case of plasma-treated titanium with keratin coating at 3% wt, it is possible to see that atomic percentage of Ti is 0,00: it is due to the thickness of the coating. As already said, the coating has a thickness of about  $11\mu\text{m}$ , while the XPS has a depth analysis of 1-10 nm: this means that, in this case, the X-ray beam does not reach the titanium surface, so the percentage of titanium detected is zero. The amount of sulfur is moderate, and it concerns samples covered or functionalized, so it is attributable to keratin presence. Zinc, silicon, calcium, sodium, fluorine and aluminum are present in very little percentages as contaminations. In Figure 5.40, Figure 5.41, Figure 5.42, Figure 5.43, Figure 5.44, Figure 5.45, Figure 5.46 the Survey spectra for the seven samples are shown.

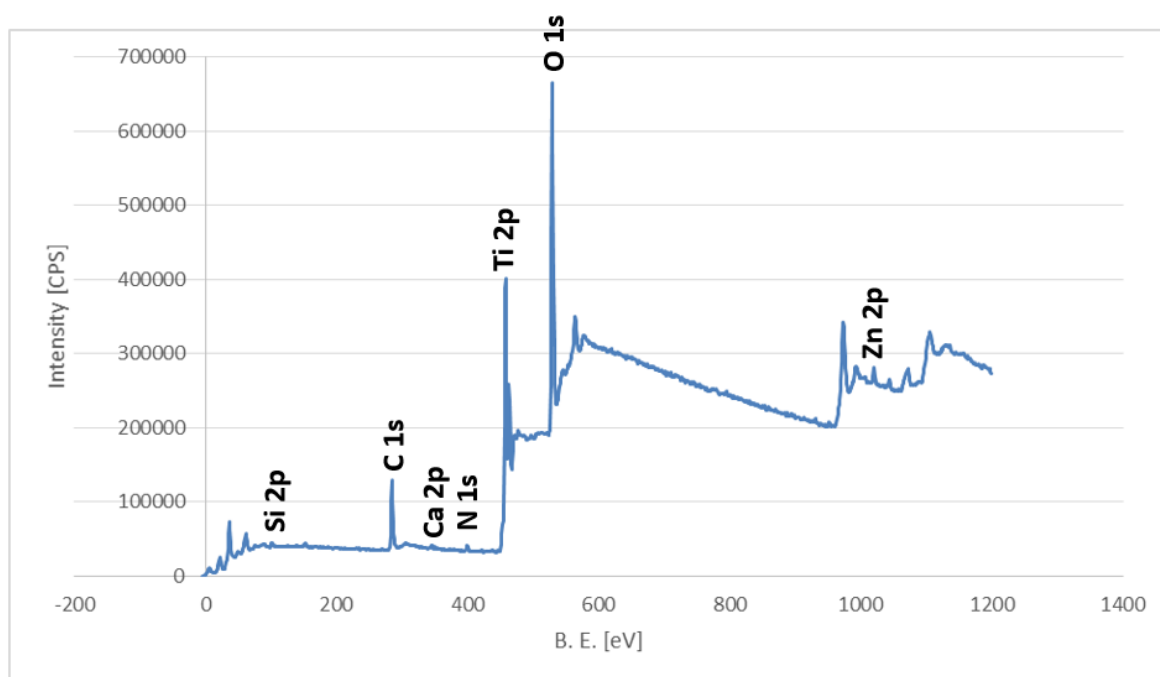


Figure 5.40: Survey spectrum for polished Ti

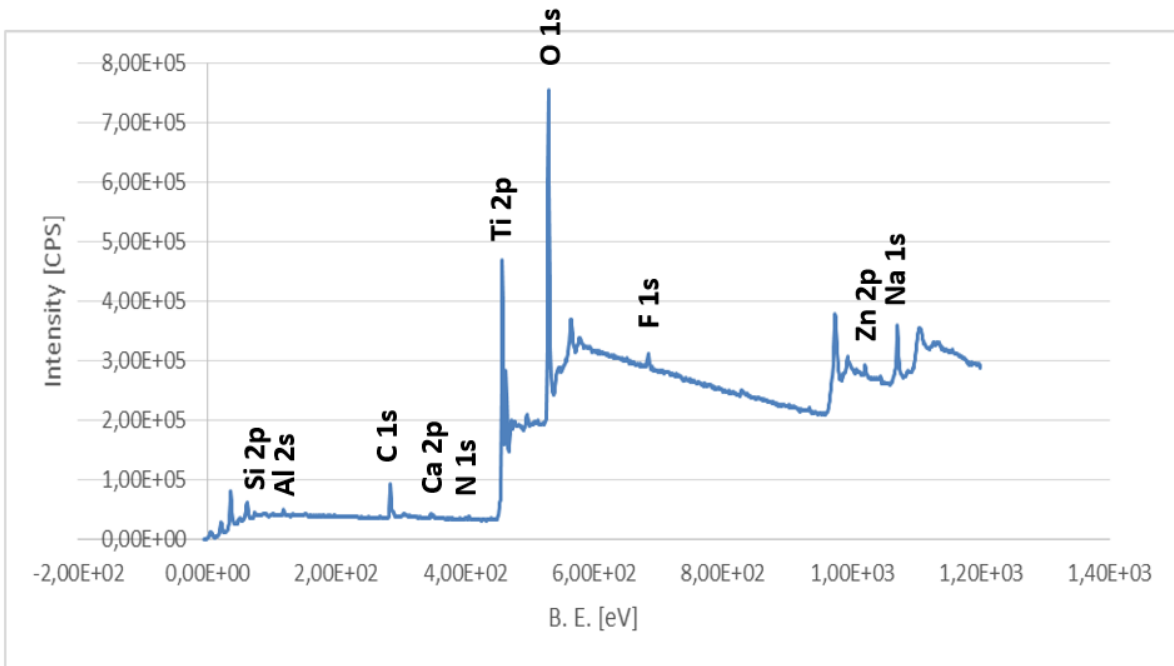


Figure 5.41: Survey spectrum for plasma-treated Ti

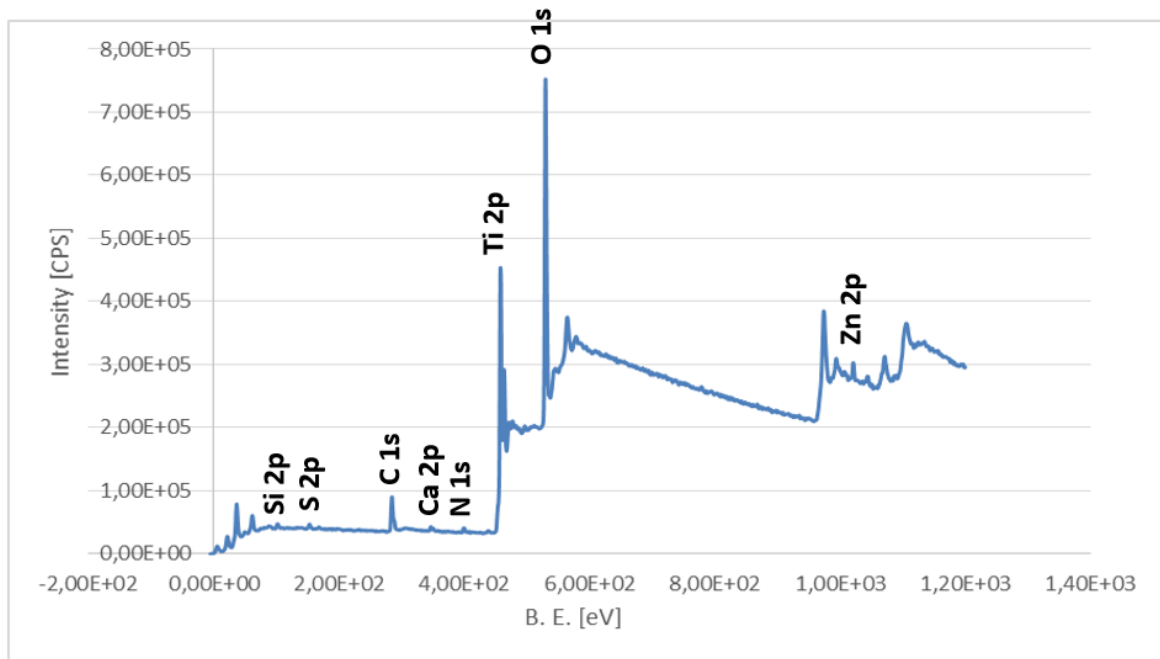


Figure 5.42: Survey spectrum for UV-treated Ti

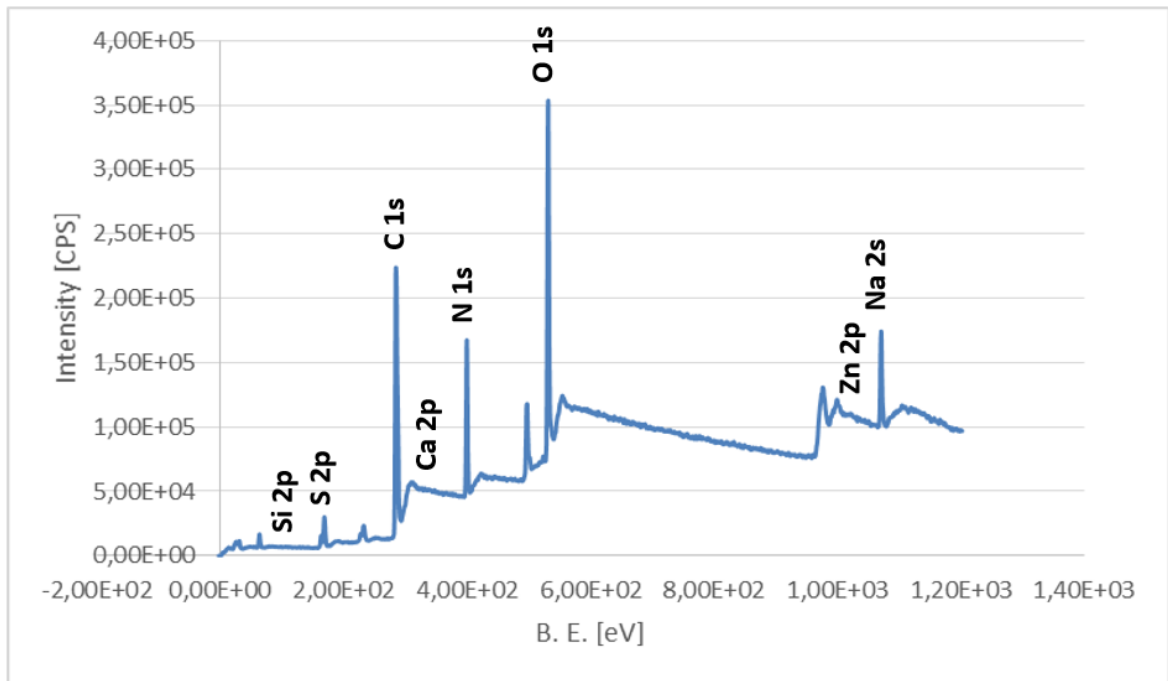


Figure 5.43: Survey spectrum for plasma-treated Ti + keratin coating (3% wt)

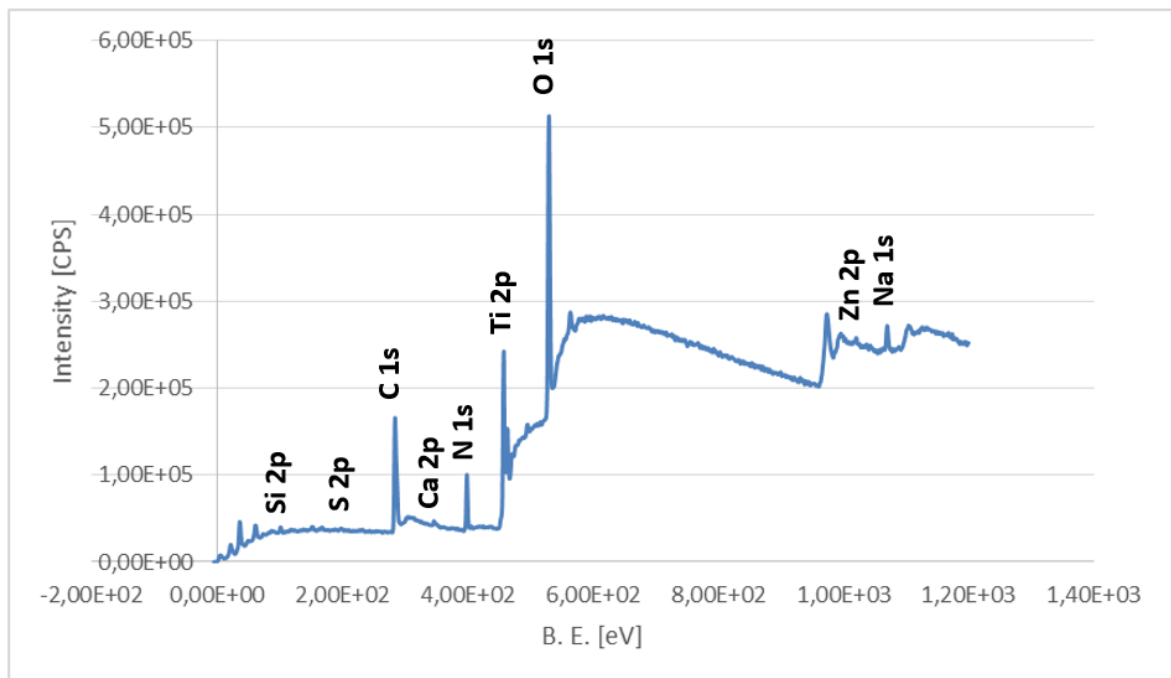


Figure 5.44: Survey spectrum for polished Ti functionalized with keratin (1% wt)

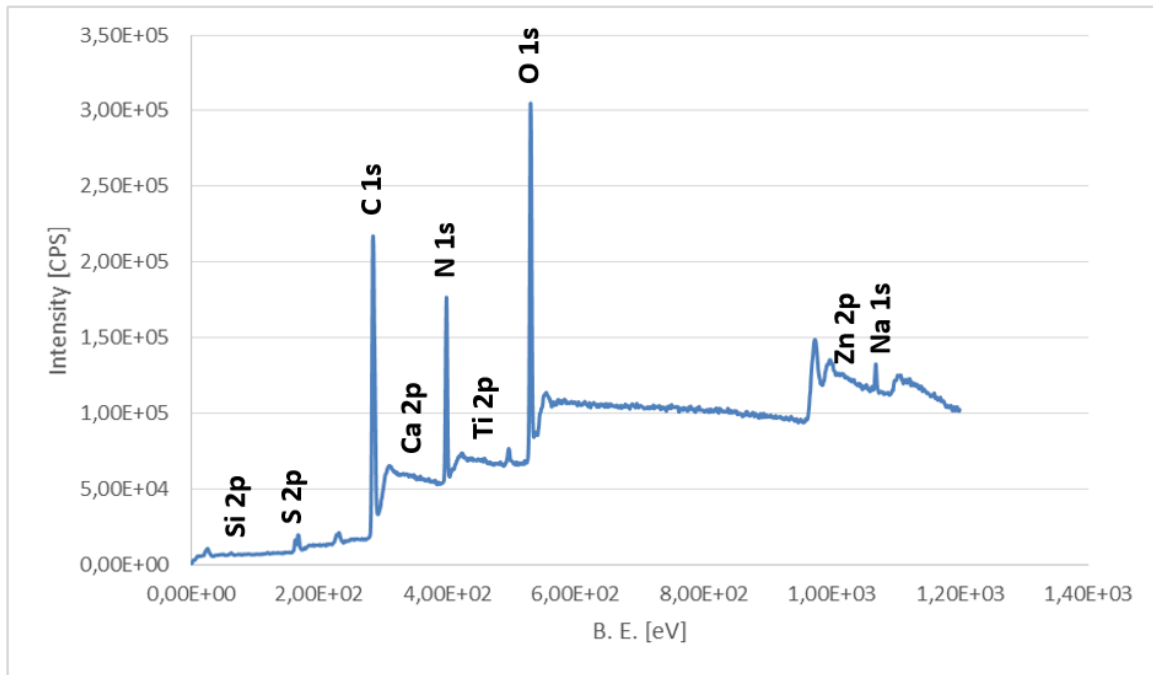


Figure 5.45: Survey spectrum for plasma-treated Ti functionalized with keratin (1% wt)

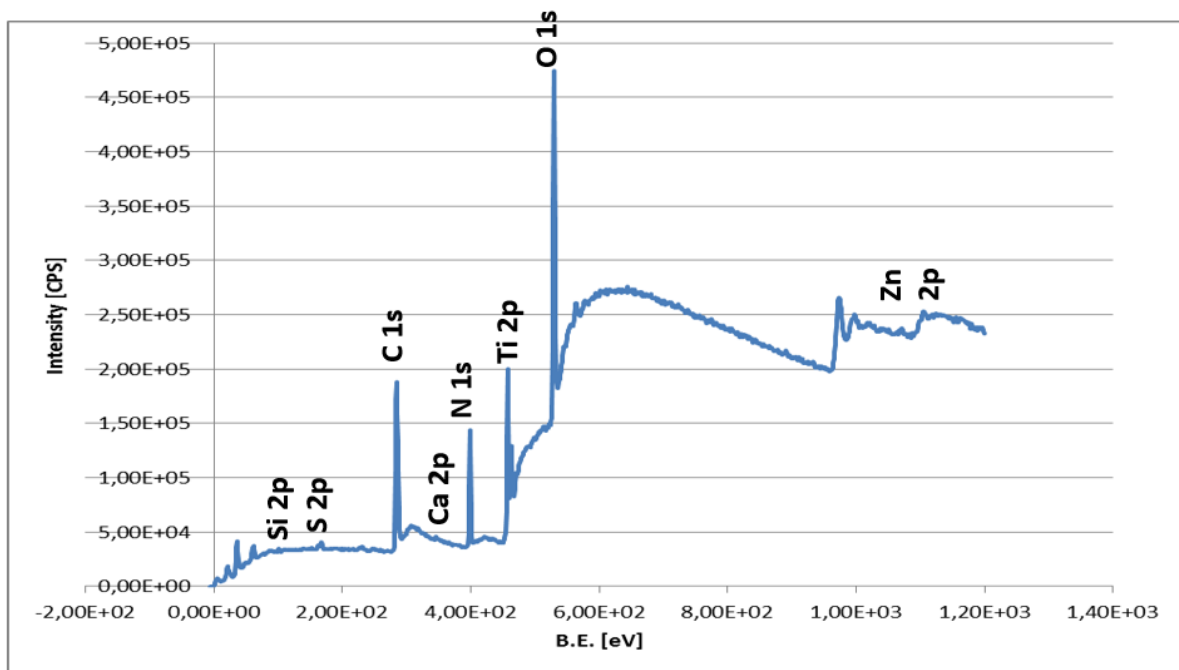


Figure 5.46: Survey spectrum for UV-treated Ti functionalized with keratin (1% wt)

For each sample, the HR spectra of oxygen, nitrogen, carbon, titanium and sulfur were then analyzed. The possible attribution of each peak was made on what is reported in literature. Considering oxygen, three specific peaks are identified, corresponding to a certain oxygen bond. Table 5.7 shows the Energy Binding values associated to different types of bond (116) (117) (118).

Table 5.7: Energy Binding for different chemical bonds for O

Binding Energy [eV]	Type of bond
530	Ti-O
531	-OH; C=O
532	-OH; C-O

In Figure 5.47, Figure 5.48, Figure 5.49, Figure 5.50, Figure 5.51, Figure 5.52 and Figure 5.53 are shown the HR oxygen spectra for the different samples.

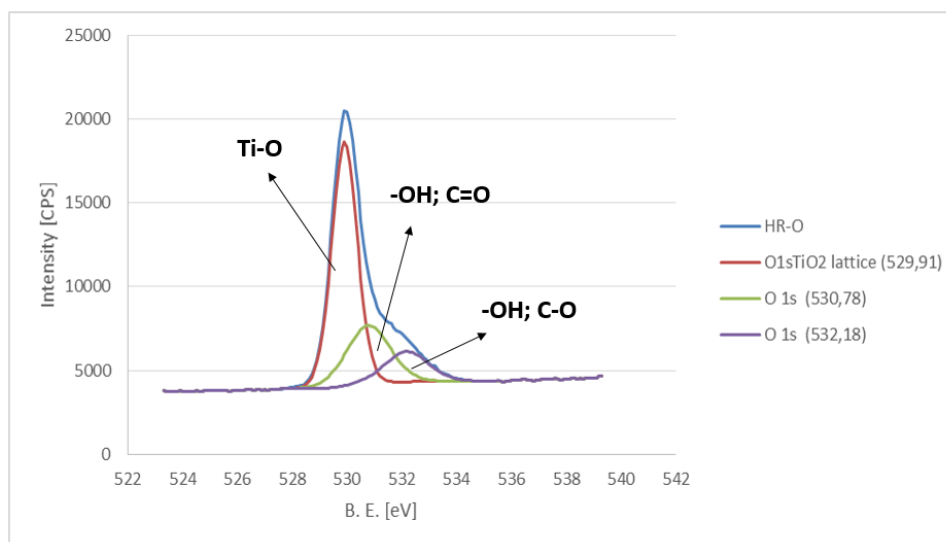


Figure 5.47: HR oxygen spectrum for polished Ti

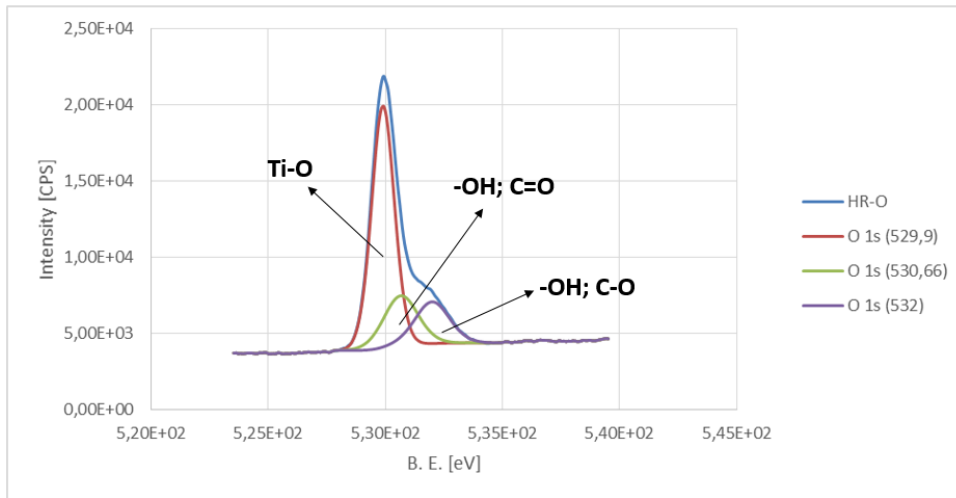


Figure 5.48: HR oxygen spectrum for plasma-treated Ti

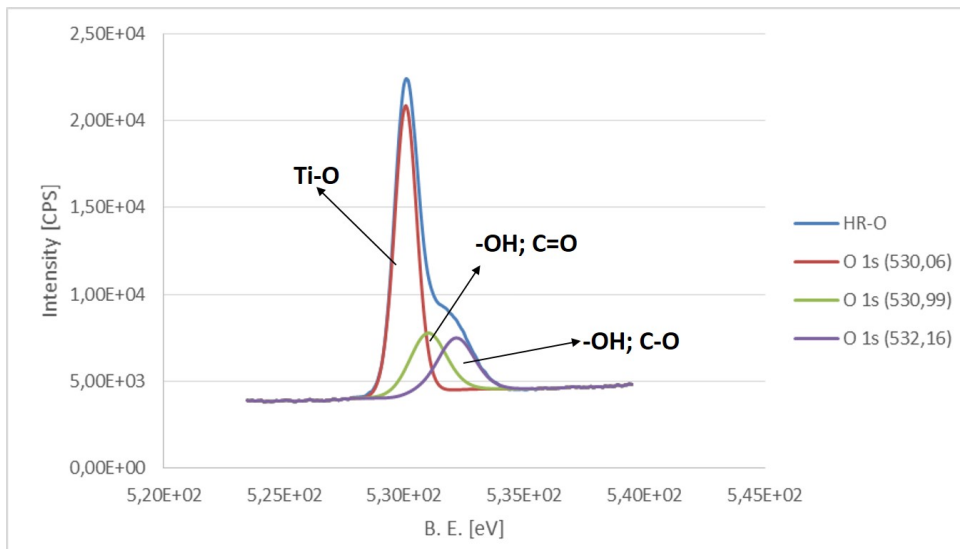


Figure 5.49: HR oxygen spectrum for UV-treated Ti

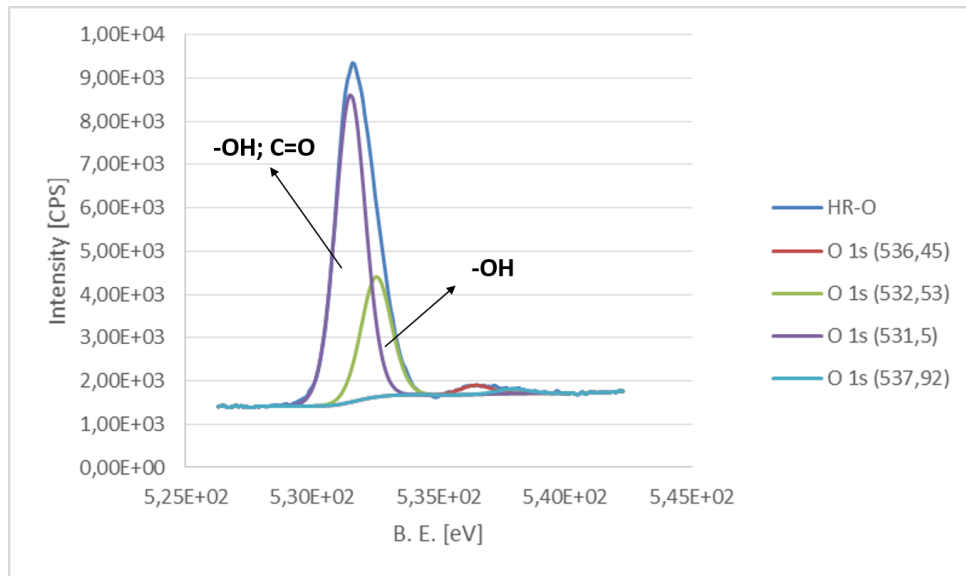


Figure 5.50: HR oxygen spectrum for plasma-treated Ti + keratin coating (3% wt)

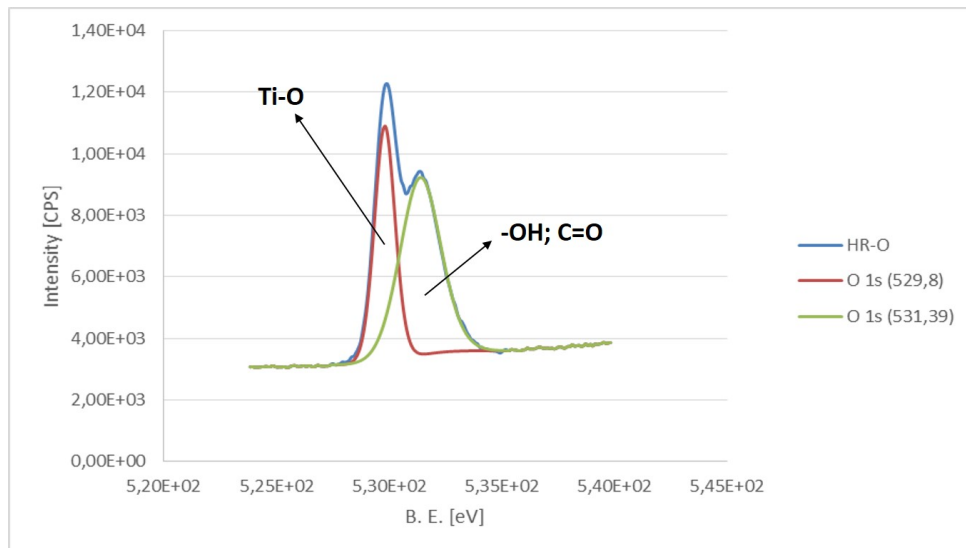


Figure 5.51: HR oxygen spectrum for polished Ti functionalized with keratin (1% wt)

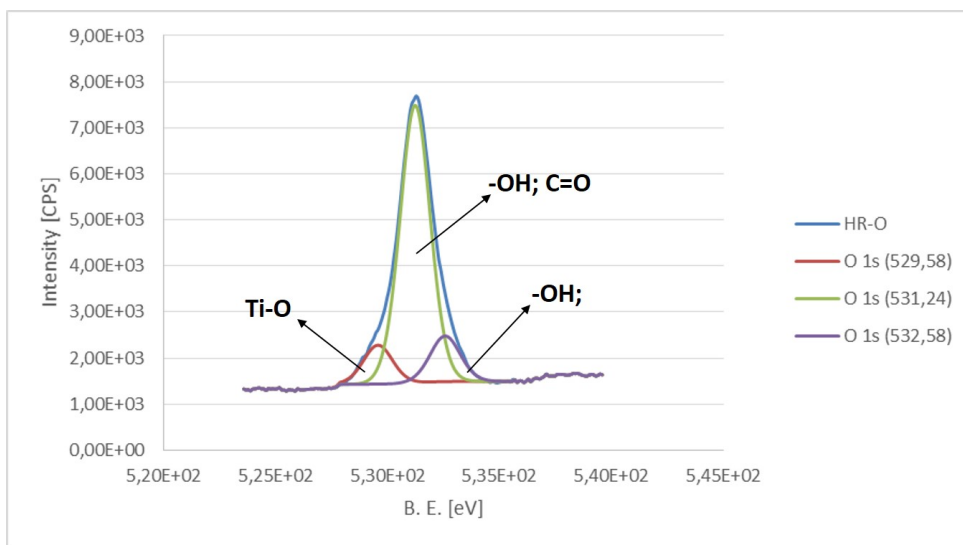


Figure 5.52: HR oxygen spectrum for plasma-treated Ti functionalized with keratin (1% wt)

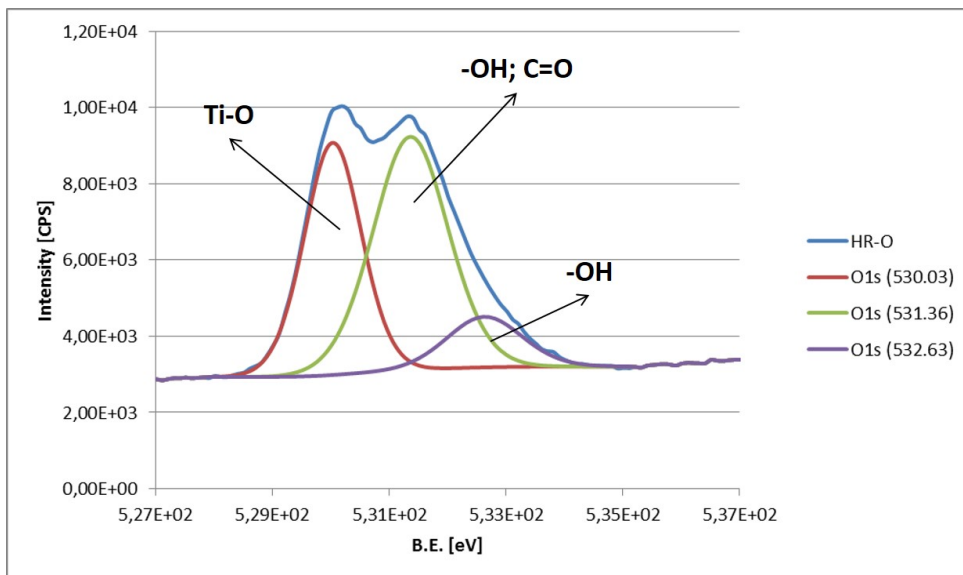


Figure 5.53: HR oxygen spectrum for UV-treated Ti functionalized with keratin (1% wt)

In Table 5.8 are shown the percentages of area for each sample. It is possible to see that, for polished Ti and plasma- and UV- treated Ti, the relative abundance for Ti-O, C-O, C=O, -OH is similar.

Considering plasma-treated Ti with keratin coating, it is possible to note a very small peak attributed to Ti-O, due probably to the thickness of the coating, whereas the percentage of C=O double bond and O-H hydroxyl groups is higher, derived probably by the presence of keratin coating.

Regarding functionalized samples, the presence of keratin causes peak's area for C=O, C-O and -OH higher than that of samples without keratin. This means that a small layer of keratin on Ti surfaces is present, confirming the success of functionalizing process.

Table 5.8: Percentages areas for HR oxygen spectra

	Energy Binding [eV]	Area [%]
<b>Polished Ti</b>	529,91	61,8
	530,78	25,1
	532,18	13,1
<b>Ti + plasma</b>	529,9	63,61
	530,66	19,74
	532	16,65
<b>Ti + UV</b>	530,06	61,7
	530,99	20,3
	532,16	18
<b>Ti + plasma + Ker coating (3% wt)</b>	536,45	2,1
	532,53	27,2
	531,5	69,6
	537,92	1,1
<b>Polished Ti + keratin (1%)</b>	529,8	40,1
	531,39	59,9
<b>Ti + plasma + ker (1% wt)</b>	529,58	10,6
	531,24	76,8
	532,58	12,6
<b>Ti + UV + ker (1% wt)</b>	530,03	38,4
	531,36	50,6
	532,63	11

Regarding nitrogen, two specific peaks are identified, corresponding to a certain nitrogen bonds. Table 5.9 shows the Energy Binding values associated to different types of bond (116) (117) (118).

Table 5.9: Energy Binding for different chemical bonds for N

Binding Energy [eV]	Type of bond
399,91	-NH <sub>2</sub>
402,1	-NH <sub>3</sub> <sup>+</sup>

In Figure 5.54, Figure 5.55, Figure 5.56, Figure 5.57, Figure 5.58, Figure 5.59, Figure 5.60 are shown the HR spectra of N for the different samples.

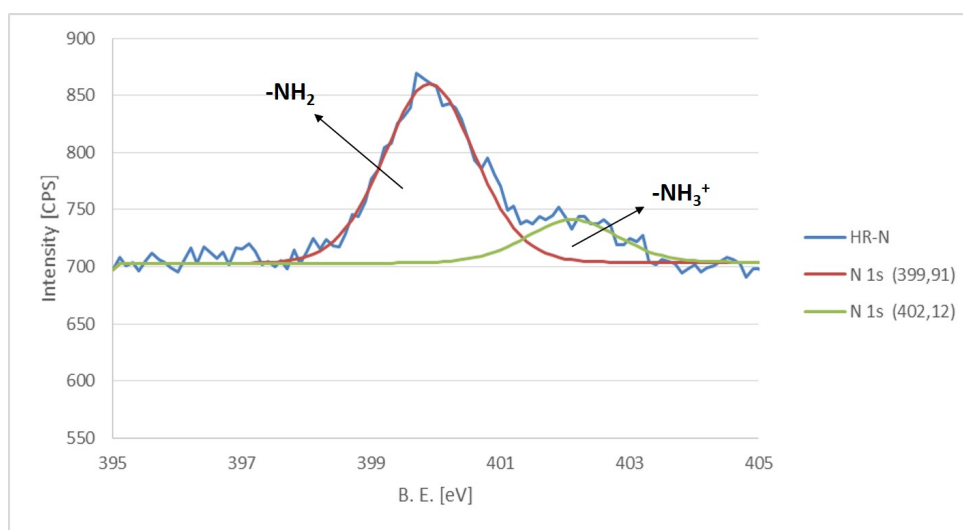


Figure 5.54: HR nitrogen spectrum for polished Ti

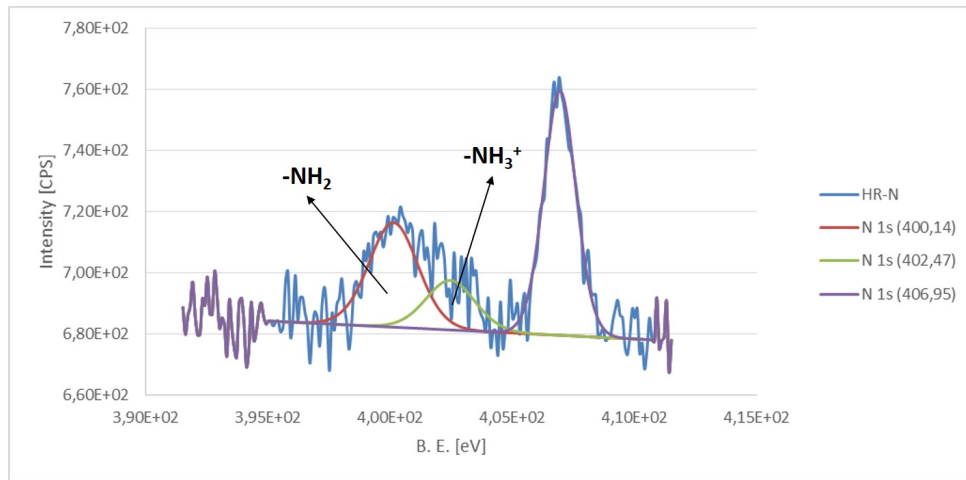


Figure 5.55: HR nitrogen spectrum for plasma-treated Ti

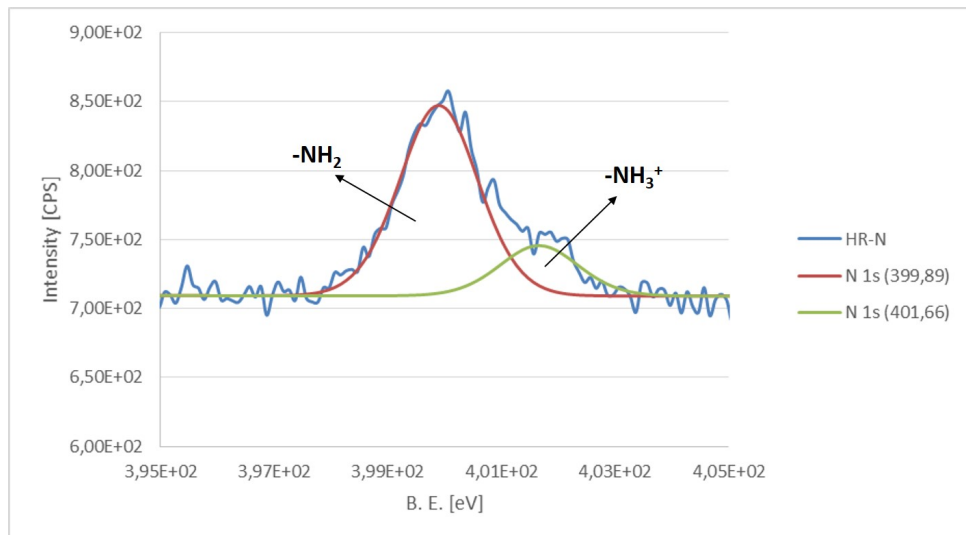


Figure 5.56: HR nitrogen spectrum for UV-treated Ti

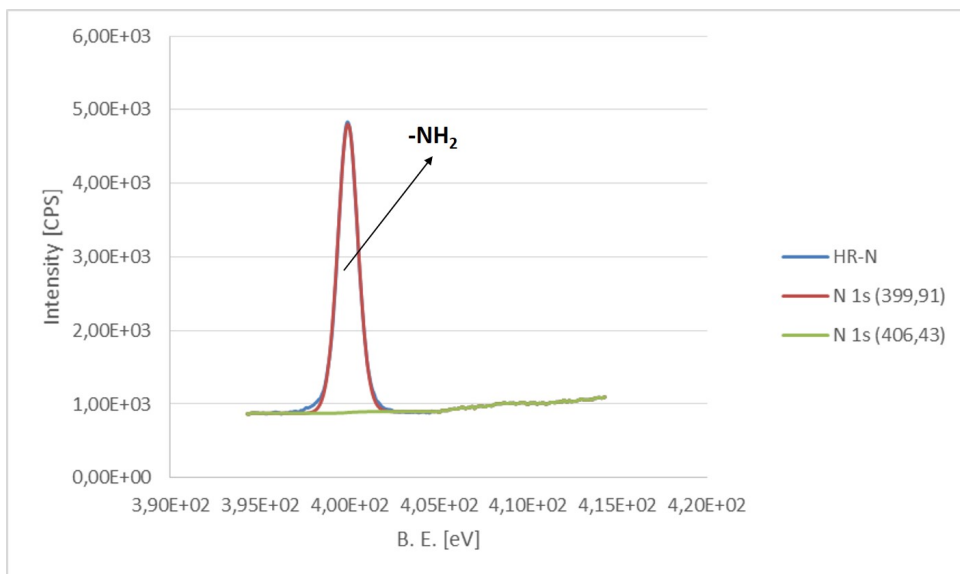


Figure 5.57: HR nitrogen spectrum for plasma-treated Ti + keratin coating (3% wt)

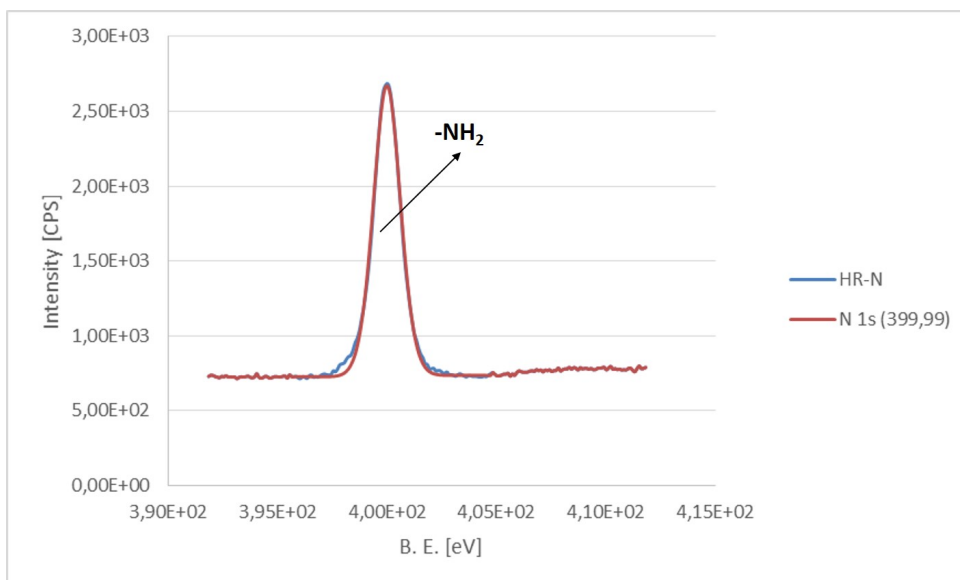


Figure 5.58: HR nitrogen spectrum for polished Ti functionalized with keratin (1% wt)

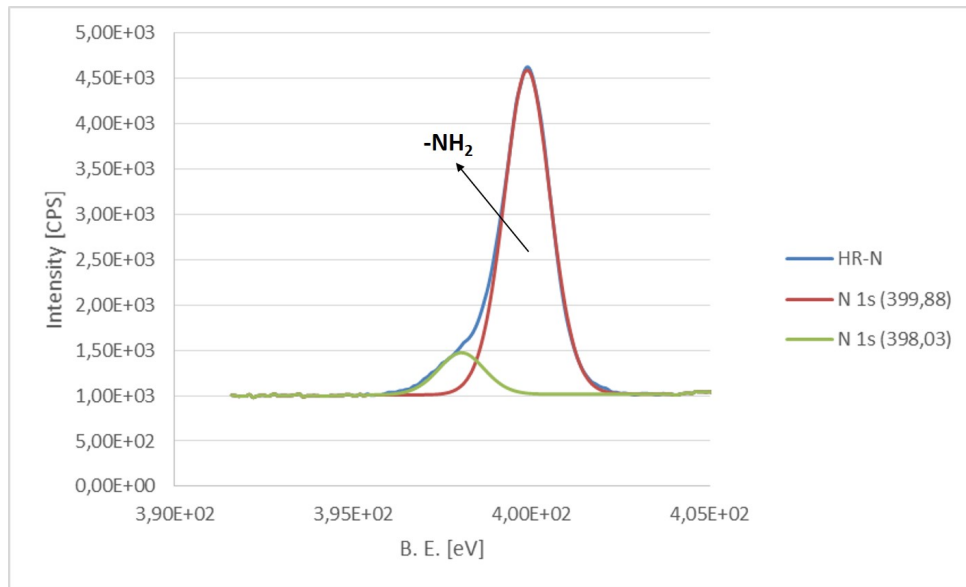


Figure 5.59: HR nitrogen spectrum for plasma-treated Ti functionalized with keratin (1% wt)

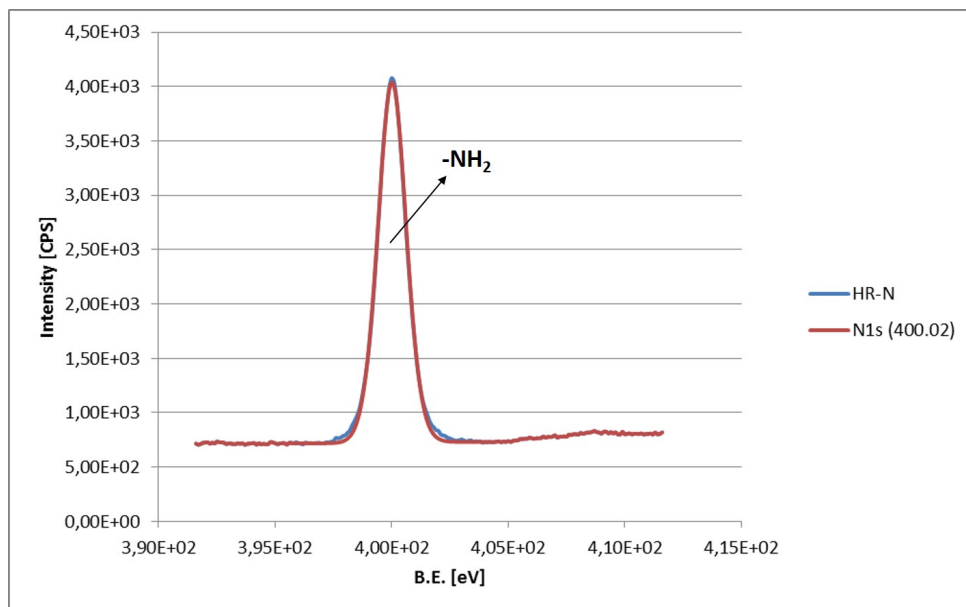


Figure 5.60: HR nitrogen spectrum for UV-treated Ti functionalized with keratin (1% wt)

In Table 5.10 are shown the percentages of areas for each sample. As it is possible to see, the functional groups present on the sample surfaces are  $-NH_2$  (400 eV) and  $NH_3^+$  (402 eV). Evaluating the areas of the peaks for each sample, it is possible to note that these areas are similar for polished, and UV-treated Ti, whereas it changes significantly considering samples with keratin coating or functionalized: for Ti surface it is possible to note the presence of both bonds, with a higher amount for  $-NH_2$  rather than  $NH_3^+$ , while for treated Ti covered or functionalized, the  $NH_3^+$  peak does not exist. In these cases, the abundance of  $-NH_2$  peak depends probably on the presence of cysteine or glycine, or other amino acids that constitute the polypeptide chains. The absence of  $NH_3^+$  on keratin coating in acidic region confirms the results found by zeta-potential analysis.

Table 5.10: Percentages areas for HR nitrogen spectra

	Energy Binding [eV]	Area [%]
<b>Polished Ti</b>	399,91	80,7
	402,12	19,3
<b>Ti + plasma</b>	400,14	33,3
	402,47	15,7
	406,95	51
<b>Ti + UV</b>	399,89	79
	401,66	21
<b>Ti + plasma + Ker coating (3% wt)</b>	399,91	100
	406,43	0
<b>Polished Ti + keratin (1%)</b>	399,9	100
<b>Ti + plasma + ker (1% wt)</b>	399,88	88,5
	398,03	11,5
<b>Ti + UV + ker (1% wt)</b>	400,02	100

Regarding carbon, different specific peaks are identified, corresponding to a certain carbon bonds. Table 5.11 shows the Energy Binding values associated to different types of bond (116) (117) (118).

Table 5.11: Energy Binding for different chemical bonds for C

Binding Energy [eV]	Type of bond
284,8	C-C; C-H; C-S
286,24	C-O; C-N; C-OH
288,17	C=O
288,87	O-C=O

In Figure 5.61, Figure 5.62, Figure 5.63, Figure 5.64, Figure 5.65, Figure 5.66, Figure 5.67 are shown the HR spectra of C for the different samples.

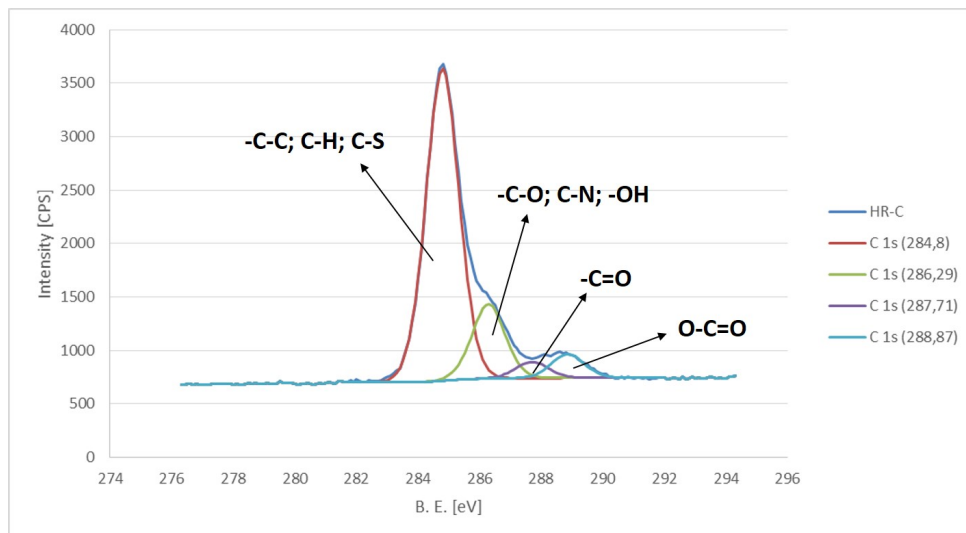


Figure 5.61: HR carbon spectrum for polished Ti

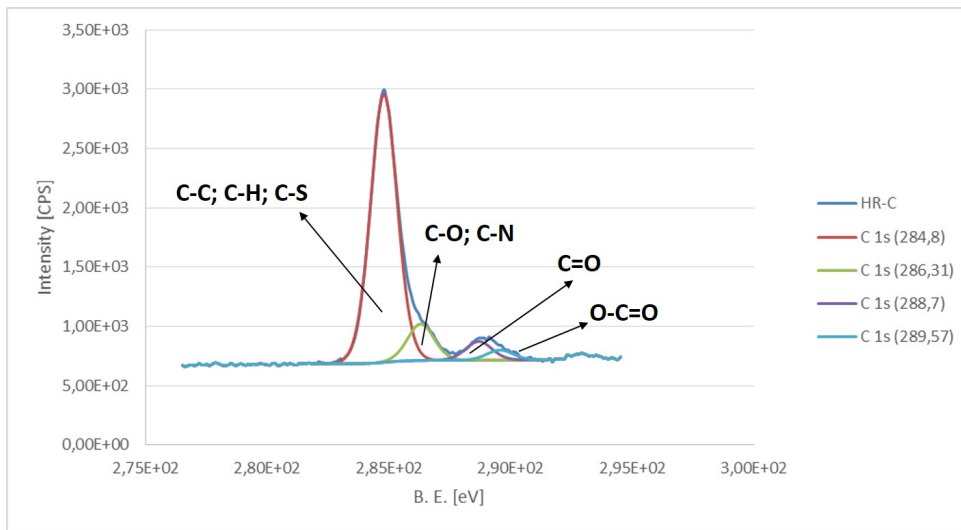


Figure 5.62: HR carbon spectrum for plasma-treated Ti

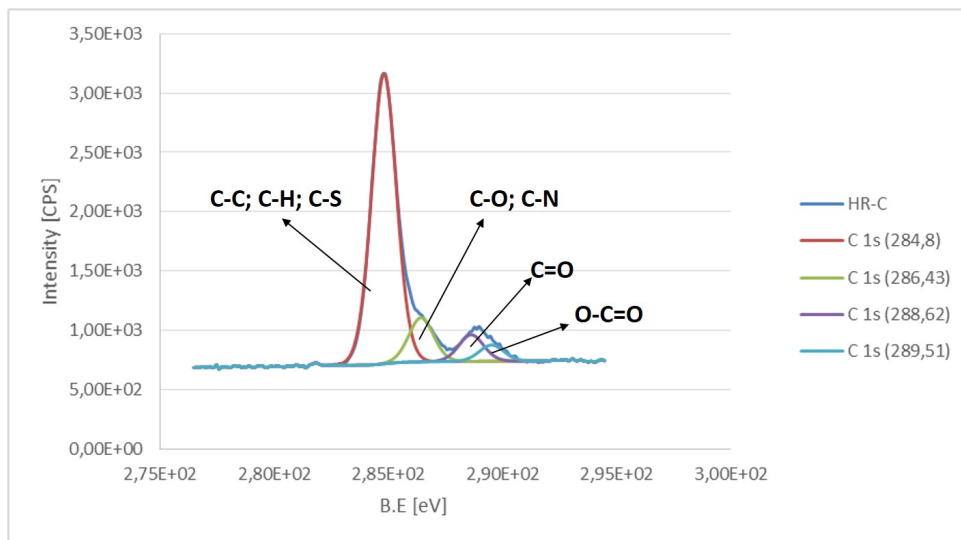


Figure 5.63: HR carbon spectrum for UV-treated Ti

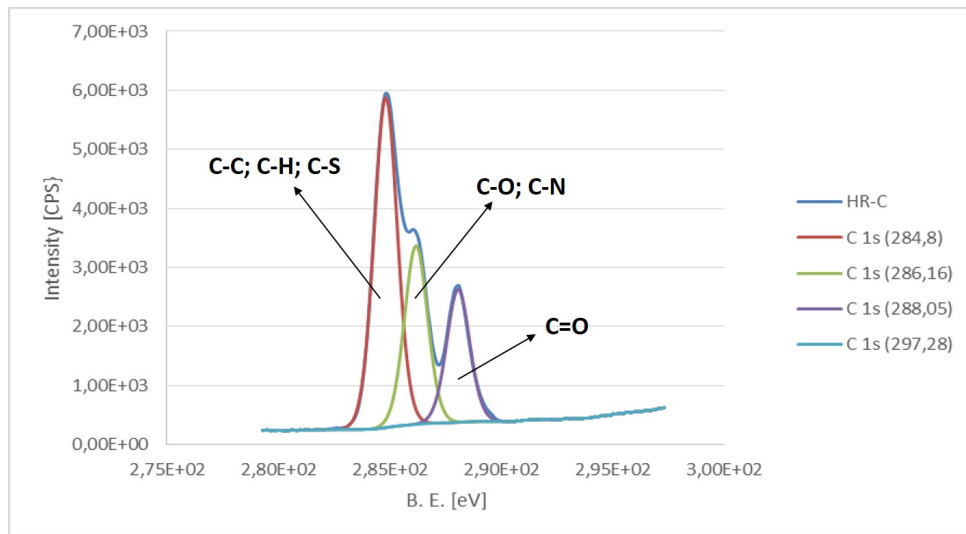


Figure 5.64: HR carbon spectrum for plasma-treated Ti + keratin coating (3% wt)

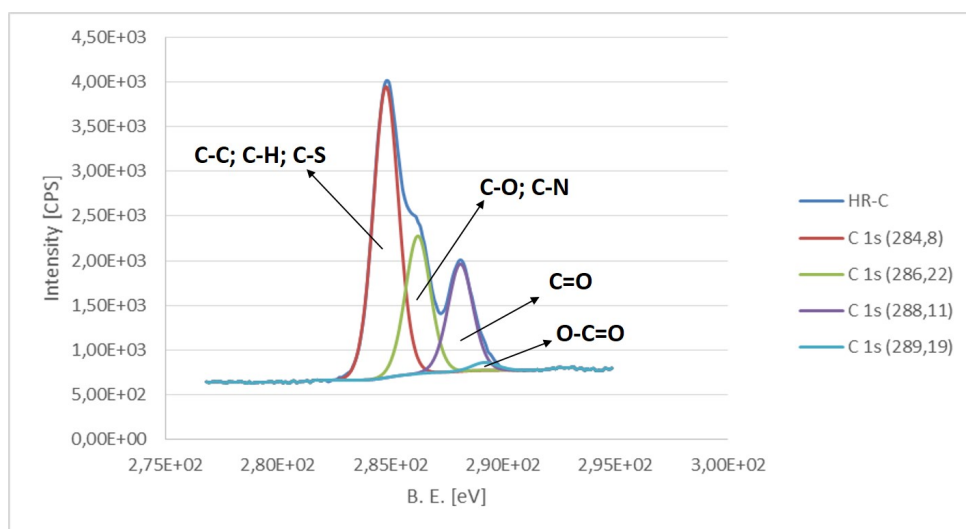


Figure 5.65: HR carbon spectrum for polished Ti functionalized with keratin (1% wt)

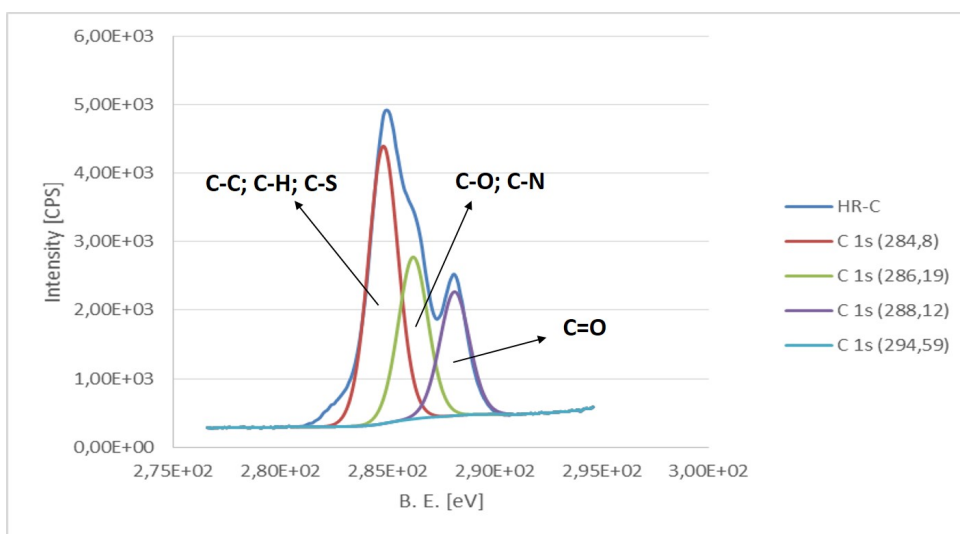


Figure 5.66: HR carbon spectrum for plasma-treated Ti functionalized with keratin (1% wt)

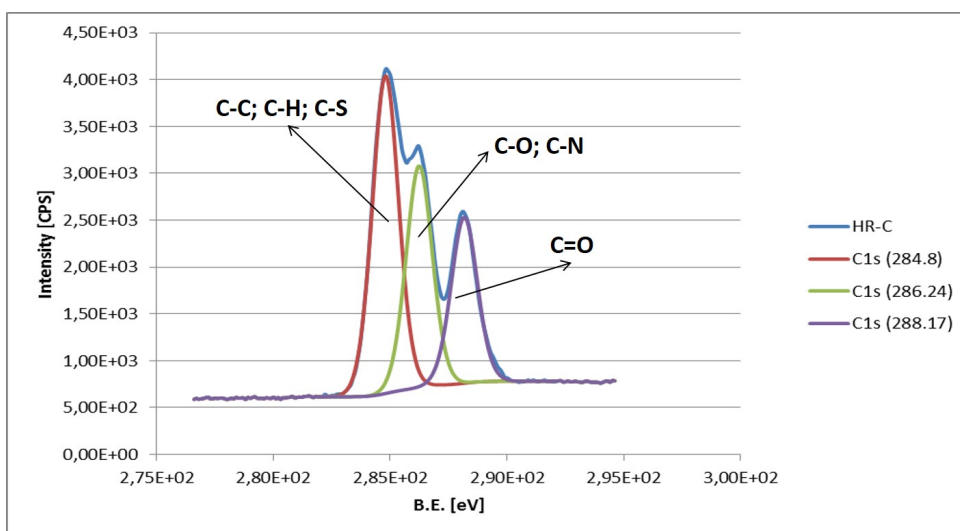


Figure 5.67: HR carbon spectrum for UV-treated Ti functionalized with keratin (1% wt)

In Table 5.12 are shown the percentages of area for each sample. In this case, the C-C, C-H, C-O and C=O bonds present are attributable to the presence of carbon as contaminant, but they are present also in the primary structure of keratin, in addition, also C-S and C-N bonds characterized keratin structure: the contribution to this peaks is twofold.

From the figures, it is possible to see a relative abundance of C-C, C-H and C-S for all the samples, whereas the peak which correspond to C-N bonds is higher in Ti covered and functionalized, because, in this cases, the keratin contribution have to be taken into account.

Regarding C=O double bond, it is possible to see that it is present in all the samples, but in different percentages: its contribution to the peak is visible in more evident way for samples which are covered or functionalized with keratin, so the abundance amount of C=O is due to the presence of keratin.

Table 5.12: Percentages areas for HR carbon spectra

	Energy Binding [eV]	Area [%]
<b>Polished Ti</b>	//	//
<b>Ti + plasma</b>	169,14	66,7
	170,34	33,3
<b>Ti + UV</b>	399,89	79,1
	401,66	20,9
<b>Ti + plasma + Ker coating (3% wt)</b>	169,26	21,6
	170,46	10,8
	168,26	27,1
	169,46	13,5
	163,48	14,5
	164,68	7,3
	161,4	3,5
	162,6	1,7
<b>Polished Ti + keratin (1%)</b>	168,28	44,8
	169,48	22,4
	163,43	21,9
	164,63	10,9
<b>Ti + plasma + ker (1% wt)</b>	168,19	35,8
	169,39	17,9
	163,54	30,9
	164,74	15,4
<b>Ti + UV + ker (1% wt)</b>	168,22	36,3
	169,42	18,2
	163,63	30,3
	164,83	15,2

Regarding titanium, different specific peaks are identified, corresponding to a certain titanium bonds, but as it is possible to see, for all the sample two are the most important. Table 5.13 shows the Energy Binding values associated to different types of bond (119).

Table 5.13: Energy Binding for different chemical bonds for Ti

Binding Energy [eV]	Type of bond
458,62	Ti 2p <sub>3/2</sub>
464,34	Ti 2p <sub>1/2</sub>

In Figure 5.68, Figure 5.69, Figure 5.70, Figure 5.71 and Figure 5.72 are shown the HR spectra of Ti for the different samples.

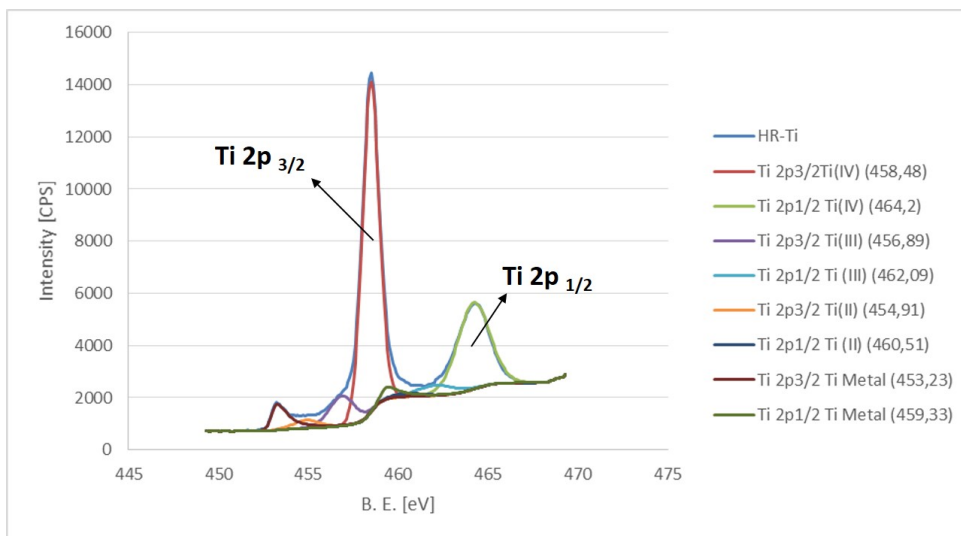


Figure 5.68: HR titanium spectrum for Polished Ti

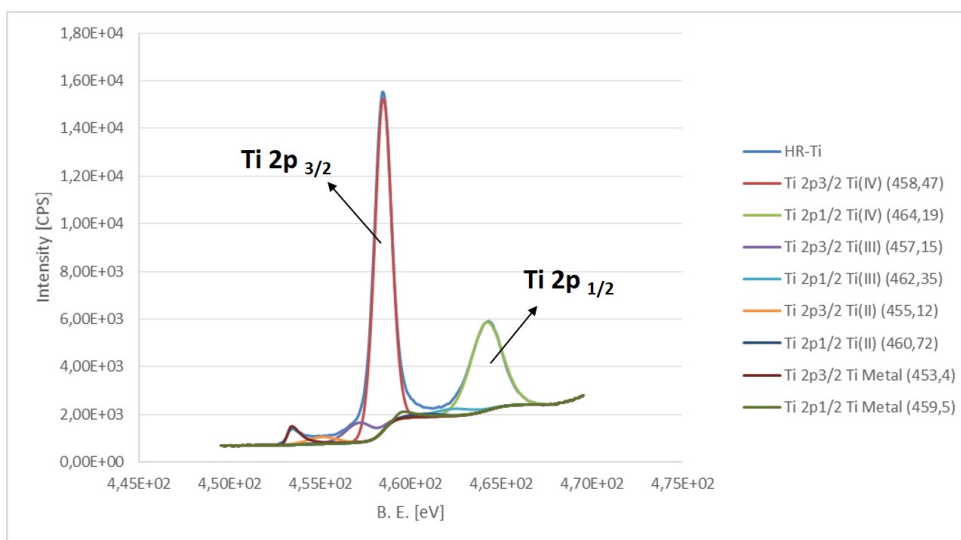


Figure 5.69: HR titanium spectrum for plasma-treated Ti

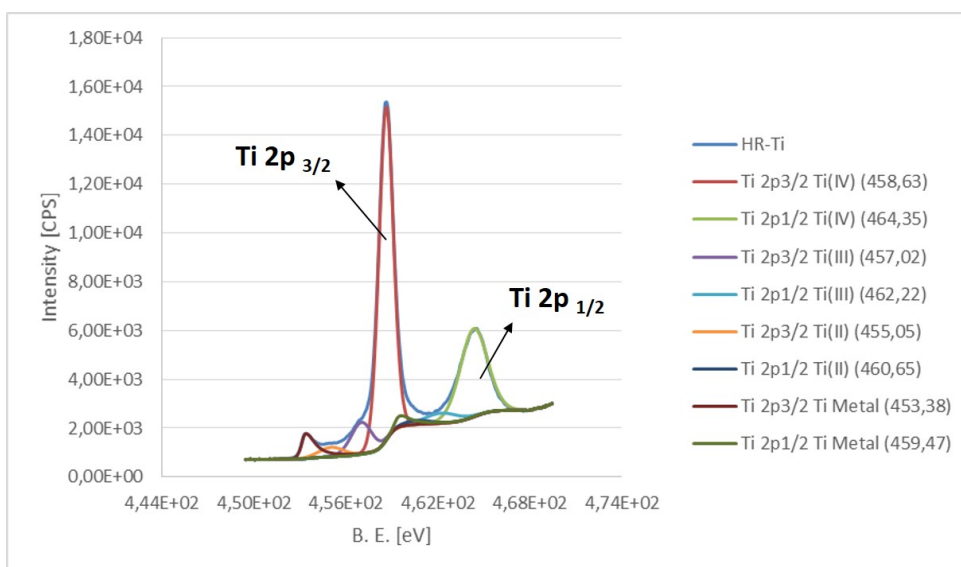


Figure 5.70: HR titanium spectrum for UV-treated Ti

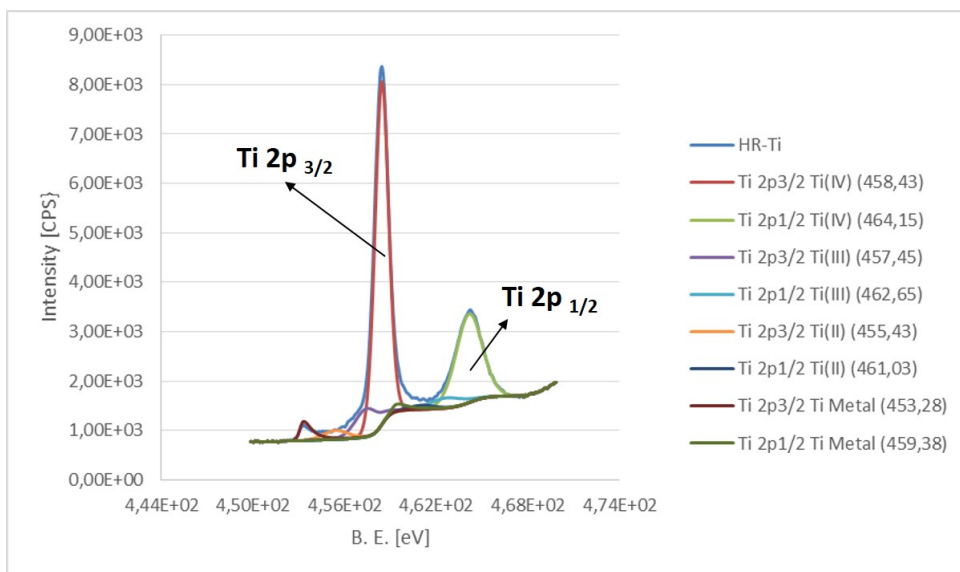


Figure 5.71: HR titanium spectrum for polished Ti functionalized with keratin (1% wt)

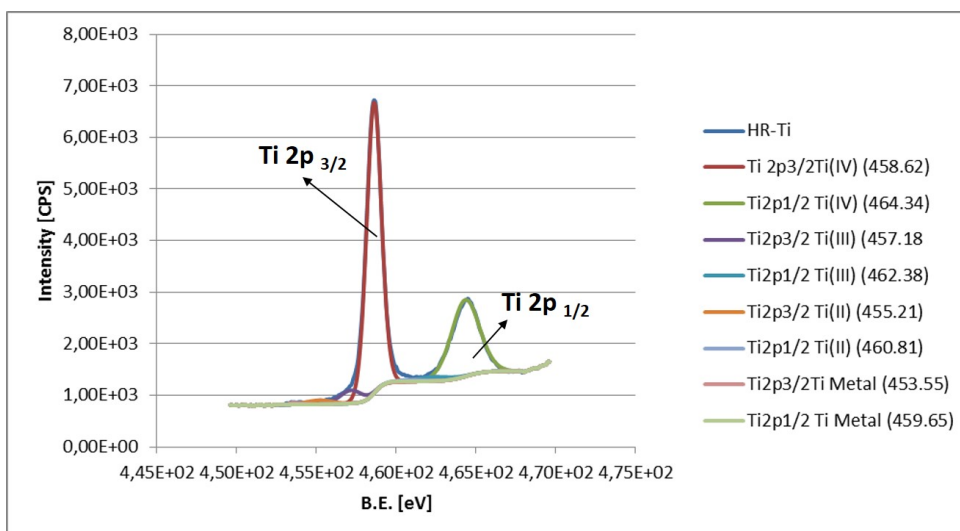


Figure 5.72: HR titanium spectrum for UV-treated Ti functionalized with keratin (1% wt)

In Table 5.14 are shown the percentages of area for each sample. As it is possible to see, the graph is characterized by a lot of peaks, but for each sample, two are the most important: peak at 458 eV and at 464 eV, corresponding to Ti 2p<sub>3/2</sub> and to Ti 2p<sub>1/2</sub>. They are related to Ti<sup>4+</sup> in the TiO<sub>2</sub> bonds, it is probably correlated with the presence of oxygen on the titanium surface. The other peaks differ from each other for very little energy values. For the plasma-treated sample coated with keratin at 3% wt, it was impossible to obtain a HR titanium spectrum, because the signal was too weak. As already said, it can be explained considering that, in this case, the coating has a thickness higher than the depth of the XPS analysis, for this reason, the electron beam did not reaches the titanium surface, so it was impossible to detect a signal. It is also possible to see that for the plasma-treated titanium functionalized with keratin at 1%, the signal of titanium was too weak to obtain a curve.

Table 5.14: Percentages areas for HR titanium spectra

	Energy Binding [eV]	Area [%]
Polished Ti	458,48	52,1
	464,2	26,1
	456,89	7,4
	462,09	3,7
	454,91	2,1
	460,51	1
	453,23	5,1
	459,33	2,5
Ti + plasma	458,47	56,2
	464,19	28,1
	457,15	5,5
	462,35	2,7
	455,12	2
	460,72	1
	453,4	3
	459,5	1,5
Ti + UV	458,63	52,2
	464,35	26,1
	457,02	7,3
	462,22	3,6
	455,05	2,6
	460,65	1,3
	453,38	4,6
	459,47	2,3
Ti + plasma + Ker coating (3% wt)	//	//
Polished Ti + keratin (1%)	458,43	53,3
	464,15	26,7
	457,45	7,6
	462,65	3,8
	455,43	2,5
	461,03	1,3
	453,28	3,2
	459,38	1,6
Ti + plasma + ker (1% wt)	//	//
Ti + UV + ker (1% wt)	458,62	60,8
	464,34	30,4
	457,18	4
	462,38	2
	455,21	1,5
	460,81	0,7
	453,55	0,4
	459,65	0,2

Regarding sulfur, different specific peaks are identified, corresponding to a certain sulfur bonds. Generally, two peaks are well-identified, which are the most important. Table 5.15 shows the Energy Binding values associated to different types of bond (116) (117) (118).

Table 5.15: Energy Binding for different chemical bonds for S

Binding Energy [eV]	Type of bond
163,63	S-S
168	S-O

In Figure 5.73, Figure 5.74, Figure 5.75, Figure 5.76, Figure 5.77, Figure 5.78 are shown the HR spectra of S for the different samples.

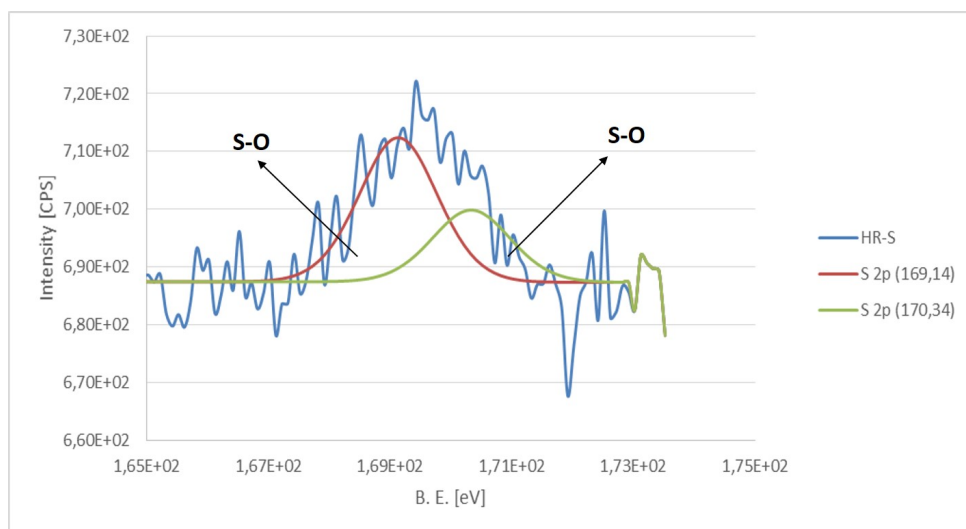


Figure 5.73: HR sulfur spectrum for plasma-treated Ti

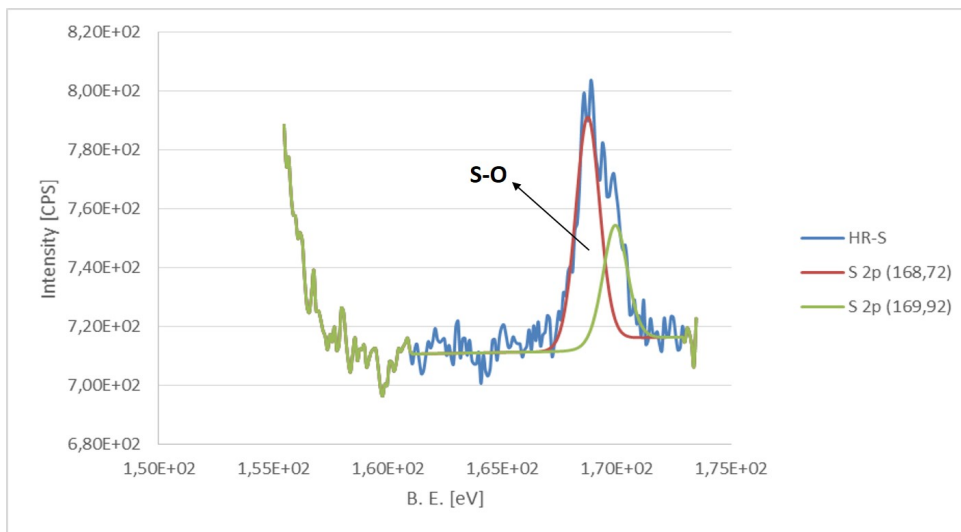


Figure 5.74: HR sulfur spectrum for UV-treated Ti

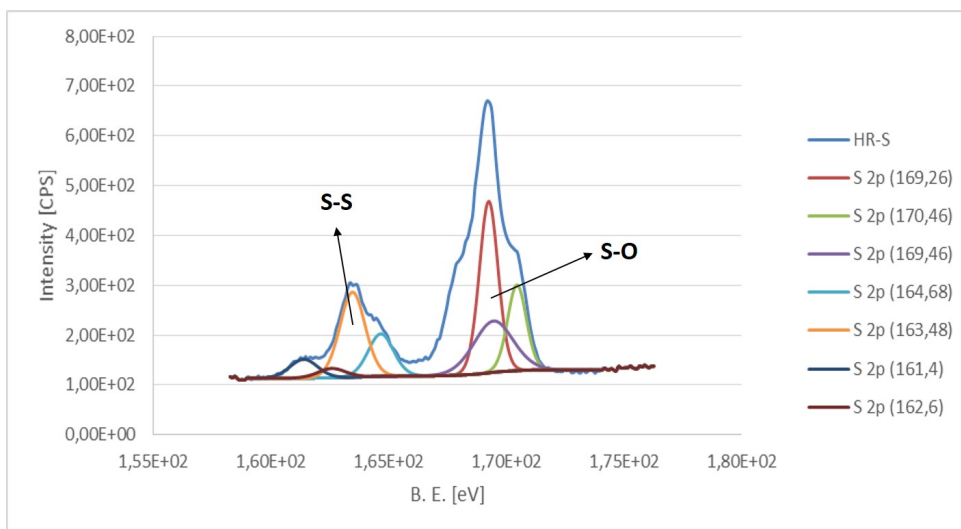


Figure 5.75: HR sulfur spectrum for plasma-treated Ti + keratin coating (3% wt)

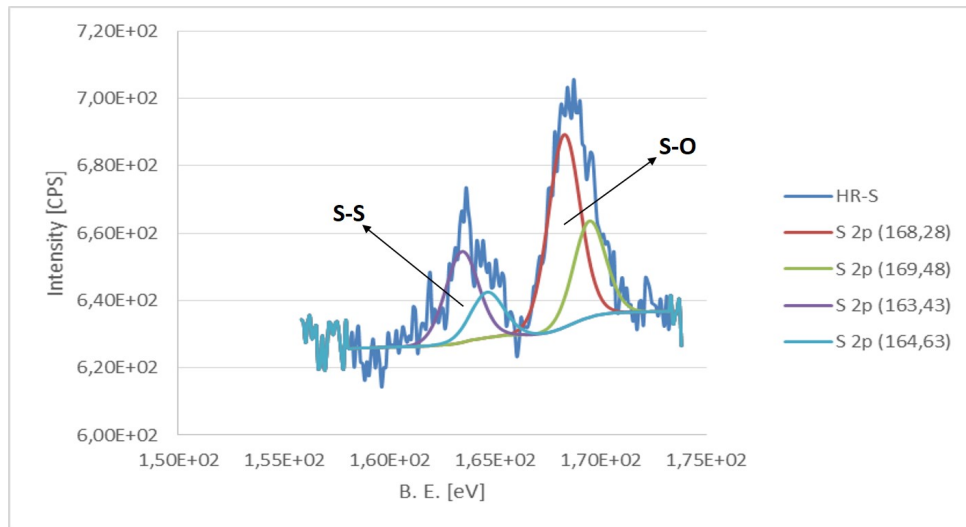


Figure 5.76: HR sulfur spectrum for polished Ti functionalized with keratin (1% wt)

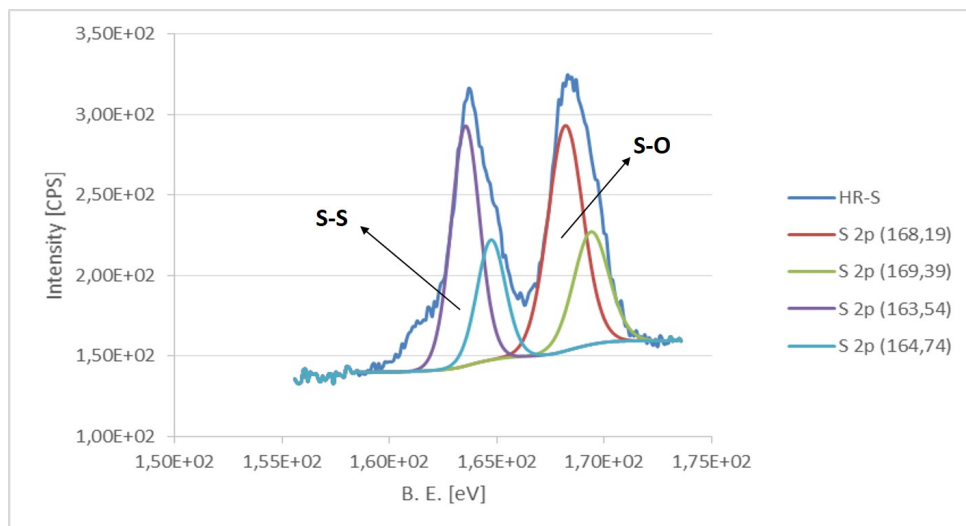


Figure 5.77: HR sulfur spectrum for plasma-treated Ti functionalized with keratin (1% wt)

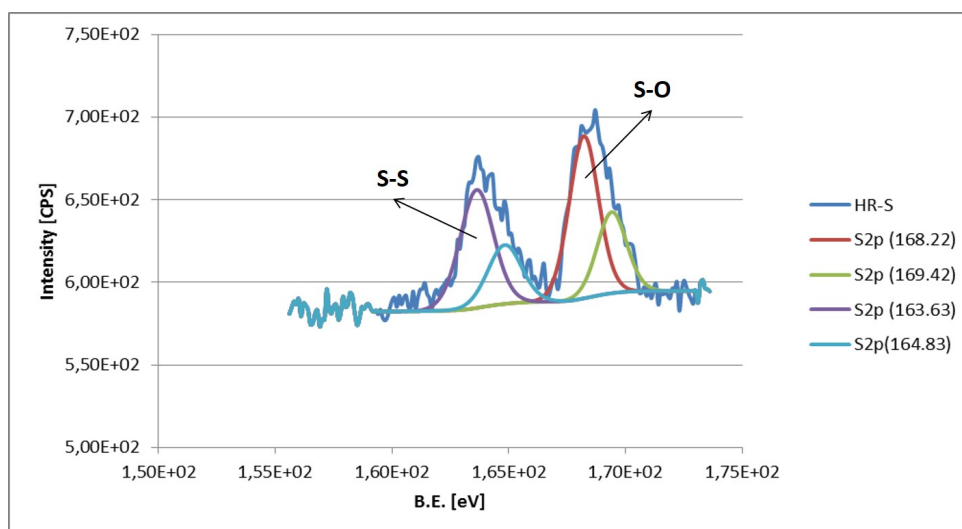


Figure 5.78: HR sulfur spectrum for UV-treated Ti functionalized with keratin (1% wt)

In Table 5.16 are shown the percentages of area for each sample. Generally, two peaks are well known: that attributed to S-O bond (168 eV) and that attributed to S-S bond (163 eV). As it is possible to see, on polished Ti there is no type of sulfur bond, the signal was too weak that it was impossible to define an HR spectrum and the different peaks. In addition, for most of the samples, the spectra exhibit a noisy signal, due probably to the weakness of the signal. As it is possible to note, for the samples uncovered the only bond present is that of S-O, whereas the S-S peak appears in the spectra of Ti with coating or functionalized: it can be explained considering the fact that keratin chain is characterized by a high abundance of disulfide bonds, so this is the greater contribution to these peaks.

Table 5.16: Percentages areas for HR sulfur spectra

	Energy Binding [eV]	Area
<b>Polished Ti</b>	529,91	61,8
	530,78	25,1
	532,18	13,1
<b>Plasma-treated Ti</b>	529,9	63,61
	530,66	19,74
	532	16,65
<b>UV-treated Ti</b>	530,06	61,7
	530,99	20,3
	532,16	18
<b>Ti + plasma + Ker coating (3% wt)</b>	536,45	2,1
	532,53	27,2
	531,5	69,6
	537,92	1,1
<b>Polished Ti + keratin (1%)</b>	529,8	40,1
	531,39	59,9
<b>Plasma-treated Ti + ker (1% wt)</b>	529,58	10,6
	531,24	76,8
	532,58	12,6
<b>UV-treated Ti + ker (1% wt)</b>	530,03	38,4
	531,36	50,6
	532,63	11

## 5.9 Roughness of titanium cylinder

The roughness was measured on the titanium bars. The aim was to evaluate surface features of the samples, in order to understand if they can be used as dental implant structure. For this type of application, the surface roughness should be lower than  $0,2 \mu\text{m}$ , in order to limit bacteria contamination and to give a topographical stimuli to fibroblast to growth, important for an effective tissue healing (120).

Roughness measurements were carried out on the bars before and after surface treatments. Several measurements were conducted, and the mean value and the standard deviation were calculated. It was found that the samples had a mean roughness of  $0,21 \mu\text{m}$ , and a deviation standard of  $0,11 \mu\text{m}$ .

After the polishing and the treatment to make surface rough, roughness is lower than the previous case, in fact the mean value was  $0,16 \mu\text{m}$  and a deviation standard of  $0,02 \mu\text{m}$ . A comparison of the surfaces of the bars before and after treatments is possible to see in Figure 5.79, in which are represented the mean values of roughness in a bar graph.

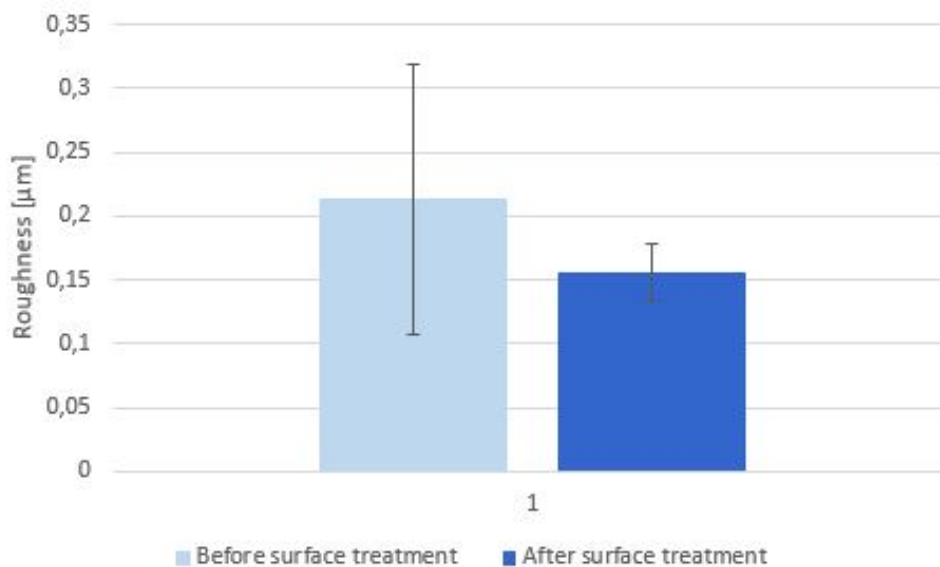


Figure 5.79: Surface roughness of titanium bars before and after surface treatments

Then a confocal laser scanning microscope was used, in order to obtain images of the surface after treatments. In Figure 5.80 (a) is shown the lateral surface of the cylinder, obtained in bright field: it is possible to see the signs, caused by treatments made to obtain rough surface. A topographic image of the same surface is shown in Figure 5.80 (b).

Then the value of  $S_a$  and  $R_a$  were calculated:  $S_a$  indicates the roughness evaluated on a surface, while  $R_a$  represents the roughness evaluated on a line. In this case,  $S_a$  value is of  $0,27 \mu\text{m}$ . Regarding  $R_a$ , the value found is  $0,82 \mu\text{m}$ :  $R_a$  value is higher if the line on which the measure is conducted go through topographic inhomogeneities. In Figure 5.81 is shown the measure of the roughness on a line.

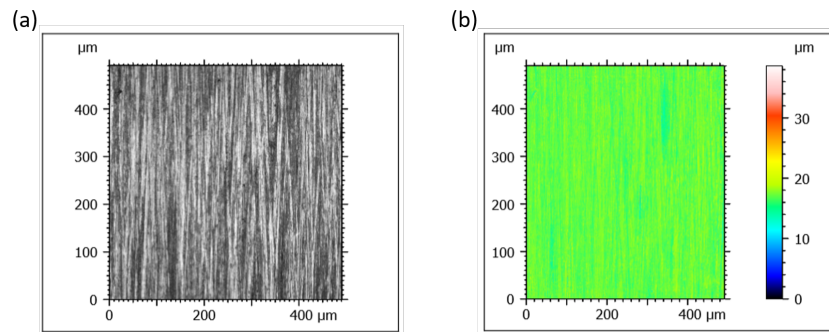


Figure 5.80: (a) Image of the lateral surface of the cylinder in bright field, (b) Topographic image of the roughness of cylinder

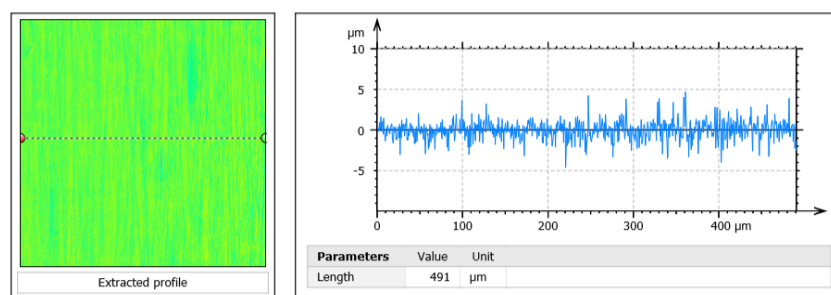


Figure 5.81: Measure of the roughness on a line

After being cut and plasma-treated, a deposition of keratin nanofibers around the surface of the cylinder was performed at CNR-IPCB Institute of Polymers Composites and Biomaterials, Napoli.

The result is shown in Figure 5.82, at two different magnification: 1600 x and 600 x. The deposition was conducted in low vacuum, in order to avoid sputtering phenomena on the sample. The nanofibers deposited are well distinguishable with respect to the substrate. They present an heterogeneity in the deposition on the surface of the cylinder, due probably to the method of deposition used: the sample does not rotate around its own axis, but around the axis of the collector.

On this system biological tests will be carried out, in order to evaluate how plasma influences the nanofibers behaviour and how cells adhesion is affected by the presence of keratin nanofibers arranged around a cylindrical samples.

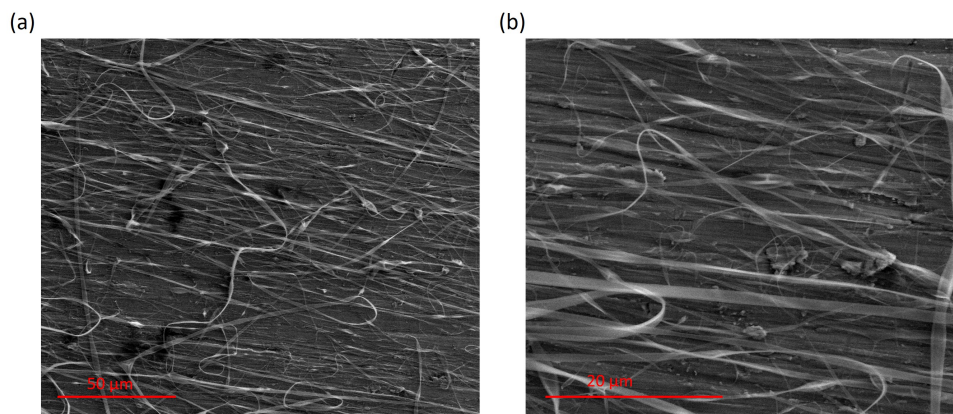


Figure 5.82: SEM image of nanofibers deposited on lateral surface of Ti cylinder at (a) 1600x and (b) 600x

# Conclusions

The aim of this work is to find the better surface treatment, which improve keratin adhesion. Different keratin solutions are prepared:

- keratin solution at 7% wt;
- keratin solution at 3% wt;
- keratin solution at 1% wt;
- Electrospun keratin nanofibers.

Surface treatments carried out on samples were:

- Polishing;
- Plasma treatment;
- UV treatment.

It was evident that keratin solution at 7% wt produced a non homogeneous coating, while that obtained with keratin solution at 3% wt was homogenous and thin, with a thickness of about 6-10  $\mu\text{m}$ . Tape test reveals that plasma treatment and UV irradiation improve adhesion of keratin to titanium substrate. Despite optimal results of UV treatments, it was decided to conducted others analysis on plasma-treated surface for its role in decontamination and activation on surface.

Scratch test was performed on polished Ti and on plasma-treated Ti with keratin coating, showing a particular behavior of keratin coating. Frictional Coefficient was measured, and it was shown that for keratin coating it was lower than that of titanium.

To test hydrophilic/hydrophobic properties wettability tests were conducted: they show that keratin coating make titanium surface more hydrophilic. It was also evaluated differences in wettability properties between untreated and plasma-treated titanium sample in contact with keratin solution at 3% wt: on plasma-treated sample, the contact angle decreases, in this way coating creates stronger bonds with substrate, and this influences adhesion properties.

Then stability in water was analyzed: samples with keratin coating were imersed in water and after 1, 7, 14, 21, 28 days, their appearance was analyzed. It was possible to see how keratin coating changes appearance after one day, infact it seemed to have swollen, but in the following days it has not undergone significant transformation. After drying at room temperature its appearance changes: keratin became a very little film and lost adhesion in some regions.

From a zeta-potential test, conducted on polished Ti, plasma-treated Ti and plasma-treated Ti with keratin coating, it was found that the surface has negative charge and a IEP in the range of pH between 3,5 and 5,5.

From an XRD analysis conducted on keratin at 3% and 7% wt in water, was found the typical peak of the beta sheet of keratin. An FT-IR analysis was conducted: graphs obtained show the typical peak of keratin for coated samples, while no signals were detechted in functionalized Ti,

but XPS analysis gives important information about this sample. It shows that plasma- and UV- treated Ti surfaces were well functionalized by keratin solution at 1% wt. Thanks to this analysis, it was also possible to confirm the role of plasma treatments in decontamination process.

Adhesive properties were studied also for keratin nanofibers deposited by electrospinning process at Centro Nazionale Ricerche CNR-ISMAR, Biella. Tape test gives bad results: all the coating was removed during the test. A FESEM analysis show the reason: no fibers were deposited on titanium surface, but the presence of numerous beads causes very weak bond at the interface between keratin and titanium.

The cylinder sample was used: after evaluating the roughness of titanium bars before and after surface treatments, in order to obtain a determined value of roughness ( $< 2 \mu\text{m}$ ), electrospun nanofibers were deposited on the lateral surface of the sample, and a SEM analysis show how they are arranged on the surface.

In conclusion, it is possible to see that treating titanium surface with plasma can improve adhesion of keratin coating on dental implant: in this way, it is possible to exploit its stimuli to fibroblast proliferation.

Future works could be focused on adhesion properties of keratin nanofibers arranged on lateral surface of dental implant, and its influence on bacterial proliferation.

# Bibliography

- [1] Wang B, Yang W, McKittrick J, Meyers MA. *Keratin: Structure, mechanical properties, occurrence in biological organisms, and efforts at bioinspiration*, 2015, University of California, San Diego, La Jolla, United States;
- [2] Staron P, Banach M, Kowalski Z. *Keratin – origins, properties, application*, Institute of Inorganic Chemistry and Technology, Cracow University of Technology, Cracow. CHEMIK 2011, 65, 10, 1019-1026;
- [3] Bragulla H, Homberger D.G. *Structure and functions of keratin proteins in simple, stratified, keratinized and cornified epithelia*. 2015, University of California, San Diego, La Jolla, United States;
- [4] Khosa M, Ullah A. *A Sustainable Role of Keratin Biopolymer in Green Chemistry: A Review*. Journal of Food Processing & Beverages, September 2013 Vol.:1, Issue:1;
- [5] <https://www.newworldencyclopedia.org/entry/Keratin>;
- [6] Atri H, Bidram E, Dunstan DE. *Reconstituted Keratin Biomaterial with Enhanced Ductility*. Materials 2015, 8(11), 7472-7485;
- [7] <https://en.wikipedia.org/wiki/Keratin>;
- [8] Jacob J T, Coulombe P A, Kwan R, Omary M B. *Types I and II Keratin Intermediate Filaments*. Cold Spring Harb Perspect Biol. 2018 Apr 2;
- [9] Szewciw L, de Kerckhove D G, Grime G W, Fudge D. *Calcification provides mechanical reinforcement to whale baleen keratin*. Proceeding of the Royal Society B: Biological Sciences 277(1694): 2597-605, April 2010;
- [10] Bhavsar P, Zoccola M, Patrucco A, Montarsolo A, Mossotti R, Rovero G, Giansetti M, Tonin C. *Superheated Water Hydrolysis of Waste Wool in a Semi-Industrial Reactor to Obtain Nitrogen Fertilizers*. ACS Sustainable Chemistry & Engineering, September 2016, 4 (12), pp 6722–6731;
- [11] Savige W E, Eager J, Maclaren J A, Roxburgh C and M *The S-monoxides of cystine, cystamine and homocystine*. Tetrahedron Lett., vol. 5, no. 44, pp. 3289–3293, 1964;
- [12] Yamada M, Narita S, Kondo T, Nojima M, Yamamoto R, Nishino T, Sakai C. *Process for solubilizing animal hair*. Google patent, US5276138A United States; 1964;
- [13] Eslahi N, Dadashian F, Hemmati Nejad N. *An investigation of keratin extraction from wool and feather waste by enzymatic hydrolysis*. Volume 43, 2013, issue 7, Preparative Biochemistry and Biotechnology, pp 624-648;

- [14] Wang Q Q, Zhang L, Wang Q Q, Liu J, Zhu P, Jiang Z. *Sodium sulphide extraction of human keratin*. *Ferroelectrics*, June 2018, 529:1, 105-112;
- [15] Shui-qing J, Lin Z, Haixia W, Gang C. *Study on effective extraction of keratin from human hair wastes*. *Integrated Ferroelectrics* 180(1):102-107, May 2017;
- [16] Varesano A, Vineis C, Tonetti C, Sanchez Ramirez D O, Mazzuchetti G. *Chemical and Physical Modifications of Electrospun Keratin Nanofibers Induced by Heating Treatments*. *Journal of Applied Polymer Science*, October 2013;
- [17] Yimei J, Chen J, Jingxiao L, Zhilian L, Luyao X, Siyuan D. *Extraction of keratin with ionic liquids from poultry feather*. *Separation and Purification Technology* Volume 132, 20 August 2014, Pages 577-583;
- [18] Tonin C, Zoccola M, Aluigi A, Varesano A, Montarsolo A, Vineis C, Zimbardi F. *Study on the conversion of wool keratin by steam explosion*. *Biomacromolecules* 2006, 7, 12, 3499-3504;
- [19] Yin J, Rastogi S, Terry A E, Popescu C. *Self-organization of oligopeptides obtained on dissolution of feather keratins in superheated water*. *Biomacromolecules*, vol. 8, no. 3, pp. 800–806, 2007;
- [20] Aas J A, Paster B J, Stokes L N, Olsen I, Dewhirst F E. *Defining the Normal Bacterial Flora of the Oral Cavity*. *Journal of clinical microbiology*, November 2005, Vol. 43, No. 11, p.5721-5732;
- [21] [https://en.wikipedia.org/wiki/Oral\\_microbiology](https://en.wikipedia.org/wiki/Oral_microbiology);
- [22] Trindade Gregio A M, Naval Machado M A, Lima A, Reis Azevedo L. *Saliva composition and functions: A comprehensive review*. *The Journal of contemporary dental practice*, February 208;
- [23] [https://en.wikipedia.org/wiki/Gram-positive\\_bacteria](https://en.wikipedia.org/wiki/Gram-positive_bacteria);
- [24] <https://www.google.com/patents/US6214576>;
- [25] Mikx F H M, De Jong M H. *Keratinolytic activity of cutaneous and oral bacteria*. *Infection and Immunity* 55 (1987), pp 621-625;
- [26] Riffel A, Brandelli A. *Keratinolytic bacteria isolated from feather waste*. *Brazilian Journal of Microbiolgy*, Vol. 37, No. 3, July/Sept. 2006;
- [27] Matikeviciene V, Masiliuniene D, Dtigiskis S. *Degradation of keratin containing wastes with keratinolytic activity*. *Environment, Technology, Resources* Vol. 1;
- [28] Cochis A, Ferraris S, Sorrentino R, Azzimonti B, Novara C, Geobaldo F, Truffa Giachet F, Vineis C, Varesano A, Abdelgeliel A S, Spriano S, Rimondin L. *Silver-doped keratin nanofibers preserve a titanium surface from biofilm contamination and favor soft-tissue healing*. *Journal of Material Chemistry B*, 2017, 5, 8366;
- [29] Nilforoushzhadeh M A, Ashtiani H R A, Jaffary F, Jahangiri F, Nikkhah N, Mahmoudbeyk M, Ansari Z, Zare S. *Dermal Fibroblast Cells: Biology and Function in Skin Regeneration*. *Journal of Skin and Stem Cell*, June;
- [30] Fernandes I R, Russo F B, Pignatari G C, Evangelinellis M M, Tavolari S, Muotri A R, Beltrão-Braga P C B. *Fibroblast sources: Where can we get them?* *Journal List, Cytotechnology*, 2016 Mar; 68(2): 223–228;

- [31] [https://en.wikipedia.org/wiki/Wound\\_healing](https://en.wikipedia.org/wiki/Wound_healing);
- [32] Wang S, Taraballi F, L. Poh, Woei TK. *Human keratin hydrogels support fibroblast attachment and proliferation in vitro*. Cell and Tissue Research, 347(3):795-802, January 2012;
- [33] Ferraris S, Guarino V, Cochis A, Varesano A, Cruz Maya I, Vineis C, Rimondini L, Spriano S. *Aligned Keratin submicrometric-fibers for fibroblasts guidance onto nanogrooved titanium surfaces for transmucosal implants*. Materials Letters 229 (2018) 1-4;
- [34] Esparza Y, Ullah A, Boluk Y, Wu J. *Preparation and characterization of thermally crosslinked poly(vinyl alcohol)/featherkeratin nanofiber scaffolds*. Materials and Designs 133(2017) 1-9;
- [35] Zhao X, Lui Y S, Chuen Choo C K, Sow W T, Huang C L, Woei Ng K, Poh Tan L, Chye Loo J S. *Calcium phosphate coated keratin-PCL scaffolds for potential bone tissue regeneration*. Materials Sciences and Engineering: C, April 2015, Vol 24, pp 746-753;
- [36] Hamouche H, Mahklouf S, Chaouchi A, Laghrouche M. *Humidity Sensor Based on Keratin bio Polymer Film*. Sensor and Actuators A, 282 (2018), pp 132-141;
- [37] Sanchez Ramirez D O, Carletto R A, Tonetti C, Truffa Giachet F, Varesano A, Vineis C. *Wool keratin film plasticized by citric acid for food packaging*. Food Packaging and Shelf Life Volume 12, June 2017, pp 100-106;
- [38] Fadillah G, Putri E N K, Febrianastuti S, Maylinda E V, Purnawan C. *Adsorption of Fe Ions from Aqueous Solution Using  $\alpha$ -Keratin-Coated Alginate Biosorbent*. International Journal of Environmental Science and Development, Vol. 9, No. 3, March 2018;
- [39] <https://en.wikipedia.org/wiki/Coating>;
- [40] Mattox D M. *Handbook of Physical Vapor Deposition (PVD) Processing*. Oxford UK Elsevier, 2010;
- [41] [https://en.wikipedia.org/wiki/Chemical\\_vapor\\_deposition](https://en.wikipedia.org/wiki/Chemical_vapor_deposition);
- [42] [http://www.wikiwand.com/en/Chemical\\_vapor\\_deposition](http://www.wikiwand.com/en/Chemical_vapor_deposition);
- [43] Amin S, Panchal H. *A Review on Thermal Spray Coating Processes*. International Journal of Current Trends in Engineering & Research (IJCTER) e-ISSN 2455-1392 Volume 2 Issue 4, April 2016 pp. 556 - 563;
- [44] Won-Seock K, Il-Han J, Jung-Ju L, Hee-Tae J. *Evaluation of mechanical interlock effect on adhesion strength of polymer-metal interfaces using micro-patterned surface topography*. International Journal of Adhesion and Adhesives 30(6):408-417, September 2010;
- [45] <https://www.materialstoday.com/metal-finishing/features/fundamentals-of-paint-adhesion>;
- [46] Baldan A *Adhesion phenomena in bonded joints International*. Journal of Adhesion & Adhesives 38 (2012) 95-116;
- [47] Neubauer R, Moritz Husmann S, Weinländer C, Kienzl N, Leitner E, Hochenauer C. *Acid base interaction and its influence on the adsorption kinetics and selectivity order of aromatic sulfur heterocycles adsorbing on Ag-Al<sub>2</sub>O<sub>3</sub>*. Institute of Thermal Engineering (3070);
- [48] Simpson V. *Foundamental studies of adhesion*. Master Thesis, University of Wollongong, 1997;

- [49] Ebnesajjad C F. *Surface Treatment of Materials for Adhesion Bonding*. Elsevier, Second edition, 2014;
- [50] Tracton A. *Coating technology handbook*. Taylor & Francis Group, LLC 2006;
- [51] <https://www.astm.org/Standards/D4541.htm>;
- [52] Chalker P R, Bull S J, Rickerby D S. *A review of the methods for the evaluation of coating-substrate adhesion*. Materials Science and Engineering, A 140 ( 1991 ) 583-592;
- [53] Cai Y, Zhang S, Zeng X, Qian M, Sun D, Weng W. *Interfacial study of magnesium-containing fluoridated hydroxyapatite coatings*. Thin Solid Films, 519 (2011) 4629–4633;
- [54] Fletcher J F, Barnes D J. *Pull-off adhesion testing of coating- improve your technique*. Elcometer Limited;
- [55] Choudhary R K, Mishra P. *Use of Acoustic Emission During Scratch Testing for Understanding Adhesion Behavior of Aluminum Nitride Coatings*. Journal of Materials Engineering and Performance, June 2016, Volume 25, Issue 6, pp 2454–2461;
- [56] Campos-Silva I, Martínez-Trinidad J, Doñu-Ruiz M A, Rodríguez-Castro G. Hernández-Sánchez E, Bravo-Bárceñas O. *Interfacial indentation test of FeB/Fe2B coatings*. Surface and Coatings Technology, Vol. 206, Issue 7, 25 December 2011, pp 1809-1815;
- [57] Bouzakis K D, Gerardis S Skordaris G, Bouzakis E. *Nano-impact test on a TiAlN PVD coating and correlation between experimental and FEM results*. Surface and Coatings Technology, Vol. 206, Issue 7, 25 December 2011, pp 1936-1940;
- [58] Mittal K L. *Adhesion Measurement of thin films*. Electrocomponent Science and Technology 1976, Vol. 3, pp. 21-42;
- [59] Martin P M. *Handbook of Deposition Technologies for Films and Coatings Science*. Applications and Technology Book, 3rd Edition, 2010;
- [60] Moira e Silva CW, Alves E, Ramos AR, Sandu CS, Cavaleiro A. *Adhesion failures on hard coatings induced by interface anomalies*. Vacuum 83 (2009) 1213-1217;
- [61] Poorna Chander K, Vashista M, Sabiruddin K, Paul S, Bandyopadhyay P P. *Effects of grit blasting on surface properties of steel substrates*. Materials and design 30 (2009) 2895-2902;
- [62] Varacalle D J, Guillen D, Deason D M, Rhodaberg W. *Effect of Grit-Blasting on Substrate Roughness and Coating Adhesion*. Journal of Thermal Spray Technology, 15(3):348-355, September 2006;
- [63] Danlos Y, Costil S, Liao H, Coddet C. *Influence of Ti-6Al-4V and Al 2107 substrate morphology on Ni-Al coating adhesion-impacts of laser treatment*. Surface and coating technology, 205 (2011) 2702-2708;
- [64] Kromer R, Costil S, Cormier J, Courapiéd D, Berthe L, Peyre P, Boustie M. *Laser surface patterning to enhance adhesion of plasma sprayed coatings*. Surface and coatings technology, 278 (2015) 171-182;
- [65] Rahamati B, Zalnezhad E, Sarhan A A D, Kamiab Z, Nasiri Tabrizi B, Abas W A B W. *Enhancing the adhesion strength of tantalum oxide ceramic thin film coating on biomedical Ti-6Al-4V alloy by thermal surface treatment*. Ceramics international, 41 (2015) 13055-13063;

- [66] <https://www.medeco.de/it/odontostomatologia/anatomia/cavita-orale/struttura-della-cavita-orale/>;
- [67] <https://freemile.com/anatomia-della-bocca/anatomia-dei-denti/>;
- [68] <https://it.wikipedia.org/wiki/Gingiva>;
- [69] Mortazavi H, Baharvand M. *Review of common conditions associated with periodontal ligament widening*. Imaging Science in Dentistry, 2016 Dec; 46(4): 229-237;
- [70] Yamamoto T, Hasegawa T, Yamamoto T, Hongo H, Amizuka N. *Histology of human cementum: Its structure, function, and development*. Journal List, Jpn Dent Sci Rev. 2016 Aug; 52 (3): 63-74;
- [71] <https://www.dental.pitt.edu/bone-structural-characteristics>;
- [72] <https://www.webmd.com/oral-health/guide/gingivitis-periodontal-disease>;
- [73] Jayesh R S, Dhinakarsamy V. *Osseointegration*. Dental science- Research article, 2015, Vol. 7; Issue 5; p. 226-229;
- [74] <https://en.wikipedia.org/wiki/Osseointegration>;
- [75] Branemark P I. *The Osseointegration Book - From Calvarium to Calcaneus*. USA: Quintessence Books; 2005. p. 24;
- [76] Branemark P I. *Tissue-Integrated Prosthesis*. Chicago: Quintessence Publishing Co.; 1985. p. 11-76;
- [77] Signoriello F, Fallschussel G K H. *Implantologia odontoiatrica: teoria e pratica*. Edinava, 198;
- [78] <http://www.ing.unitn.it/~colombo/Materiali%20per%20l'implantologia%20dentale/9.%20L'implantologia%20dentale.htm>;
- [79] <https://www.smilesolutionsbyemmidental.com/blog/the-anatomy-of-a-dental-implant>;
- [80] Oshida Y, Tuna E B, Aktoren O, Gençay K. *Dental Implant Systems*. International Journal of Molecular Sciences, 2010, 11, 1580-1678;
- [81] Fatma B, Cengiz Y. *The Mechanical Behaviors of Various Dental Implant Materials under Fatigue*. Hindawi Advances in Materials Science and Engineering Volume 2018, Article ID 5047319, 10 pages;
- [82] Violan D, Galofre M, Nart J, Teles R P. *In vitro evaluation of a multispecies oral biofilm on different implant surfaces*. Biomed Mater 2014;9:035007;
- [83] Han A, Tsoi J K H, Pires Rodrigues F, Leprince J G, Palin W M. *Bacterial adhesion mechanisms on dental implant surfaces and the influencing factor*. International Journal of Adhesion and Adhesive 69 (2016) 58-71;
- [84] Teughels W, Van Assche N, Sliepen I, Quirynen M. *Effect of material characteristics and/or surface topography on biofilm development*. Clinical Oral Implants Research, 2016, 17, 68-81;
- [85] Cerone G. *TESI: Trattamenti superficiali alla nanoscala (topografia e nanofibre di cheratina) su titanio per incrementare l'adesione di fibroblasti gengivali e ridurre l'adesione batterica*. Master degree thesis, Politecnico di Torino, Ottobre 2016;

- [86] [https://en.wikipedia.org/wiki/Plasma\\_activation](https://en.wikipedia.org/wiki/Plasma_activation);
- [87] <https://www.gambetti.it/portfolio-articoli/tucano-plasma-a-bassa-pressione/>;
- [88] <https://it.scribd.com/doc/312685009/titanio-ti-6al-4v>;
- [89] [http://www.tecotex.it/documenti/Pure-Health\\_brochure.pdf](http://www.tecotex.it/documenti/Pure-Health_brochure.pdf);
- [90] Iwasa F, Hori N, Ueno T, Minamikawa H, Yamada M, Ogawa T. *Enhancement of osteoblast adhesion to UV-photofunctionalized titanium via an electrostatic mechanism*. *Biomaterials* 31 (2010) 2717–2727;
- [91] Beachley V, Wenab X. *Effect of electrospinning parameters on the nanofiber diameter and length*. *Materials Science and Engineering: C*, Vol. 29, Issue 3, 30 April 2009, pp 663-668;
- [92] Kurecic M. *Electrospinning: Nanofibre Production Method*. *Tekstilec*, 56(1):4-12, March 2013;
- [93] Haider A, Haider S, Kanga I. *A comprehensive review summarizing the effect of electrospinning parameters and potential applications of nanofibers in biomedical and biotechnology*. *Arabian Journal of Chemistry*, Vol. 11, Issue 8, December 2018, pp 1165-1188;
- [94] Kalidindi R S R, Subasri R. *Sol-gel nanocomposite hard coatings*. *Anti-Abrasive Nanocoatings, Current and Future Applications*, 2015, pp 105-136;
- [95] <https://www.nanoscience.com/techniques/scanning-electron-microscopy/>;
- [96] [https://en.wikipedia.org/wiki/Scanning\\_electron\\_microscope](https://en.wikipedia.org/wiki/Scanning_electron_microscope);
- [97] [http://www.vcbio.science.ru.nl/public/pdf/fesem\\_info\\_eng.pdf](http://www.vcbio.science.ru.nl/public/pdf/fesem_info_eng.pdf);
- [98] [http://www.chimica.unifi.it/upload/sub/LAUREA/PUB/20122013/ELABORATI/anichini\\_cosimo\\_e.pdf](http://www.chimica.unifi.it/upload/sub/LAUREA/PUB/20122013/ELABORATI/anichini_cosimo_e.pdf);
- [99] Mitutoyo. *Quick guide to surface roughness measurement. Reference guide for laboratory and workshop*. Bulletin No. 2229;
- [100] [https://en.wikipedia.org/wiki/Confocal\\_microscopy](https://en.wikipedia.org/wiki/Confocal_microscopy);
- [101] ZEISS LSM800 for Materials brochure;
- [102] Toshihiro T, Joonho L, Piotr R S. *Interfacial Free Energy and Wettability*. *Treatise on Process Metallurgy Volume 2: Process Phenomena* 2014, pp 61-77;
- [103] Luxbacher T. *The Zeta Potential for Solid Surface Analysis*. 1st edition, Austrian March 2014;
- [104] <http://rtilab.com/techniques/ftir-analysis/>
- [105] *Introduction to Fourier Transform Infrared Spectrometry*, Thermo Nicolet Corporation, 2001;
- [106] [https://it.wikipedia.org/wiki/Legge\\_di\\_Bragg](https://it.wikipedia.org/wiki/Legge_di_Bragg);
- [107] <https://xpssimplified.com/whatisxps.php>;
- [108] [http://www.casaxps.com/help\\_manual/manual\\_updates/xps\\_spectra.pdf](http://www.casaxps.com/help_manual/manual_updates/xps_spectra.pdf);
- [109] Sartori A. *Surface modification of titanium for improvement of soft tissue adhesion and reduction of bacterial contamination*. Master thesis, Politecnico di Torino, April 2018;

- [110] Mekayarajjanonth T, Winkler S. *Contact angle measurement on dental implant biomaterials*. Journal of Oral Implantology, 25 (1999), pp. 230-236;
- [111] Fowkes F M. *Acid-base interaction in polymer adhesion*. Surface and Coatings Research, Lehigh University, Bethlehem, Pa 18015;
- [112] <https://webspectra.chem.ucla.edu/irtable.html>;
- [113] Aluigi A, Corbellini A, Rombaldoni F, Zoccola M, Canetti M. *Morphological and structural investigation of wool derived keratin nanofibres crosslinked by thermal treatment*. International Journal of Biological Macromolecules 57 (2013) 30-37;
- [114] Wang K, Li R, Ma J, Jian Y. *Extracting keratin from wool by using L-cysteine*. Green Chemistry 18(2), July 2015;
- [115] Tesi
- [116] Molina R, Espinos J P, Yubero F, Erra P, Gonzalez-Elipe A R. *XPS analysis of downstream plasma treated wool: Influence of the nature of the gas on the surface modification of wool*. Applied Surface Science, 252, (2005) 1417-1429;
- [117] Michael J R, Johnston H. *Sorption and binding of nanocrystalline gold by Merino wool fibres—An XPS study*. Journal of Colloid and Interface Science 310 (2007) 425-430;
- [118] <http://www.xpsfitting.com>;
- [119] Trino L D, Bronze-Uhle E S, George A, Mathew M T, Lisboa-Filho P N. *Surface Physicochemical and Structural Analysis of Functionalized Titanium Dioxide Films*. Colloids and Surfaces A: Physicochemical and Engineering Aspects Volume 546, 5 June 2018, Pages 168-178;
- [120] Ferraris S, Truffa Giachet F, Miola M, Bertone E, Varesano A, Vineis C, Cochis A, Sorrentino R, Rimondini L, Spriano S. *Nanogrooves and keratin nanofibers on titanium surfaces aimed at driving gingival fibroblasts alignment and proliferation without increasing bacterial adhesion*. Materials Science and Engineering C, 76 (2017) 1-12;

**Images**

- F1** Khosa M, Ullah A. *A Sustainable Role of Keratin Biopolymer in Green Chemistry: A Review*. Journal of Food Processing & Beverages, September 2013 Vol.:1, Issue:1;
- F2** <https://www.newworldencyclopedia.org/entry/Keratin>;
- F3** Alberts B, Bray D, Lewis J, Raff M, Roberts K, Watson J D. *Molecular Biology of the Cell*, 1994, 3rd edition, Garland Press, New York;
- F4** <https://www.newworldencyclopedia.org/entry/Keratin>;
- F5** Wang B, Yang W, McKittrick J, Meyers MA. *Keratin: Structure, mechanical properties, occurrence in biological organisms, and efforts at bioinspiration*, 2015, University of California, San Diego, La Jolla, United States;
- F6** Wang B, Yang W, McKittrick J, Meyers MA. *Keratin: Structure, mechanical properties, occurrence in biological organisms, and efforts at bioinspiration*, 2015, University of California, San Diego, La Jolla, United States;
- F7** Wang B, Yang W, McKittrick J, Meyers MA. *Keratin: Structure, mechanical properties, occurrence in biological organisms, and efforts at bioinspiration*, 2015, University of California, San Diego, La Jolla, United States;
- F8** Wang B, Yang W, McKittrick J, Meyers MA. *Keratin: Structure, mechanical properties, occurrence in biological organisms, and efforts at bioinspiration*, 2015, University of California, San Diego, La Jolla, United States;
- F9** Wang B, Yang W, McKittrick J, Meyers MA. *Keratin: Structure, mechanical properties, occurrence in biological organisms, and efforts at bioinspiration*, 2015, University of California, San Diego, La Jolla, United States;
- F10** Wang B, Yang W, McKittrick J, Meyers MA. *Keratin: Structure, mechanical properties, occurrence in biological organisms, and efforts at bioinspiration*, 2015, University of California, San Diego, La Jolla, United States;
- F11** Szewciw L, de Kerckhove D G, Grime G W, Fudge D. *Calcification provides mechanical reinforcement to whale baleen keratin*. Proceeding of the Royal Society B: Biological Sciences 277(1694): 2597-605, April 2010;
- F12** Wang B, Yang W, McKittrick J, Meyers MA. *Keratin: Structure, mechanical properties, occurrence in biological organisms, and efforts at bioinspiration*, 2015, University of California, San Diego, La Jolla, United States;
- F13** Shui-qing J, Lin Z, Haixia W, Gang C. *Study on effective extraction of keratin from human hair wastes*. Integrated Ferroelectrics 180(1):102-107, May 2017;
- F14** <https://www.inovanewsroom.org/ilh/2017/05/wound-healing-center-at-invaloudoun-treats-complex-wound-and-ostomy-cases/>;
- F15** Wang S, Taraballi F, L. Poh, Woei TK, Human keratin hydrogels support fibroblast attachment and proliferation in vitro, Cell Tissue Res (2012) 347, pp 795–802;
- F16** Wang S, Taraballi F, L. Poh, Woei TK, Human keratin hydrogels support fibroblast attachment and proliferation in vitro, Cell Tissue Res (2012) 347, pp 795–802;
- F17** Esparza Y, Ullah A, Boluk Y, Wu J. *Preparation and characterization of thermally crosslinked poly(vinyl alcohol)/featherkeratin nanofiber scaffolds*. Materials and Designs 133(2017) 1-9;
- F18** Esparza Y, Ullah A, Boluk Y, Wu J. *Preparation and characterization of thermally crosslinked poly(vinyl alcohol)/featherkeratin nanofiber scaffolds*. Materials and Designs 133(2017) 1-9;

- F19** Zhao X, Lui Y S, Chuen Choo C K, Sow W T, Huang C L, Woei Ng K, Poh Tan L, Chye Loo J S. *Calcium phosphate coated keratin-PCL scaffolds for potential bone tissue regeneration*. Materials Sciences and Engineering: C, April 2015, Vol 24, pp 746-753;
- F20** Fadillah G, Putri E N K, Febrianastuti S, Maylinda E V, Purnawan C. *Adsorption of Fe Ions from Aqueous Solution Using  $\alpha$ -Keratin-Coated Alginate Biosorbent*. International Journal of Environmental Science and Development, Vol. 9, No. 3, March 2018;
- F21** <https://www.sigmaaldrich.com/materials-science/material-science-products.html?TablePage;>
- F22** Pajkic Z, Wolf H, Gerdes T, Willert-Porada M. *Microwave plasma fluidized bed arc-PVD coating of particulate materials*, Surface and Coatings Technology, May 2008, 202(16):3927-3932;
- F23** Mattox D.M. Handbook of Physical Vapor Deposition (PVD) Processing, Oxford UK Elsevier, 2010;
- F24** Mathur S, Shen H, Altmayer J. *Nanostructured functional ceramic coatings by molecule-based chemical vapor deposition.*, Reviews on Advanced Materials Science, 15(2007) 16-23;
- F25** <https://www.slideshare.net/anshukg/chemical-vapor-deposition-cvd;>
- F26** [https://www.researchgate.net/figure/Thermal-spray-process-principle-Source-An-Introduction-to-Thermal-Spray-Issue-4-C\\_fig1\\_307944165;](https://www.researchgate.net/figure/Thermal-spray-process-principle-Source-An-Introduction-to-Thermal-Spray-Issue-4-C_fig1_307944165;)
- F27** Amin S, Panchal H. A Review on Thermal Spray Coating Processes. International Journal of Current Trends in Engineering & Research (IJCTER) e-ISSN 2455-1392 Volume 2 Issue 4, April 2016 pp. 556 – 563;
- F28** <http://www.advanced-coating.com/english/spraying-hvof.htm;>
- F29** Li J, Li C, Yang G, Li C. *Effect of vapor deposition in shrouded plasma spraying on morphology and wettability of the metallic Ni20Cr coating surface*. Elsevier Journal of Alloys and Compounds, Vol. 735, 25 February 2018, pp 430-440;
- F30** <https://www.indiamart.com/proddetail/phosphate-coating-16503155030.html;>
- F31** *Aluminum Electroplating Using Bromide Salts*, FEBRUARY 1, 2018, MANUFACTURING & PROTOTYPING, MATERIALS;
- F32** [http://jffjonesjewelers.com/rhodium-plating/;](http://jffjonesjewelers.com/rhodium-plating/)
- F33** . Amin S, Panchal H. A Review on Thermal Spray Coating Processes. International Journal of Current Trends in Engineering & Research (IJCTER) e-ISSN 2455-1392 Volume 2 Issue 4, April 2016 pp. 556 – 563;
- F34** . Amin S, Panchal H. A Review on Thermal Spray Coating Processes. International Journal of Current Trends in Engineering & Research (IJCTER) e-ISSN 2455-1392 Volume 2 Issue 4, April 2016 pp. 556 – 563;
- F35** Baldan A *Adhesion phenomena in bonded joints International*. Journal of Adhesion & Adhesives 38 (2012) 95-116;
- F36** Neubauer R, Moritz Husmann S, Weinländer C, Kienzl N, Leitner E, Hochenauer C. *Acid base interaction and its influence on the adsorption kinetics and selectivity order of aromatic sulfur heterocycles adsorbing on Ag-Al<sub>2</sub>O<sub>3</sub>*. Institute of Thermal Engineering (3070);
- F37** Baldan A *Adhesion phenomena in bonded joints International*. Journal of Adhesion & Adhesives 38 (2012) 95-116;

- F38** Baldan A *Adhesion phenomena in bonded joints International*. Journal of Adhesion & Adhesives 38 (2012) 95–116;
- F39** Baldan A *Adhesion phenomena in bonded joints International*. Journal of Adhesion & Adhesives 38 (2012) 95–116;
- F40** Tracton A. *Coating technology handbook*. Taylor & Francis Group, LLC 2006;
- F41** Ray A. *Intermolecular forces give rise to cohesion in water molecules*. Jul 16, 2017;
- F42** Ray A. *Intermolecular forces give rise to cohesion in water molecules*. Jul 16, 2017;
- F43** Ray A. *Intermolecular forces give rise to cohesion in water molecules*. Jul 16, 2017;
- F44** Baldan A *Adhesion phenomena in bonded joints International*. Journal of Adhesion & Adhesives 38 (2012) 95–116;
- F45** Tracton A. *Coating technology handbook*. Taylor & Francis Group, LLC 2006;
- F46** Chalker P R, Bull S J, Rickerby D S. . *A review of the methods for the evaluation of coating-substrate adhesion*. Materials Science and Engineering, A 140 ( 1991 ) 583-592;
- F47** <https://dfdinstruments.com/astm-d4541-iso-4624/>;
- F48** Cai Y, Zhang S, Zeng X, Qian M, Sun D, Weng W. *Interfacial study of magnesium-containing fluoridated hydroxyapatite coatings*. Thin Solid Films, 519 (2011) 4629–4633;
- F49** Tracton A. *Coating technology handbook*. Taylor & Francis Group, LLC 2006;
- F50** [http://www.substech.com/dokuwiki/doku.php?id=adhesion\\_tests](http://www.substech.com/dokuwiki/doku.php?id=adhesion_tests);
- F51** Sergici Onur A, Randall N. *Scratch Testing of Coatings*. Advanced Materials and Processes, April 2006;
- 52** Choudhary R K, Mishra P. *Use of Acoustic Emission During Scratch Testing for Understanding Adhesion Behavior of Aluminum Nitride Coatings*. Journal of Materials Engineering and Performance, June 2016, Volume 25, Issue 6, pp 2454–2461;
- F53** Choudhary R K, Mishra P. *Use of Acoustic Emission During Scratch Testing for Understanding Adhesion Behavior of Aluminum Nitride Coatings*. Journal of Materials Engineering and Performance, June 2016, Volume 25, Issue 6, pp 2454–2461;
- F54** Tracton A. *Coating technology handbook*. Taylor & Francis Group, LLC 2006;
- F55** Campos-Silva I, Martínez-Trinidad J, Doñu-Ruiz M A, Rodríguez-Castro G. Hernández-Sánchez E, Bravo-Bárceñas O. *Interfacial indentation test of FeB/Fe2B coatings*. Surface and Coatings Technology, Vol. 206, Issue 7, 25 December 2011, pp 1809-1815;
- F56** Tracton A. *Coating technology handbook*. Taylor & Francis Group, LLC 2006;
- F57** Tracton A. *Coating technology handbook*. Taylor & Francis Group, LLC 2006;
- F58** Moira e Silva CW, Alves E, Ramos AR, Sandu CS, Cavaleiro A. *Adhesion failures on hard coatings induced by interface anomalies*. Vacuum 83 (2009) 1213-1217;
- F59** Moira e Silva CW, Alves E, Ramos AR, Sandu CS, Cavaleiro A. *Adhesion failures on hard coatings induced by interface anomalies*. Vacuum 83 (2009) 1213-1217;
- F60** Varacalle D J, Guillen D, Deason D M, Rhodaberg W. *Effect of Grit-Blasting on Substrate Roughness and Coating Adhesion*. Journal of Thermal Spray Technology, 15(3):348-355, September 2006;
- F61** Varacalle D J, Guillen D, Deason D M, Rhodaberg W. *Effect of Grit-Blasting on Substrate Roughness and Coating Adhesion*. Journal of Thermal Spray Technology, 15(3):348-355, September 2006;

- F62** Varacalle D J, Guillen D, Deason D M, Rhodaberg W. *Effect of Grit-Blasting on Substrate Roughness and Coating Adhesion*. Journal of Thermal Spray Technology, 15(3):348-355, September 2006;
- F63** Kromer R, Costil S, Cormier J, Courapied D, Berthe L, Peyre P, Boustie M. *Laser surface patterning to enhance adhesion of plasma sprayed coatings*. Surface and coatings technology, 278 (2015) 171-182;
- F64** Kromer R, Costil S, Cormier J, Courapied D, Berthe L, Peyre P, Boustie M. *Laser surface patterning to enhance adhesion of plasma sprayed coatings*. Surface and coatings technology, 278 (2015) 171-182;
- F65** Kromer R, Costil S, Cormier J, Courapied D, Berthe L, Peyre P, Boustie M. *Laser surface patterning to enhance adhesion of plasma sprayed coatings*. Surface and coatings technology, 278 (2015) 171-182;
- F66** Rahamati B, Zalnezhad E, Sarhan A A D, Kamiab Z, Nasiri Tabrizi B, Abas W A B W. *Enhancing the adhesion strength of tantalum oxide ceramic thin film coating on biomedical Ti-6Al-4V alloy by thermal surface treatment*. Ceramics international, 41 (2015) 13055-13063;
- F67** Rahamati B, Zalnezhad E, Sarhan A A D, Kamiab Z, Nasiri Tabrizi B, Abas W A B W. *Enhancing the adhesion strength of tantalum oxide ceramic thin film coating on biomedical Ti-6Al-4V alloy by thermal surface treatment*. Ceramics international, 41 (2015) 13055-13063;
- F68** Tracton A. *Coating technology handbook*. Taylor & Francis Group, LLC 2006;
- F69** <https://headandneckcancerguide.org/adults/introduction-to-head-and-neck-cancer/oral-cancers/basics/anatomy/>;
- F70** <https://www.alamy.de/zahn-anatomie-infografiken-realistische-weisse-zahn-mockup-oral-care-health-concept-medizinische-banner-oder-poster-vector-illustration-image212420561.html>;
- F71** <https://dentalspecialistsmk.com/gum-treatment/>;
- F72** <https://www.aomsurgery.com/dental-implants/cost-of-implants/>;
- F73** Panda A. *Types of Dental Implants: Endosteal, Transosteal & Subperiosteal*. Dental Braces, Health Tips, Feb 2017;
- F74** Sakaguchi R, Powers J *Craig's Restorative Dental Materials*. 13rd edition, Mosby, 2012, Pages 355-367;
- F75** <https://www.slideshare.net/AElhlawany/dental-implants-47922112>
- F76** <https://pt.slideshare.net/marcusharris086/types-of-dental-implant>;
- F77** <https://www.friscooralsurgery.com/procedures/dental-implants/>
- F78** Fatma B, Cengiz Y. *The Mechanical Behaviors of Various Dental Implant Materials under Fatigue*. Hindawi Advances in Materials Science and Engineering Volume 2018, Article ID 5047319, 10 pages;
- F79** Violan D, Galofre M, Nart J, Teles R P. *In vitro evaluation of a multispecies oral biofilm on different implant surfaces*. Biomed Mater 2014;9:035007;
- F80** Violan D, Galofre M, Nart J, Teles R P. *In vitro evaluation of a multispecies oral biofilm on different implant surfaces*. Biomed Mater 2014;9:035007;
- F81** Ramesh T, Nayak K, Amirbahman A, Tripp C P, Mukhopadhyay s. *Application of ultraviolet light assisted titanium dioxide photocatalysis for food safety: A review*. Innovative Food Science & Emerging Technologies Volume 38, Part A, December 2016, pp 105-115;

- F82** Iwasa F, Hori N, Ueno T, Minamikawa H, Yamada M, Ogawa T. *Enhancement of osteoblast adhesion to UV-photofunctionalized titanium via an electrostatic mechanism*. *Biomaterials* 31 (2010) 2717–2727;
- F83** Ghorani B, Tucker N. *Fundamentals of electrospinning as a novel delivery vehicle for bioactive compounds in food nanotechnology*. *Food Hydrocolloids* Volume 51, October 2015, Pages 227-240;
- F84** <https://nptel.ac.in/courses/116102006/20>;
- F85** Angamma C J, Jayaram, S H. *A theoretical understanding of the physical mechanisms of electrospinning*. Proceedings of ESA Annual Meeting on Electrostatics 2011 pp. 1-9, Cleveland, USA, June 2011, 2011;
- F86** <https://www.steeldoor.org/T-DOC/ansi-250-3.php>
- F87** <https://www.elcometer.com/en/coating-inspection/adhesion-testers/cross-hatch-adhesion-testers/elcometer-107-cross-hatch-cutter.html>;
- F88** Kalidindi R S R, Subasri R. *Sol-gel nanocomposite hard coatings*. *Anti-Abrasive Nanocoatings, Current and Future Applications*, 2015, pp 105-136;
- F89** <https://www2.nau.edu/micro-analysis/wordpress/index.php/instrumentation/>;
- F90** <https://www.nanoscience.com/techniques/scanning-electron-microscopy/>;
- F91** Jusman Y, Cheok Ng S, Osman N A A. *Investigation of CPD and HMDS Sample Preparation Techniques for Cervical Cells in Developing Computer-Aided Screening System Based on FE-SEM/EDX*. *The Scientific World Journal*, September 2014;
- F92** Mitutoyo. *Quick guide to surface roughness measurement. Reference guide for laboratory and workshop*. Bulletin No. 2229;
- F93** [https://www.keyence.com/ss/products/microscope/roughness/equipment/line\\_01.jsp](https://www.keyence.com/ss/products/microscope/roughness/equipment/line_01.jsp);
- F94** ZEISS LSM800 for Materials brochure;
- F95** ZEISS LSM800 for Materials brochure;
- F96** Toshihiro T, Joonho L, Piotr R S. *Interfacial Free Energy and Wettability*. *Treatise on Process Metallurgy Volume 2: Process Phenomena* 2014, pp 61-77;
- F97** Luxbacher T. *The Zeta Potential for Solid Surface Analysis*. 1st edition, Austriam March 2014;
- F98** Luxbacher T. *The Zeta Potential for Solid Surface Analysis*. 1st edition, Austriam March 2014;
- F99** <https://photobioschool.ru/en/methods-en/ftir-spectroscopy/>;
- F100** Bunaciu A A, Udriș Tioiu E G, Aboul-Enein H Y. *X-Ray Diffraction: Instrumentation and Applications*. *Critical Reviews in Analytical Chemistry* 45(4), April 2015;
- F101** [https://it.wikipedia.org/wiki/Legge\\_di\\_Bragg](https://it.wikipedia.org/wiki/Legge_di_Bragg);
- F102** <https://xpssimplified.com/whatisxps.php>;
- 103** <http://imma-eneas.schematic.lautschriftmagazin.de/diagram/xps-instrumentation.html>;
- F104** <https://www2.nau.edu/micro-analysis/wordpress/index.php/instrumentation/>;
- F105** <https://www.nanoscience.com/techniques/scanning-electron-microscopy/>;
- F106** <https://www.indiamart.com/proddetail/hydrolyzed-keratin-17905041862.html>;

**Tables**

**T1** Rajabinejad H, Zoccola M, Patrucco A, Montarsolo A, Rovero G and Tonin C. *Physico-chemical properties of keratin extracted from wool by various methods*. Textile Research Journal 1–10 ;

**T2** [https://en.wikipedia.org/wiki/Gram-positive\\_bacteria](https://en.wikipedia.org/wiki/Gram-positive_bacteria);